The Pennsylvania State University
The Graduate School

NEUTRINO AND ELECTROMAGNETIC COUNTERPARTS OF GALAXY AND ASTROPHYSICAL BLACK HOLE MERGERS

A Dissertation in
Physics
by
Chengchao Yuan

© 2022 Chengchao Yuan

Submitted in Partial Fulfillment
of the Requirements
for the Degree of

Doctor of Philosophy

August 2022

The dissertation of Chengchao Yuan was reviewed and approved by the following:

Peter Mészáros
Eberly Chair Professor Emeritus, Astronomy & Astrophysics and Physics
Director Emeritus, Center for Multimessenger Astrophysics
Dissertation Co-Advisor
Chair of Committee

Kohta Murase
Associate Professor of Physics and Astronomy & Astrophysics
Dissertation Co-Advisor

Miguel Alejandro Mostafá
Professor of Physics and Astronomy & Astrophysics
Associate Dean for Research and Innovation

Douglas Cowen
Professor of Physics

Donghui Jeong
Associate Professor of Astronomy & Astrophysics

Nitin Samarth
Professor of Physics
George A. and Margaret M. Downsbrough Department Head

Abstract

The historical coincident detection of gravitational waves (GWs) and electromagnetic (EM) counterparts from the binary neutron star merger event GW 170817 heralds a new era in multi-messenger astronomy. At the same time, since the first discovery of the high-energy astrophysical neutrinos in 2012 by IceCube, neutrino astrophysics has made significant progress and has started playing an increasingly important role in multi-messenger analyses. We are currently in the stage where we can probe the nature of the extreme astrophysical phenomena with the synergies between EM photons, neutrinos, GWs, and cosmic rays.

In this dissertation, I start with an overview of the development of multi-messenger astrophysics and its application to astrophysical mergers. I will present our work on the cumulative diffuse neutrino background from galaxy/cluster mergers and show that our scenario can explain the diffuse neutrino flux without violating the extragalactic γ-ray background constraints (chapter 2). We further demonstrate that the synchrotron and inverse Compton emissions produced by secondary electrons/positrons are consistent with the radio and X-ray observations of merging galaxies such as NGC 660 and NGC 3256 (chapter 3). In chapters 4 & 5, we focus on the jet-induced neutrino and EM counterparts from supermassive black hole (SMBH) mergers subsequent to GW radiation and discuss the detection perspectives for the ongoing and next-generation neutrino, optical, and GW missions. The short γ-ray bursts, which are generally thought to arise from compact binary object (CBO) mergers, could be promising candidates for multi-messenger studies. We then consider a special scenario where short GRBs are embedded in disks of active galactic nuclei (AGN) and investigate their GeV signatures in chapter 6.

In a separate effort, we study the stacking and multiplet constraints on the blazar contribution to the cumulative diffuse neutrino flux, assuming a generic relationship between neutrino and γ-ray luminosities (chapter 7). We show that these two limits are complementary, and our results support the argument that blazars are disfavored as the dominant sources of the 100-TeV neutrino background. This work provides rather general and stringent constraints for future studies of blazar neutrinos.

Table of Contents

List of Figures

List of Tables

Acknowledgments

I would first of all like to express my deep gratitude to my mentor, Dr. Peter Mészáros. In 2015, Peter invited me to visit Penn State as an undergraduate intern working in the high-energy astrophysics group. It was the first time I got a glimpse of neutrino astrophysics. Since then, I embarked on an adventure pursuing the tracks of these elusive but attracting particles lurking in the universe. I always found Peter's guidance and support in every progress I made during this journey. I learned a great deal from him through numerous discussions. He is always there to help whenever I encounter obstacles in a research project, from theoretical calculations to paper writing to scientific presentations and more. His kindness, patience, and expertise in high-energy astrophysics (and beyond) have constantly encouraged me to be a better scientist and a better person.

I am also very grateful to my advisor, Dr. Kohta Murase. His enthusiasm and diligence for science have greatly motivated me throughout my graduate study. I remember many times we discussed the technical problems over email until midnight. He can always provide insightful ideas and suggestions for my work. With his great help, I was able to convert an initial idea into a journal article with a high degree of completeness. His careful, rigorous, and responsible working attitude also inspired me to pursue perfection in my research.

Over the past few years, I have enjoyed working and exchanging ideas with many talented peers, postdocs, and professors. I would like to thank Dr. Donghui Jeong, Dr. Shigeo S. Kimura, Dr. B. Theodore Zhang, Dr. Dafne Guetta, Dr. Imre Bartos, Dr. Asaf Pe'er, Dr. Nicholas Senno, Dr. Ali Kheirandish, Dr. Marco Ajello, Dr. Nick Rodd, Dr. Zsuzsa Márka, Dr. Szabolcs Márka, Ph.D. candidate Jose Carpio, and Ph.D. candidate Yu Jiang. I gratefully acknowledge my dissertation committee: Dr. Miguel Mostafá, Dr. Douglas Cowen, and Dr. Donghui Jeong, for their helpful comments and suggestions on my road to a Ph.D.

Finally, I would like to express my deep gratitude to my family for their endless and unconditional love, help, and support. I also would like to express my loving thanks to my partner, Yijia Li, for being part of my life. It is a pleasure to thank my friends at Penn State, Zhaowei Zhang, Jiayin Dong, Zhao Guo, and Matthias Yang He, for the wonderful times we shared, especially the Friday night dinners and board games. In addition, I would like to thank Jiali Lu, Yifan Zhao, Run Xiao, Tongzhou Zhao, Guang Yang, Monong Yu, Ding Ding, Songyang Pu, Yicheng Zhang, Ningxiao Zhang, and many others, who made my life at State College memorable.

The work presented in this dissertation is supported by NASA under the Grant No. NNX13AH50G, by the Alfred P. Sloan Foundation and NSF grant No. PHY-1620777, No. AST-1517363, No. AST-2108466, No. AST-2108467, No. PHY-1911796, No. PHY-2110060, and No. AST-1908689, by the JSPS Research Fellowship and KAKENHI No. 20H01901, No. 20H05852, and No. 19J00198, by the Eberly Foundation and the IGC Fellowship, and by the European Research Council via ERC consolidating grant 773062 (acronym O.M.J.). The findings and conclusions do not necessarily reflect the view of the funding agencies.

Chapter 1
Introduction

1.1 The Multi-Messenger Astrophysics

Our understanding of the Universe has been continuously updated with the emergence of new techniques of astronomical observations. Since the time of Galileo, we have accumulated knowledge of the astronomical object and the Universe itself based on the information carried by visible light. Multi-wavelength astronomy was established and developed during the last few decades as the advancing radio, infrared, ultra-violet, optical, X-ray, and γ-ray telescopes were built. In contrast to the long-standing use of the first messenger produced by the electromagnetic (EM) force, the astrophysical applications of messengers such as cosmic rays (CRs), neutrinos, and gravitational waves (GWs), were realized after the mid-20th century. Currently, we are able to combine the unique properties of two or more of these messengers to explore the physics of astrophysical phenomena from different perspectives.

1.1.1 Electromagnetic (EM) Photons

Extensive multi-wavelength studies of the EM emissions from gamma-ray bursts (GRBs), tidal disruption events (TDEs), supernovae, active galactic nuclei (AGNs), and galaxies had provided valuable information to construct the theoretical models before the CRs, neutrinos, and GWs were used for astrophysical observations. From radio ($\sim$GHz) to γ-ray bands ($<$1 TeV), the telescopes and observatories, such as the Very-Large Array (VLA), Atacama Large Millimeter/submillimeter Array (ALMA), Hubble Space Telescope (HST), James Webb Space Telescope (JWST), Chandra X-ray Observatory, Swift Telescope, and the *Fermi* Space Telescope, can typically achieve decent angular resolution and flux sensitivities, which leads to the expanding samples of the sources

and increasingly precise models. In 2015, *Fermi* collaboration reported the spectrum of the extragalactic gamma-ray background (EGB) between 100 MeV and ∼800 GeV by summing the isotropic gamma-ray background (IGRB) intensity and the cumulative intensity from resolved sources [1]. In the following text, we will show the power of combining the EGB spectrum with diffuse neutrino observations in constraining the redshift distributions and radiation mechanisms of cosmological sources.

In the higher energy range between 100 GeV and 100 TeV, the ground-based Imaging Air Cherenkov Telescopes (IACTs), e.g., Major Atmospheric Gamma Imaging Cherenkov Telescopes (MAGIC), High Energy Stereoscopic System (HESS), Very Energetic Radiation Imaging Telescope Array System (VERITAS), and the High-Altitude Water Cherenkov Observatory (HAWC) [2] observe the luminous sources in the very-high-energy (VHE) γ-ray bands by measuring particle and electromagnetic cascades in the atmosphere or water tanks induced by the interactions between VHE γ-rays and the medium. The detection of VHE γ rays of the two GRBs, GRB 190114C [3, 4] and GRB 180720B [5], broadens our view of relativistic jets and shocks, and demonstrates the great potential of the VHE γ-ray astrophysics. In the future, with the deployment and operation of the next-generation detectors such as the Cherenkov Telescope Array (CTA) [6] and the water Cherenkov detector array in the Large High Altitude Air Shower Observatory (LHAASO-WCDA) [7], we expect to see more distant γ-ray sources at TeV-PeV γ-ray energies due to their very wide energy ranges and excellent angular resolution and sensitivities (see Fig. 1.1).

From the multi-messenger point of view, contemporaneous multi-wavelength observations by different types of telescopes would be indispensable to distribute the alert to non-EM detectors and follow up the detections using other messengers. In practice, the telescopes with a large field of view (FOV), e.g., the Square Kilometer Array (SKA), Large Spectroscopic Survey Telescope (LSST) [8], Swift, *Fermi*, and the Space Variable Object Monitor (SVOM) [9], can quickly localize the position of the target. After that, we can use the putative positional information from the initial follow-up imaging to guide the observation of narrower FOV telescopes. The Zwicky Transient Facility (ZTF) [10] will play an important role in generating real-time alerts for transients in optical bands and determining the significance of multi-messenger follow-ups.

1.1.2 Cosmic Rays (CRs)

In the early 20th century, Victor Hess first discovered the CRs in his ballon experiment by determining that the radiation intensity increases with altitude. Over the past few

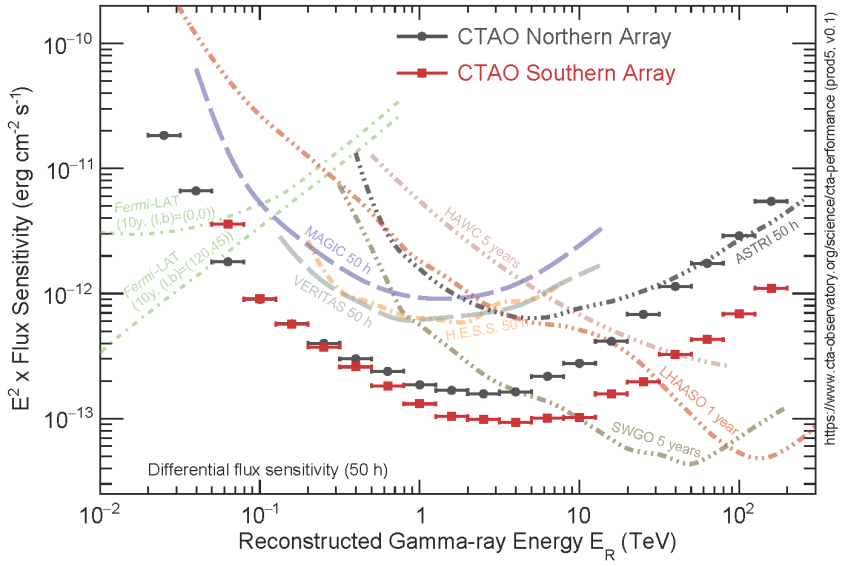

Figure 1.1. Differential sensitivities for CTA (50 hours), MAGIC (50 hours), VERITAS (50 hours), HESS (50 hours), HAWC (5 years), LHAASO (1 year), SWGO (5 years), and *Fermi* Large Area Telescope (*Fermi*-LAT), to obtain 5σ detection of a point-like source.

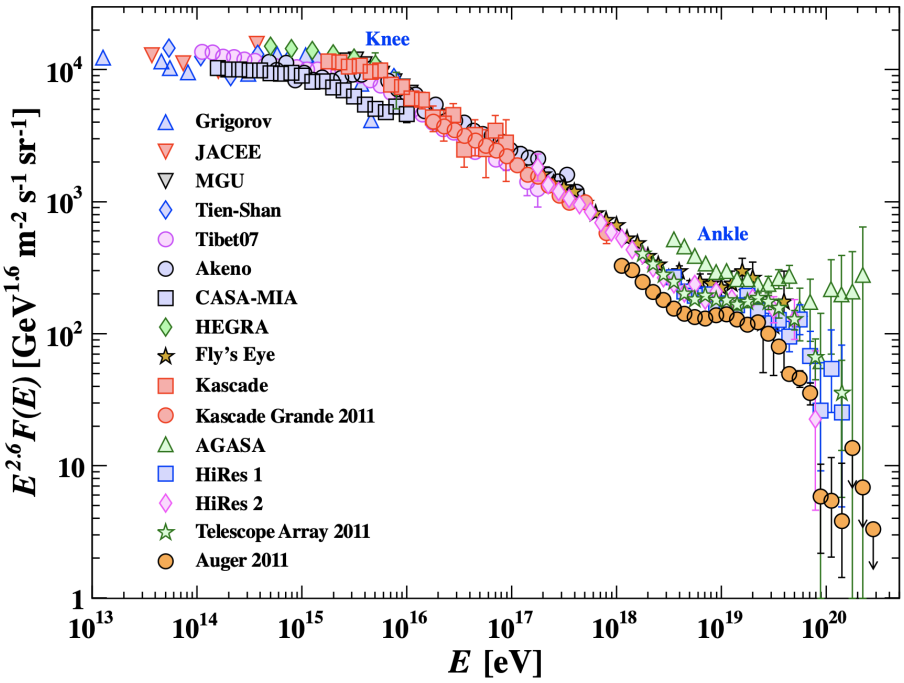

Figure 1.2. All particle CR energy spectrum (multiplied by $E^{2.6}$) from air shower measurements [11]. See the text for a detailed description.

decades, the spectrum of CRs has been measured up to the EeV (10^{21} eV) range. However, its origin is presently unclear.

CRs are charged relativistic particles that can be described by a broken power-law over more than twelve orders of magnitude starting from $\sim$ GeV (semi-relativistic) to multi-EeV (ultra-high-energy). Fig. 1.2 shows the differential energy spectrum of all-composite CRs multiplied by $E^{2.6}$ to display the changes in the spectral index. Below the knee ($\sim 10^{15}$ eV), the observed spectrum $E^{-2.6}$ is consistent with the superposition of the diffusion coefficient $D(E) \propto E^{\delta}$ in the Milky Way, and the injected spectrum E^{-2} predicted by diffuse shock acceleration (also known as Fermi acceleration) [12]. It is generally believed that the galactic supernova remnants (SNR) dominate the CR injections in this energy range [13]. Between $\sim 10^{15}$ eV and $\sim 10^{18}$ eV (the "ankle"), the spectral index changes to -3.0, e.g., $F(E) \propto E^{-3.0}$. Such a steepening might be caused by either a change of the diffusion regime or the cut-offs of the individual elements of the galactic component [11, 14, 15]. Above the ankle, the magnetic field in the Milky Way cannot trap these ultra-high-energy CRs (UHECRs), implying an extragalactic origin. The strong steepening at $\sim 6 \times 10^{19}$ eV measured by the Pierre Auger cosmic ray observatory (Auger) [16] confirms the so-called GZK cut-off (named after Greisen, Zatsepin, and Kuz'min) [17, 18] caused by the interactions between UHECRs and cosmic microwave background photons. Considering the time delay ($\Delta t \sim 10^4 - 10^5$ years) and the deflections ($\Delta\theta \sim$ several $\times\, 1^\circ$) while diffusing/propagating in the galactic and extragalactic magnetic fields, it would be very challenging to correlate the detected CRs to their sources.

The physical conditions of UHECR accelerators are stringently constrained: they should either have very strong magnetic fields or be very large. Given the typical turbulent magnetic field strength B and the size [1] of the accelerator R, we estimate the theoretical maximum energy of CRs [19]

$$E_{\rm cr,max} \lesssim ZeBR, \tag{1.1}$$

where Z is the atomic number of accelerated particles. Specifying the CR energy, candidates that satisfy this requirement (for protons) are shown in Fig. 1.3 (the famous Hillas plot). The binary neutron stars, AGN jets, blazars, GRBs, and galaxy clusters can be promising UHECR sources. Since the high-energy astrophysical neutrinos are tightly associated with CRs, these UHECR accelerators are also regarded as important neutrino emitters.

[1] For the relativistic jet with Lorentz factor Γ, $R = \Gamma \times$ comoving size

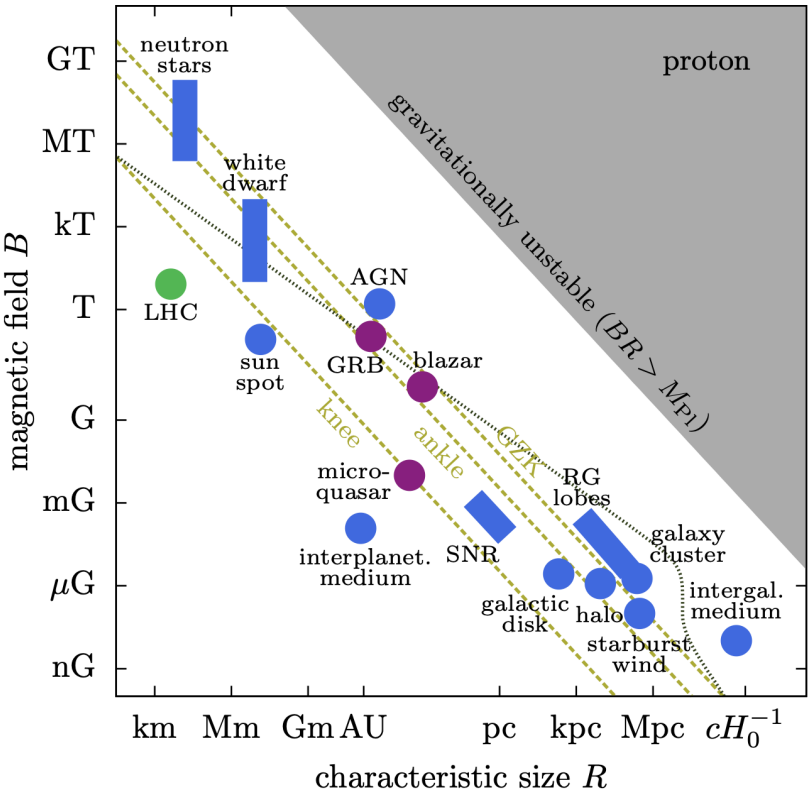

Figure 1.3. Source candidates that satisfy the Hillas criteria in the B-R plane. The dashed lines correspond to the CR energies $E_{\rm cr,max}$=$10^{14.5}$ eV (knee), $10^{18.5}$ eV (ankle), and $10^{19.6}$ eV (GZK).

1.1.3 High-Energy Astrophysical Neutrinos

Neutrinos were originally introduced by Pauli to particle physics to explain the continuous energy distribution in β decay experiment. They are natural particles that have a finite but very small rest mass, e.g., $m_\nu < 0.8$ eV/c^2 at 90% confidence level from the latest direct neutrino-mass measurement [20]. Moreover, neutrinos only participate in weak interactions and can easily penetrate dense environments without significant attenuation. For PeV neutrinos, the interaction cross section with nucleons is $\sigma_{\nu N} \sim 10^{-33}$ cm^2, which is one hundred million times smaller than the Thomson cross section that measures the scattering between EM radiation and free charged particles. With this property, we can use astrophysical neutrinos as probes to study the innermost and densest regions of astronomical objects where photons cannot escape. On the other hand, we need to build very large detectors to capture these elusive particles.

Neutrino astrophysics has made substantial progress since the IceCube Neutrino

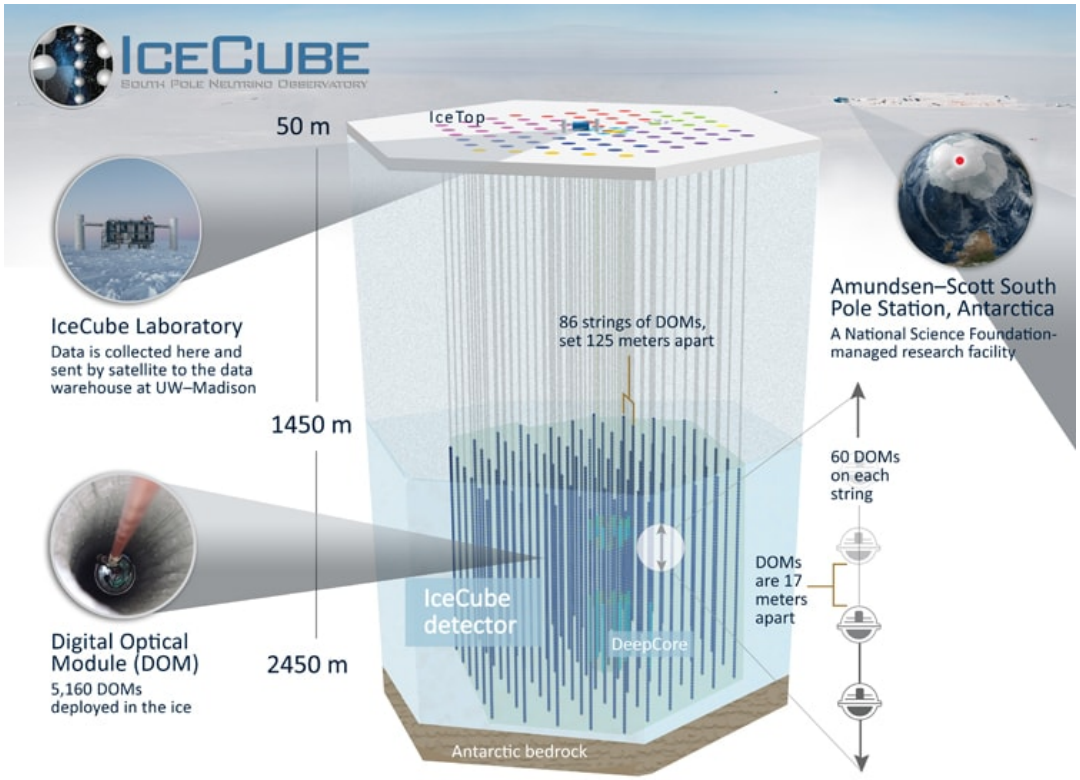

Figure 1.4. Schematic picture of the IceCube Observatory. IceCube is a cubic-kilometer detector located at the Antarctic. It consists of 5160 digital optical modules attached on 86 vertical strings. The detector measures the Cherenkov light from the secondary particles induced by the high-energy neutrinos.

Observatory in Antarctic [21, 22] (hereafter, IceCube) was completed. When a high-energy neutrino enters the detector, the neutrino will interact with the ice and produce secondary particles that travel through the detector at speeds close to c. In this process, Cherenkov light would be emitted and detected by the digital optical modules attached to the vertical strings (see Fig. 1.4). We can then reconstruct the energy and arriving direction of the incoming neutrino using Cherenkov light patterns.

During the last half-decade, scores of high-energy (HE) astrophysical neutrinos with energies between $\sim$ 10 TeV and a few PeV have been detected by IceCube, and the number keeps growing [23–26]. The arrival directions of these neutrinos are compatible with an isotropic distribution even in the $10-100$ TeV range, suggesting that a large part of these diffuse neutrinos come from extragalactic sources. Non-observation of diffuse Galactic γ-rays from the Galactic plane and other extended regions independently suggest that the Galactic contribution (e.g., by Fermi bubbles or local supernova remnants) is unlikely to be dominant [27–30]. However, despite extensive efforts, the physical nature

of the sources of the diffuse neutrinos still remains in dispute. Possible candidates include gamma-ray bursts (GRBs) [31–37], low-power GRBs [38–44], radio-loud active galactic nuclei (AGNs) [45–53], radio-quiet/low-luminosity AGNs [54–57], and AGNs embedded in galaxy clusters and groups[2].

It is generally accepted that the bulk of astrophysical neutrinos are generated by charged pion ($\pi^{\pm}$) decays, and that these pions are the secondaries from cosmic ray (CR) particles undergoing hadronuclear (pp) or photohadronic ($p\gamma$) interactions between the CRs and ambient target gas nuclei or photons. Meanwhile, these collisions also lead unavoidably to neutral pions (π^0) as well, which subsequently decay into a pair of γ-rays. The relevant interactions can be written as

$$\begin{aligned}
p + p \rightarrow & p + \pi^{\pm} + \pi^0 + ... \\
p + \gamma \rightarrow & n + \pi^{\pm} + \pi^0 + ... \\
\pi^+ \rightarrow & \mu^+ + \nu_\mu \\
& \mu^+ \rightarrow e^+ + \nu_e + \bar{\nu}_\mu \\
\pi^- \rightarrow & \mu^- + \bar{\nu}_\mu \\
& \mu^- \rightarrow e^- + \bar{\nu}_e + \nu_\mu \\
\pi^0 \rightarrow & \gamma + \gamma \\
n \rightarrow & p + e^- + \bar{\nu}_e.
\end{aligned} \tag{1.2}$$

Hence, the diffuse neutrino flux is expected to have an intimate connection with the diffuse CR and γ-ray backgrounds, and multi-messenger analyses need to be applied to constrain the origin of these diffuse high-energy cosmic particle fluxes [58–60].

1.1.4 Gravitational Waves (GWs)

GWs, the ripples of spacetime, are predicted by general relativity when the system generates a time-changing mass quadrupole moment. We expect the source to be massive and fast-accelerating to produce a detectable GW. The merging compact objects, including black holes and neutron stars, are the primary sources for the ground-based GW detectors that are sensitive in the high-frequency band, e.g., 10 Hz to 10^4 Hz. Experiments dedicated to the detection of GWs date back to the middle of the last century. In 2015, the first direct detection of GWs from a stellar-mass binary black hole (BH-BH) merger, GW150914 [61], by the Laser Interferometric Gravitational Wave

[2]Groups of galaxies are smaller clusters, numbering from a few to dozens of galaxies.

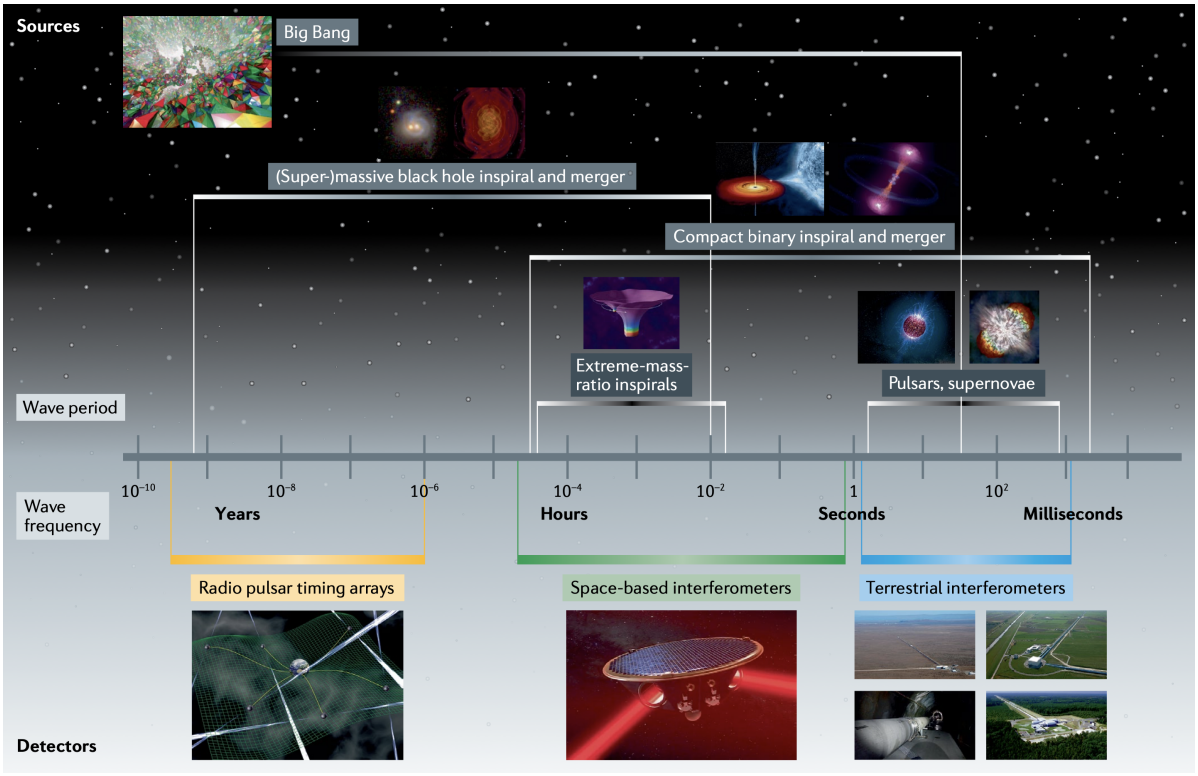

Figure 1.5. GW frequency bands of various source populations, ranging from 10^{-9} Hz to 10^{4} Hz [62]. GW telescope classes are shown below the frequency spectrum.

Observatory (LIGO), not only tested the general relativity but also opened a new window to explore the Universe. Since then, the zoo of compact binary object (CBO) mergers, including BH-BH mergers, black hole - neutron star (BH-NS) mergers, and binary neutron star (NS-NS) mergers, keeps expanding in the observation runs of LIGO and Virgo interferometer (VIRGO). The LIGO-VIRGO observations of CBO mergers allow us to study the dynamics of compact binary systems in their last second before the coalescence and have profound implications to the physics of GRBs and kilonovae.

Fig. 1.5 depicts the GW frequency bands of various source populations, ranging from 10^{-9} Hz to 10^{4} Hz. The corresponding telescope categories are also listed. Ground-based interferometers such as LIGO, VIRGO, and future Japanese KAGRA will become the main force for observing the high-frequency GWs from $\sim$ 10 Hz to 10^{4} Hz produced by CBO mergers and potentially the core-collapse supernovae. The upgrades to the current LIGO [63] and VIRGO, together with the involvement of future KAGRA and the LIGO-India interferometer, would significantly improve the ability of the LIGO-VIRGO-KAGRA network to detect and locate the GW events. The arm lengths of the current and future ground-based interferometers are typically multi-kilometers. The much longer

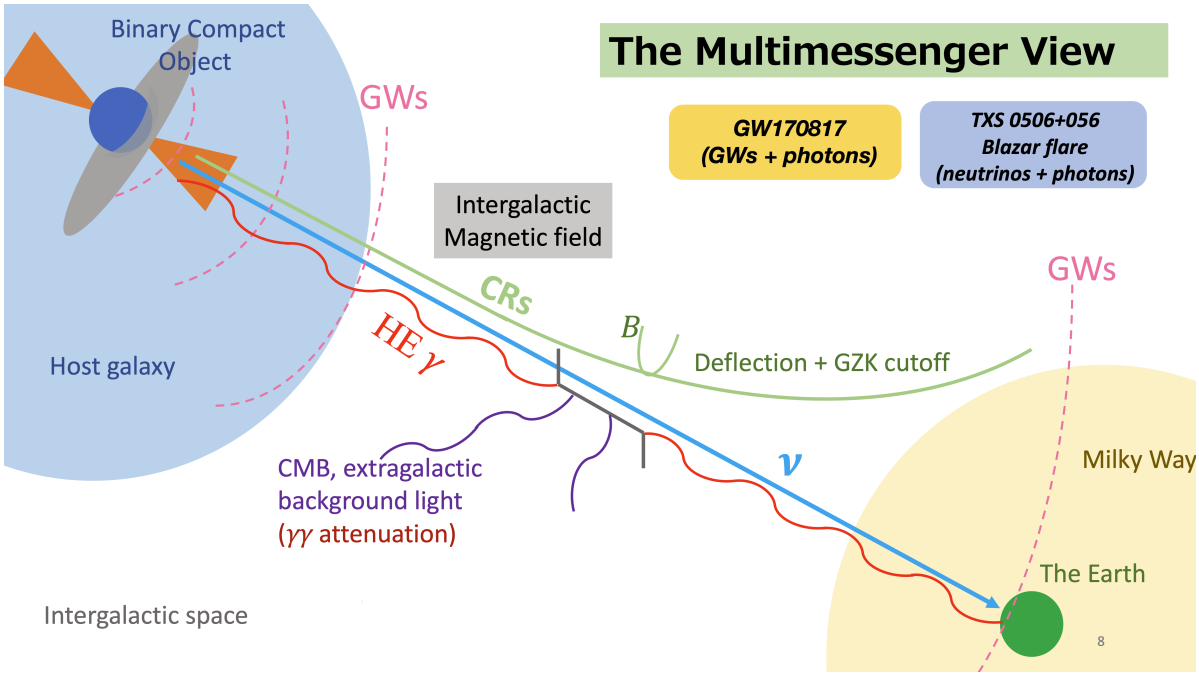

Figure 1.6. A schematic demonstration of the propagation of astrophysical messengers (high-energy γ-rays, neutrinos, GWs, and CRs) after leaving the source.

arms are needed if we want to "sense" the low-frequency GWs. The next-generation space-based missions, such as the Laser Interferometer Space Antenna (LISA) [64], will play a leading role in detecting the low-frequency GW signals, e.g., 10^{-4} Hz - 1 Hz, benefiting from the larger separation ($\sim 2.5 \times 10^9$ m) between each satellite. The massive and supermassive black hole (SMBH) mergers in the mass range $10^3 - 10^7\ M_\odot$ are the dominant sources in this frequency band. Unlike the laser interferometer GW detectors mentioned before, the pulsar timing array works with the radio pulse from an array of millisecond pulsars that are $\sim$ few $\times$ 0.1 kpc away from the Earth. Using PTA, we can explore the extremely low frequency (10^{-9} Hz $- 10^{-6}$ Hz) GWs from $10^7 - 10^{10}\ M_\odot$ SMBH coalescences [65].

1.1.5 The Physical Picture of Multi-Messenger Astrophysics

The joint study of different messengers (EM photons, neutrinos, GWs, and perhaps CRs) can provide a holistic view of the physical processes and configurations of the sources. Fig. 1.6 schematically demonstrates how the messengers may propagate and what kind of interactions they may undergo before reaching the Earth. The high-energy γ rays can annihilate with other lower energy background photons, such as those from the

extragalactic background light (EBL) and the cosmic microwave background (CMB). As a result, the γ rays from distant sources, e.g., $z \gtrsim 0.1$, with energy $E_\gamma \gtrsim 100$ GeV will be significantly attenuated. During the propagation, the UHECRs will be deflected by galactic and extragalactic magnetic fields. The GZK cut-off also limits the maximum energy of the detected CRs. On the other hand, due to the weak scattering between neutrinos/GWs and matter, we can observe the VHE astrophysical neutrinos and GWs that point directly back to their sources.

1.2 Astrophysical Mergers in the Era of Multi-Messenger Astrophysics

In this dissertation, we focus on three promising sources, including galaxy/cluster mergers, SMBH mergers, and short GRBs formed by CBO mergers that are embedded in AGN disks, for the joint detection with EM photons, neutrinos, and GWs. In this section, we provide an overview of these astrophysical mergers and the motivation of our work.

1.2.1 Galaxy and Cluster Mergers

In the standard hierarchical galaxy formation scenario, galaxies form inside extended dark matter halos. When dark matter halos merge, the galaxies in these halos also merge, and the collision of the cold gas in the merging galaxies leads to shocks on a galactic scale in the galactic interstellar medium (ISM) gas. Later in the process of cosmological structure formation, at lower redshifts where galaxy groups and galaxy clusters have started forming, mergers among the dark matter halos containing these groups and clusters are also expected. These mergers are very energetic and result in shocks in the intergalactic medium (IGM) gas of the participating groups/clusters. One vivid example is the Bullet Cluster [66, 67]. Both these galactic and group/cluster shocks can accelerate CRs. The subsequent pp collisions between the shock-accelerated CRs and the thermal atomic nuclei in the gaseous environment are the major mechanism that generates HE neutrinos in these systems.

In chapter 2, we consider this scenario of both galactic scale shocks in the galactic ISM and group/cluster scale shocks in the intergalactic gas across redshifts. Whereas in a previous study [68] only galaxy mergers (mergers of two galaxies of approximately the same size) at $z \sim 1$ were considered, here take into account the redshift evolution of the halo merger rate, and consider both galaxy and cluster mergers, including both major

and minor mergers (the latter being those where the participating galaxies or clusters have mass ratios $\zeta \neq 1$). We calculate the CR productions in the corresponding shocks at redshifts $0 \leq z \leq 10$ and we find that high redshift ($z \gtrsim 1-2$) halo mergers contribute a significant part of the observed diffuse HE neutrinos and γ-rays without violating the non-blazar EGB constraint.

The *pp* interactions between accelerated CR and intergalactic medium can also generate high-energy non-thermal electrons and positrons (see Eq. 1.2). With the existence of galactic magnetic fields, these secondary particles can produce detectable radio and X-ray emissions via synchrotron and synchrotron self-Compton (SSC) processes. In chapter 3, we formulate a model which is capable of reproducing the radio and X-ray observations of specific systems using synchrotron and synchrotron self-Compton (SSC) or external inverse Compton (EIC) emissions from high-energy secondary electron-positron pairs produced by the CR interactions in such systems. Here the EIC is caused by scatterings with the cosmic microwave background (CMB), infrared/optical starlight (SL) and extragalactic background light (EBL). We show that our scenario can explain the observations of interacting galaxies, NGC 660 and NGC 3256. In addition, since the radiation spectrum of the merging galaxies is determined by the dynamics of the galaxy interactions and the resulting physical conditions, this enables us to provide constraints on the galactic magnetic field B, shock velocity v_s, galactic gas mass $M_{\rm g}$, etc.

1.2.2 Supermassive Black Hole Mergers

Recent observations have provided increasing evidence that a large fraction of nearby galaxies harbors supermassive black holes (SMBHs). One influential scenario for the formation of these SMBHs is that they, like the galaxies, have grown their mass through hierarchical mergers (e.g., Ref. [69]). SMBH mergers are ubiquitous across the history of the Universe, especially at high redshifts where the minor galaxy mergers are more frequent. When galaxies merge, the SMBHs residing in each galaxy may sink to the center of the newly merged galaxy and subsequently form a SMBH binary [70, 71]. The SMBHs gradually approach each other as the gravitational radiation takes away the angular momentum, which eventually leads to their coalescence, accompanied by a GW burst. The GW burst from the final stage of coalescing can be detected by future missions such as LISA [72], providing through this channel valuable and prompt information about the merger rates, SMBH masses, and redshift. In addition, SMBH mergers are usually associated with mass accretion activities and relativistic jets, which may lead to detectable EM and neutrino emissions. For example, SMBH mergers may trigger AGN

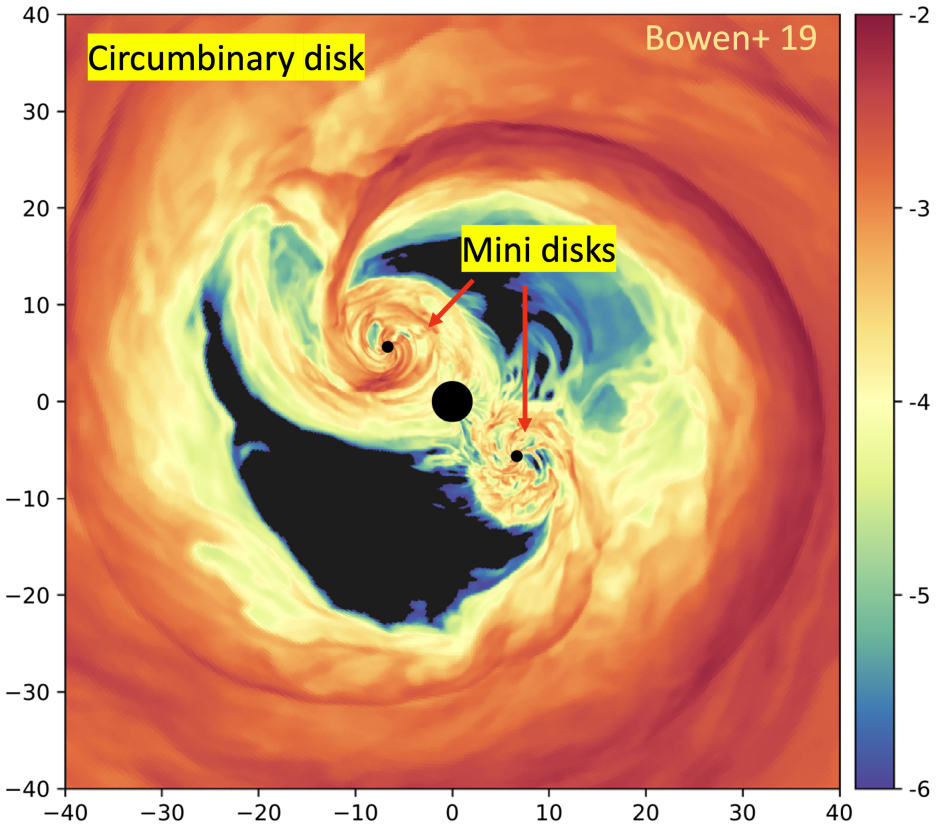

Figure 1.7. A snapshot of the density distribution of the circumbinary disk around the binary SMBH system and the mini-disks around each SMBH. The simulation was performed by Ref. [75].

activities [73]. In this picture, the merger of SMBHs will become an important target for future multi-messenger astronomy (e.g., Ref. [74]).

Numerical simulations have demonstrated that SMBH mergers are typically accompanied by a circumbinary disk around the binary system (see Fig. 1.7 from Ref. [75]) and mini-disks surrounding each SMBH. The pre-merger circumnuclear material is thought to form from disk winds driven by the inspiralling binary SMBHs, in which a post-merger jet is launched, powered by the rotational energy of the remnant of the merger. In chapter 4, we present a concrete model for high-energy neutrino emission from four possible sites in the relativistic jet of SMBH mergers, namely, the collimation shock (CS), internal shock (IS), forward shock (FS), and reverse shock (RS). We show that month-to-year high-energy neutrino emission from the post-merger jet after the gravitational wave event is detectable by IceCube-Gen2 within approximately five to ten years of operation in optimistic cases where the cosmic-ray loading is sufficiently high and a mildly

super-Eddington accretion is achieved.

In chapter 5, we study the EM emission produced in relativistic jets launched after the coalescence of SMBHs. The physical picture is that the disk winds originating from the circumbinary disk and mini-disks around each SMBH form a pre-merger wind bubble, and jets powered by the Blandford-Znajek (BZ, [76]) mechanism are launched after the merger. The jets push ahead inside the pre-merger disk wind material, resulting in the formation of forward and reverse shocks. In the forward shock region, electrons are accelerated to high energies with a power-law distribution as observed in afterglows of gamma-ray bursts (GRBs) [77]. These particles then produce broadband non-thermal EM emissions through synchrotron and synchrotron self-Compton (SSC) processes.

1.2.3 Compact Binary Mergers

The (stellar-mass) compact binary mergers, including NS-NS mergers, NS-BH mergers, and BH-BH mergers, have attracted persistent interest in multi-messenger astrophysics due to the unique signatures in EM and GW observations. The evolution channel of a CBO depends on many factors. The two most prominent would be the mass distribution in the binary system and the environment. Fig. 1.8 depicts the evolution and the fate of a compact binary system. For instance, if the merger occurs in a gaseous environment, an accretion disk can be formed, and the super-Eddington accretion activity of the remnant would lead to a relativistic jet, which makes it a luminous γ-ray emitter. It is generally believed that short GRBs result from compact binary object (CBO) mergers [78–83], such as NS-NS mergers and potentially NS-BH mergers, whereas long GRBs are generated during the death of massive stars [84–89].

In 2017, the coincident detection of gravitational waves (GWs) and the corresponding electromagnetic counterpart from the binary neutron star merger GW170817, located in the host galaxy NGC 4933, marked a triumph of multi-messenger astronomy [90–92]. The spatial and temporal association between GW170817 and the γ-ray burst GRB 170817A also consolidates the theory that CBO mergers are the origin of short GRBs. Extensive efforts have shown that the broadband emission is consistent with a relativistic jet viewed from an off-axis angle [92–102]. Moreover, Ref. [103] investigated the upscattered cocoon emission as the source of the γ-ray counterpart. The long-lasting high-energy signatures of the central engine left after the coalescence was studied in Ref. [104].

Alternatively, unlike in the case of GW170817, one can expect a sub-population of short GRBs which occur in the accretion disks of AGNs. Studies of the CBO formation and evolution in AGN disks demonstrate that hierarchical mergers of embedded binary black

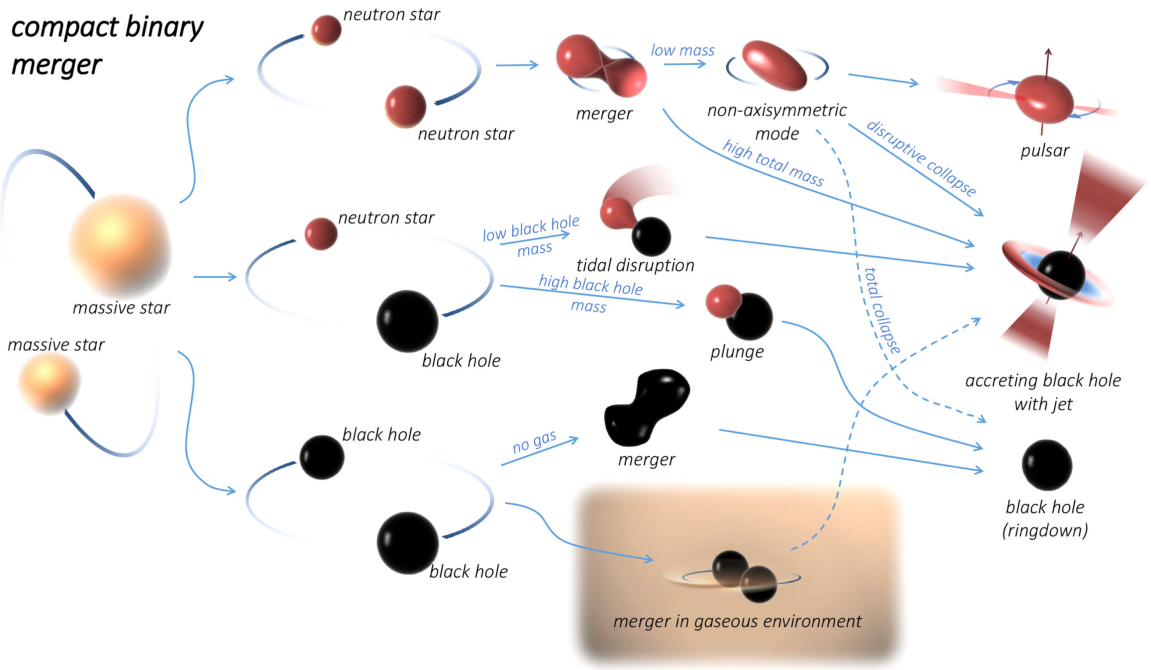

Figure 1.8. Evolution channels and fates of compact binary mergers including NS-NS mergers (upper channel), NS-BH merger (middle channel), and BH-BH mergers (bottom channel). Credit: Imre Bartos and Marek Kowalski [120].

hole systems are promising for reconstructing the parameters of LIGO/VIRGO detected mergers [105–108]. These mergers can harden the black hole mass distribution [109–112] as well. [113] pointed out that mergers involving neutron stars, such as GW190814 and GW190425, could also arise in AGN disks. Recent progress on the optical counterpart to GW190521 could support this [114], although the confirmation needs further observations [115]. Ref. [116] systematically studied the electromagnetic signatures of both long GRBs and short GRBs in AGN disks and discussed the conditions for shock breakout. Refs. [117] and [118] focused more on the neutrino production of embedded explosions. However, Ref. [119] showed that CBO environments are likely to be thin because of outflows that are common in super-Eddington accretion.

In chapter 6, we study γ-ray emission from short GRBs that are embedded in AGN disks. Inside the accretion disk, the embedded objects can migrate towards a migration trap due to angular momentum exchange via the torques originating from the disk density perturbations. At the migration trap, the gas torque changes sign, and an equilibrium is achieved as the outwardly migrating objects meet inwardly migrating objects. Numerical calculations show that compact binaries are typically formed near the migration trap at distances around $R_d \sim 20 - 300 R_S$ to the central supermassive

black hole (SMBH, [121]), where $R_S = 2GM_\star/c^2$ is the Schwarzschild radius. Employing one-dimensional N-body simulations, Ref. [111] obtained a more distant location for typical mergers at $\sim 10^{-2}$–10^{-1} pc ($\sim 10^3 - 10^4 R_{\rm S}$ for a SMBH with mass $M_\star = 10^8 M_\odot$). We concentrate on the embedded GRBs with distances $R_d \sim 10 - 10^3 R_{\rm S}$. We will show that AGN disks would not influence the γ-ray emission if the CBO mergers happen further outside in the disk. We also note that $R_d = 10 R_{\rm S}$ is an extreme case where the population is stringently limited. The outflows from the binary systems with super-Eddington accretion rates are expected to form a low-density cavity-like structure before the merger occurs [119]. Within such a cavity, a successful GRB jet is likely to develop since the ambient gas density is not sufficiently high to stall the jet, in contrast to the choked-jet case discussed in Ref. [118]. Future multi-messenger analyses of AGN short GRBs can provide unprecedented insights for understanding the formation and evolution of CBOs inside the AGN disks as well as the origin of their high-energy emission.

Constraints on Blazar Neutrinos

Blazars, including flat-spectrum radio quasars (FSRQs) and BL Lac objects, form a subclass of AGNs. They typically exhibit on-axis relativistic jets and dominant brightness in the γ-ray sky. Recently, the IceCube collaboration announced the spatial and temporal coincidence between a muon track neutrino event IceCube-170922A and a blazar TXS 0506+056 [122] at the significance $\sim 3\sigma$. Intuitively, if this association is physical, the intimate link between this IceCube neutrino event and the blazar may favor blazars as the main sources of the cumulative neutrino flux, but this is not the case [123].

The maximum likelihood stacking searches for cumulative neutrino flux from the second *Fermi*-LAT AGN catalog (2LAC) as well as the point-source searches using the IceCube muon track events and blazars in *Fermi*-LAT 3LAC have independently shown that *Fermi*-LAT-resolved blazars only contribute a small portion of the IceCube cumulative neutrino flux [124–126] and the hadronic models of blazar activity are strongly constrained [127], if the specific correlation $L_\nu \propto L_{\rm ph}$ is assumed as a prior. [128] evaluated the contribution of unresolved sources and showed that the blazar contribution to the cumulative neutrino flux is constrained unless one makes an *ad hoc* assumption that lower-luminosity blazars entrain a larger amount of CRs.

In addition to the stacking analysis, the absence of clustering in high-energy neutrino events, i.e., neutrino multiplets and auto-correlation, can also provide relevant constraints on various classes of proposed sources as the dominant origin of the cumulative neutrino flux [129–134]. The constraints are sensitive to the redshift evolution of the sources, which

are especially powerful for weakly or non-evolving sources such as BL Lac objects [123,129]. But the limits are weaker for rapidly evolving sources such as FSRQs, which could significantly alleviate the constraints, as remarked by Ref. [123]. Ref. [135] studied the constraints on evolving blazar populations and confirmed that fast-evolving sources (e.g., $\xi_z = 5.0$) might indeed relax the neutrino multiplet limits.

In a separate effort, we study the stacking and multiplet constraints on the blazar contribution to the diffuse neutrino background in chapter 7. We consider the "joint" implications of these independent analyses for the global blazar population and extend the constraints to a common case where a generic relationship between neutrino and γ-ray luminosities, e.g., $L_\nu \propto (L_{\rm ph})^{\gamma_{\rm lw}}$, is presumed, which is more general than what has been previously considered in such analyses. We treat $\gamma_{\rm lw}$ as a free parameter and attempt to reveal the $\gamma_{\rm lw}$-dependence of the upper limits on all-blazar contributions. Our results show that these two limits are complementary and support the argument that blazars are disfavored as the dominant sources of the 100-TeV neutrino background. This work provides rather general constraints for future studies of blazar neutrinos.

Chapter 2
Cumulative Neutrino and γ-Ray Backgrounds from Galaxy and Cluster Mergers

Note: The material in this Chapter is based on my paper [136], with co-authors Peter Mészáros, Kohta Murase, and Donghui Jeong.

2.1 Introduction

Neutrino astrophysics has made substantial progress since the IceCube Neutrino Observatory in Antarctic [21, 22] was completed. During the last half decade, scores of high-energy (HE) astrophysical neutrinos with energies between ~ 10 TeV and a few PeV have been detected by IceCube, and the number keeps growing [23–26]. The arrival directions of these neutrinos are compatible with an isotropic distribution even in the $10 - 100$ TeV range, suggesting that a large part of these diffuse neutrinos come from extragalactic sources. Non-observation of diffuse Galactic γ-rays from the Galactic plane and other extended regions independently suggest that the Galactic contribution (e.g., by Fermi bubbles or local supernova remnants) is unlikely to be dominant [27–30]. However, despite extensive efforts, the physical nature of the sources of the diffuse neutrinos still remains in dispute. Possible candidates include gamma-ray bursts (GRBs) [31–37], low-power GRBs [38–44], radio-loud active galactic nuclei (AGNs) [45–53], radio-quiet/low-luminosity AGNs [54–57], and AGNs embedded in galaxy clusters and groups[1]. It is generally accepted that the bulk of astrophysical neutrinos are generated by charged pion

[1]Groups of galaxies are smaller clusters, numbering from a few to dozens of galaxies.

($\pi^{\pm}$) decays, and that these pions are the secondaries from cosmic ray (CR) particles undergoing hadronuclear (pp) or photohadronic ($p\gamma$) interactions between the CRs and ambient target gas nuclei or photons. Meanwhile, these collisions also lead unavoidably to neutral pions (π^0) as well, which subsequently decay into a pair of γ-rays. Hence, the diffuse neutrino flux is expected to have an intimate connection with the diffuse CR and γ-ray backgrounds, and multi-messenger analyses need to be applied to constrain the origin of these diffuse high-energy cosmic particle fluxes [58–60].

Galaxy clusters and groups have been considered as promising candidate sources of IceCube's neutrinos, and CR accelerators can be not only AGNs but also intragalactic sources, accretion shocks, and mergers of clusters and groups [137,138]. Star-forming and starburst galaxies (SFGs & SBGs, respectively) have also been suggested as promising candidates for HE neutrino sources [58, 139–145]. In particular, starburst galaxies have dense gaseous environments and have been of interest as efficient CR reservoirs. Previous studies have assumed not only supernova and hypernova remnants (SNRs & HNRs, respectively) but also galaxy mergers, disk-driven outflows and possible weak jets from AGNs as CR accelerators embedded in the star-forming galaxies [58, 68, 140, 144–146]. Hypernovae (HNe) are a subclass of Type Ib/c supernovae (SNe), essentially a hyper-energetic version of Ib/c SNe. The typical ejecta energy of HNe is 10^{52} erg, which is one order of magnitude larger than for SNe. Like SNRs, a hypernova remnant (HNR) leads to an extended structure that results from a hypernova explosion. In any case, an important constraint on such models is provided by the extragalactic γ-ray background (EGB) in the 100 MeV $-$ 820 GeV range, derived from the observation by the *Fermi*-LAT satellite [1]. Recent studies of the blazar flux distribution at γ-ray energies above 50 GeV indicate that blazars account for $86^{+16}_{-14}\%$ of the total EGB flux [147]. This provides a strong constraint, namely, only a fraction $\lesssim 30\%$, with a best fit of 14%, can be ascribed to any remaining non-blazar component of the EGB [148].

With this constraint, the SBG scenario is apparently disfavored as the dominant origin of IceCube neutrinos [60]. However, so far, this conclusion depends on the interpretation of the medium-energy neutrino data in the $10 - 100$ TeV range. For example, the cumulative neutrino background may consist of two components, in which the high-energy data above ~ 100 TeV can be explained by the SBGs. On the other hand, the $10 - 100$ TeV component motivates CR accelerators that are "dark" in γ-rays [59] to satisfy multi-messenger constraints. The γ-rays may be attenuated inside their sources, or they might be absorbed during the propagation. Possible candidates include choked-jet GRBs or high-redshift sources such as Pop-III HNRs embedded in starbursts [149].

In this paper, we focus on halo mergers as an origin of HE neutrinos. In the standard hierarchical galaxy formation scenario, galaxies form inside extended dark matter halos. When dark matter halos merge, the galaxies in these halos also merge, and the collision of the cold gas in the merging galaxies leads to shocks on a galactic scale in the galactic interstellar medium (ISM) gas. Later in the process of cosmological structure formation, at lower redshifts where galaxy groups and galaxy clusters have started forming, mergers among the dark matter halos containing these groups and clusters are also expected, These mergers are very energetic and result in shocks in the intergalactic medium (IGM) gas of the participating groups/clusters. One vivid example is the Bullet Cluster [66, 67]. Both these galactic and group/cluster shocks can accelerate CRs. The subsequent pp collisions between the shock-accelerated CRs and the thermal atomic nuclei in the gaseous environment is the major mechanism that generates HE neutrinos in these systems.

Here, we consider this scenario of both galactic scale shocks in the galactic ISM and group/cluster scale shocks in the intergalactic gas across redshifts. Whereas in a previous study [68] only galaxy mergers (mergers of two galaxies of approximately the same size) at $z \sim 1$ were considered, here take into account the redshift evolution of the halo merger rate, and consider both galaxy and cluster mergers, including both major and minor mergers (the latter being those where the participating galaxies or clusters have mass ratios $\zeta \neq 1$). We calculate the CR productions in the corresponding shocks at redshifts $0 \leq z \leq 10$ and we find that high redshift ($z \gtrsim 1-2$) halo mergers contribute a significant part of the observed diffuse HE neutrinos and γ-rays.

This paper is organized as follows. In Sec. 2.2, we introduce the halo mass function and the halo distribution that is used in the following sections. The merger rate and the CR energy input rate are given in Sec. 2.3. In Sec. 2.4 we discuss the redshift dependence of the CR maximum energies and the neutrino product efficiency, and we present the resulting neutrino and the γ-ray spectra in Sec. 2.5. The results and implications are discussed in Sec. 2.6. We summarize our results in Sec. 2.7. Throughout, we assume a standard flat-ΛCDM universe with present-day density parameter $\Omega_{m,0} = 0.3$ and Hubble parameter $H_0 = 71.9$ km s^{-1} Mpc^{-1} [150].

2.2 Halo Mass Function

Using the formalism of Ref. [152], the halo mass function, the number of dark matter halos per unit comoving volume contained within the logarithmic mass interval $d \ln M$,

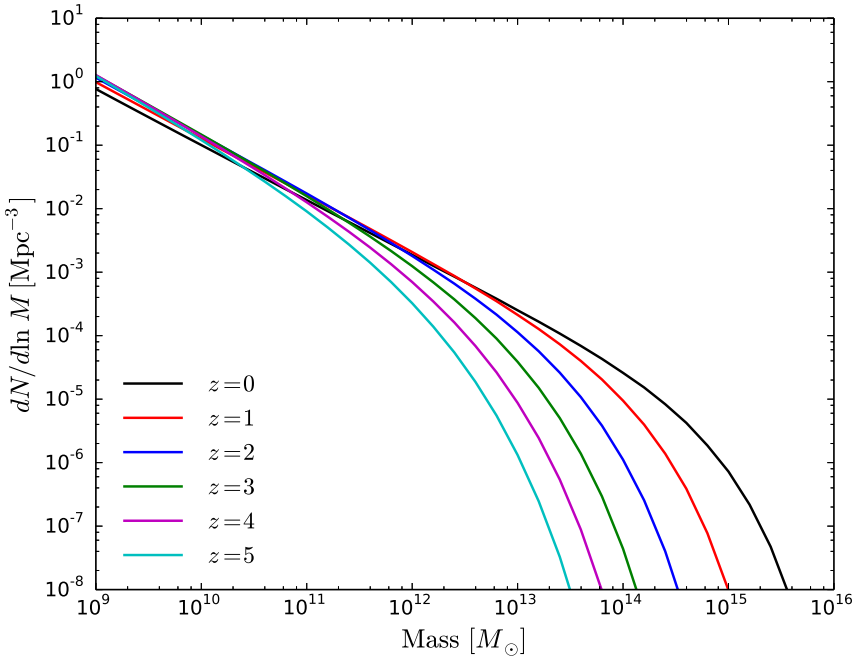

Figure 2.1. Dark matter halo mass function $dN/d\ln M$ at $z = 0, 1, 2, 3, 4, 5$. Here, we use the fitting formula from Ref. [151].

is given by

$$\frac{dN}{d\ln M} = \frac{\bar{\rho}}{M} f(\nu) \frac{d\ln\sigma_M^{-1}}{d\ln M}, \tag{2.1}$$

with the background matter density $\bar{\rho} = \Omega_{m,0}\rho_{cr}$ where $\rho_{cr} = (3H^2/8\pi G)$ is the critical density, and the variance σ_M of the linear density contrast $\delta \equiv (\Delta\rho/\bar{\rho})$ is smoothed over the scale $R = \left(\frac{3M}{4\pi\bar{\rho}}\right)^{1/3}$:

$$\sigma_M^2 = \int \frac{k^2 dk}{2\pi^2} P(k) |\hat{W}(kR)|^2 \,. \tag{2.2}$$

Here, $P(k)$ is the linear matter power spectrum we calculate following Ref. [153], and $\hat{W}(kR) = 3j_1(kR)/kR$ for a top-hat filtering function. The significance $\nu = \delta_c/\sigma_M$ is related to the linear critical density δ_c above which virialized halos can form[2]. In the spherical collapse model, for example, a spherical region of radius R collapses and virializes at redshift z when the smoothed linear overdensity $\delta_R(r, z)$ exceeds $\delta_{c,0} \approx 1.686$. In the flat ΛCDM Universe, the linear growth factor, the time evolution of the linear

[2]In some references, e.g. in Ref. [151], $\nu = (\delta_c/\sigma_M)^2$ is used instead of our definition here.

density contrast, is given by

$$\mathcal{D}(z) = \frac{\delta_c(z)}{\delta_{c,0}} \propto \frac{5}{2}\Omega_{m,0}\sqrt{\Omega_{m,0}(1+z)^3 + 1 - \Omega_{m,0}} \times \int_z^\infty \frac{1+z'}{\left[\Omega_{m,0}(1+z')^3 + 1 - \Omega_{m,0}\right]^{3/2}} dz'. \tag{2.3}$$

We normalize $\mathcal{D}(z)$ to be unity at $z = 0$.

For the multiplicity function $f(\nu)$, we adapt the Sheth-Tormen [151] fitting formula, expressed in the form

$$f_{S-T}(\nu) = A\sqrt{\frac{2a}{\pi}}\left[1 + (\nu^2 a)^{-p}\right]\nu \exp\left[-\frac{a\nu^2}{2}\right], \tag{2.4}$$

with parameters $A = 0.3222$, $a = 0.707$, and $p = 0.3$ that provide the the best fit to numerical N-body simulations [154–156]. We show the resulting mass function $\frac{dN}{d\ln M}$ for redshifts between $z = 0$ and $z = 5$ in Fig. 2.1. Our mass function slightly underestimates that from the N-body simulations at high masses of $\gtrsim 10^{15}\ M_\odot$, but it does not affect the main results of this paper. We shall use the mass functions in the following sections to estimate the redshift evolutions of galactic radius, gas density and shock velocity.

2.3 Merger Rate and Cosmic-ray Luminosity Density

In this section, we calculate the CR input rate due to galaxy and halo mergers by using the halo mass function we have obtained in Sec. 2.2, and we estimate the energy converted into CRs from shocks in the gas component of the merging halos as follows.

There are three time scales characterizing the CR acceleration due to galactic halo mergers: the age of the Universe $t_{\rm age}$, the halo merger time $t_{\rm merger}$ which corresponds to the average time required to undergo one merger, and the CR injection time (that is the shock-crossing time) $t_{\rm dyn}$, which are, for a merger that happens at redshift z, given by

$$\begin{aligned} t_{\rm age} &= \int_z^\infty \left|\frac{dt}{dz'}\right| dz' \\ t_{\rm merger} &= \left[\int d\zeta\, \frac{dN_m}{dz d\zeta}\left|\frac{dz}{dt}\right|\right]^{-1} \\ t_{\rm dyn} &= \lambda \frac{R_g(z)}{v_s(z)}\,. \end{aligned} \tag{2.5}$$

Here, $|dt/dz| = 1/[(1+z)H(z)]$, $dN_m/dzd\zeta$ is the dimensionless merger rate per redshift interval dz and per unit halo mass ratio ζ [157, 158], $R_g(z)$ is the mean galaxy radius, and $\lambda \sim 1$ parametrizes the orientation and geometrical uncertainty of the galaxy merger. With these time scales, the probability that a halo with mass M experiences merger within the age of the universe is given by $P(M,z) = \exp(-t_{\rm merger}/t_{\rm age})$. Hence, assuming that the CRs are mainly protons, the *comoving* CR energy input rate per the logarithm of the CR energy ε_p is

$$\begin{aligned}\varepsilon_p Q_{\varepsilon_p}(z) = \frac{E_{\rm merger}}{t_{\rm age}\mathcal{C}} =& \epsilon_p \mathcal{C}^{-1} \int_{M_{\rm min}}^{M_{\rm max}} dM \\ & \left[\frac{1}{2}\xi_g(M,z) M v_s^2\right] \frac{dN}{dM} \frac{P(M,z)}{t_{\rm age}},\end{aligned} \tag{2.6}$$

where $\xi_g(M_h,z) = M_{\rm gas}/M_h$ is the mass fraction in gas form, ϵ_p is the CR energy fraction (nominally taken as 0.1) and $\mathcal{C} = \ln(\varepsilon_p^{\rm max}/\varepsilon_p^{\rm min})$ is the normalization factor for a standard flat CR spectrum $N(\varepsilon_p) \propto \varepsilon_p^{-2}$. For $z \sim 1$, the typical maximum energy, $\varepsilon_p^{\rm max}$, is $\sim 10^{17}$ eV and $\mathcal{C} \simeq 18.4$ [68]. However, $\varepsilon_p^{\rm max}$ varies with redshift, as we discuss in the next section.

2.3.1 Gas Fraction $\xi_g(M,z)$

The gas-mass fraction ξ_g of dark matter halos depends on the star formation rate (SFR) and on the stellar mass $M_* = \chi_*(M_h,z)M_h$. Here, we obtain $\chi_* = M_*/M_h$ from the $M_*(M_h)$ function inferred from observations by Ref. [159][3]. We also use the gas fraction in normal galaxy $f_g = M_{\rm gas}/(M_{\rm gas}+M_*)$[4] measured in Ref. [160]. Combining the two observational results, we have constructed the redshift evolution of the gas-mass fraction in dark matter halos. That is, the gas-mass fraction ξ_g is related to f_g through $\xi_g^{\rm evo} = M_{\rm gas}/M_h = \frac{\chi_* f_g}{1-f_g}$, and using Eq. (26) in Ref. [160], we find that

$$\xi_g^{\rm evo} = \chi_* \frac{f_g}{1-f_g} = \chi_* \frac{K}{M_*^{1-\beta'}} {\rm sSFR}^{\beta'} \tag{2.7}$$

where $K = 10^{\alpha_{\rm SFR}}$ is a constant and the quantity sSFR (specific star formation rate) is the star formation rate per unit galaxy stellar mass. For the gas fraction in normal

[3] In Ref. [159], the $M_* - M_h$ relation from $z = 0-8$ is parameterized by equation (3). Here, we extend the domain of that function to $z = 10$ considering that the uncertainty from high-redshift contributions is small.

[4] In Ref. [160], the gas fraction is written as $f_{\rm mol}$ instead.

galaxies we use the parameters $(\alpha_{\rm SFR}, \beta') = (9.22 \pm 0.02, 0.81 \pm 0.03)$, together with the expression for sSFR given in the appendix of Ref. [160]. In Fig. 2.2 (see red curves), we show the redshift evolution of the mean gas-mass fraction,

$$\langle \xi_g^{\rm evo} \rangle = \frac{\int \xi_g^{\rm evo} \frac{dN}{dM} dM}{\int \frac{dN}{dM} dM}, \tag{2.8}$$

as well as the constant gas fraction, $\xi_g = 0.05$.

In our calculation, we take the lower and upper limit of the integration in Eq. (2.6) as $M_{\rm min} = 10^{10}$ $\rm M_\odot$ and $M_{\rm max} = 10^{15}$ $\rm M_\odot$, respectively. There are two main reasons to choose the lower bound 10^{10} $\rm M_\odot$. First, considering the applicability of the $M_*(M_h)$ relation from Ref. [159] and the gas fraction function (Eq. 2.7), it is safe to truncate the halo mass at $M_h \sim 10^{10}$ $\rm M_\odot$. Typically, dwarf galaxies reside in halos with mass less than 10^{10} $\rm M_\odot$ and we only have the constraints from observations at $z \simeq 0$. In our model, we consider the contribution from galaxy mergers up to the redshift $z = 10$ where the $M_*(M_h)$ function is not well tested for the lower halo masses. Also, the gas fraction function (Eq. 2.7) is modeled from (normal) star-forming galaxies [160] and may not be valid for dwarf galaxies. Second, we estimate the low-mass halo contribution to CR luminosity density by extending the lower bound to 10^8 $\rm M_\odot$ and found that the the contribution from $10^8 - 10^{10}$ $\rm M_\odot$ halos is $\lesssim 10\%$ of the total luminosity density in the low redshift ($z \lesssim 3$), which implies that the conclusion of this paper does not depend sensitively on the mass range.

2.3.2 Shock Velocity v_s

In the hierarchical clustering of large-scale structure scenario, the galactic-size halos are contained inside larger cluster-size halos. The peculiar velocities of the galactic-size halos are, therefore, of order of the virial velocity of the cluster-sized halo. Here, we approximate the shock velocity of the galaxy merger from the pairwise velocity dispersion projected along the line of approach of two galaxies. For galaxies with a luminosity $L \approx L^*$ (where L^* is the characteristic luminosity), Ref. [161] showed that the two-point correlation function at $r < 20h^{-1}$ Mpc can be approximated by a power law

$$\xi(r) = \left(\frac{r}{r_0}\right)^{\gamma}, \tag{2.9}$$

where $\gamma \approx 1.7$ and $r_0 \approx 5h^{-1}$ Mpc is the correlation length, inside which galaxies are strongly correlated. Combining the hierarchical form of the three-point correlation

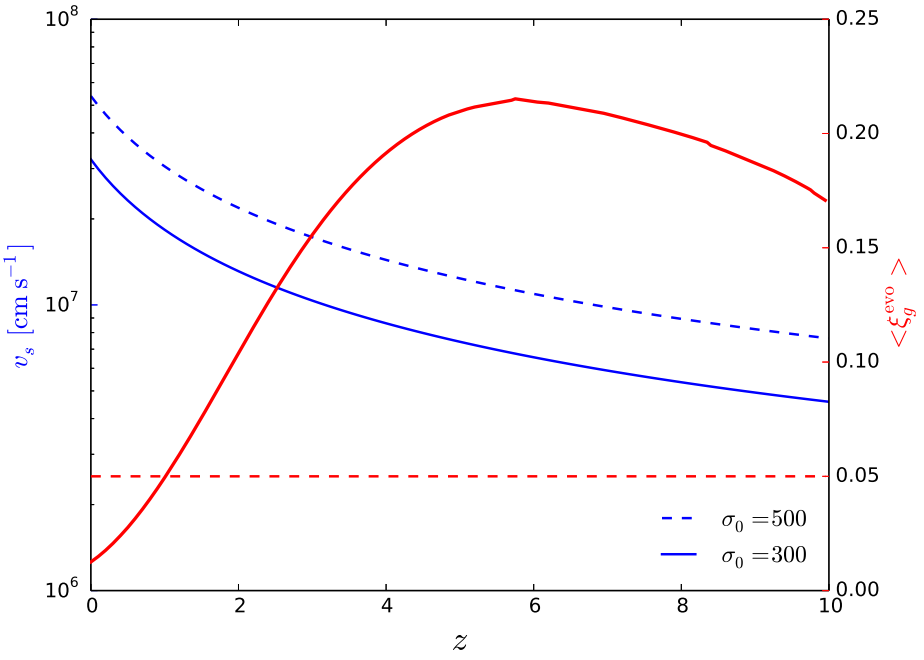

Figure 2.2. Redshift-dependent gas fraction $\xi_g(z)$ (red solid line) compared to a constant gas fraction $\xi_g = 0.05$ (red dashed line) for redshift-dependent shock velocity with $\sigma_0 = 300$ (blue solid line) and with $\sigma_0 = 500$ (blue dashed line), respectively.

function of galaxies [162] and the cosmic virial theorem derived from the Layzer-Irvine equation, the collision (or shock) velocity can be written as

$$\begin{aligned} v_s &= \sqrt{\bar{\sigma}^2(r)} \\ &\simeq \sigma_0 \left(\frac{r_0}{5h^{-1}\ \mathrm{Mpc}}\right)^{\gamma/2} \left(\frac{r}{1h^{-1}\ \mathrm{Mpc}}\right)^{-\gamma}\ \mathrm{km\ s^{-1}}. \end{aligned} \tag{2.10}$$

Given the average density of halos, we can estimate the average separation of galaxies through

$$r = \left(\int \frac{dN}{dM} dM\right)^{-1/3}. \tag{2.11}$$

For our calculation it is necessary to consider the redshift dependance of the correlation function $\xi(r)$ in the nonlinear regime. As a useful approximation, we adopt the stable clustering (SC) hypothesis [163, 164], in which only the size (or separation between structures) of the clusters changes in time while the internal density structure of clusters stays intact. This leads to $\xi(r, z) \propto (1+z)^{\gamma-3}$ and $r_0 \propto (1+z)^{-(3-\gamma)/\gamma}$. Note that we only need the evolution of the nonlinear scale r_0, which is defined by $\xi(r_0, z) = 1$. A

more accurate treatment [165] describes the evolution of $\xi(r,z)$ from the linear to the nonlinear regime, and this treatment was generalized by Ref. [166] and by Ref. [167] using another formula for the nonlinear function. This generalized method gives $\xi(r,z)$ in the quasilinear regime and confirms that $\xi(r,z) \propto (1+z)^{\gamma-3}$ is valid in the nonlinear limit as well. Therefore, in this paper, we use $r_0^{\rm SC} \propto (1+z)^{-(3-\gamma)/\gamma}$ in Eq. (2.10) to find the shock velocities. We show the redshift dependence of the shock velocity $v_s(z)$ in Fig. 2.2 (see blue curves).

Note that, in our approximation of the shock velocity Eq. (2.10), the galaxy separation r given by Eq. (2.11) is overestimated, since this latter equation takes an average of the galaxies in a cosmological volume including clusters and voids. The mean separation of the galaxies in clusters, therefore, must be smaller than the value that we have adopted here, and this overestimate of r would give a slight underestimate of v_s inside clusters. As a possible way to correct for this, we note that redshift surveys give $\sigma_0 \sim 500$ [168–170] as an average value for mergers in clusters. A qualitatively appropriate correction for the cluster shock velocity may be obtained by scaling up σ_0 in Eq. (2.10) from the local average value, concluding that a realistic value of σ_0 for clusters is in the range $500 \lesssim \sigma_0 \lesssim 600$. In terms of rates, most galaxy mergers occur in the smaller mass halos containing fewer galaxies, as opposed to large clusters. Considering the observational and theoretical uncertainties, we expect that the values of σ_0 lie in the range of $100 \lesssim \sigma_0 \lesssim 1000$, and we take $300 \lesssim \sigma_0 \lesssim 500$ as fiducial values.

2.4 Neutrino and γ-Ray Production

Since in our model we need to consider the neutrino/γ-ray production rate up to redshift $z = 10$, we introduce here the redshift evolution function of the gas density, $g(z) = n(z)/n(z=0)$. To define this function we use the result that a sphere of gas will collapse and virialize once its density exceeds the value $1.686\mathcal{D}(z)^{-1}\rho_c(z)$ [171]. The mean density of the virialized gas is $\Delta_c\rho_c(z)$, where $\rho_c(z) = 3H(z)^2/(8\pi G)$, and an approximation of $\Delta_c(z)$ is $\Delta_c \approx 178\Omega_m^{0.45}$ [172], where $\Omega_m = \Omega_{m,0}(1+z)^3/[\Omega_{m,0}(1+z)^3 + 1 - \Omega_{m,0}]$. Since clusters are the largest virialized objects in the universe, we take $\rho_{\rm cl}(z) = g(z)n_{\rm cl,0}m_p \propto \Delta_c\rho_c(z)$, and we assume that galaxies, halos and clusters all share a universal $g(z)$,

$$g(z) = \frac{\Delta_c\rho_c(z)}{\Delta_{c,0}\rho_c(0)} = (1+z)^{1.35}[\Omega_{m,0}(1+z)^3 + 1 - \Omega_{m,0}]^{0.55}. \tag{2.12}$$

In the following sections, the relations $n_{\rm g}(z) = g(z)n_{\rm g,0},\ n_{\rm cl}(z) = g(z)n_{\rm cl,0}$ will be used for the post-shock magnetic field and *pp* optical depth.

2.4.1 Galaxy Mergers

The maximum energy of CRs accelerated in the merger shocks will also evolve with z due to the redshift dependance of the typical galactic radius and magnetic field characterizing the shocks. The magnetic field behind the shock in a galaxy merger is commonly parametrized as a fraction of the ram pressure [68], $B_s^2/8\pi = \frac{1}{2}\epsilon_B n_{\rm g} m_p v_s^2 \propto \rho v_s^2$. This implies a magnetic field

$$\begin{aligned} B_s &= \sqrt{4\pi\epsilon_B n_{\rm g,0} m_p g(z) v_s^2} \\ &\simeq 14\,\epsilon_{B,-2}^{1/2} n_{\rm g,0}^{1/2} g(z)^{1/2} \times \left(\frac{v_s}{300\ {\rm km\ s^{-1}}}\right)\ \mu{\rm G}. \end{aligned} \tag{2.13}$$

The magnetic field in the disk region is expected to be higher than that in the halo region. Although details depend on the geometry, for simplicity, we assume that a reasonably strong magnetic field is expected over scales between the galaxy radius $R_{\rm g}$ and a gas scale height $h_{\rm g}$, which is taken as the characteristic scale height $h \sim (3h_{\rm g}R_g^2/2)^{1/3}$ in this work. Then, the maximum CR energy is estimated to be [173]

$$\begin{aligned} \varepsilon_p^{\rm max} &\sim \tfrac{3}{20} e B_s h \tfrac{v_s}{c} \simeq 1.3\times10^{16}\ {\rm eV}\left(\tfrac{B_s}{30\ \mu G}\right)\times \\ &\qquad \left(\tfrac{h}{3\ {\rm kpc}}\right)\left(\tfrac{v_s}{300\ {\rm km\ s^{-1}}}\right). \end{aligned} \tag{2.14}$$

The CRs are advected to the far downstream, and produce neutrinos and γ-rays during the advection. In reality, one needs to calculate neutrinos and γ-rays from the post-shock region especially when the *pp* optical depth in the CR acceleration region is dominant. The emissions occur during $t_{\rm dyn} \sim h/v_s \simeq 9.8$ Myr $(h/3$ kpc$)(300$ km s$^{-1}/v_s)$. In this work, for simplicity, we take the CR reservoir limit, in which the CRs mostly escape into the ISM and the neutrino and γ-ray production mainly occurs in the ISM.

After the CRs are accelerated in the shock, they will propagate in the host galaxy and cluster. In this process, neutrinos and γ-rays are generated from pions produced in inelastic *pp* collisions. The meson production efficiency is $1-\exp(-f_{pp})$ where $f_{pp} = c\kappa_{pp}\sigma_{pp} g(z)\sum n_{i,0} t_i$ is the effective *pp* optical depth. In this expression, $n_{i,0}$ is the local gas density of the medium, e.g. galaxies and clusters, $\sigma_{pp} = \sigma_{pp}(\varepsilon_p)$ is the *pp* cross section given by Ref. [174], $\kappa_{pp} = 0.5$ is the inelasticity coefficient and $g(z)$ (see Eq. (2.12)) represents the redshift evolution of the gas density.

Let us consider galaxies that are merging at z. Inside the merged galaxy, $f_{pp}^{\rm g}$ is determined by the time spent by the CRs undergoing pp collisions, which depends on the CR injection time and and the diffusion time in the medium. The dynamical time is given by the third of Eq. (2.5), while the diffusion time is $t_{\rm diff} = h(z)^2/(6D_{\rm g})$, where $h(z)$ is the effective gas size at z and D_g is the diffusion coefficient in the galactic ISM gas. Here, we use a combined large and small angle diffusion expression as in Ref. [144], $D = D_c[(\varepsilon/\varepsilon_{c,g})^{1/2} + (\varepsilon/\varepsilon_{c,g})^2]$, where $D_c = cr_L(\varepsilon_{c,g})/4$ and $\varepsilon_{c,g}$ is determined from $r_L(\varepsilon_{c,g}) = l_c/5$. Here, r_L and l_c are the Larmor radius and coherence length in the galaxy environment respectively. For local normal galaxies, the gas density in the disk is $n_{\rm g,0} \sim 1$ cm^{-3}, whereas the average density in the galactic halo is smaller, $n_{\rm g,0} \sim 0.1$ cm^{-3}. The magnetic field of local normal galaxies is ~ 4 μG and that of star-forming galaxies is ~ 6 μG, respectively [175,176]. For the density and magnetic field of merging galaxies, we take values higher than those of normal galaxies, since the galaxies may enter the starburst phase during the merger. Specifically we adopt a mean value $n_{\rm g,0} = 1$ cm^{-3}. Thus, we have

$$t_{\rm diff} \simeq 3.2 \times 10^5 \text{ yr } \left(\frac{h(z)}{3 \text{ kpc}}\right) \left[(\varepsilon/\varepsilon_{c,g})^{1/2} + (\varepsilon/\varepsilon_{c,g})^2\right]^{-1} \tag{2.15}$$

where

$$\varepsilon_{c,g} \simeq 1.7 \times 10^9 \text{ GeV } \left(\frac{h(z)}{3 \text{ kpc}}\right) \left(\frac{B_g}{30 \ \mu G}\right). \tag{2.16}$$

Calculations of the neutrino and γ-ray emission depend on details of the spatial extension and time evolution of the shock region and its surrounding environment. The latter is also modified by the shock, star-formation, and outflow. For simplicity, we treat a double-galaxy merger system as one CR reservoir for the injection by the merger shock, which is conservative since there should also be the emissions from the accelerator. A similar treatment for neutrino sources with active accelerators is used in the galaxy cluster model [137,138]. Then, the effective pp optical depth is estimated to be $f_{pp}^{\rm g} = \kappa_{pp} c g(z) n_{\rm g,0} \sigma_{pp} \min[t_{\rm dyn}, t_{\rm diff}] \simeq 0.24 \ g(z) \left(\frac{n_{\rm g,0}}{1 \text{ cm}^{-3}}\right) \left(\frac{\sigma_{pp}}{50 \text{ mb}}\right) \left(\frac{\min[t_{\rm dyn}, t_{\rm diff}]}{10 \text{ Myr}}\right)$ in the merging galaxy system. The ambient magnetic field energy may be taken to be a fraction of the merging galaxy system's virial energy, as $B_{\rm g}^2 R_{\rm g}^3 \propto G M_{\rm g}^2/R_{\rm g}$, i.e. $B_{\rm g} \propto \rho_{\rm g} R_{\rm g} \propto g(z) R_{\rm g}(z)$.

The typical galactic radii evolve with redshift z, and considering the merger history of galaxies, it is apparent that the mean radii of galaxies at z should be smaller than $R_{\rm g,0}/(1+z)$, where $R_{\rm g,0} \approx 10$ kpc is the radius of local Milky Way-like galaxies. Ref. [177] studied the redshift evolution of the galaxy effective radius r_e using *Hubble Space Telescope*

(HST) samples of galaxies at $z = 0 - 10$, finding $r_e \propto (1+z)^{-1.0} - (1+z)^{-1.3}$ with $r_e \propto (1+z)^{-1.10\pm0.06}$ as a median. Hence, in this paper, we assume that the average galaxy radius evolves with respect to z as $R_{\rm g} = R_{\rm g,0}(1+z)^{-1.10}$.

As for the scale height $h_g(z)$, based on the surface photometry analysis of edge-on spiral galaxies, e.g. NGC 4565, it has been shown that the scale height of gas in local disk galaxies is approximately $h_{g,0} \approx 300 - 400$ pc [178, 179]. Later studies of NGC 891 [180], NGC 5097 [181] etc. also agree with this estimate. Considering that a merger can lead to entering a star-forming phase, we assume $h_{g,0} = 500pc$ and we assume the same redshift dependence as for $R_{\rm g}$, e.g. $h_{\rm g}(z) = (1+z)^{-1.10} h_{\rm g,0}$. Then we take $h = (3h_{\rm g}R_{\rm g}^2/2)^{1/3}$.

2.4.2 Interactions in the Host Cluster and Cluster Mergers

After escaping the galaxy, the CRs may continue to collide with the gas of the host cluster, where $t_{\rm diff} = R_{\rm cl}(z)^2/(6D_{\rm cl})$. Here, we assume a magnetic field $B_{\rm cl,0} \approx 1\ \mu G$ with a coherence length $l_{c,\rm cl} \approx 30$ kpc. This implies $\varepsilon_{c,\rm cl} \approx 5.6 \times 10^9$ GeV. For a cluster of mass 10^{15} $M_\odot$, the virial radius is $R_{\rm cl,0} = (3M/(4\pi\rho_{\rm cl,0}))^{1/3} \approx 2.1$ Mpc. Since $R_{\rm cl}$ is the approximate boundary of clustered/correlated galaxies, it should have the same redshift dependence as $r_0^{\rm SC}$. Using the stable clustering approximation, we obtain $R_{\rm cl} \propto (1+z)^{-(3-\gamma)/\gamma}$. Similarly, we can calculate the diffusion time in clusters as $t_{\rm diff,cl} = 1.2[(\varepsilon/\varepsilon_{c,\rm cl})^{1/2} + (\varepsilon/\varepsilon_{c,\rm cl})^2]^{-1}$ Gyr. Assuming that the injection time of CRs ($t_{\rm inj}$) at redshift z is the cluster age (of order the Hubble time) $t_{\rm age}(z)$, likewise we obtain the optical depth $f_{pp}^{\rm cl} = \kappa_{pp} c g(z) n_{\rm cl,0} \sigma_{pp} \min[t_{\rm inj}, t_{\rm diff,cl}] \simeq 0.24\ g(z) \left(\frac{n_{\rm cl,0}}{10^{-3}\ {\rm cm}^{-3}}\right) \left(\frac{\sigma_{pp}}{50\ {\rm mb}}\right) \left(\frac{\min[t_{\rm age}, t_{\rm diff}]}{10\ {\rm Gyr}}\right)$, where $n_{\rm cl,0}$, the intercluster gas density, is assumed to have the typical value $n_{\rm cl,0} \sim 10^{-4} - 10^{-2}$ cm^{-3} [182], which can be higher in cooling core clusters. The magnetic field may also depend on z as $B_{\rm cl} \propto \rho_{\rm cl} R_{\rm cl} \propto g(z) R_{\rm cl}(z)$.

Halo mergers will also lead to galaxy group and galaxy cluster mergers, after some halos have grown above a certain size which may be taken to be roughly of order $M_h \sim 10^{13}$ $M_\odot$. We simplify the calculations as follows. For low-mass mergers, we expect that the *pp* interactions occur mainly in gas with an ISM density characteristic of galaxies, while for high-mass mergers the *pp* interactions occur mainly in gas with an IGM density characterizing the intra-cluster gas. In addition, there will be a component of *pp* interactions due to low-mass merger CRs which escape from the colliding galaxy system into the IGM. Thus, we expect that the all-flavor neutrino production rate consists of a

galaxy part $\varepsilon_\nu Q_{\varepsilon_\nu}^{(\rm g)}$ and a cluster/group part $\varepsilon_\nu Q_{\varepsilon_\nu}^{(\rm cl)}$ plus a weaker galaxy-cluster term,

$$\begin{aligned}\varepsilon_\nu Q_{\varepsilon_\nu}^{(\rm g)} =& \frac{1}{2}(1-e^{-f_{pp}^{\rm g}})\varepsilon_p Q_{\varepsilon_p}^{(\rm LM)} \\ \varepsilon_\nu Q_{\varepsilon_\nu}^{(\rm cl)} =& \frac{1}{2}[(1-e^{-f_{pp}^{\rm cl}})\varepsilon_p Q_{\varepsilon_p}^{(\rm HM)} \\ &+ \eta(1-e^{-f_{pp}^{\rm cl}})e^{-f_{pp}^{\rm g}}\varepsilon_p Q_{\varepsilon_p}^{(\rm LM)}],\end{aligned} \tag{2.17}$$

where the energies of the neutrinos and CR protons are related by $\varepsilon_\nu \approx 0.05\varepsilon_p$. Note that the luminosity density evolution of neutrinos and γ-rays is different from that of CRs in general. In the first line of Eq. 2.17 $\varepsilon_p Q_{\varepsilon_p}^{(\rm LM)}$ is the CR input rate (see Eq. 2.6) from galaxy mergers in low-mass (LM) halos, e.g. $[10^{10}\ {\rm M}_\odot, 10^{13}\ {\rm M}_\odot]$. In the second line $\varepsilon_p Q_{\varepsilon_p}^{(\rm HM)}$ is the CR input rate of the high-mass (HM) halo mergers, in the interval $[10^{13}\ {\rm M}_\odot, 10^{15}\ {\rm M}_\odot]$. The factors $\frac{1}{2}(1-e^{-f_{pp}^{\rm i}})\varepsilon_p Q_{\varepsilon_p}^{(\rm j)}$ are the neutrino luminosity density from CRs originating from mergers of mass (j) in gas of density i. For our fiducial parameters, these two components constitute the largest fraction of the neutrino budget. Nevertheless, for completeness, we have included in the third line of Eq. 2.17 the sub-dominant effect due the CRs produced in galaxy mergers which may escape the host galaxies and collide with intra-cluster gas to produce neutrinos. (This can be important only if the pp interactions in galaxy mergers are inefficient.) We introduce a parameter η to represent the fraction of galaxy mergers that occur inside clusters which lead to some CRs escaping into the gas halo. This can occur preferentially at lower redshifts. Since the boundary between LM and HM is ambiguous and the fraction η can change with redshift, this parameter is very uncertain, and may conservatively be estimated as between 0.1 and at most 0.5. Fortunately, the contribution of this higher-order third component depending on η is small compared to the first two components in Eq. 2.17, due to the factor $e^{-f_{pp}^{\rm g}}$. At $z = 1$, the ratio between the third line and the first line is $\leq 10\%$ even if η is assumed to be unity, and it is increasingly negligible at higher redshift since $f_{pp}^{\rm g}$ increases as the gas density increases. Therefore, the exact value of η does not significantly influence our final results.

2.5 Diffuse Neutrino and γ-Ray Spectra

With the above, we are able to determine the CR energy input rate, $\varepsilon_\nu Q_{\varepsilon_\nu}^{(\rm g)}$ and $\varepsilon_\nu Q_{\varepsilon_\nu}^{(\rm cl)}$. Fig. 2.3 shows the CR input power over the whole mass interval $10^{10}{\rm M}_\odot - 10^{15}{\rm M}_\odot$ as a function of z as well as the LM and HM components of ($\sigma_0 = 300,\ \xi_g^{\rm evo}$) scenario.

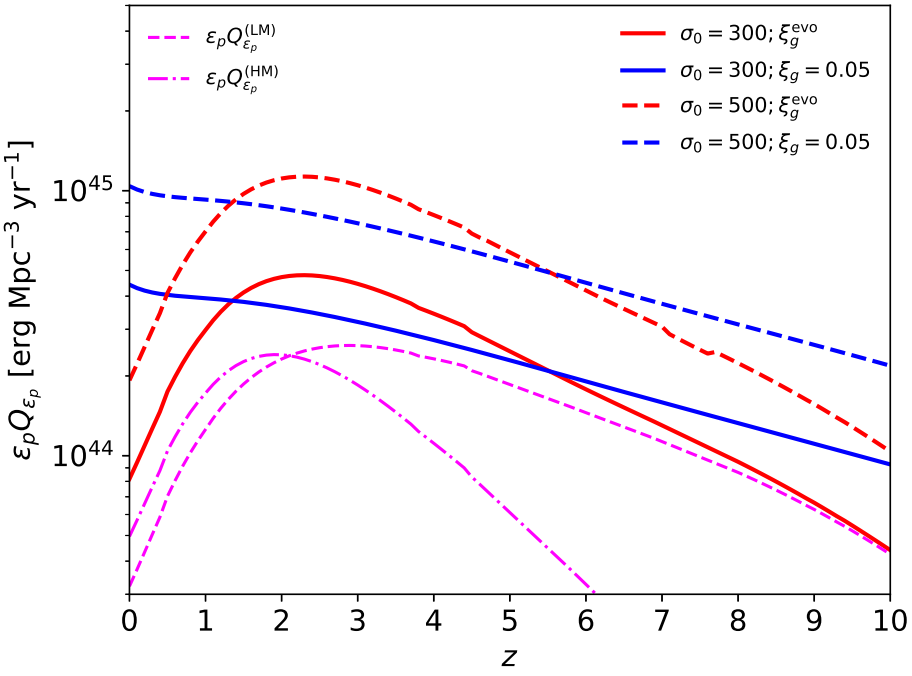

Figure 2.3. CR energy input rate versus redshift. The red lines correspond to a redshift-dependent gas fraction ξ_g^{evo} and the blue lines are for a redshift-independent gas fraction $\xi_g = 0.05$, while the solid lines are for $\sigma_0 = 300$ and the dashed are for $\sigma_0 = 500$, repectively. The dashed and dash-dotted magenta lines are LM and HM components of ($\sigma_0 = 300$, ξ_g^{evo}) scenario. Here LM and HM denote the low-mass (10^{10} $\mathrm{M}_\odot - 10^{13}\mathrm{M}_\odot$) and high-mass ($10^{13}$ $\mathrm{M}_\odot - 10^{15}\mathrm{M}_\odot$) intervals, respectively.

As can be seen from the redshift distribution of the CR energy input, using a redshift evolving gas fraction ξ_g^{evo}, a significant fraction of this occurs at redshifts $z \gtrsim 3$, above which a significant $\gamma\gamma$ attenuation of the accompanying high-energy γ rays at $\gtrsim 20 - 30$ GeV energies can be expected [149, 183]. In addition, from Fig. 2.3, we find that the high-mass and low-mass components are comparable in local mergers, implying that the cluster/group merger contribution is also important. Also, the galaxy merger contribution to the CR luminosity density is more important at $z \gtrsim 2$.

Given the neutrino input rate, the all-flavor neutrino flux can be expressed as [59]

$$\varepsilon_\nu^2 \Phi_{\varepsilon_\nu} = \frac{c}{4\pi} \int \frac{\varepsilon_\nu Q_{\varepsilon_\nu}^{(\mathrm{g})} + \varepsilon_\nu Q_{\varepsilon_\nu}^{(\mathrm{cl})}}{(1+z)} \left| \frac{dt}{dz} \right| dz \ , \tag{2.18}$$

Based on the branching ratio between charged and neutral pions, the *initial* diffuse γ-ray energy spectrum is expected to be given by $\varepsilon_\gamma^2 \Phi_{\varepsilon_\gamma} = \frac{2}{3} \varepsilon_\nu^2 \Phi_{\varepsilon_\nu}|_{\varepsilon_\nu = 0.5\varepsilon_\gamma}$. Since however the high-energy γ rays can annihilate with lower energy photons, such as those from the

extragalactic background light (EBL) and the cosmic microwave background (CMB), we introduce an attenuation factor $\exp[-\tau_{\gamma\gamma}(\varepsilon_\gamma, z)]$ to the integration, where $\tau_{\gamma\gamma}$ is the $\gamma\gamma$ optical depth at redshift z. In this paper, we use the optical depth provided by Refs. [184, 185] for low-redshift ($z \leq 5$) and high-redshift ($z > 5$) inputs, respectively. The attenuated γ-ray flux is then

$$\varepsilon_\gamma^2 \Phi_{\varepsilon_\gamma} = \frac{c}{4\pi} \int \frac{2}{3} \left[\frac{\varepsilon_\nu Q_{\varepsilon_\nu}^{(\mathrm{g})} + \varepsilon_\nu Q_{\varepsilon_\nu}^{(\mathrm{cl})}}{(1+z)} \left| \frac{dt}{dz} \right| \right] \times \exp[-\tau_{\gamma\gamma}(\varepsilon_\gamma, z)] dz \tag{2.19}$$

with $\varepsilon_p = 10\varepsilon_\gamma(1+z)$. In addition, the electron-positron pairs produced in the $\gamma\gamma$ annihilations will subsequently scatter off the ambient diffuse photon backgrounds, leading to an electromagnetic cascade which in part compensates for the attenuation, while reprocessing the photon energy towards lower energies, which can be detected by, e.g. the *Fermi*-LAT instrument. In this paper, for simplicity, we use the universal form for the resulting cascaded γ-ray spectrum given by Refs. [144, 186, 187],

$$\varepsilon_\gamma \frac{dN}{d\varepsilon_\gamma} \propto G(\varepsilon_\gamma) = \begin{cases} \left(\frac{\varepsilon_\gamma}{\varepsilon_\gamma^{\mathrm{br}}} \right)^{-1/2} & \varepsilon_\gamma \leq \varepsilon_\gamma^{\mathrm{br}} \\ \left(\frac{\varepsilon_\gamma}{\varepsilon_\gamma^{\mathrm{cut}}} \right)^{-1} & \varepsilon_\gamma^{\mathrm{br}} < \varepsilon_\gamma < \varepsilon_\gamma^{\mathrm{cut}} \end{cases} \tag{2.20}$$

where $\varepsilon_\gamma^{\mathrm{cut}}$ is defined by $\tau_\gamma(\varepsilon_\gamma^{\mathrm{cut}}, z) = 1$ and $\varepsilon_\gamma^{\mathrm{br}} = 0.0085 \text{ GeV}(1+z)^2 \left(\frac{\varepsilon_\gamma^{\mathrm{cut}}}{100\mathrm{GeV}} \right)^2$.

The all-flavor diffuse neutrino and γ-ray fluxes are plotted in Fig. 2.4, together with the IceCube observed astrophysical neutrinos. The red points and cyan points correspond to the all-flavor averaged neutrino flux [26, 188] and the 6-year high energy starting-events (HESE) [189], respectively. The *Fermi*-LAT observed total extragalactic γ-ray background (EGB) [1] is shown by the blue points. The yellow area is the best-fit to the up-coming muon neutrinos scaled to three-flavor. Fig. 2.4 shows the results for an assumed redshift-dependent gas fraction ξ_g^{evo}, as illustrated in Fig. 2.4(a) for $\sigma_0 = 300$ and in Fig. 2.4(b) for $\sigma_0 = 500$, showing the effect of the corresponding different shock velocities v_s. In each figure, the magenta line represents the neutrino flux while the green line illustrates the corresponding γ-ray flux after cascading down. The galaxy and cluster contributions to the neutrino flux are plotted in dashed lines and dash-dotted lines. The non-blazar [147] component of the unresolved extragalactic gamma-ray background is shown as the pink area.

For illustration purposes, we consider next the corresponding results using the redshift-

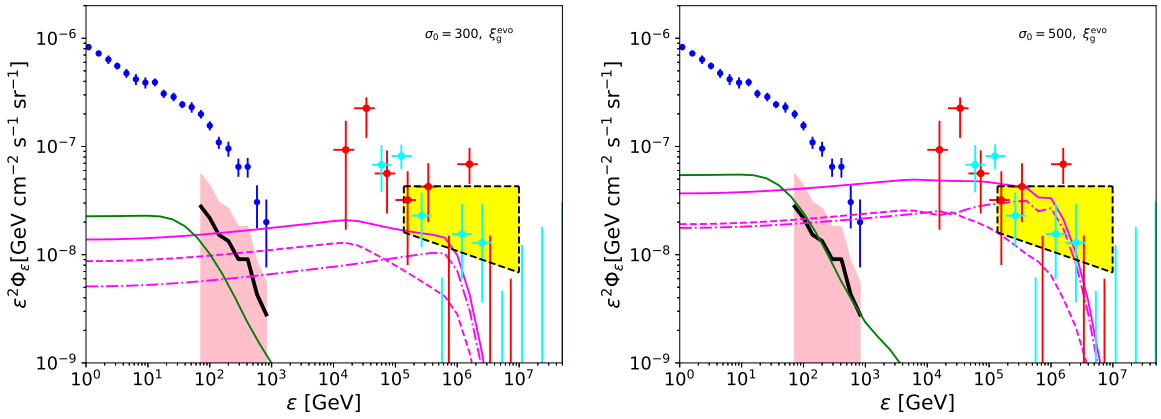

Figure 2.4. Left panel: Neutrino (all flavor) and γ-ray fluxes from halo mergers with redshift-evolving gas fraction $\xi_g^{\rm evo}$, $R_{g,0} = 10$ kpc, $H_{g,0} = 500$ pc. The shock velocity is obtained using $r_0^{\rm sc}(z)$ and $\sigma_0 = 300$. The magenta line is the neutrino spectrum while the green line is the corresponding γ-ray spectrum. Galaxy and cluster contributions to the neutrino flux are illustrated as the dashed and dash-dotted lines, respectively. Right panel: same as left panel except $\sigma_0 = 500$ is utilized for v_s.

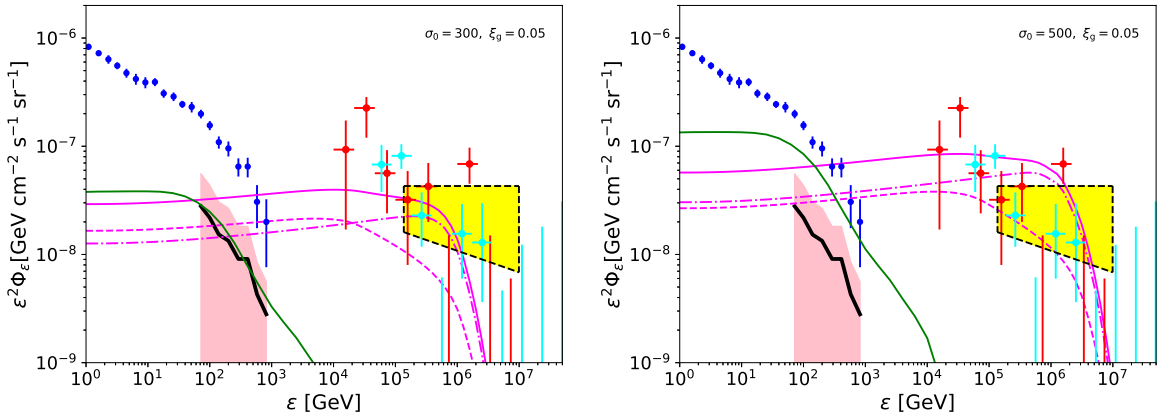

Figure 2.5. Left panel: same as Fig. 2.4 (a), $\sigma_0 = 300$, except that $\xi_g = 0.05$ is used to estimate the redshift evolution of the halo gas fraction. Right panel: same as left figure except with $\sigma_0 = 500$.

independent gas fraction $\xi_g = 0.05$, which are shown in figures 2.5 (a) and 2.5 (b). The comparison between the galaxy and cluster components indicates that the high-energy neutrinos are dominantly produced by the propagation of CRs in the clusters. This is a consequence of the rapid redshift evolution of the galaxy radius, since the size of the host galaxy limits the maximum CR energy as well as the neutrino production efficiency by restricting the diffusion time. In addition, a redshift-dependent $\xi_g^{\rm evo}$ boosts the CR budget to a relatively higher redshift ($z \approx 3$), as can be seen from the red line in Fig.2.3,

which as was expected leads to a reduction in the γ-ray flux. From these figures, we can also see that even with the moderate sensitivity of the results to the parameters r_0 and σ_0, the results can broadly fit a significant fraction of the IceCube data without violating the non-blazar EGB. Conversely, the γ-ray and neutrino fluxes are significantly constrained in this scenario, indicating that the halo and galaxy mergers can be regarded as promising sources of neutrinos in the context of multi-messenger studies.

2.6 Conclusion and Discussion

In this work, we investigated the contribution of halo mergers to the diffuse neutrino and γ-ray backgrounds, and tested whether the non-blazar diffuse γ-ray background *Fermi* constraint is violated. Our results differ from previous work by Ref. [68] in that we studied both galaxy and cluster/group mergers out to higher redshifts, up to $z \approx 10$, by considering the redshift evolution of the average galactic radius, the shock velocity and the gas content inside the halos, as well as the galactic/intergalactic magnetic fields.

The redshift evolution of galaxy radius implies that there exist more protogalaxies, or equivalently more mergers at higher redshift. In fact, the merger rate calculated using our approximate approach verifies this conjecture, as well as being consistent with the Illustris simulations [190]. Also, our estimates of the gas fraction $\xi_g^{\rm evo}$ based on the correlation between the galactic gas content and the star formation rate shows that the gas in high-redshift halos is relatively denser than in the current epoch halos. The net effect is that high-redshift halo mergers can contribute a significant fraction of the cosmic rays that are capable of producing high-energy neutrinos, as shown in Fig. 2.3. This is crucial since the accompanying γ-ray photons in the ensuing pp collisions at high redshifts can be sufficiently absorbed via $\gamma\gamma$ annihilations against CMB and EBL photons. In both cases with $\xi_g^{\rm evo}$, our results indicate that high-redshift galaxy/halo mergers can explain a large fraction of the IceCube observed diffuse neutrinos up to $\sim$PeV, with an accompanying γ-ray diffuse observed flux which is below the non-blazar $Fermi$ constraints.

We note that according to our calculation, the diffuse flux of CRs that survive from energy losses via pp collisions is less than 10^{-8} GeV cm^{-2} sr^{-1} s^{-1}, which is lower than the observed CR flux around the knee or sub-ankle energy.

The CR acceleration efficiency ϵ_p is expected to be ~ 0.1 based on the diffusive shock acceleration theory. The redshift dependences of gas fraction $\xi_g^{\rm evo}$ and galaxy radius are relatively well-modeled from current theories and observations, so our scenario can put

a tighter constraint on the shock velocity of galaxy mergers. However, there are large uncertainties in the model. For example, the maximum energy depends on the magnetic field strength that is highly uncertain. On the other hand, the fiducial value of ~ 10 PeV is not far from the knee energy at ~ 3 PeV, so our assumption is reasonable. One of the most important uncertainties is caused by the shock velocity. Our fiducial parameters ($\sigma_0 = 300$ with $\xi_g^{\rm evo}$) imply a lower neutrino flux compared to the observations. This could be overcome by assuming a higher velocity with a stronger magnetic field. Or it may be possible to achieve the IceCube flux at $\gtrsim 0.1$ PeV without exceeding the *Fermi* constraint by increasing the cluster contribution. However, the cluster contribution is more uncertain. Non-thermal emissions from merging/accreting clusters have been studied by various authors [191, 192]. The Mach number of shocks on the cluster scales is so low due to the high temperature of the intra-cluster medium that the shock may not be strong enough to have a hard spectrum of $s \sim 2$.

We note that, in addition to mergers, also cluster accretion shocks and powerful jets from radio-loud AGNs can contribute to CR acceleration inside the clusters/groups, as considered in the previous literature, e.g., Refs. [58, 138] and references therein. One of the generic features of the CR reservoir scenario is that different possibilities for CR acceleration are not mutually exclusive, and additional contributions from various CR accelerators may enhance the neutrino flux. Another CR source that can be associated with galaxy mergers is that the compression of the ISM gas can trigger an intense starburst. As discussed by Ref. [193], two processes in colliding galaxies could induce starburst: radial gas inflows can fuel a nuclear starburst, while gas turbulence and fragmentation can drive an extended starburst in clusters. Such intense star-formation can naturally lead to the injection of CRs from the ensuing massive stellar deaths, including from SNRs and HNRs. In addition, CRs may also be injected from disk-driven outflows and weak jets from AGNs [48, 140, 194]. The CR contributions from these sources, which would be additional to CRs from the mergers considered here, are significantly model-dependent, and we do not attempt here a quantification of their relative importance.

One important factor that may influence the final results is the CR power-law index s, since the factor ε^{2-s}, the maximal CR energy as well as a new $\mathcal{C} = ((\varepsilon_p^{\rm max})^{2-s} - (\varepsilon_p^{\rm min})^{2-s})/(2-s)$ are required to correct Eq. 2.6 when s deviates from 2.0. As presented in Eq. 2.6, we assume that the shock is non-radiative and infinitesimally thin and hence the Fermi first order acceleration in the strong shock limit implies $s = 2$. However, a finite width of the shock can steepen the spectrum to $s \gtrsim 2.0$, while a radiative shock would produce a CR spectrum with a power-law index lower than 2.0. For radiative shocks,

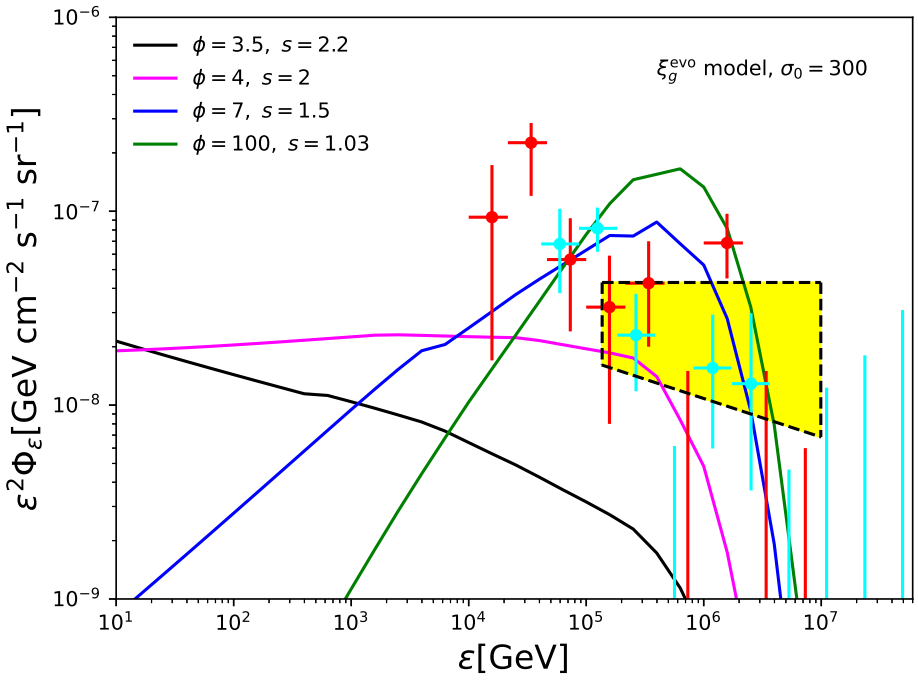

Figure 2.6. The neutrino fluxes for different compression ratios and CR power-law indices. The black, magenta, blue and greens lines correspond to the power-law indices $s = 2.2,\ 2.0,\ 1.5$ and 1.03.

Ref. [195] showed that the power-law index of the accelerated CRs is $s = (\phi + 2)/(\phi - 1)$ where ϕ is the compression ratio. Moreover, Ref. [196] assume $\phi = 7$ and $s = 1.5$ as fiducial values when studying the radiative cooling of SNR shocks. Note that the compression ratio for radiative shocks with an isothermal adiabatic index $\gamma = 1$ can be written as $\phi = M^2 \gg 1$, where M is the upstream Mach number. We asume thus $s = 1$ in this extreme case. To illustrate how the neutrino spectra are affected by the radiative cooling and/or the width of the shocks, we plot in Fig. 2.6 the neutrino fluxes for four cases $s = 2.2, 2.0,\ 1.5$ and 1.03 which correspond to $\phi = 3.5,\ 4,\ 7,\ 100$, respectively. As can be seen, a harder CR power-law index (lower s) will produce more high-energy neutrinos. Thus, in principle, a mildly radiative-cooling shock ($1.5 \leq s \leq 2$) can more easily achieve the high-energy neutrino flux in the range 10 TeV to $\sim$ PeV. On the other hand, $s \gtrsim 2.1 - 2.2$ is disfavored because of the damping factor ε^{2-s}, which is consistent with previous work [58]. Note that the hard spectrum is expected for the cold gas environment that would be valid in sufficiently low-mass halo mergers. If the temperature is so high, the Mach number is expected to be low, as expected for cluster mergers. In this case, the spectrum is softer for massive clusters, and details are beyond

the scope of this work.

Additional contributions may arise from the galaxies moving through the cluster or dark matter halo, as their hypersonic peculiar motion will result in a shock as they plow through the intra-cluster gas, which as a result can also contribute to the diffuse γ rays and neutrinos. Supposing as an extreme case that the loss of the galaxies' kinetic energy due to the gravitational drag is completely converted into CR energy, we estimate a CR energy budget of

$$\varepsilon_p Q_{\varepsilon_p}^{(\mathrm{IGM})} = \epsilon_p \mathcal{C}_{\mathrm{IGM}}^{-1} \int dM_h \frac{4\pi G^2 M_h^2 \rho_{cl}}{v_s} \frac{dN}{dM_h} \ln\left(\frac{R_{\mathrm{cl}}}{R_g}\right), \tag{2.21}$$

which is three orders of magnitudes lower than halo mergers estimated in the previous sections, because of the tenuous intergalactic gas density. Hence, these shocks contribute only a relatively small amount of diffuse neutrinos and are negligible compared to the mergers.

2.7 Summary

In summary, we found that the CR luminosity density by halo mergers can be comparable to that from starburst galaxies, which can be expected from galaxy mergers. In particular, the CR input from galaxy mergers and cluster/group mergers is comparable in the local universe, and the former is more important at higher redshifts, $z \gtrsim 2$ (see the dashed and dash-dotted lines in Figure (2.3). This emphasizes the importance of our results for CR reservoir models. We have considered the neutrino and γ-ray production in galaxy-galaxy and cluster/group merger environments and found that such mergers could explain a large portion of the IceCube diffuse neutrino flux. Since many more galaxy-scale, low-mass halo mergers occur at relatively high redshifts, the contribution to the diffuse γ-ray background observed by *Fermi* is more suppressed, due to the $\gamma\gamma$ absorption. Despite the various uncertainties due to the lack of high redshift observations of the galactic and cluster morphologies, the gas distribution and the galactic/intergalactic magnetic fields, some of the crucial and sensitive parameters including the gas fraction ξ_g^{evo} are relatively well constrained. The parameter space left for variance of both the neutrino and γ-ray spectra is restricted by our results, as demonstrated in Figs. 2.4 and 2.5. One of the large uncertainties comes from the spectral index, and we demonstrated the cases of harder CR spectral indices, $1.5 \lesssim s \lesssim 2$, which could be expected in strong radiative shocks.

One of the predictions of the halo merger model is that the effective number density

of these sources is expected to be $\sim 10^{-5}$ Mpc^{-3}, which is similar to the number density of starburst galaxies and AGN with disk-driven outflows. The present model is testable in the sense that such halo merger sources are detectable with next-generation detectors such as IceCube-Gen2 via searches for multiplets, auto-correlation, and cross-correlation signals [197]. One must keep in mind that the contributions from galaxy/halo mergers are degenerate with those from other possibilities, such as the starburst and AGN contributions, since a large fraction of starburst and AGN activities can be induced by these mergers. To distinguish among these models, cross-correlation or auto-correlation studies in neutrinos and γ-rays should be useful. Also, to identify the merging sources, it will be important to investigate these sources at multi-wavelengths.

Acknowledgements

We are grateful to Zhao-Wei Zhang and Kazumi Kashiyama for useful discussions. This research was partially supported by NASA NNX13AH50G (C-C.Y., P.M.), the Alfred P. Sloan Foundation and NSF grant No. PHY-1620777 (K.M.) and NSF grant No. AST-1517363 (D.J.).

Disclaimer

The findings and conclusions do not necessarily reflect the view of the funding agencies.

2.8 Appendix 1: Halo Merger Rate

In this section we present a comparison between our halo merger rate with the Illustris simulations [190]. In our calculation, we assign a mean merger probability $P(M,z) = \exp(-t_{\rm merger}/t_{\rm age})$ to each dark matter halo during $t_{\rm age}$. Here, $t_{\rm merger}$, which can be obtained from the second equation of Eq.(2.5), averages all possible mass ratios, e.g. $\zeta \in (0,1]$. In our calculation, we do not need to use the cumulative merger rate over mass directly, instead the factor $\frac{dN}{dM}\frac{P(M,z)}{t_{\rm age}}$ in the integrand of Eq. (2.6) is used to illustrate the number of mergers for a halo with mass M and at redshift z. However, in order to compare our results with the simulations, it is worthwhile to estimate the average

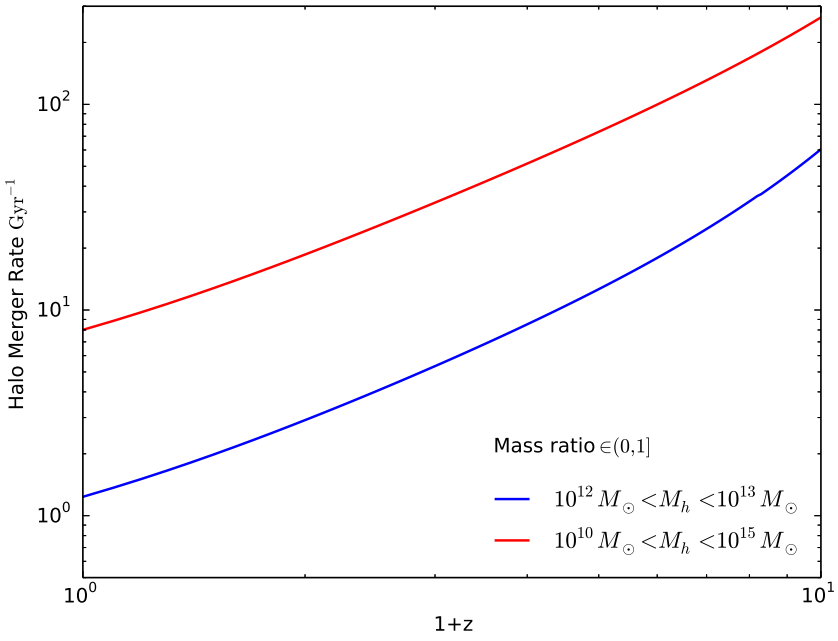

Figure 2.7. Merger rates from Eq. (22). The blue line represents the whole mass range (10^{10} $M_\odot \sim 10^{15}$ $M_\odot$) and the red line corresponds to 10^{12} $M_\odot < M_h < 10^{13}$ $M_\odot$

.

cumulative merger rate using our approach,

$$\mathcal{R}(z) = \frac{\int \frac{dN}{dM} \frac{P(M,z)}{t_{age}} dM}{\int \frac{dN}{dM} dM}. \tag{2.22}$$

The merger rate is shown in Fig. 2.7 where the blue line represents the whole mass range (10^{10} $M_\odot \sim 10^{15}$ $M_\odot$) and the red line corresponds to 10^{12} $M_\odot < M_h < 10^{13}$ $M_\odot$. In both cases, the mass ratio covers the entire interval as in the middle equation of Eq. (2.5) which is integrated over ζ from 0 to 1. The merger rate given by Illustris simulations is shown in the lower panel.

One can compare our results with solid black lines in the right panel of Fig. 2 in Ref. [190], since the increase in the merger rates given by simulations (as shown as colored lines) seen at low redshifts is due to a limitation of the splitting algorithm. As can be seen, our merger rate in the same mass interval is comparable to the merger rate in the right panel with the mass ratio $\geq 1/1000$. Considering that we are using a totally different method and this approach is primarily designed to evaluate the merger probabilities of halos of various masses and at different redshifts, the moderate degree of

discrepancy can be considered acceptable.

Chapter 3
Secondary Radio and X-Ray Emissions from Galaxy Mergers

Note: The material in this Chapter is based on my paper [198], with co-authors Peter Mészáros, and Kohta Murase.

3.1 Motivation

Star-forming galaxies including starbursts have been considered as possible reservoirs of cosmic rays (CRs) and sources of associated neutrinos and gamma rays [199–201], in which the CRs can be supplied by not only supernovae but also hypernovae, superbubbles and active galactic nuclei [144, 194, 202–205]. Interacting galaxies, which may be accompanied by starburst activities, have also been considered as additional accelerators of CRs [68,206]. Under the conditions typical of galaxy merger systems synchrotron emission can extend from the radio band to the X-ray regime, while the inverse Compton scattering may be important in the ultraviolet (UV) and up to beyond the X-ray band.

In this work we formulate a model which is capable of reproducing the radio and X-ray observations of specific systems using synchrotron and synchrotron self-Compton (SSC) or external inverse Compton (EIC) emissions from high-energy secondary electron-positron pairs produced by the CR interactions in such systems. Here the EIC is caused by scatterings with the cosmic microwave background (CMB), infrared/optical starlight (SL) and extragalactic background light (EBL). In addition, since the radiation spectrum of the merging galaxies is determined by the dynamics of the galaxy interactions and the resulting physical conditions, this enables us to provide constraints on the magnetic field B, shock velocity v_s, gas mass $M_{\rm g}$, etc. Different from Ref. [207] where shock-accelerated electrons are employed to describe the radio emissions of two colliding

galaxies, UGC 12914/5 and UGC 813/6, we present an alternative model based on the secondary emission from inelastic *pp* collisions to reproduce simultaneously the radio and X-ray observations of NGC 660 and NGC 3256. In general, secondary electrons are more natural to explain the electromagnetic emissions in merging galaxies. For the observed CRs, the electron acceleration efficiency, the fraction of plasma energy deposited to electrons, is at least two orders lower than the proton acceleration efficiency, e.g. $K_{e/p} = \epsilon_e/\epsilon_p \sim 10^{-4} - 10^{-2}$ [208, 209]. This value is also consistent with the observations of Galactic supernova remnants. Furthermore, the recent particle-in-cell simulation shows a similar value, $K_{e/p} \simeq 10^{-3}$ [210–212]. The ratio of the primary electrons (from shock accelerations) and the secondary electrons and positrons is approximately

$$\frac{\mathcal{E}_{e,\mathrm{primary}}}{\mathcal{E}_{e,\mathrm{sec}}} \simeq \frac{6\epsilon_e}{\min[1, f_{pp,\mathrm{g}}]\epsilon_p} \lesssim 10^{-1}.$$

where $f_{pp,\mathrm{g}}$ is the effective *pp* optical depth in the emitting region. Therefore in our model with the typical electron/proton acceleration efficiencies, emission from primary electrons directly accelerated in shocks is subdominant compared to that from secondary electrons and positrons from *pp* collisions and pion decays. This is consistent with Ref. [213] where they suggest that the secondary emissions overwhelm the primary component in nearly proton calorimetric sources. It is possible that primary electrons can provide a non-negligible contribution if $K_{e/p} \gtrsim 0.1$, considering that $K_{e/p}$ is poorly constrained theoretically and observationally for this system. In the following text, we focus on the primary electron/positron scenario and omit the primary electron contribution.

As a well-studied interacting system, NGC 660 is a galaxy formed by the collision of two galaxies [214], which has been observed in both radio [215–223], microwave, infrared, UV and X-ray [224–227] bands. Also, the magnetic field in the core region of NGC 660 is constrained in the range of 16 ± 5 μG through polarization studies [228]. In this paper, we take NGC 660 as an example and use our model to reproduce the radio, UV and X-ray fluxes. We also apply our model to constrain the shock velocity and gas mass of the core region of NGC 660 by using the magnetic field 16 ± 5 μG as a precondition. To show that our model's applicability can be extended to other similar systems, we also consider another well-studied galaxy formed through a merger, NGC 3256, as a supplementary template.

This paper is organized as follows. In Sec. 3.2, we formulate the secondary electron-positron spectrum and calculate resulting electromagnetic emissions, including synchrotron radiation and SSC/EIC components. In Sec. 3.3 , we apply the formalism in

Sec. 3.2 to the core regions of NGC 660 and NGC 3256. A summary and discussion, including comparison with previous work in the context of starburst galaxies, is given in Sec. 3.4.

3.2 Secondary Electron Spectrum and Electromagnetic Emissions

The pions produced in the *pp* collisions between shock-accelerated CR ions and the galaxy gas generate, besides high-energy neutrinos and γ-rays, also copious quantities of high-energy electron-positron pairs. These high-energy leptons may produce observable synchrotron emissions while propagating inside the galactic magnetic fields. Here, considering the conservation of lepton numbers and muon decays, we approximate the total electron-positron injection spectrum to be the same with the neutrino production spectrum. Following the procedure in Ref. [206], the electron injection spectrum can be written as

$$\begin{aligned}\varepsilon^2 \mathcal{N}_e(\varepsilon) =& \frac{1}{3}\varepsilon^2 \frac{dN_\nu}{d\varepsilon} = \frac{1}{12}\epsilon_p \mathcal{C}^{-1} M_{\rm g} v_{\rm s}^2 \\ & \times \min\left[1, f_{pp,{\rm g}}\right]_{\varepsilon_p \simeq 20\varepsilon}\,,\end{aligned} \tag{3.1}$$

where ϵ_p is the CR ion acceleration efficiency (normally fixed as 0.1), $\mathcal{C} = \ln(\varepsilon_{p,\rm max}/\varepsilon_{p,\rm min})$ is the normalization coefficient for a ε^{-2} spectrum, $M_{\rm g}$ is the gas mass of the merging region, v_s is the shock/collision velocity and $f_{pp,{\rm g}} = \kappa_{pp} c n_{\rm g} \sigma(\varepsilon_p) \min[t_{\rm esc}, t_{\rm dyn}]$ is *pp* optical depth inside the galaxy. In this expression, $\kappa_{pp} = 0.5$ is the proton inelasticity, c is the speed of light, $n_{\rm g}$ is the gas density, $t_{\rm esc}$ is the escape time of CRs, $t_{\rm dyn} \simeq R_{\rm g}/v_{\rm s}$ is the dynamic time of the merger and $\sigma(\varepsilon_p)$ is the *pp* cross section given by Refs. [174]. As galaxies merge, strong shocks occur with a complicated morphology over a galaxy scale, while merging cores of the two galaxies lead to a dense core region. Particles are accelerated by the shocks, and then will be distributed in a galaxy scale. The CRs diffusing in the core region will make neutrinos and gamma rays efficiently. In this work, as a simplified approximation without covering the details of the shock structure, we assume that shocks are CR accelerators, which inject high energy CRs to the core region of the merging systems and initiate subsequent interactions. Fig. 3.1 shows the schematic. After leaving the accelerator, the particles can propagate diffusively or get advected away through galactic winds, therefore the net escape rate is the sum of diffusion rate and advection rate, e.g. $t_{\rm esc}^{-1} \approx t_{\rm diff}^{-1} + t_{\rm ad}^{-1}$. Although the maximum CR energy $\varepsilon_{p,\rm max}$

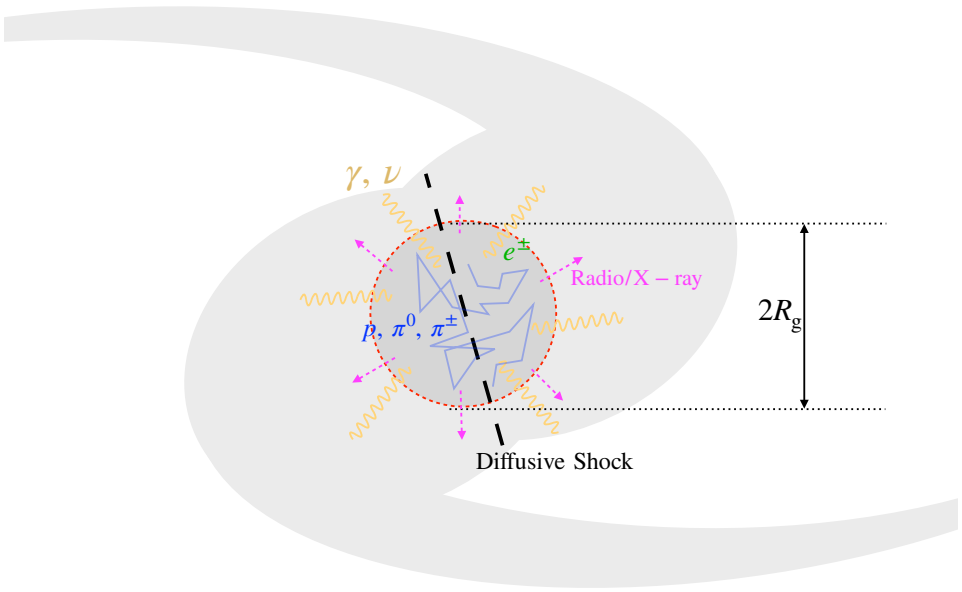

Figure 3.1. Schematic figure showing the merger of two galaxies. The shock was simplified as a straight line across the dense core region. It is also in the core region where interactions occur and neutrinos as well as electromagnetic radiation are produced.

and effective pp optical depth $f_{pp,\mathrm{g}}$ depend on the geometry of the colliding galaxies, for simplicity and consistency, we assume that the neutrinos are produced inside the core region of the interacting system and calculate the electromagnetic radiation therein. This hypothesis is in good agreement with the radio maps of NGC 660 and NGC 3256. Hence, to fully depict the physical condition of the core region, we introduce several quantities, the radius R_{g}, the average magnetic field B as well as the previously defined gas mass M_{g} and shock velocity v_s. Using these parameters, we can write down the maximum CR energy, gas density and diffusion time explicitly as $\varepsilon_{p,\mathrm{max}} = \frac{3}{20} e B_s R_{\mathrm{g}} \frac{v_s}{c}$ [173], $n_{\mathrm{g}} = M_{\mathrm{g}}/(\frac{4}{3}\pi m_p R_{\mathrm{g}}^3)$ and $t_{\mathrm{diff}} = R_{\mathrm{g}}^2/(6D_{\mathrm{g}})$, respectively. Here, m_p is the proton mass, D_{g} is the diffusion coefficient and B_s is the post-shock magnetic field which can be parameterized as a fraction of the ram pressure $B_s^2/8\pi = \frac{1}{2}\epsilon_B n_{\mathrm{g}} m_p v_s^2$ [68]. As for the diffusion coefficient D_{g}, we use a combined large and small angle diffusion equation as in

Refs. [144, 229] and [206] and then it can be written explicitly as

$$t_{\rm diff} \simeq 4.28\ {\rm Myr} \left(\frac{R_{\rm g}}{3\ {\rm kpc}}\right)^2 \left(\frac{D_0}{10^{29}\ {\rm cm^2\ s^{-1}}}\right)^{-1} \times \left[(\varepsilon/\varepsilon_{c,{\rm g}})^{1/2} + (\varepsilon/\varepsilon_{c,{\rm g}})^2\right]^{-1} \tag{3.2}$$

where D_0 is defined by $D_0 \simeq cl_c/20$, $l_c \simeq 0.1R_{\rm g}$ is the coherence length of the magnetic field fluctuations and $\varepsilon_{c,{\rm g}} \approx eBl_c$ is the characteristic energy. As for the advection, the typical values of wind velocity in star-forming galaxies and star burst galaxies range from 500 km s^{-1} [230, 231] to 1500 km s^{-1} [232]. Here, we use a moderate value $v_{\rm w} \approx 1000$ km s^{-1} for interacting galaxies since these galaxies may enter star-forming/starburst phase. In this case we have the advection time $t_{\rm ad} \simeq R_{\rm g}/v_{\rm w} \approx 2.94 \times 10^6$ yr $\left(\frac{v_{\rm w}}{1000\ {\rm km\ s^{-1}}}\right)^{-1} \left(\frac{R_{\rm g}}{3\ {\rm kpc}}\right)$.

Inside the galaxy, the electron-positron injection spectrum can be modified due to additional injections via two-photon annihilation, $\gamma\gamma \to e^-e^+$, since the core region can be opaque to high-energy gamma-ray photons above a certain threshold energy $\varepsilon_{\gamma\gamma}^{\rm cut}$. In the pion decay scenario, the gamma-ray spectrum and the neutrino spectrum are correlated by $\varepsilon_\gamma^2 \frac{dN_\gamma}{d\varepsilon_\gamma} = \frac{2}{3}\varepsilon_\nu^2 \frac{dN_\nu}{d\varepsilon_\nu}|_{\varepsilon_\gamma = 2\varepsilon_\nu}$. From energy conservation, we may approximately relate the electron-positron injection rate to the gamma-ray production rate, and the former spectrum can be written as

$$\varepsilon^2 \mathcal{N}_e^{\gamma\gamma}(\varepsilon_e) = 2\varepsilon^2 \frac{dN_\gamma}{d\varepsilon_\gamma}|_{\varepsilon_\gamma = 2\varepsilon_e} = \frac{1}{3}\varepsilon^2 \frac{dN_\nu}{d\varepsilon_\nu}|_{\varepsilon_\nu = \varepsilon_e},\ \varepsilon_e > \varepsilon_{\gamma\gamma}^{\rm cut}/2. \tag{3.3}$$

The total electron-positron injection spectrum is therefore the summation of Equations 3.1 and 3.3, or equivalently we can introduce a modification factor $\chi(\varepsilon) = 1 + \exp(-\varepsilon_{\gamma\gamma}^{\rm cut}/2\varepsilon)$ to Equation 3.1.

With these preparatory work, we can now derive the secondary electron-positron distributions and calculate the synchrotron and inverse Compton emissions. Considering the dynamic time $t_{\rm dyn} = R_{\rm g}/v_s$, we have the rate of lepton production

$$Q(\varepsilon, t) = \frac{\mathcal{N}_e(\varepsilon)\chi(\varepsilon)}{t_{\rm dyn}} \times \min\{1, e^{-\frac{t - t_{\rm dyn}}{t_{\rm esc}}}\}, \tag{3.4}$$

where the exponential factor describes the escape of CRs after the dynamical time scale and is obtained through the equation $\partial N/\partial t = -N/t_{\rm esc}$. To get the electron distribution inside the galaxy, we solve the transport equation of a simplified leaky-box model

$$\frac{\partial N_e}{\partial t} = Q(\varepsilon, t) - \frac{N_e}{t_{\rm esc}} + \frac{\partial}{\partial \varepsilon}[b(\varepsilon) N_e(\varepsilon, t)] \tag{3.5}$$

where $b(\varepsilon)$ is the electron energy loss rate due to synchrotron radiation, SSC/EIC and advection ($b_{\rm ad} \simeq \varepsilon/t_{\rm ad}$). In our calculations, we assume Q and the diffusion coefficient $D_{\rm g}$ do not depend on the positions in the merging system.

In the synchrotron limit $\gamma_e \gg 1$, the synchrotron radiation power in the frequency range ω to $\omega + d\omega$ by one electron with Lorentz factor γ_e can be written in the well-known formula

$$P_{\rm syn}(\omega, \gamma_e)d\omega = \frac{\sqrt{3}e^3 B \sin\theta_p}{2\pi m_e c^2} F(X) d\omega \tag{3.6}$$

where θ_p is the angle between the electron velocity and the magnetic field, which is assumed to be $\pi/2$ in our case,

$$X = \frac{\omega}{\omega_c},\ \omega_c = \frac{3}{2}\gamma_e^2 \frac{eB}{m_e c}.$$

The function $F(X)$ is given by

$$F(X) = X \int_X^\infty K_{5/3}(\xi) d\xi.$$

Then, it is straightforward to write down the integrated radiation power

$$b_{\rm syn}(\varepsilon) = \int P_{\rm syn}(\omega, \varepsilon/m_e c^2) d\omega.$$

It is useful to define the synchrotron cooling time

$$t_{\rm syn}(\varepsilon) = \frac{\varepsilon}{b_{\rm syn}(\varepsilon)}. \tag{3.7}$$

While SSC and EIC also play a role in electron-positron cooling, we will show later that these processes are subdominant comparing to synchrotron cooling. Now with the preparations on synchrotron radiation, we are able to solve the kinetic equation. One special solution to the differential equation is the steady state solution ($\partial N_e/\partial t = 0$),

$$N_e^{\rm steady} = Q(\varepsilon, t) \left(\frac{1}{t_{\rm esc}} + \frac{1}{t_{\rm syn}} \right)^{-1} \tag{3.8}$$

To verify this expression, it is worthwhile to solve the time evolution of electron-positron spectra numerically. For illustration purposes, we assume $M_{\rm g} = 10^9\ M_\odot$, $v_s = 100$ km s^{-1}, $R_{\rm g} = 5$ kpc and $\varepsilon_{\gamma\gamma}^{\rm cut} = 1$ TeV. Fig. 3.2 shows the synchrotron cooling rate ($t_{\rm syn}^{-1}$; solid lines) as functions of lepton energy for different galactic magnetic fields as well as the

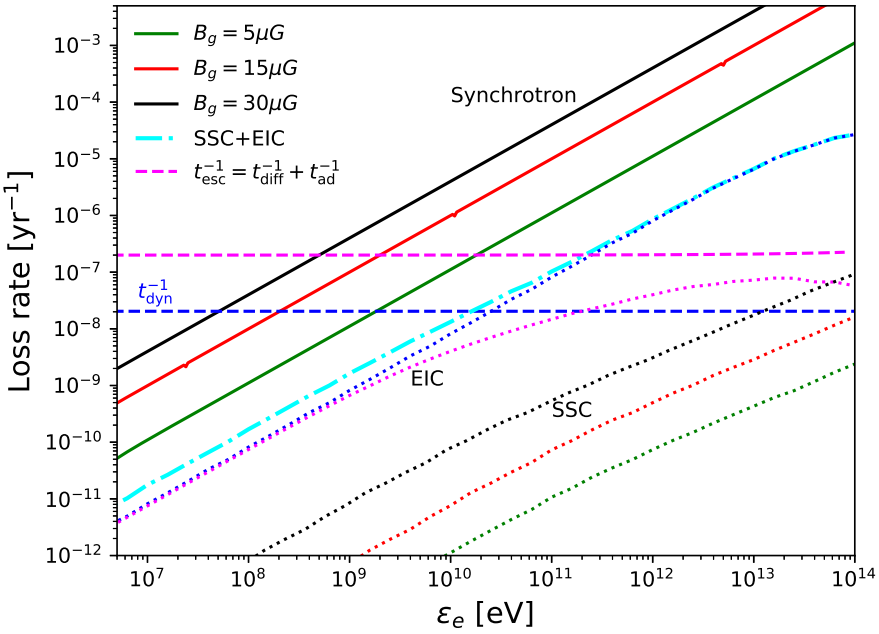

Figure 3.2. Electron loss rates versus electron energy ε_e. Solid lines correspond to cooling rates due to synchrotron radiation in different magnetic fields, e.g. 5μG (green), 15μG (red) and 30μG (black). The cyan dash-dotted line is the cooling rate of inverse Compton scattering (SSC+EIC). Blue and magenta dotted lines illustrate the contributions of CMB and EBL to the EIC cooling rate, while the black, red and green dotted lines are SSC cooling rates at the magnetic fields 5μG (green), 15μG (red) and 30μG (cyan), respectively. Magenta and blue dashed lines are the escape rate and the reciprocal of dynamic time, respectively.

escape rate ($t_{\rm esc}^{-1}$) and the reciprocal of dynamic time ($t_{\rm dyn}^{-1}$; dashed lines). As the magnetic field becomes stronger, the synchrotron cooling tends to be faster since $P(\omega, \gamma_e)$ increases. Using the finite difference method, the time evolution of pair spectra for the magnetic field $B = 5$ μG is shown in the Fig. 3.3, where we use the parameter $\eta = t/t_{\rm dyn}$ to label the stages of pair injection. The thick red solid line corresponds to the steady electron distribution given by the Equation 3.8. The theoretical steady distribution almost coincide with the numerical steady solutions. To show this, we multiply the theoretical solution $N_e^{\rm steady}$ by a factor of ten to separate these curves. Fig. 3.3 also illustrates the evolution of the cumulative number of electron inside the core region. From this figure, we conclude that the electron injection enters the steady phase when $\eta \gtrsim 0.2$.

Inverse Compton scattering between high-energy electron-positron pairs and external CMB/SL/EBL photons (denoted by EIC) as well as SSC may become more pronouncing

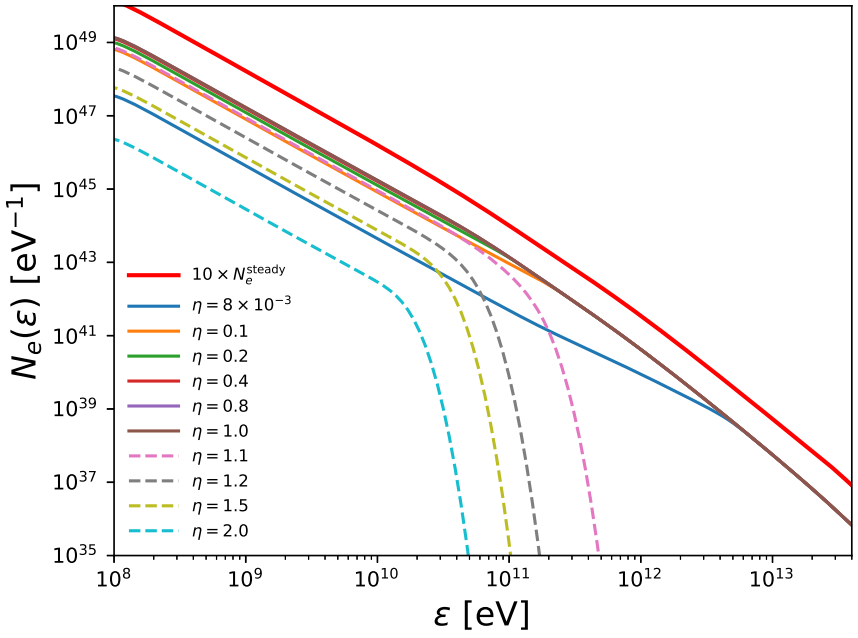

Figure 3.3. Secondary electron-positron spectra at different times assuming the magnetic field $B = 5$ μG. The parameter $\eta = t/t_{\rm dyn}$ represents the time of electron-positron injection. Thin lines are numerical solutions to the CR transport equation while the thick red line is the analytical steady-state solution $N_e^{\rm steady}$. To separate $N_e^{\rm steady}$ from numerical solutions, we multiply $N_e^{\rm steady}$ by a factor of 10.

in lepton cooling process when the electron-positron spectrum becomes harder. Here we formulate the SSC/EIC power per unit comoving volume as [233],

$$E\frac{dN_x}{dEdt} = \int d\gamma_e \frac{dN_e}{d\gamma_e} \int d\varepsilon_\gamma \left(\frac{dn_\gamma}{d\varepsilon_\gamma}\right)_x E\left\langle c' \frac{d\sigma_{IC}}{dE}\right\rangle \tag{3.9}$$

where $x =$ SSC or EIC, and the differential cross section is [234]:

$$\begin{aligned}\left\langle \frac{d\sigma_{IC}}{dE} c'\right\rangle =& \frac{3}{4}\sigma_T c \frac{1}{\gamma_e^2 \varepsilon_\gamma} \times \\ & \left[1 + v - 2v^2 + \frac{v^2 w^2 (1-v)}{2(1+vw)} + 2v \ln v\right].\end{aligned} \tag{3.10}$$

In the expression of the cross section, σ_T is the Thomson cross section, $v = \frac{E}{4\varepsilon\gamma_e^2(1-\xi)}$, $\xi = E/(\gamma_e m_e c^2)$ and $w = \frac{4\varepsilon_\gamma \gamma_e}{m_e c^2}$. For SSC, $dn_\gamma/d\varepsilon_\gamma$ corresponds to the photon spectrum

of synchrotron emission and it can be written as

$$\varepsilon_\gamma \left(\frac{dn_\gamma}{d\varepsilon_\gamma}\right)_{\rm SSC} = \frac{1}{2R_{\rm g}^2 ch} \int P_{\rm syn}\left(\varepsilon_\gamma/\hbar, \frac{\varepsilon_e}{m_e c^2}\right) N_e(\varepsilon_e) d\varepsilon_e \tag{3.11}$$

The intergalactic starlight photon density can be estimated by using the IR/optical spectral energy density (SED; see the inset of the left panel of Fig. 3.5), e.g. $\varepsilon_\gamma (dn/d\varepsilon_\gamma)_{\rm SL} \sim 2d_L^2 F_{\nu,{\rm SL}}/(R_g^2 ch)$, where d_L is the luminosity distance of the galaxy. In this paper, we use two modified Planck functions to approximate the left and right bulks of the IR/optical data,

$$F_{\nu,{\rm SL}}(\nu) = \sum_{i=L,R} A_i \left(\frac{h\nu}{1{\rm eV}}\right)^{\zeta_i} \frac{1}{\exp(\frac{h\nu}{\varepsilon_i}) - 1}. \tag{3.12}$$

As for EIC, $(dn_\gamma/d\varepsilon_\gamma)_{\rm EIC}$ is given by the summation of CMB black body spectrum, $(dn/d\varepsilon_\gamma)_{\rm SL}$ and the EBL photon density spectrum provided by "model C" from [184].

Like the synchrotron radiation, we can define the cooling time for SSC and EIC,

$$t_x(\varepsilon_e) = \varepsilon_e \left[\int dE \int d\varepsilon_\gamma \left(\frac{dn_\gamma}{d\varepsilon_\gamma}\right)_x E \left\langle c' \frac{d\sigma_{IC}}{dE} \right\rangle\right]^{-1}_{\gamma_e = \frac{\varepsilon_e}{m_e c^2}}, \tag{3.13}$$

The cyan dash-dotted line in Fig. 3.2 shows the combined cooling rate $t_{\rm IC}^{-1} = t_{\rm SSC}^{-1} + t_{\rm EIC}^{-1}$ as a function of electron energy. Fig. 3.2 illustrates also the components of the total IC cooling rate, e.g. CMB (blue dotted line), EBL (magenta dotted line) and SSC at the magnetic fields 30 μG (black dotted line), 15 μG (red dotted line) and 5 μG (green dotted line). The flattening of the EIC loss rate is due to the Klein-Nishina regimes as the electron Lorentz factor increases. From this figure, we find that the cooling process is dominated by synchrotron radiation and the cooling due to EIC is predominant comparing to SSC. Hence, in the following section where the application to NGC 660 is discussed, we only consider $t_{\rm syn}$ in the CR transport equation (Equation 3.5). In general, for a power-law electron distribution, the SSC cooling rate should have the same slope. However, in Fig. 3.2, the physical cause of the slight slowing down of the growth of the SSC cooling rate is that the steady-state electron spectrum becomes steeper due to synchrotron cooling (see the red line in Fig. 3.3) and this can influence the synchrotron photon density spectrum through Equation 3.11. With the equations above, we can write

down the equations for synchrotron and SSC/EIC fluxes

$$
\begin{aligned}
F_\nu^{\rm syn} &= \frac{1}{4\pi d_L^2}\int 2\pi\cdot P_{\rm syn}\left(2\pi\nu,\frac{\varepsilon_e}{m_e c^2}\right)N(\varepsilon_e)d\varepsilon_e \\
F_\nu^{x} &= \frac{h}{4\pi d_L^2}\left[E\frac{dN_x}{dEdt}\right]_{E=h\nu},\ x=\text{SSC or EIC},
\end{aligned}
\tag{3.14}
$$

where the coefficient 2π and Planck constant h come from $|d\omega/d\nu|$ and $|dE/d\nu|$, respectively. In general, we need to keep in mind that inverse Compton (or more especially SSC) emission can be significant at some frequency even when the magnetic field is strong and the core region is more compact such that the synchrotron photon field is more intense. We will show later that SSC and EIC can also be important for NGC 3256.

3.3 Radio and X-Ray Constraints on $M_{\rm g}$ and v_s

With the above, we are able to calculate the synchrotron and SSC/EIC fluxes. The spectrum of synchrotron radiation extends broadly from radio band to X-ray regime while SSC/EIC may become important from optical band to X-ray band. In this section we investigate the possibility of explaining the radio and X-ray observations simultaneously using the formalism presented in Sec. 3.2. Since in our model the physical state of the core region of merging galaxies is determined by five parameters: the radius $R_{\rm g}$, the magnetic field B, the gas mass $M_{\rm g}$, the shock velocity v_s and the time parameter $\eta = t/t_{\rm dyn}$, our model provides one useful method to study the dynamics of galaxy mergers. In this section, we present an application to the interacting system NGC 660 and show that our model can be used to reproduce the radio and X-ray observation. In addition, we find that $M_{\rm g}$ and v_s in the core region of NGC 660 can be constrained under appropriate assumptions. To show that our model can be used widely to general galaxy merging systems, we consider also the galaxy NGC 3256. From Fig. 3.3, we find that the interacting system can be approximately treated as a steady state. Hence, to simplify the constraint, we employ a steady state solution to approximate the secondary electron-positron distribution throughout the paper.

3.3.1 NGC 660

NGC 660 is usually believed as a galaxy formed by the collision and merger of two galaxies. The distance to us is $d_L \sim 12.3$Mpc and the HI extent is 47 kpc. Radio maps by VLA reveal a smooth core region [235]. Ref. [236] showed that the de-convoluted

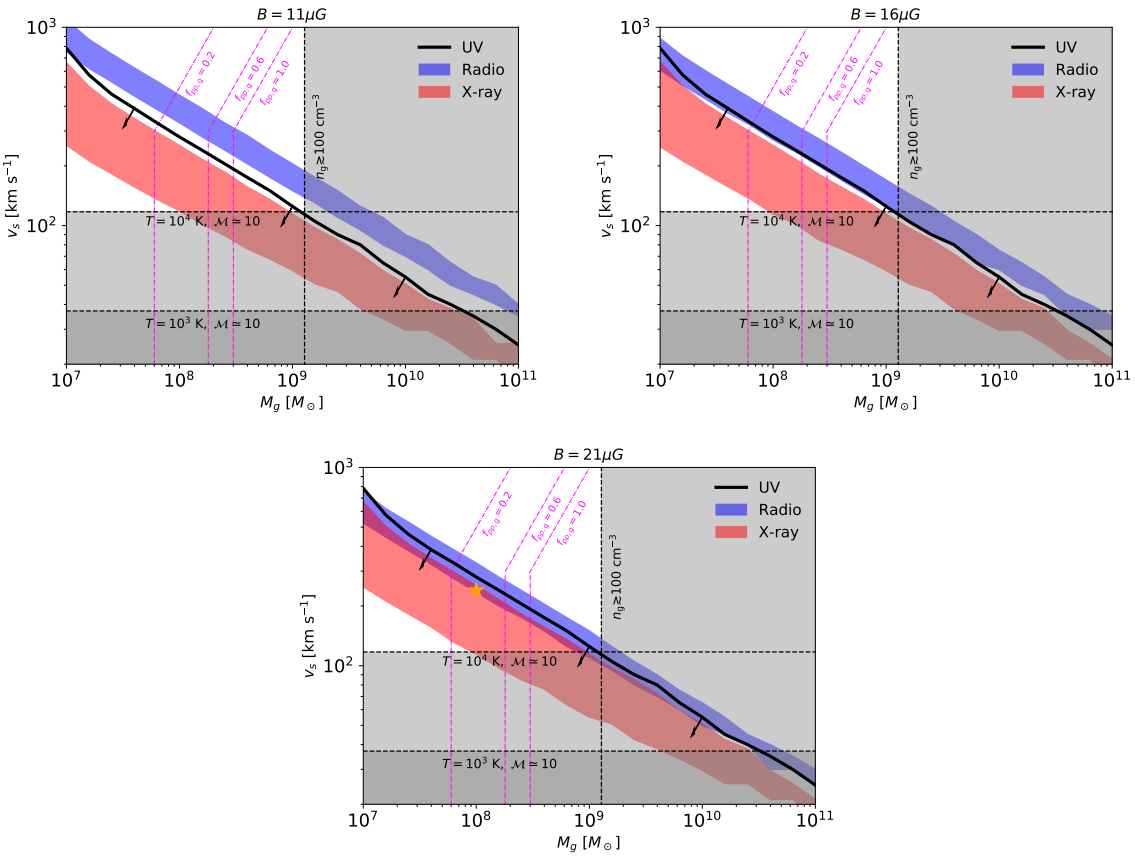

Figure 3.4. Constraints on $M_{\rm g}-v_s$ plane from radio, UV and X-ray tolerance areas. From upper left, upper right to the bottom panels, magnetic fields are assumed to be $B = 11$ μG, 16 μG and 21 μG, respectively. In each figure, blue and red areas correspond to the radio and X-ray constraints and the black line shows the upper boundary under the UV constraint. The vertical dashed line and gray area show the constraints from the core region gas density $n_{\rm g} \lesssim 100$ cm^{-3}, whereas the horizontal dashed lines and gray area correspond to the strong shock requirements ($\mathcal{M} \simeq 10$) for the temperature 10^4 K and 10^3 K. The magenta dash-dotted contours correspond to different pp optical depth $f_{pp,{\rm g}}$. The orange star in the overlapping region labels the test case: $B = 21$ μG, $v_s = 240$ km s^{-1}, $M_g = 10^8$ M$_\odot$.

angular size of the radio and X-ray emitting region is less than 10 arcsec or equivalently the radius $R_{\rm g} \lesssim 0.5$ kpc. Hence, in our calculations, we use $R_{\rm g} \simeq 0.5$ kpc as the fiducial radius of the core region. In addition, Ref. [228] studied the magnetic fields using VLA data in 16 interacting galaxies and they find that the average magnetic field of NGC 660 is 16 ± 5 μG. In the X-ray regime, the data from Chandra telescope gives the X-ray flux $1.24^{+0.37}_{-0.54} \times 10^{-13}$ erg cm^{-3} s^{-1} [237] in the range $0.5 - 10$ keV. In mid-2013, a radio outburst was observed using e-MERLIN and after the outburst the X-ray flux also increased to $1.85^{+0.19}_{-0.16} \times 10^{-13}$ erg cm^{-3} s^{-1}. The origin of the outburst was investigated

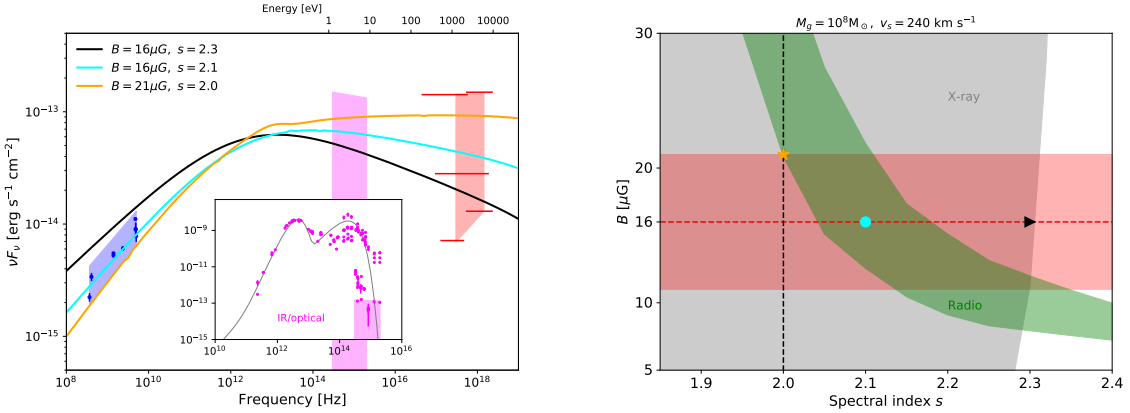

Figure 3.5. Left panel shows the spectral energy distribution for NGC 660, extending from the radio band to the X-ray regime. Blue points are radio fluxes at various frequencies and the red points are X-ray data in the energy range $0.2 - 10$ keV. Observations from microwave to UV are illustrated as magenta points in the inset. The gray line is the Planck-function approximation to the IR/optical data. The bulk of the microwave, IR and optical spectrum is due to starlight and dust re-radiation. The fitting areas of radio, UV and X-ray data are shown as the blue, magenta and red areas, respectively. The black, cyan and orange lines are spectra that correspond to the black wedge, cyan circle and orange star in the right panel. In the right panel, the gray and green areas are X-ray and radio constraints on $s - B$ plane. The red area shows the constraints on the magnetic from previous polarization studies, 16 ± 5 μG.

in mid-2013 and it might be produced by AGN activities in the galaxy center. In our work, we focus on the emissions from the smooth core region, therefore we use the data recorded before the outburst. Above all, with the magnetic field estimated by Ref. [228], the parameters left to be determined are $M_{\rm g}$ and v_s.

The left panel of Fig. 3.5 shows the spectral energy distribution for NGC 660 from radio band to X-ray band. Blue points are radio fluxes at 365 MHz [215], 408 MHz [216], 1.4 GHz [217, 218] 2.38 GHz [219], 4.78 GHz [220], 4.85 GHz [221, 222] and 5 GHz [223]. The red points are X-ray data before the radio burst in the energy range $0.2 - 10$ keV, which are provided by Chandra [224, 225], XMM-Newton [226] and ROSAT [227]. Since this source was observed with short exposure times, the photon count rates were converted to the X-ray fluxes by assuming a spectral index in the energy range for each red bar in this figure. More details on the data reductions can be found in the corresponding references. In our model, the synchrotron spectrum can reproduce the slope of radio spectra, which is the primary motivation of our work. However as for the X-ray data, the slope is quite uncertain and depends on different observations and models. Therefore in the X-ray band we attempt to explain integrated fluxes from different observations in the energy range $0.2 - 10$ keV. The broadband observations

from microwaves to UV are shows as magenta points in the inset.[1]. The gray line shows the approximation to the IR/optical data using Equation 3.12, with the parameters $A_L = 5.15 \times 10^{10}$ Jy, $\zeta_L = 3.9$, $\varepsilon_L = 0.004$ eV; $A_R = 3.44$ Jy, $\zeta_R = 1.8$, $\varepsilon_L = 0.3$ eV. To measure the consistency between synchrotron spectrum and the observations, we set three fitting areas, as shown in the left panel of Fig. 3.5. The blue and red areas correspond to the error tolerances of radio and X-ray data respectively. As for the microwave, infrared and UV data points, we need to keep in mind that the dust in the galaxy and star forming activities may dominate the emissions in these bands. Hence we assume the secondary radiation in the shock region merely contributes to the background and use the UV data as the upper limit in our model (see the magenta area). One vexing problem of the UV limit is that the dust absorption in the host galaxy cannot be neglected and the photometry correction is model dependent. Hence, in our calculation, we use the UV limit just as a reference.

NGC 660 has been identified as a star-forming/starburst galaxy [214], which provides one complementary constraint on the gas mass once the radius $R_{\rm g}$ is specified. The gas density in starburst galaxies can be up to $n_{\rm g} \simeq 100$ cm^{-2} and thus we conclude that the gas mass in the core region satisfies $M_{\rm g} \lesssim \frac{4\pi}{3}\mu m_p n_{\rm g} R_{\rm g}^3$, where $\mu \simeq 1.24$ is the mean molecular weight. The vertical dashed lines and the gray areas in Fig. 3.4 illustrate the gas density constraint. Another caveat is that a strong shock with the Mach number $\mathcal{M} \gtrsim 10$ is required to produce a power-law electron spectrum with index $s \simeq 2(\mathcal{M}^2+1)/(\mathcal{M}^2-1) \simeq 2$. Observations reveal that NGC 660 has the dust temperature and kinetic temperature around 40 K and 200 K [214, 238], respectively. Here, we use $T \simeq 10^4$ K as an optimized value since the core region may contain warm gas and evaluate the lower limit of the shock velocity $v_s \gtrsim \mathcal{M}\sqrt{\frac{\gamma k_B T}{\mu m_p}}$ which is shown as the upper horizontal dashed lines and gray areas in Fig. 3.4. For illustration purpose, we show also the constraint obtained by assuming a relatively lower temperature $T = 10^3$ K (the lower dashed lines). Meanwhile, we include the contours of pp optical depth $f_{pp,{\rm g}}$ in the $v_s - M_\odot$ plane (magenta dash-dotted lines in Fig. 3.4). As we can see, pp interactions are more efficient in a region with large gas mass and low shock velocity v_s due to the higher gas density $n_{\rm g}$ and longer collision time. When v_s decreases to one critical value, which is determined by $t_{\rm dyn} = t_{\rm esc}$, the particle escape dominates the interaction time. Therefore, the oblique lines become vertical.

Considering the uncertainty of magnetic field, we select $B = 11$ μG, 16 μG and 21 μG as three fiducial values. Fig. 3.4 shows the constraints on $M_{\rm g} - v_s$ plane from the

[1]A full list of references can be found in the page NED:INDEX NGC 660

radio, UV and the X-ray error tolerances (see the blue, magenta and red areas in Fig. 3.5). From these figures, we find that the permissible areas in the $M_{\rm g} - v_s$ plane overlap only at higher magnetic fields, which means that to fit the radio, UV and X-ray data simultaneously, a stronger magnetic field is favored. This conclusion is also consistent with the orange line in the left panel of Fig. 3.5, which shows the flux predicted by our model for the test point, the orange star ($B = 21\ \mu$G, $M_g = 10^8\ {\rm M}_\odot$, $v_s = 240$ km s^{-1}), in the overlapping region of Fig. 3.4. Meanwhile, we find that the contributions from SSC and EIC are subdominant comparing with synchrotron emissions in the case of NGC 660. For a lower magnetic field, the tension between radio data and X-ray data is inevitable. To fit the radio data, the synchrotron spectrum will overshoot X-ray flux and UV upper limit. On the other hand, to alleviate the tension, we need to make the synchrotron spectrum higher in the radio regime while keeping the X-ray flux unchanged. This can be achieved by increasing the magnetic field, since the synchrotron spectra converge at high energy band (e.g. X-ray) even if we increase the magnetic field. We provide one brief proof here. From Fig. 3.2, we see that synchrotron cooling dominate the electron spectrum ($t_{\rm syn}^{-1} \gg t_{\rm esc}^{-1}$) when the electron energy is high, which means $N_e^{\rm steady} \simeq Q(\varepsilon_e, t) t_{\rm syn} = \frac{\varepsilon_e Q(\varepsilon_e, t)}{b_{\rm syn}(\varepsilon_e)}$. Combining $N_e^{\rm steady}$ with Equations 3.6 and 3.14, we obtain

$$\begin{aligned} F_\nu^{\rm syn} &\propto \int \varepsilon_e Q(\varepsilon_e, t) \frac{P(\omega, \varepsilon_e)}{\int P(\omega', \varepsilon_e) d\omega'} d\varepsilon_e \\ &\propto \int \varepsilon_e Q(\varepsilon_e, t) \frac{F(X)}{\int F(X') d\omega'} d\varepsilon_e. \end{aligned} \tag{3.15}$$

At high energy limit, the function $F(X)$ has the asymptotic form $F(X) \simeq \sqrt{2\pi X} e^{-X}$ and the flux no longer depends on the magnetic field. A more physical interpretation is that once B is high enough, the energy of electrons is radiated away through synchrotron fast cooling. In this case, the flux only depends on the electron injection rate. Meanwhile, it's easy to see that the flux will increase as B increases in a lower energy band (e.g. radio regime) since electrons lose more energy in a stronger magnetic field. Above all, for a flat CR spectrum with the spectral index $s \sim 2$, a higher magnetic field will keep the X-ray flux unchanged with increasing the radio flux and therefore can be used to fit the radio and X-ray data simultaneously.

This simple single-zone model meets difficulty explaining the radio and X-ray observations at the same time with a relatively lower B. This motivates us to exploit the chance of improving the fitting by varying the CR spectral index s in the range

1.8-2.4. As s deviates from 2.0, the normalization coefficient in Equation 3.1 changes to $(\varepsilon_{\rm max}^{2-s} - \varepsilon_{\rm min}^{2-s})/(2-s)$ and a correction factor ε^{2-s} should be applied to the electron spectrum. To demonstrate the impact of s and B on the fitting, we select and fix the gas mass and shock velocity to be 10^8 $M_\odot$ and 240 km s^{-1}, the orange star in the overlapping region in Fig. 3.4. The right panel of Fig. 3.5 shows the constraints in the $s-B$ plane from polarization studies (red area), radio (green area) and X-ray (gray area) observations. Firstly, we find that magnetic field almost does not influence the X-ray results, which is consistent with the previous analysis. There exist a cut off around $s = 2.35$, beyond which the X-ray flux could be too low to explain the observations. Secondly, as the index s increases, the electron spectrum becomes steeper, or on other words, more low-energy electrons are injected. Consequently, radio flux got flattened while X-ray flux steepened. Therefore, a low magnetic field is required to counteract radio flux increase and as a result we expect the green area for radio constraint. One straightforward conclusion we can make from this figure is that, a relative larger spectral index can be used to reproduce the radio and X-ray data simultaneously, e.g. the parallelogram region formed by the green and red areas. To show that explicitly, we select three representative points in the $s-B$ plane, e.g. orange star ($s = 2.0,\ B = 21\ \mu$G), cyan circle ($s = 2.1,\ B = 16\ \mu$G) and black wedge ($s = 2.3,\ B = 16\ \mu$G). The corresponding X-ray and radio fluxes are shown in the left panel of Fig. 3.5. Obviously, from this figure, a moderately larger s in the range $\sim 2.1 - 2.2$ with the optimized magnetic field $B = 16\ \mu$G can provide a good fitting. These indices are also consistent with the observations of starburst galaxies such as M82 and NGC 253.

From the discussions above, we showed that our one-zone model can be used to explain the radio, UV and X-ray observations of the NGC 660 core region. Given our model is correct, one can constrain the gas mass $M_{\rm g}$, magnetic field B, CR spectral index s and collision velocity v_s in that region.

3.3.2 NGC 3256

NGC 3256 is also a galaxy formed by the collision of two galaxies and the redshift of NGC 3256 is $z \approx 0.009364$ [239]. In a ΛCDM universe with $\Omega_{\rm m} = 0.286$ and $H_0 = 69.6$ km s^{-1} Mpc^{-1}, the luminosity distance to us is $d_L = 40.6$ Mpc. It provides a nearby template for studying the properties of merging galaxies. Nearly infrared observations [240] reveal that the major axis and minor axis sizes are a =1.277 arcmin and b =1.251 arcmin respectively. In our calculation, we assume an equivalent angular size $\theta_{\rm g} = \sqrt{ab} = 1.264$ arcmin and the corresponding radius $R = 14.92$ kpc. However,

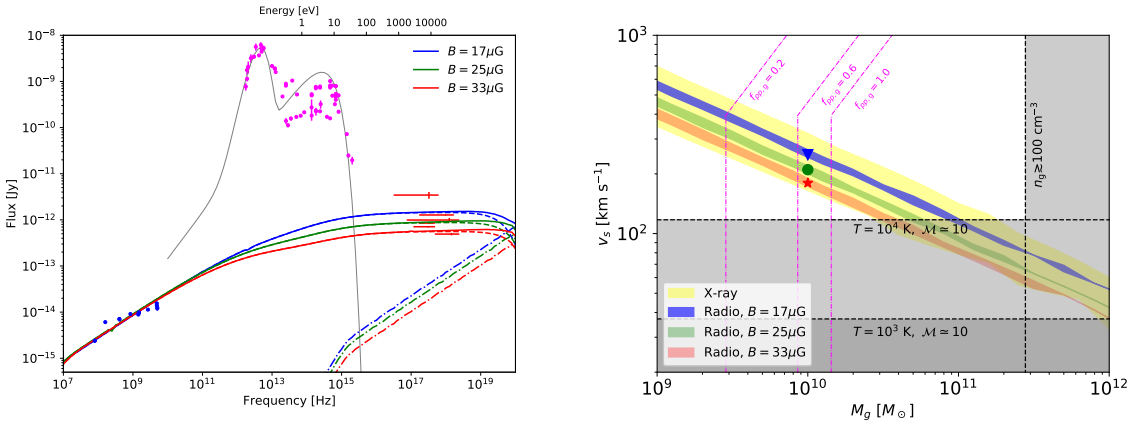

Figure 3.6. Left panel: The spectral energy distribution for NGC 3256. Blue and red points are radio and X-ray fluxes, respectively. The observations from the infrared band to the UV band, which are mainly attributed to dust and starlight, are shown as magenta points. The blue, green and red lines are best-fitting spectra obtained from three selected points in the right panel for different magnetic fields. The dashed and dash-dotted lines correspond to the synchrotron and IC components. The right panel shows the X-ray (yellow area) and radio constraints for the magnetic fields 17 μG (blue area), 25 μG (green area) and 33 μG (red area). The gray areas, black dashed lines and magenta dash-dotted lines have the same meaning with Fig. 3.4.

instead of using the galaxy radius, we focus on the core/nucleus region where collisions occur. Ref. [241] investigated the morphology of many merging galaxies including NGC 3256 using Hubble Space Telescope WFPC2 camera and the radius of the core region of NGC 3256 is approximately 3 kpc. In the following calculations, we adopt $R_g = 3$ kpc. Like NGC 660, Ref. [228] also provided the average magnetic field for NGC 3256, which is 25 ± 8 μG. Therefore, in this section we us 17 μG, 25 μG and 33 μG as three fiducial values of the magnetic field. In the $0.3 - 10$ keV band, NGC 3256 has been observed by ASCA Medium Sensitivity Survey [242], XMM-Newton [243, 244] and ROSAT [245]. As for the radio band, we use the data from broad-band observations in the frequency range 80 MHz to 5.0 GHz [216, 246–249]. Blue and red points in left panel of Fig. 3.6 show the radio and X-ray fluxes respectively. In this figure, we also plot the fluxes from infrared to UV bands as magenta points [2]. The gray line in this figure is our approximation to the IR/optical data with the parameters $A_L = 6.87 \times 10^{10}$ Jy, $\zeta_L = 3.9$, $\varepsilon_L = 0.004$ eV; $A_R = 2.06$ Jy, $\zeta_R = 1.0$, $\varepsilon_L = 0.7$ eV.

Using the same procedure for NGC 660, we attempt to reproduce the observations of NGC 3256. We find that we can fit the radio and X-ray data simultaneously in the

[2] A full list of references can be found in the page NED:INDEX for NGC 3256

whole magnetic field range 17 μG $-$ 33 μG by using a simple CR spectral index $s = 2$. The right panel illustrates the constraints from X-ray and radio observations. The X-ray constraint (yellow area) remains unchanged as consequence that the flux in X-ray band is not sensitive to the magnetic field. Radio constraints at 17 μG, 25 μG and 33 μG are shown as blue, green and red areas. Like Fig. 3.4, the gray areas and black dashed lines correspond to the gas density and strong shock constraints. Using the magnetic field given by polarization studies, our model can explain a significant fraction of X-ray flux. Left panel shows the spectra of three test points in the right panel, e.g. blue wedge (17 μG, 10^{10} M$_\odot$, 250 km s^{-1}), green circle (25 μG, 10^{10} M$_\odot$, 210 km s^{-1}) and red star (33 μG, 10^{10} M$_\odot$, 180 km s^{-1}). As anticipated, to fit the radio data, a stronger magnetic field implies a lower X-ray flux (see the red line). As for NGC 3256, since the radius of the nucleus is smaller and the starlight photon density is proportional to $(d_L/R_g)^2$, the starlight contribution to EIC is more significant than NGC 660. Meanwhile, considering that strong magnetic field can also boost SSC, in this case inverse Compton scattering is no longer negligible. The dashed lines and dash-dotted lines in the left panel of Fig. 3.6 show the synchrotron and IC contributions for various magnetic fields.

Above all, our simple one-zone model with $s \sim 2$ can be used to explain the radio and a large fraction of X-ray observation and the constraint is in good agreement with previous magnetic studies.

3.4 Summary and Discussion

In this paper, we have investigated the synchrotron and SSC/EIC emissions from secondary electron-positron pairs in merging galaxies and found that these emissions can be used to reproduce the radio and X-ray observations of such systems, as calculated in detail for two of the best-studied galaxies formed by galaxy mergers, NGC 660 and NGC 3256. Combining the magnetic field in the core regions measured through polarization analyses, we showed that our model can be used to constrain the gas mass $M_{\rm g}$ and shock velocity v_s under a steady-state approximation for the electron-positron distribution. For NGC 660, in order to alleviate the tensions between the radio and X-ray constraints, a higher magnetic field 16 μG $\lesssim B \lesssim$ 21 μG is required, which is consistent with the uncertainty of the magnetic field given by Ref. [228]. Utilizing 16 μG $\lesssim B \lesssim$ 21 μG as the fiducial range of magnetic field, we have found that the permissible ranges for the gas mass and shock velocity are constrained to the reasonable ranges 10^8 $M_\odot \sim 10^{11}$ $M_\odot$ and 500 km s^{-1} $\sim$ 40 km s^{-1}, respectively. Moreover, a steeper CR distribution with

the spectral index $2.1 \lesssim s \lesssim 2.2$ could be helpful to resolve the tensions between radio and X-ray observations. On the other hand, for NGC 3256, contributions from inverse Compton scattering could be significant since the the core region is compact in the sense of photons. With the constraint 17 μG $\lesssim B \lesssim$ 33 μG, our model with a hard spectral index $s \sim 2$ can explain the radio and X-ray data simultaneously. From these two examples, we show that our simple one-zone model can reproduce the radio and X-ray observations of galaxy merger systems. Considering the complexity and the diversity observed from system to system, each merging galaxy should be diagnosed independently. We note that since the factor $\frac{1}{2}M_{\rm g}v_s^2$ dominates the electron injections, as can be seen in Equation 3.1, $M_{\rm g}$ and v_s are degenerate in our model. Despite this, our model provides one useful approach to reproduce the radio and X-ray observations and to study the dynamics of galaxy mergers as well as the physical parameters of the shock regions.

Unavoidably, *pp* collisions in our model can produce gamma rays through π^0 decays. In the framework of hadronic process, we estimate the gamma-ray flux from π^0 decays

$$\begin{aligned} \varepsilon_\gamma F_{\varepsilon_\gamma}(\varepsilon_\gamma) &= \frac{2}{3}\varepsilon_\nu F_{\varepsilon_\nu}(\varepsilon_\nu)|_{\varepsilon_\gamma=2\varepsilon_\nu} \\ &\lesssim \left(\frac{1}{24\pi d_L^2 t_{\rm dyn}}\right)\epsilon_p \mathcal{C}^{-1} M_{\rm g} v_{\rm s}^2. \end{aligned} \tag{3.16}$$

As for NGC 660, we have $\varepsilon_\gamma F_{\varepsilon_\gamma} \lesssim 1.7 \times 10^{-13}$ erg s^{-1} cm^{-2} while the gamma-ray flux of NGC 3256 satisfies $\varepsilon_\gamma F_{\varepsilon_\gamma} \lesssim 2.9 \times 10^{-13}$ erg s^{-1} cm^{-2}. Both of these fluxes are lower than the flux sensitivities of current gamma-ray detectors, such as *Fermi* LAT[3], H.E.S.S [250], MAGIC [251], HAWC [252] and VERITAS [253]. In the future, the 50-hour sensitivity of the proposed Cherenkov Telescope Array (CTA) in the TeV range can reach $\sim 10^{-13}$ erg s^{-1} cm^{-2} [254][4] and our model for the merging galaxies can be further constrained by gamma-ray observations.

Secondary particle interactions can produce observable emissions not only in interacting galaxy systems but also in star-forming and/or starburst galaxies, where supernovae can accelerate high-energy CRs and trigger subsequent particle interactions. Previous studies incorporating π^0 decays, bremsstrahlung, inverse Compton and synchrotron emissions have shown that CR interactions can be used to explain the gamma-ray observations of the starburst galaxy M82 [255], the Cygnus X region [256] and the

[3]The Pass 8 sensitivity: `https://www.slac.stanford.edu/exp/glast/groups/canda/lat_Performance.htm`

[4]The sensitivity can be also found in `http://www.cta-observatory.org/science/cta-performance/`

ultra-luminous infrared galaxy Arp 220 [257]. Interestingly, for Arp 220 we can estimate the CR luminosity density from a galaxy merger scenario in the central molecular zone as $L_{\rm cr,merger} \simeq \frac{1}{2}\epsilon_p M_{\rm g} v_s^2 \left(\frac{R}{v_s}\right)^{-1} \approx 9.87\times10^{43}\left(\frac{v_s}{500{\rm km\ s^{-1}}}\right)^3$ erg s^{-1}, using the gas mass $M_{\rm g} = 6\times10^8$ M$_\odot$ [258] and $R = 70$ pc [259], which is roughly twice as much as the best-fitting supernova CR luminosity [260], $L_{\rm cr,SNe} \simeq E_{\rm cr,SN}\mathcal{R}_{\rm SN} \approx 4.76\times10^{43}$ erg s^{-1}, for a typical CR energy injected by supernovae of $E_{\rm cr,SN} \approx 10^{50}$ erg and a supernova rate $\mathcal{R}_{\rm SN} \approx 15$ yr^{-1}. This demonstrates that our galaxy merger scenario can fill the gap between the observed gamma-ray flux of Arp 220 and the 2015 gamma-ray prediction from the supernova model [257, 260]. Even more conservatively, taking the uncertainty in the supernova CR injection energy 5×10^{49} erg $\lesssim E_{\rm cr,SN} \lesssim 10^{51}$ erg [144] into consideration, we estimate a luminosity $0.21 \lesssim L_{\rm cr,merger}/L_{\rm cr,SN} \lesssim 4.15$, which indicates that our model can explain a significant part of the gamma-ray observation.

Various authors, e.g., Refs. [200] and [261], have investigated the contributions from secondary particles (e.g., pions and electrons/positrons) in star-forming/starburst galaxies to the MeV-GeV gamma-ray background and found that these sources can describe a significant portion of the extragalactic gamma-ray background. In this paper, our work has expanded the scope of the applicability of the secondary particle interaction model to galaxy merging systems by introducing a phenomenological approach where CR productions, electron-positron distributions and electromagnetic emissions can be predicted from the basic parameters of the merging regions. This enables us, furthermore, to constrain the gas mass, shock velocity and magnetic field given that supernova CR luminosities and star-formation rates are revealed.

Since galaxy mergers are also promising sources of high-energy neutrinos, these systems may be detected by astrophysical neutrino detectors, such as the IceCube Neutrino Observatory , e.g., Refs. [21, 262] for review. So far, IceCube has detected the diffuse astrophysical high-energy neutrino background [26,263–265], as well as one possible source, blazar TXS 0506+056 [266]. The physical origin of the bulk of these neutrinos is still under debate, but the success of multi-messenger obswervations following IceCube-170922A show that neutrino astronomy has become an important and indispensable part of multi-messenger astrophysics [267]. Our model for high-energy emissions from galaxy mergers connects the electromagnetic emissions from merging regions to the neutrino emission and CR acceleration. With the prospects for detecting or setting the limits on their high-energy neutrino emission by current and/or next-generation neutrino detectors [197, 206], our work will be able to provide a new perspective on future multi-messenger studies of the evolution of galaxies.

Acknowledgements

We are grateful to Shigeo Kimura and Zhao-Wei Zhang for useful discussions. The authors would like to thank the referee for constructive comments and suggestions. This research was partially supported by NASA NNX13AH50G (C.C.Y., P.M.), and the Alfred P. Sloan Foundation and NSF grant PHY-1620777 (K.M.).

Disclaimer

The findings and conclusions do not necessarily reflect the view of the funding agencies.

Chapter 4
High-Energy Neutrino Emission Subsequent to GW Radiation from SMBH Black Hole Mergers

Note: The material in this Chapter is based on my paper [268], with co-authors Kohta Murase, Shigeo S. Kimura, and Peter Mészáros.

4.1 Introduction

The coincident detection of gravitational waves (GWs) and the broadband electromagnetic (EM) counterpart from the binary neutron star (NS) merger event GW 170817 [269, 270] heralds a new era of multi-messenger astronomy. Since the initial discovery of GWs from binary black hole (BH) mergers by the advanced Laser Interferometric Gravitational Wave Observatory (LIGO) [271, 272], intense efforts have been dedicated to searching for the possible associated neutrino emissions from binary NS/BH mergers (see a review [273] and [274–279]). The joint analysis of different messengers would shed significantly more light on the physical conditions of compact objects, as well as on the origin of their high-energy emissions. One vivid example that manifests the power of including high-energy neutrino observations as an additional messenger is the detection of the IceCube-170922A neutrino coincident with the flaring blazar TXS 0506+056 [280]. The combined analyses of EM and neutrino emissions from TXS 0506+056 provided stringent constraints on the blazar's particle acceleration processes and the flare models [281–289].

High-energy neutrino astrophysics began in 2012–2013 by the discovery of the cosmic high-energy neutrino background [263, 264]. Despite the fact that the diffuse neutrino background has been studied for several years [26, 188, 265, 290], its origin still remains

unknown, having given rise to a number of theoretical models aimed at explaining the observations (see, e.g., Refs. [291, 292] for reviews). Candidate source classes include bright jetted AGN [48, 49, 51, 293, 294], hidden cores of AGN [54, 295–297], galaxy clusters and groups [58, 137, 138], and starburst galaxies [58, 139] that contain supernovae and hypernovae as cosmic-ray (CR) accelerators [144] or AGN winds or galaxy mergers [68, 194, 206]. All the above models require CR acceleration up to 10–100 PeV to explain PeV neutrinos, because the typical neutrino energy produced by pp or $p\gamma$ interactions is $E_\nu \sim (0.03 - 0.05)E_p$ [58], where E_p and E_ν are energies of protons and neutrinos, respectively. The same CR interactions also produce neutral pions that decay into high-energy gamma rays, which quickly interact with much lower-energy diffuse interstellar photons, degrading the gamma rays down to energies below $\sim$ TeV, which can be compared to the diffuse GeV-TeV gamma-rays background observed by *Fermi* [1, 298]. An important constraint that all such models must satisfy is that the resulting secondary diffuse gamma-ray flux must not exceed the diffuse isotropic gamma-ray background [58, 296]. The various models mentioned above satisfy, with varying degrees of the success, the observed neutrino and gamma-ray spectral energy densities, but there is uncertainty concerning the occurrence rate of the posited sources at various redshifts, due to our incomplete observational knowledge about the behavior of the corresponding luminosity functions at high redshifts.

Recent observations have provided increasing evidence that a large fraction of nearby galaxies harbor supermassive black holes (SMBHs). One influential scenario for the formation of these SMBHs is that they, like the galaxies, have grown their mass through hierarchical mergers (e.g., Ref. [69]). SMBH mergers are ubiquitous across the history of the Universe especially at high redshifts where the minor galaxy mergers are more frequent. When galaxies merge, the SMBHs residing in each galaxy may sink to the center of the new merged galaxy and subsequently form a SMBH binary [70, 71]. The SMBHs gradually approach each other as the gravitational radiation takes away the angular momentum, which eventually leads to their coalescence, accompanied by a GW burst. The GW burst from the final stage of coalescing can be detected by future missions such as the *Laser Interferometer Space Antenna* (LISA) [72], providing through this channel valuable and prompt information about the merger rates, SMBH masses and redshift. In addition, SMBH mergers are usually associated with mass accretion activities and relativistic jets, which may lead to detectable EM and neutrino emission. For example, SMBH mergers may trigger AGN activities [73]. In this picture, the merger of SMBHs will become an important target for future multi-messenger astronomy (e.g., Ref. [74]).

In this paper, we present a concrete model for high-energy neutrino emission from four possible sites in the relativistic jet of SMBH mergers, namely, the collimation shock (CS), internal shock (IS), forward shock (FS) and reverse shock (RS). In Sec. 4.2 we discuss the physical conditions in the jet and the gaseous envelope surrounding the merging SMBHs. In Sec. 4.3 we discuss the various relevant dynamic and particle interaction timescales. In Sec. 4.4 we calculate the neutrino emission from each site and investigate the neutrino detection rates for IceCube and its successor, IceCube-Gen2. We also integrated over redshift for parametrized merger rates compatible with our current knowledge and show that our model can contribute a significant portion to the diffuse neutrino background without violating the gamma-ray constraints. We summarize and discuss the implications of our results in Sec. 4.5.

Throughout the paper, we use the conventional notation $Q_x = Q/10^x$ and quantities are written in CGS units, unless otherwise specified. The integration over redshift is carried out in the ΛCDM universe with $H_0 = 71$ km s^{-1} Mpc^{-1}, $\Omega_{\rm m} = 0.3$ and $\Omega_\Lambda = 0.7$.

4.2 Physical Conditions of the Premerger Circumnuclear Environment and the Jet

The premerger circumnuclear material is thought to form from disk winds driven by the inspiralling binary SMBHs, in which a postmerger jet is launched, powered by the rotational energy of the remnant of the merger. It consists of two components originating respectively from the winds from the circumbinary disks around the binary system and from the minidisks surrounding each SMBH. Differently from the relativistic jet, the bulk velocity of the winds is nonrelativistic and the mass outflow carried by the wind spreads out quasi-spherically above and below the disks [299–301]. Although many jet and wind models have been proposed, currently there is no unambiguous way to demarcate the wind and the jet temporally. In this work, from the practical standpoint, we conjecture that the accretion by the binary system before the merger dominates the circumnuclear material, while the jet is launched after the merger and subsequently it propagates inside the existing premerger disk wind. This viewpoint is supported by numerical models of disk winds and relativistic jets. One of the most promising theoretical models to power relativistic jets is the Blandford-Znajek (BZ) mechanism [76], which posits that the jet is primarily driven by the rotational energy of the central SMBH, while it is widely accepted that the accretion outflows dominantly produce the nonrelativistic winds. In

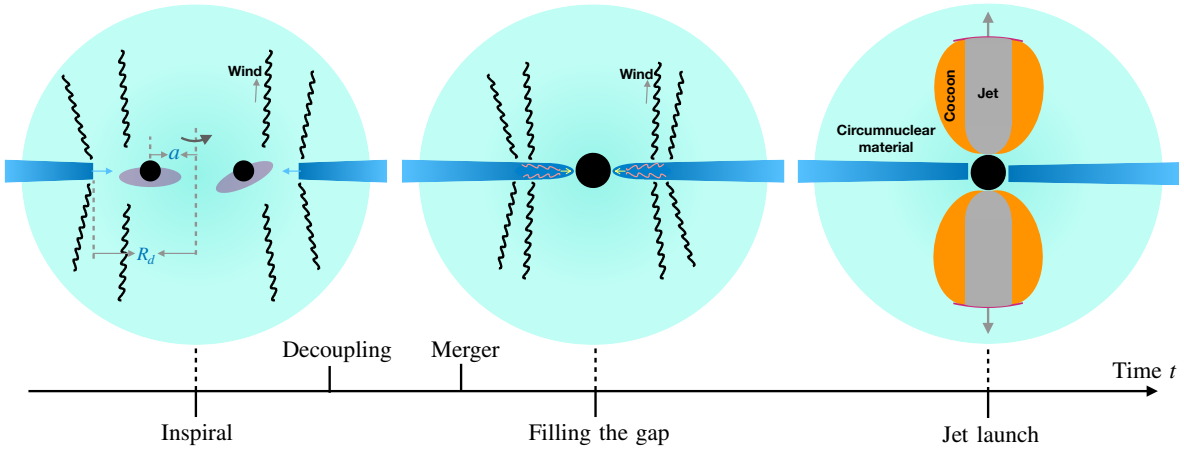

Figure 4.1. Schematic description of the merger of SMBHs with minidisks. The black wavy lines in the first and second panels illustrate the disk wind that forms the premerger circumnuclear material. The second panel shows the evolution of the circumbinary disk after the merger, while the third panel shows the postmerger jet-cocoon system. The stages of the evolution are marked on the time arrow below the figures.

this case, it is reasonable to assume that the launch of the jets occurs after the binary SMBH coalescence, as a more massive SMBH is formed, and the wind bubble arises from the inspiral epoch during which the powerful tidal torque powers the strong winds. The schematic picture in Fig. 4.1 illustrates the evolution of the system.

As the jet penetrates deeply into the premerger disk wind, it sweeps up the gaseous material, leading to a high-pressure region which forces the encountered gas to flow sideaway to form a cocoon [302–308] (see also Refs. [309–311] for the jet propagation in expanding mediums). In this process, a forward shock and a reverse shock are also formed due to the interaction between the jet and the premerger disk wind. The shocks together with the shocked material are generally referred to as the jet head. A collimation shock will appear if the cocoon pressure is high enough to bend the jet boundary toward the axis of the jet, which as a consequence, collimates the jet. Moreover, the velocity fluctuation in the plasma inside the jet may produce internal shocks [312].

For the purpose of conciseness, we use the abbreviations CS, IS, FS and RS to represent the collimation shock, internal shock, forward shock and revers shock in the following text, respectively. We show that all four of these sites can be CR accelerators, and we discuss the neutrino emissions from each site. In 4.2.1, we describe the premerger physical processes in details and derive a quantitative estimation of the premerger circumnuclear environment, while the jet structure and the shock properties are discussed in 4.2.2.

4.2.1 Premerger Circumnuclear Environment

The existence of circumbinary and minidisks may have a profound impact on the evolution of the binary system especially in the early inspiral stage where angular momentum losses due to gravitational radiation are subdominant compared with that from the circumbinary disk [313–315]. There are significant uncertainties in formulating a rigorous model of the disk-binary interactions throughout the merger, and this is beyond the scope of this work. Here, we consider three major factors that can dominate the disk and binary evolution in the late inspiral phase, namely, the viscosity, the tidal torques on the disks, and the gravitational radiation of the binary system, and use these to formulate a simplified treatment for deriving the density profile of the premerger circumnuclear material. This treatment can be justified because the previously launched disk wind material will be overtaken by the fast wind from the late inspiral stage, which implies that we only need to model the disk-binary interactions in a short time interval immediately before the merger occurs.

Considering a circumbinary disk of inner radius R_d around a SMBH binary of total mass $M_{\rm BH}$, the viscosity time for the disk is (e.g., Ref. [316])

$$t_{\rm vis} = \frac{1}{\alpha\Omega_K}\left(\frac{R_d}{H}\right)^2 \simeq 0.31 \text{ yr } M_{\rm BH,6}^{-1/2} R_{d,14}^{3/2} \alpha_{-1}^{-1} (h/0.3)^{-2}, \tag{4.1}$$

where $\alpha \sim 0.1$ is the viscosity parameter, H is the disk scale height, $\Omega_K = \sqrt{GM_{\rm BH}/R_d^3}$ is the Kepler rotation angular velocity, $M_{\rm BH} = 10^6\ M_{\rm BH,6} M_\odot$ is the total mass of the binary SMBHs, and the dimensionless parameter h is defined by $h = H/R_d$. In this study, we consider high mass accretion rates, and assume optically thick circumbinary disks with $h \approx 0.3$. For illustrative purposes we take the SMBH mass to be $M_{\rm BH} = 10^6 M_\odot$ as in Ref. [317] and assume the mass ratio of the two SMBHs is $\zeta = 1$. Initially, before the merger, the binary system has a large semi-major axis a, implying that the influence of the GWs for the disk is inferior to that of the viscosity, e.g., $t_{\rm GW} \gg t_{\rm vis}$. Here, the timescale of the GW inspiral is (e.g., Ref. [318])

$$t_{\rm GW} = \frac{5}{64}\frac{c^5 a^4}{G^3 M_{\rm BH}^3}\frac{(1+\zeta)^2}{\zeta} \simeq 1.0\times 10^4 \text{ yr } M_{\rm BH,6}^{-3} a_{14}^4, \tag{4.2}$$

As the two SMBHs gradually approach each other, the effects of the GWs become increasingly important. However, the circumbinary disk is still able to respond promptly to the slowly shrinking binary system until $t_{\rm GW} = t_{\rm vis}$. In this phase, the ratio of R_d

and a remains roughly constant, e.g., $R_d \sim 2a$, as a result of the balance of the internal viscosity torque and the tidal torque exerted by the binary system. Later on, when the semi-major axis shortens down to or below a certain length, the binary system starts to evolve much faster and the gas in the circumbinary disk cannot react fast enough since GWs take away an increasingly large amount of energy from the binary system. The critical radius is referred to as the decoupling radius. Equating $t_{\rm vis}$ with $t_{\rm GW}$ we obtain the decoupling radius as

$$R_{d,\rm dec} \simeq 4.8 \times 10^{12}\ {\rm cm}\ M_{\rm BH,6}\alpha_{-1}^{-2/5}(h/0.3)^{-4/5}. \tag{4.3}$$

The accretion activity also produces disk winds that blow away a fraction of the accreted mass, resulting in a premerger circumnuclear material above and below the circumbinary disk. In this study, we assume that the accretion rate is mildly larger than the Eddington rate, as $\dot{M}_{\rm BH} = \dot{m}\dot{M}_{\rm Edd} \equiv 10\dot{m}L_{\rm Edd}/c^2 \sim 0.2(\dot{m}/10)\ {\rm M}_\odot\ {\rm yr}^{-1}$. Given the accretion rate, we parameterize the mass outflow rate as $\dot{M}_w = \eta_w\dot{M}_{\rm BH}$. After the disk becomes decoupled, R_d remains roughly constant until merger occurs. The time interval between the disk decoupling and the merger, $t_{\rm m}$, can be estimated using Eq. (4.2) in combination with $t_{\rm GW} = a/|da/dt|$. After the merger, the gap between the disk and the newly formed SMBH cannot be preserved and the gas starts to fill the cavity in the viscosity timescale (e.g., Ref. [319]). Our estimate suggests that both $t_{\rm m} \sim 8 \times 10^{-4}$ yr$M_{\rm BH,6}\alpha_{-1}^{-8/5}(h/0.3)^{-16/5}$ and $t_{\rm vis} \sim 3 \times 10^{-3}\ {\rm yr}\ M_{\rm BH,6}\alpha_{-1}^{-8/5}(h/0.3)^{-16/5}$ at decoupling are approximately of the order of 10^{-3} yr, which is much shorter than the timescales to be considered later for the neutrino production. In such a short time duration, the wind formed at decoupling can reach only up to $\sim 10^{13} - 10^{14}$ cm, but one may extrapolate the density profile to a farther radius by incorporating different disk winds into one smooth profile. Therefore, we neglect the modifications to the disk wind due to these two short term processes and we use the density profile at the decoupling to derive the jet structure. Moreover, we assume that the jet driven by the BZ mechanism is launched immediately after the cavity is occupied by gas. The evolution of the binary system is shown in the schematic pictures in Fig. 4.1. Given the wind mass outflow rate $\dot{M}_w$ and the decoupling radius $R_{d,\rm dec}$, we have the density distribution of the premerger circumnuclear material

$$\varrho_w(r) = \frac{\eta_w\dot{M}_{\rm BH}(1+\chi)}{4\pi r^2}\sqrt{\frac{R_{d,\rm dec}}{2GM_{\rm BH}}}, \tag{4.4}$$

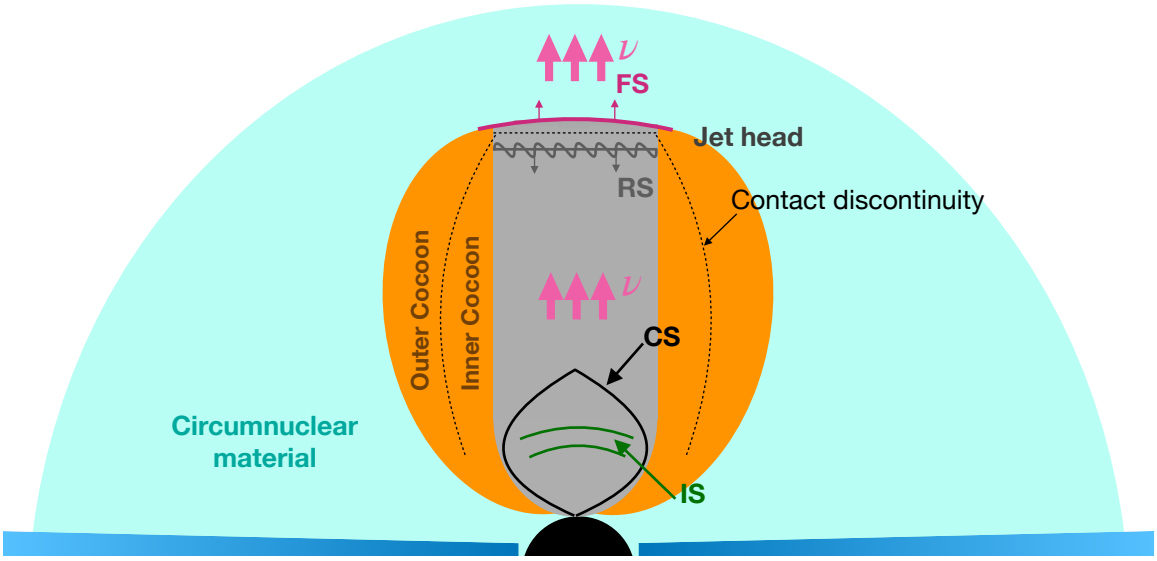

Figure 4.2. Schematic description of the structure of the collimated jet, where CS, IS, FS and RS stand for collimation shock, internal shock, forward shock and reverse shock. The contact discontinuity is illustrated as the dashed line.

where the enhancement factor $\chi \approx \frac{\dot{M}_{\rm mini}}{\dot{M}_w}\frac{\sqrt{2GM_{\rm BH}/R_{d,\rm dc}}}{v_{\rm mini}}$ takes into account the contribution of minidisks. In this expression, $\dot{M}_{\rm mini}$ represents the rate of accretion to the binary system from the minidisks, while $v_{\rm mini} \approx \sqrt{2GM_{\rm BH}/(a/2)}$ is the typical escape velocity from the minidisks. We expect $R_d \sim 2a$, which implies that $v_{\rm mini}$ is about twice as much as the wind velocity of the circumbinary disk, i.e. $v_{\rm mini} \approx 2\sqrt{2GM_{\rm BH}/R_{d,\rm dc}}$. On the other hand, we expect a lower mass accretion rate onto the minidisk, e.g., $\dot{M}_{\rm mini} < \dot{M}_{\rm BH}$, as a result of the suppression due to the binary tidal torque. In this case, we conclude that the factor χ is close to unity. The parameter η_w depends strongly on $\dot{m}$ and on the disk magnetic field. For the standard and normal evolution (SANE) model the magnetic field is weak and η_w ranges from 10^{-1} to 10^{-4} for super- and sub-Eddington accretions [320–322], respectively. However, more powerful outflows could be produced in the magnetically arrested disk (MAD) model. In this case, η_w can reach $10^{-2} - 10^{-1}$ [323]. Here, we assume a fiducial value, $\eta_w \sim 10^{-2}$ and we will discuss the impact of a higher η_w, e.g., $\eta_w = 0.1$, later.

4.2.2 Postmerger Jet Structure and CR Acceleration

The central engines of strong, highly relativistic jets are generally assumed to be related to magnetized accretion flows and rotation of compact objects. According to general

relativistic magnetohydrodynamics (GRMHD) simulations, the threading magnetic flux $\Phi_B = \pi B_H R_g^2$ can reach the maximum saturation value [324], $\Phi_B \sim 50\ \dot{M}_{\rm BH}^{1/2} R_g c^{1/2}$, for a given accretion rate $\dot{M}_{\rm BH}$ and horizon radius $R_g = GM_{\rm BH}/c^2$. Here, B_H is the magnetic field that threads the SMBH horizon and we assume that the accretion rate remains unchanged before and after the merger, e.g., $\dot{M}_{\rm BH} \sim 0.2\ \ M_\odot\ {\rm yr}^{-1}\ (\dot{m}/10)$, where the parameter $\dot{m}$ is defined as the ratio of $\dot{M}_{\rm BH}$ and the Eddington value $\dot{M}_{\rm Edd} \equiv 10 L_{\rm Edd}/c^2$. In the case of the magnetically arrested accretion, we estimate the jet kinetic luminosity to be

$$L_{k,j} \approx \eta_j \dot{M}_{\rm BH} c^2 \simeq 3.4 \times 10^{46}\ (\dot{m}/10)(\eta_j/3)\ {\rm erg\ s^{-1}}, \tag{4.5}$$

where η_j is the efficiency with which the accretion system converts accretion energy into jet energy [324]. Since this parameter is degenerate with $\dot{m}$, we assume $\eta_j = 3$ in the following text.

Once the jet kinetic luminosity is specified, the shock structure is determined by the ambient gas density distribution and the Lorentz factor of the unshocked material, Γ_j. We now discuss the conditions under which the jets are collimated and for which CRs can be efficiently accelerated in each of the shock regions including the CS, IS, RS and FS. The jet is typically collimated for a sufficiently high cocoon density. Considering a jet of opening angle θ_j, jet kinetic luminosity $L_{k,j}$ and isotropic equivalent kinetic luminosity $L_{k,\rm iso} \approx 2L_{k,j}/\theta_j^2$, the jet head position for the collimated jet is estimated to be (e.g., [305, 325]),

$$R_h \approx \Xi^{1/5} L_{k,j}^{1/5} \hat{\varrho}_w^{-1/5} \theta_j^{-4/5} t_j^{3/5} \tag{4.6}$$

where $\Xi = 16/\pi$ is a constant, t_j is the jet propagation time reckoned from the launch of the jet and $\hat{\varrho}_w = (1/R_h)\int_{2R_g}^{R_h} \varrho_w(r) dr$ is the average density over the cocoon volume assuming that the cocoon's shape is cylindrical. Combining Eq. (4.6) with the definition of $\hat{\varrho}_w$, we are able to solve R_h and $\hat{\varrho}_w$. According to the jet-cocoon model, the collimation shock forms at

$$R_{cs} \approx (2\pi)^{-1/2} \Xi^{-1/5} c^{-1/2} \hat{\varrho}_w^{-3/10} \theta_j^{-1/5} t_j^{2/5} L_{k,j}^{3/10}. \tag{4.7}$$

One precondition for these equations is that the jet should be collimated, which requires $R_{\rm cs} \lesssim R_h$. From the black lines of Fig. 4.3, we find that the jets with the typical parameters $\theta_j \approx 1/\Gamma_{\rm cj} \simeq 0.33$ and $L_{k,j} \simeq 3.4 \times 10^{46}$ erg s^{-1} satisfies this requirement if $t_j \gtrsim 10^{-3}$ yr, where $\Gamma_{\rm cj} \approx 1/\theta_j \simeq 3$ is the Lorentz factor of the downstream material of the collimation shock.

In the precollimation region, we assume the Lorentz factor of the unshocked material to be comparable to that of blazars, e.g., $\Gamma_j \sim 10$, which is typically lower than the case

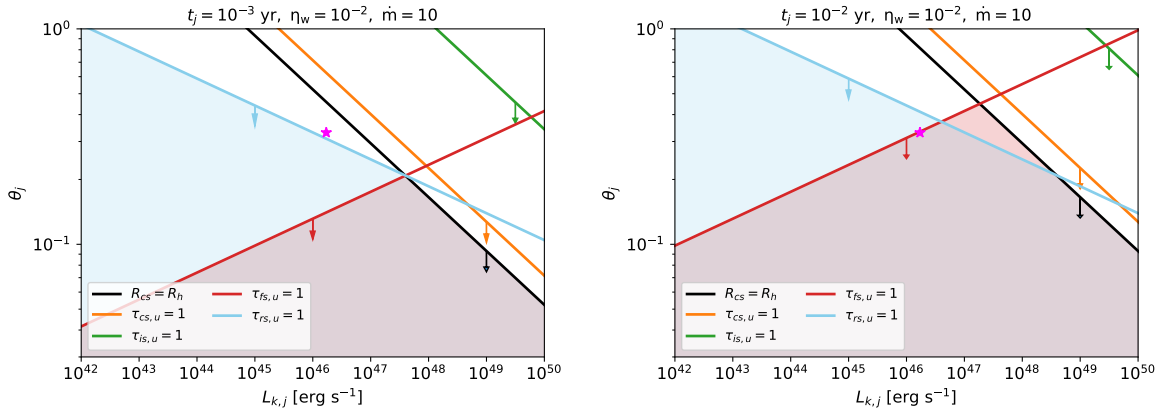

Figure 4.3. Radiation constraints, $\tau_{i,u} < 1$, on $\theta_j - L_{k,j}$ plane at $t_j = 10^{-3}$ yr (left panel) and $t_j = 10^{-2}$ yr (right panel) for i =CS (orange lines), IS (green lines), FS (red lines) and RS (blue lines). The magenta stars show the parameters that are used, $\theta_j^{-1} = 3$ and $L_{k,j} \simeq 3.4 \times 10^{46}$ erg s^{-1}. The black solid line in each panel corresponds to the jet collimation condition, $R_{\rm cs} \lesssim R_h$. The blue and red areas illustrate the FS and RS constraints respectively, whereas the overlapped areas represent the joint constraints.

of GRBs. Internal shocks usually arise in this region as a result of velocity fluctuations inside the outflow, resulting in faster and slower gas shells. Numerical simulations indicate that the fast material shells with Lorentz factor Γ_r will catch up with the slower ones with Γ_s nearly at the position of the collimation shock (e.g., Ref. [326]). Hence, we may approximate the radius of the internal shocks to be

$$R_{\rm is} \approx \min\left[R_{\rm cs},\ 2\Gamma_j^2 c t_{\rm var}\right], \tag{4.8}$$

where $t_{\rm var} \simeq 10^5$ s is the variability time.

Fig. 4.2 schematically describes the structure of the jet-cocoon system as well as the shocks inside the jet. We consider CR acceleration and neutrino production in four different shock sites, including the CS, IS, FS and RS, as the jet propagates. One necessary condition for efficient CR acceleration through the shock acceleration mechanism is that the shock should have a sufficiently strong jump between the upstream and downstream material. Therefore, a collisionless shock mediated by plasma instabilities would be necessary rather than a radiation-mediated shock where velocity discontinuities are smeared out [327, 328]. Motivated by this, we obtain one necessary constraint on the upstream of the shock for particle acceleration (see Ref. [40, 277] for details)

$$\tau_u = n_u \sigma_T l_u \lesssim \min[1, \Pi(\Gamma_{\rm sh})] \tag{4.9}$$

where τ_u is the upstream optical depth, n_u is the comoving number density of upstream material, σ_T is the Thomson cross section, l_u is the length scale of the upstream fluid, $\Gamma_{\rm sh}$ stands for the relative Lorentz factor between the shock downstream and upstream, $\Pi(\Gamma_{\rm rel})$ is the function that depends on details of the pair enrichment. Although the pairs are important for ultrarelativistic shocks, we impose $\tau_u < 1$ for conservative estimates. However, our results are not much affected by this assumption, because the neutrino production continues to occur when the system becomes optically thin. The Lorentz factors for the shocks that are considered lie in the range $1 < \Gamma_{\rm sh} \lesssim 5$, therefore we focus on the first constraint in Eq. (4.9) for our mildly relativistic shocks. As for the collimation shocks, combining the number density of the upstream $n_{{\rm cs},u} \approx L_{k,{\rm iso}}/(4\pi\Gamma_j^2 R_{\rm cs}^2 m_p c^3)$ with the comoving length of upstream fluid $l_{{\rm cs},u} \sim R_{cs}/\Gamma_j$, we have for the optical depth

$$\tau_{{\rm cs},u} \approx n_{{\rm cs},u} l_{{\rm cs},u} \sigma_T \approx \frac{L_{k,{\rm iso}}\sigma_T}{4\pi\Gamma_j^3 R_{\rm cs} m_p c^3}. \tag{4.10}$$

In the precollimated region, particles are mainly accelerated by internal shocks. The downstream of the internal shock can be regarded as the upstream of the collimation shock, and one may use $n_{{\rm is},u} \sim n_{{\rm is},d}/\Gamma_{\rm rel-is} \sim n_{{\rm cs},u}/\Gamma_{\rm rel-is}$ (ignoring coefficients), where $\Gamma_{\rm rel-is} \approx \Gamma_r/2\Gamma_j$ is the relative Lorentz factor between the upstream and the downstream of internal shocks. Here, we assume $\Gamma_{\rm rel-is} \approx 5$ and obtain

$$\tau_{{\rm is},u} \approx \frac{L_{k,{\rm iso}}\sigma_T}{4\pi R_{\rm is} m_p c^3 \Gamma_j^3 \Gamma_{\rm rel-is}^2} \tag{4.11}$$

where the relationship $l_{{\rm is},u} \sim R_{\rm is}/\Gamma_j/\Gamma_{\rm rel-is}$ is used because the upstream unshocked flows are moving with a higher Lorentz factor Γ_r.

In the jet head, the gas is rapidly decelerated to subrelativistic speeds, implying that the Lorentz factor is close to unity, e.g.,, $\Gamma_h \gtrsim 1$. Nevertheless, the shock still satisfies the criteria for strong shocks. The ambient gas enters the jet head through the forward shock and forms the outer cocoon, whereas the shocked material from the jet constitutes the inner cocoon. The dashed lines in Fig. 4.2 show the contact discontinuity that separates the outer and inner cocoon components. In this case, we estimate that the head shock upstream number density is $n_{{\rm fs},u} = n_{\rm ext} = \varrho_w(R_h)/m_p$, where $n_{\rm ext}$ is the number density of the exterior premerger circumstellar material at R_h. With this we can write down the optical depth as

$$\tau_{{\rm fs},u} \approx \frac{\varrho_w(R_h)\sigma_T R_h}{m_p}. \tag{4.12}$$

This simplified treatment is computationally convenient, albeit with the caveat that it is optimistic when computing the maximum energy of CRs accelerated by the FS. Similarly, repeating this procedure, we can get the corresponding quantities for the reverse shock, $n_{\rm rs,u} = n_{\rm cs,d} \sim n_{\rm cs,u}\Gamma_{\rm rel-cs}$ and $l_{\rm rs,u} \sim R_h/\Gamma_{\rm cj}$, where $\Gamma_{\rm rel-cs} \approx \Gamma_j/2\Gamma_{\rm cj}$ is the relative Lorentz factor. Substituting these quantities into Eq. (4.9) yields

$$\tau_{\rm rs,u} \approx \frac{L_{k,\rm iso}\sigma_T R_h}{4\pi R_{\rm cs}^2 m_p c^3 \Gamma_j^3 \Gamma_{\rm rel-cs}^{-2}}. \tag{4.13}$$

Fig. 4.3 shows the radiation-mediated shock constraints at $t_j = 10^{-3}$ yr (left panel) and $t_j = 10^{-2}$ yr (right panel). The magenta star corresponds to the parameter set that is used in this work. The conditions for the jet collimation are shown by the black solid lines. From this figure, we find that the jet typically gets collimated in a short time $\sim 10^{-3}$ yr after the jet is launched. When the jet is collimated, the upstreams of the CS and IS are optically thin, implying that CRs may be efficiently accelerated at these two sites. However, the forward shock and reverse shock could still be radiation dominated for $t_j \lesssim 10^{-3}$ yr, and subsequently become optically thin as the exterior gas envelop gets less denser. Therefore, there is a time t_* at which the optical depth becomes unity, e.g., $\tau_{\rm fs,u}(t_*) = 1$, and $\tau_{\rm fs,u}$ continues decreasing after that time. Since in the time interval $t_j \lesssim t_*$ the CR acceleration and the neutrino production are suppressed, we introduce a Heaviside function $H(t_j - t_*)$ in the expression for the CR and neutrino spectra to ensure that CRs are only accelerated after the onset time t_*.

4.3 Interaction Timescales

4.3.1 Nonthermal Target Photon Fields

In the following, we focus on the cases where the shock is collisionless and radiation unmediated. In astrophysical environments, neutrinos are produced through the decay of pions created by CRs via pp and/or $p\gamma$ interactions. Since the collimated jet is optically thin, we focus on nonthermal photons produced by the accelerated electrons and treat each site as an independent neutrino emitter, where the subtle interactions between particles from different regions are not considered. Here, we take a semianalytical approach to model the synchrotron and synchrotron-self-Compton (SSC) components of the target photon fields.

We assume a power-law injection spectrum of electrons in terms of the Lorentz factor

$dN_e/d\gamma_e \propto \gamma_e^{-p}$ for $\gamma_{e,\rm min} < \gamma_e < \gamma_{e,\rm max}$, where p is the spectral index, $\gamma_{e,\rm min}$ and $\gamma_{e,\rm max}$ are the maximum and minimum electron Lorentz factors. Defining ϵ_e as the fraction of internal energy that is transferred to electrons and assuming the shocked gas mainly consists of hydrogen, rather than e^+e^- pairs, one has $\gamma_{e,\rm min} = \epsilon_e\zeta_e\Gamma_{\rm rel}(m_p/m_e)$, where the parameter ζ_e has the typical value in the range $0.3-0.4$ (e.g., Refs. [233, 329]), and $\Gamma_{\rm rel}$ is the relative Lorentz factor between the upstream and the downstream, e.g., $\Gamma_{\rm rel-cs}$ for electrons from the collimation shock. The maximum electron Lorentz factor from the collimation shock acceleration can be obtained by equating the acceleration time $t_{e,\rm acc} \approx \gamma_e m_e c/(eB_{\rm cs,d})$ with the radiation cooling time $t_{e,c} \approx 6\pi m_e c/[\gamma_e\sigma_T B_{\rm cs,d}^2(1+\tilde{Y})]$, where $B_{\rm cs,d} \approx (32\pi\epsilon_B\Gamma_{\rm rel-cs}^2 n_{\rm cs,u} m_p c^2)^{1/2}$ is the downstream magnetic field, $\epsilon_B \simeq 0.01$ is the amplification factor that describes the fraction of the internal energy of unshocked materials converted to the magnetic field, $\tilde{Y}$ is the Compton parameter and given in Ref. [330]. Explicitly, we write the maximum Lorentz factor as

$$\gamma_{e,\rm max} = \left[\frac{18\pi e}{\sigma_T B_{\rm cs,d}(1+\tilde{Y})}\right]^{1/2}. \tag{4.14}$$

Another important quantity that characterizes the shape of the radiation spectrum is the cooling Lorentz factor,

$$\gamma_{e,c} = \frac{6\pi m_e c}{t_{e,c}\sigma_T B_{\rm cs,d}^2(1+\tilde{Y})}, \tag{4.15}$$

above which electrons lose most of their energy by radiation. In this expression, $t_{e,c} \approx \min[t_j, t_{\rm cs,dyn}]$ is the radiation cooling time scale, where $t_{\rm cs,dyn} \approx R_h/(\Gamma_{\rm cj}c)$ is the dynamical time of the collimation shock.

Using $\gamma_{e,\rm min}$, $\gamma_{e,c}$ and $\gamma_{e,\rm max}$, the typical, cooling and maximum synchrotron emission energies in the jet comoving frame are respectively given by

$$\begin{aligned}
\varepsilon_{\gamma,m} &= \frac{3}{2}\hbar\gamma_{e,\rm min}^2\frac{eB_{\rm cs,d}}{m_e c}, \\
\varepsilon_{\gamma,c} &= \frac{3}{2}\hbar\gamma_{e,\rm c}^2\frac{eB_{\rm cs,d}}{m_e c}, \\
\varepsilon_{\gamma,M} &= \frac{3}{2}\hbar\gamma_{e,\rm max}^2\frac{eB_{\rm cs,d}}{m_e c}.
\end{aligned} \tag{4.16}$$

If $\gamma_{e,\rm min} > \gamma_{e,c}$, the electrons are in the fast cooling regime and we obtain the energy

spectrum of the synchrotron radiation (e.g. Refs. [233, 329, 331])

$$\varepsilon_\gamma^2 \frac{dn_\gamma^{\rm syn}}{d\varepsilon_\gamma} = \frac{L_\gamma^{\rm syn}}{4\pi R_{\rm cs}^2 \Gamma_{\rm cj}^2 c \mathcal{C}_\gamma^{\rm syn}} \times \begin{cases} \left(\frac{\varepsilon_\gamma}{\varepsilon_{\gamma,c}}\right)^{\frac{4}{3}}, & \varepsilon_\gamma < \varepsilon_{\gamma,c} \\ \left(\frac{\varepsilon_\gamma}{\varepsilon_{\gamma,c}}\right)^{\frac{1}{2}}, & \varepsilon_{\gamma,c} < \varepsilon_\gamma < \varepsilon_{\gamma,m} \\ \left(\frac{\varepsilon_{\gamma,m}}{\varepsilon_{\gamma,c}}\right)^{\frac{1}{2}} \left(\frac{\varepsilon_\gamma}{\varepsilon_{\gamma,m}}\right)^{\frac{2-p}{2}}, & \varepsilon_{\gamma,m} < \varepsilon_\gamma < \varepsilon_{\gamma,M} \end{cases} \tag{4.17}$$

where $L_\gamma^{\rm syn} = \epsilon_e L_{k,\rm iso}/(1+\tilde{Y})$, and $\mathcal{C}_\gamma^{\rm syn}$ is the normalization coefficient that ensures $\int \varepsilon_\gamma (dn_\gamma^{\rm syn}/d\varepsilon_\gamma) d\varepsilon_\gamma = L_\gamma^{\rm syn}/[4\pi R_{\rm cs}^2 \Gamma_{\rm cj}^2 c]$, and $\epsilon_e/(1+\tilde{Y})$ represents the fraction of jet kinetic energy transferred to synchrotron radiation. In this work we assume $\epsilon_e = 0.1$. As for SSC, we neglect the Klein-Nishina effect, since the highest energy photons do not contribute significant $p\gamma$ interactions. The SSC spectrum in the Thomson regime is then given by

$$\varepsilon_\gamma^2 \frac{dn_\gamma^{\rm ssc}}{d\varepsilon_\gamma} = \frac{L_\gamma^{\rm ssc}}{4\pi R_{\rm cs}^2 \Gamma_{\rm cj}^2 c \mathcal{C}_\gamma^{\rm ssc}} \times \begin{cases} \left(\frac{\varepsilon_\gamma}{\varepsilon_{\gamma,c}^{\rm ssc}}\right)^{\frac{4}{3}}, & \varepsilon_\gamma < \varepsilon_{\gamma,c}^{\rm ssc} \\ \left(\frac{\varepsilon_\gamma}{\varepsilon_{\gamma,c}^{\rm ssc}}\right)^{\frac{1}{2}}, & \varepsilon_{\gamma,c}^{\rm ssc} < \varepsilon_\gamma < \varepsilon_{\gamma,m}^{\rm ssc} \\ \left(\frac{\varepsilon_{\gamma,m}^{\rm ssc}}{\varepsilon_{\gamma,c}^{\rm ssc}}\right)^{\frac{1}{2}} \left(\frac{\varepsilon_\gamma}{\varepsilon_{\gamma,m}^{\rm ssc}}\right)^{\frac{2-p}{2}}, & \varepsilon_{\gamma,m}^{\rm ssc} < \varepsilon_\gamma < \varepsilon_{\gamma,M}^{\rm ssc} \end{cases} \tag{4.18}$$

where $L_\gamma^{\rm ssc} \approx \tilde{Y} L_\gamma^{\rm syn}$ and the break energies are defined as $\varepsilon_{\gamma,m}^{\rm ssc} = 2\gamma_{e,\min}^2 \varepsilon_{\gamma,m}$, $\varepsilon_{\gamma,c}^{\rm ssc} = 2\gamma_{e,c}^2 \varepsilon_{\gamma,c}$ and $\varepsilon_{\gamma,M}^{\rm ssc} = \gamma_{e,\max} m_e c^2$. Likewise, the normalization factor $\mathcal{C}_\gamma^{\rm ssc}$ is determined by $\int \varepsilon_\gamma (dn_\gamma^{\rm ssc}/d\varepsilon_\gamma) d\varepsilon_\gamma = L_\gamma^{\rm ssc}/[4\pi R_{\rm cs}^2 \Gamma_{\rm cj}^2 c]$. In the early stage of the jet propagation, the electrons are commonly in the fast cooling regime, and the equation controlling the distribution of nonthermal photons is

$$\varepsilon_\gamma \frac{dn_\gamma}{d\varepsilon_\gamma} = \varepsilon_\gamma \frac{dn_\gamma^{\rm syn}}{d\varepsilon_\gamma} + \varepsilon_\gamma \frac{dn_\gamma^{\rm ssc}}{d\varepsilon_\gamma}. \tag{4.19}$$

The cooling of the electrons tends to be less efficient when the magnetic field decreases as jet expands, and the energy spectra for slow cooling electrons should be used if the order of $\gamma_{e,c}$ and $\gamma_{e,m}$ is reversed, i.e., $\gamma_{e,c} > \gamma_{e,\min}$. In this case, the synchrotron and SSC spectra should be rewritten by swapping $\varepsilon_{\gamma,m}$ and $\varepsilon_{\gamma,c}$ in Eq. (4.17), and swapping $\varepsilon_{\gamma,m}^{\rm ssc}$ and $\varepsilon_{\gamma,c}^{\rm ssc}$ in Eq. (4.18), respectively. We also need to replace the index 1/2 by $(3-p)/2$

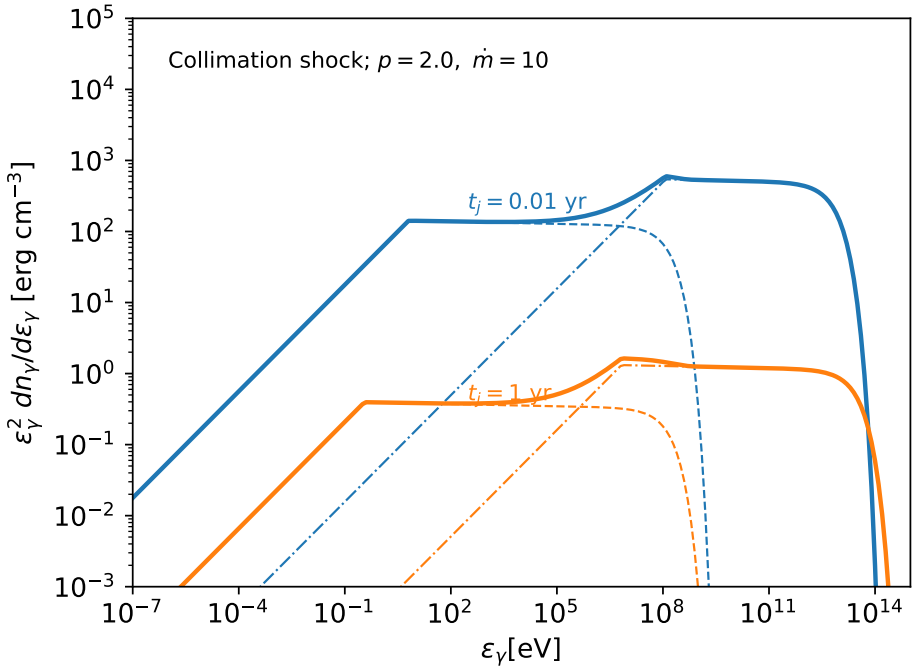

Figure 4.4. Collimation shock photon density distribution in the jet comoving frame at $t_j = 0.01$ yr (blue lines) and $t_j = 1$ yr (orange lines) for the super-Eddington accretion rate $\dot{m} = 10$. The synchrotron and SSC components are shown as dashed and dash-dotted lines, respectively. The parameters, $\epsilon_e = 0.1$, $\epsilon_B = 0.01$, $\dot{m} = 10$ and $\Gamma_{\rm cj} = \theta_j^{-1} = 3$ are used.

in both equations. Considering that only electrons with γ_e greater than $\gamma_{e,c}$ can convert their kinetic energies to electromagentic emission, we introduce one extra parameter

$$\eta_e = \frac{\int_{\gamma_{e,c}}^{\gamma_{e,\rm max}} \gamma_e (dN_e/d\gamma_e) d\gamma_e}{\int_{\gamma_{e,\rm min}}^{\gamma_{e,\rm max}} \gamma_e (dN_e/d\gamma_e) d\gamma_e} \lesssim 1,\ \gamma_m < \gamma_c < \gamma_M \tag{4.20}$$

into the photon density for the slow cooling case. We adopt the spectral index $p = 2.0$ for electrons. Fig. 4.4 shows the distribution of photon densities in the jet comoving frame for collimation shocks at $t_j = 0.01$ yr (blue lines) and $t_j = 1$ yr (orange lines) for the super-Eddington accretion rate $\dot{m} = 10$.

Similarly we can derive the photon distribution in other shocks given the dynamic times for IS, FS and RS, e.g., $t_{\rm is,dyn} \approx R_{\rm is}/(\Gamma_j c)$, $t_{\rm fw,dyn} \approx R_h/(\beta_h c) \approx t_{\rm rs,dyn}$, where $\beta_h c = c\sqrt{1 - 1/\Gamma_h^2}$ is jet head speed and

$$\Gamma_h = \min\left[\Gamma_{\rm cj}, \sqrt{1 + \tilde{L}^{1/2}}\right] \tag{4.21}$$

is the jet head Lorentz factor. In this expression, we follow Ref. [305] to define $\tilde{L}$

$$\tilde{L} = \Xi^{2/5} L_{k,j}^{2/5} \hat{\varrho}_w^{-2/5} c^{-2} \theta_j^{-8/5} t_j^{-4/5}. \tag{4.22}$$

Since the jet head decelerates while sweeping up the exterior circumnuclear material and ends up being sub-relativistic ($\Gamma_h \gtrsim 1.0$), we use the jet head velocity rather than the Lorentz transformation to compute $t_{fs,\rm dyn}$. The photon spectra for the IS, FS and RS look similar to Fig. 4.4, so for the purpose of conciseness, we merely show $dn_\gamma/d\varepsilon_\gamma$ for the CS case.

4.3.2 Timescales for the CRs and Pions

To calculate the neutrino emission, we need to estimate the cooling and acceleration timescales of the protons. Here we consider the CS case as an example, and it is straightforward to rewrite the relevant equations to cover the IS, FS and RS scenarios. For the CS case, the acceleration time for protons with an energy ε_p is estimated to be $t_{p,\rm acc} \approx \varepsilon_p/(eB_{\rm cs,}dc)$. While propagating in the jet, the high-energy protons are subject to photomeson ($p\gamma$) interactions, the Bethe-Heitler (BH) process, proton-proton (pp) inelastic collisions and synchrotron radiation. The energy loss rate due to $p\gamma$ interactions is

$$t_{p\gamma}^{-1} = \frac{c}{2\gamma_p^2} \int_{\bar{\varepsilon}_{\rm th}}^{\infty} d\bar{\varepsilon}_\gamma \sigma_{p\gamma} \kappa_{p\gamma} \bar{\varepsilon}_\gamma \int_{\frac{\bar{\varepsilon}_\gamma}{2\gamma_p}}^{\infty} d\varepsilon_\gamma \varepsilon_\gamma^{-2} \frac{dn_\gamma}{d\varepsilon_\gamma}, \tag{4.23}$$

where $\gamma_p = \varepsilon_p/(m_p c^2)$ is the proton Lorentz factor, $\bar{\varepsilon}_{\rm th} \simeq 145$ MeV is the threshold energy for $p\gamma$ meson production, and $\bar{\varepsilon}_\gamma$ is the photon energy in the proton rest frame. In this equation, $\sigma_{p\gamma}$ and $\kappa_{p\gamma}$ represent the $p\gamma$ cross section and inelasticity, respectively. We use the results of Ref. [38] for $\sigma_{p\gamma}$ and $\kappa_{p\gamma}$. Similarly we use Eq. (4.23) to evaluate the BH cooling rate, $t_{\rm BH}^{-1}$, by replacing $\sigma_{p\gamma}$ and $\kappa_{p\gamma}$ with $\sigma_{\rm BH}$ and $\kappa_{\rm BH}$ whose fitting formulae are given by Refs. [332] and [333], respectively. The time scale of pp interactions can be written as $t_{pp}^{-1} \approx n_{\rm cs,}d\sigma_{pp}\kappa_{pp}c$, where $\kappa_{pp} \approx 0.5$ is the inelasticity and σ_{pp} is the cross section for inelastic pp collisions. As for the synchrotron radiation, the cooling timescale for protons is estimated to be $t_{p,\rm syn} = 6\pi m_p^4 c^3/(m_e^2 \sigma_T B_{\rm cs,}d^2 \varepsilon_p)$. Assuming $\epsilon_e = 0.1$ and $\epsilon_B = 0.01$, Fig. 4.5 shows the cooling rates, acceleration and dynamical timescales for CS, IS, FS and RS scenarios at the jet time $t_j = 10^{-2}$ yr. The vertical lines represent the maximum proton energy by *Fermi* acceleration, $\varepsilon_{p,\rm acc} \approx \frac{3}{20} eB_{i,}d t_{i,\rm dyn} c$. From Fig. 4.5, we also find that the pp interactions are subdominant in comparison with photomeson ($p\gamma$) process. Given the timescales for protons, we are able to derive the energy-dependent

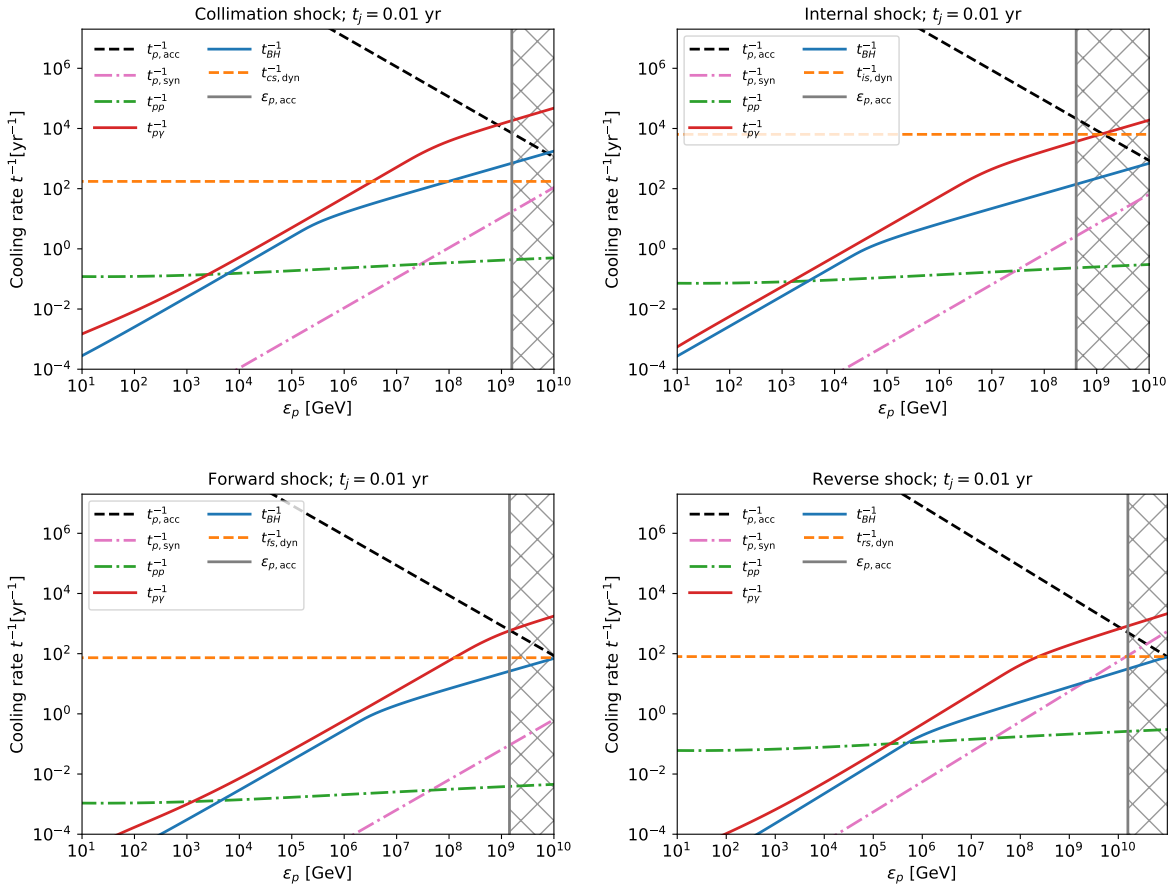

Figure 4.5. Snapshots of cooling, acceleration and dynamic timescales for CS (left up), IS (right up), FS (left down) and RS (right down) at $t_j = 10^{-2}$ yr. The vertical line represents the maximum proton energy from acceleration, $\varepsilon_{p,\rm acc}$, whereas the hatches imply the unreachable proton energies. The parameters, $\epsilon_e = 0.1$, $\epsilon_B = 0.01$, $\dot{m} = 10$, $\Gamma_j = 10$ and $\Gamma_{\rm cj} = \theta_j^{-1} = 3$ are used.

neutrino production efficiencies from $p\gamma$ and pp interactions respectively

$$f_{p\gamma-\rm cs} = \frac{t^{-1}_{p\gamma}}{t^{-1}_{p,c} + t^{-1}_{\rm cs,dyn}}, \qquad f_{pp-\rm cs} = \frac{t^{-1}_{pp}}{t^{-1}_{p,c} + t^{-1}_{\rm cs,dyn}}, \tag{4.24}$$

where $t^{-1}_{p,c} \equiv t^{-1}_{p\gamma} + t^{-1}_{\rm BH} + t^{-1}_{pp} + t^{-1}_{p,\rm syn}$ is the total cooling rate and the dynamic time $t_{\rm cs,dyn}$ is included to constrain the timescale of interactions. If $t^{-1}_{\rm cs,dyn}$ is high, protons tend to leave this site very fast before sufficiently participating in the interactions listed above. Likewise, we can obtain the neutrino production efficiencies for the IS, FS and RS. As expected, in Fig. 4.5 we find that $p\gamma$ interactions dominate the neutrino production,

instead of the pp collisions. The reason is that the jet is neither dense enough nor has a sufficiently large size to allow efficient pp interactions.

The secondary pions produced from $p\gamma$ and pp interactions may also lose energy through synchrotron and hadronic processes, e.g., πp collisions. The pion synchrotron cooling timescale is $t_{\pi,\rm syn} = (m_\pi^4/m_p^4)t_{p,\rm syn}$, where $m_\pi \approx 139.57$ MeV is the mass of charged pions. Approximately, the hadronic cooling time scale can be written as $t_{\pi p} \approx n_{{\rm cs},d}\sigma_{\pi p}\kappa_{\pi p}c$, where $\sigma_{\pi p} \sim 5 \times 10^{-26}$ cm^2 and $\kappa_{\pi p} \sim 0.8$ are used in our calculation. Using the rest life time charged pions, $t_\pi \simeq 8.2 \times 10^{-16}$ yr, the charged pion decay rate is estimated to be $t_{\pi,\rm dec}^{-1} \approx 1/(\gamma_\pi t_\pi)$. For a PeV pion, the decay rate is approximately 1.7×10^8 yr^{-1}, which is much larger than the reciprocal of the dynamic time ($t_{\rm cs,dyn}^{-1}$) and the cooling rate ($t_{\pi,\rm syn}^{-1}$), implying that the pion decay efficiency is nearly unity, e.g.,

$$f_{\pi,{\rm sup}-{\rm cs}} \approx 1 - \exp\left(-\frac{t_{\pi,\rm dec}^{-1}}{t_{\rm cs,dyn}^{-1} + t_{\pi,\rm syn}^{-1}}\right) \sim 1. \tag{4.25}$$

We see that this is true in the other sites as well, and the relation $f_{\pi,\rm sup} \sim 1$ will be used in the following text. For neutrinos from secondary muon decay, we introduce another suppression factor besides $f_{\pi,\rm sup}$, e.g., $f_{\mu,\rm sup} = 1 - \exp(-t_{\mu,\rm dec}^{-1}/t_{\mu,c}^{-1})$. For a 100 PeV muon, the decay rate is $t_{\mu,\rm dec}^{-1} \approx 1/(\gamma_\mu t_\mu) \simeq 1.5 \times 10^4$ yr^{-1}, where t_μ is the muon lifetime. We conclude the ratio $t_{\mu,\rm dec}^{-1}/t_{\mu,c}^{-1} \approx (m_\mu^4/m_p^4)t_{p,\rm syn}/(\gamma_\mu t_\mu) \simeq 38 \times (\varepsilon_\mu/100\ {\rm PeV})^{-2}(B_d/10{\rm G})^{-2}$, depending on the shock site and jet time t_j. In the energy range studied in this paper and considering that the neutrino emission can last from years to decades (which will be shown later), the approximation of $f_{\mu,\rm sup} \approx 1$ is valid. Ultrahigh-energy neutrinos (with $\gtrsim 1$ EeV) from the muon decay can be suppressed by $f_{\mu,\rm sup}$ in the very early stage (e.g., $t_j < 10^{-2}$yr), which could change the observed flavor ratio.

4.4 High-Energy Neutrino Emission from Shocks in the Jets

4.4.1 Neutrino Fluences

Assuming that the high-energy protons have the canonical shock acceleration spectrum with a spectral index $p = 2$ and an exponential cutoff at the maximum proton energy, we obtain the single flavor isotropic neutrino spectrum by pion decay at each site in the

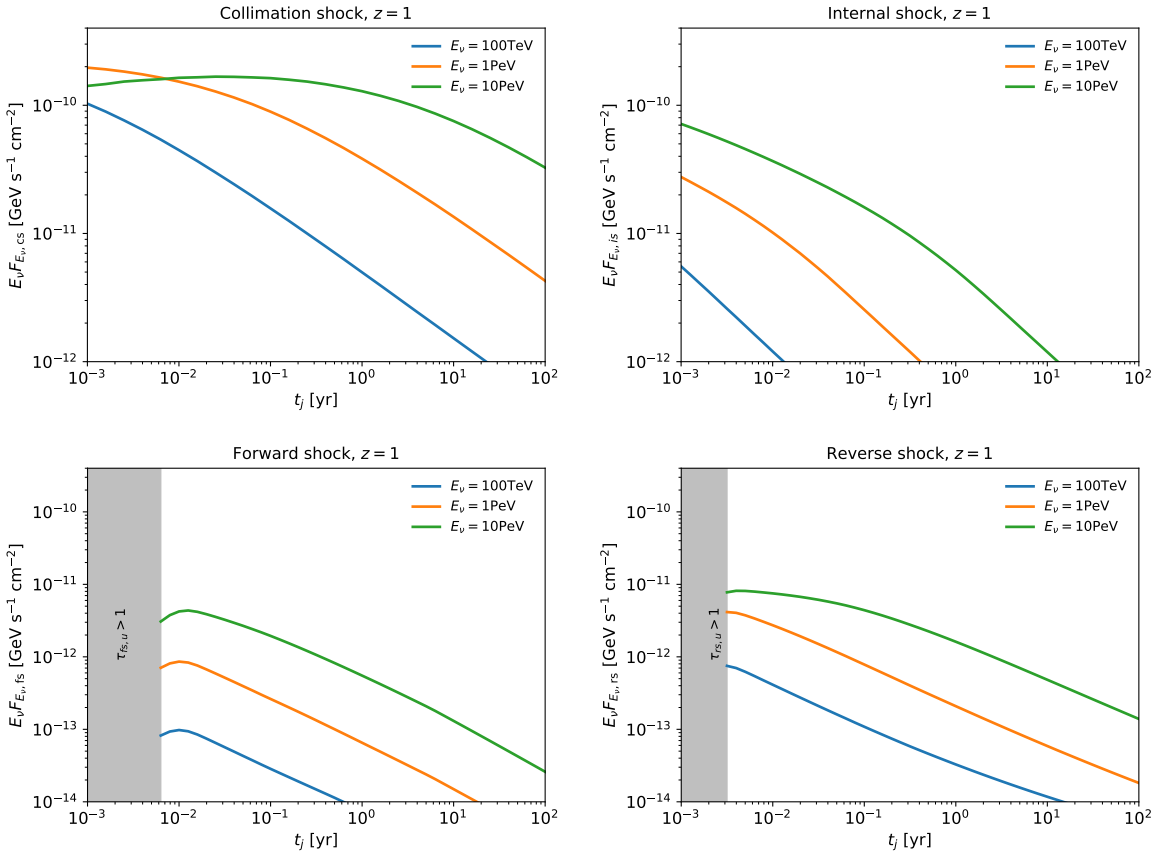

Figure 4.6. Muon neutrino fluxes versus jet time t_j for the CS (up left), IS (up right), FS (bottom left) and RS (bottom right) scenarios. The optimistic parameters (e.g., $\dot{m} = 10$, $\epsilon_p = 0.5$) are used. The blue, orange and green curves correspond to the specified neutrino energies in the observer's frame $E_\nu = 100$ TeV, 1 PeV and 10 PeV. For the FS and RS cases, the neutrino emissions are isotropic and $L_{k,j}$ is used in Eq. (4.26) instead of $L_{k,\rm iso}$. The relativistic jet is on-axis and located at $z = 1$.

observer's frame

$$E_\nu F_{E_\nu,i} \approx \frac{\epsilon_p L_{k,\rm iso}}{4\pi d_L^2 \mathcal{C}_p}\left(\frac{1}{8}f_{p\gamma-i} + \frac{1}{6}f_{pp-i}\right) f_{\pi,{\rm sup}-i} \times H(t_j - t_*) e^{-\frac{\varepsilon_p}{\varepsilon_{p,\rm max}}}|_{E_\nu \approx 0.05\varepsilon_p(1+z)^{-1}}, \tag{4.26}$$

where the label i=CS, IS, FS or RS represents the site of neutrino production, ϵ_p is the CR acceleration efficiency, $\mathcal{C}_p = \ln(\varepsilon_{p,\rm max}/\varepsilon_{p,\rm min})$ is the normalization parameter, $\varepsilon_{p,\rm min} \approx \Gamma_{\rm cj}\Gamma_{\rm rel-i} m_p c^2$ is the proton minimum energy in the cosmological comoving frame, $\varepsilon_{p,\rm max}$ is the maximum proton energy, and d_L is the luminosity distance between the source and the observer. In this paper, we assume efficient baryon loading rate $\epsilon_p = 0.5$. Noting that the maximum proton energy is constrained by the cooling energy

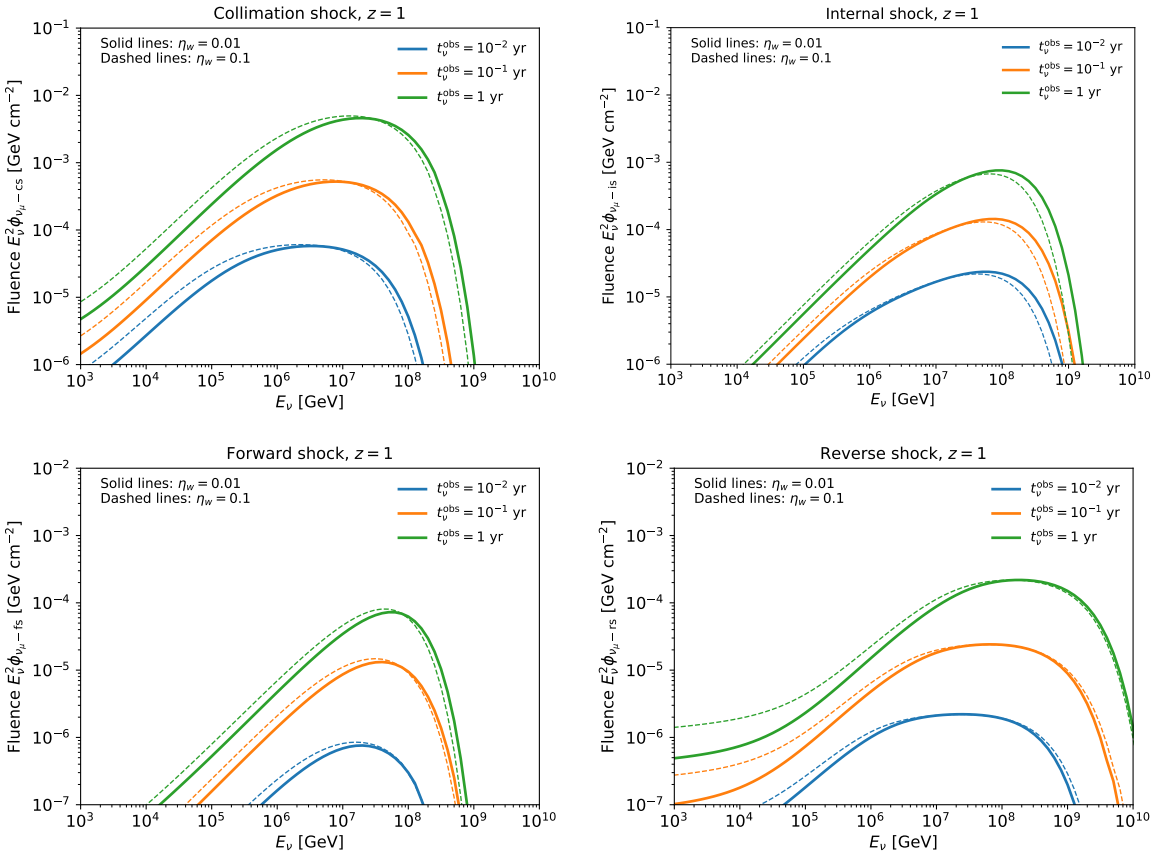

Figure 4.7. Observed muon neutrino fluences for the CS (up left), IS (up right), FS (bottom left) and RS (bottom right) scenarios at various observation times $t_\nu^{\rm obs} = 10^{-2}$ yr (blue lines), 10^{-1} yr (orange lines) and 1 yr (green lines) after the merger. The optimistic parameters (e.g., $\dot{m} = 10,\ \epsilon_p = 0.5$) are used to obtain these curves. The solid lines are obtained from fiducial parameters, e.g., $\eta_w = 0.01$, whereas $\eta_w = 0.1$ is used for the thin dashed lines as a reference. For the FS and RS cases, the neutrino emissions are isotropic and $L_{k,j}$ is used in Eq. (4.26) instead of $L_{k,\rm iso}$. The relativistic jet is on-axis and located at $z = 1$.

$\varepsilon_{p,c}$ and the maximum proton energy from acceleration $\varepsilon_{p,\rm acc}$ in the jet comoving frame, we conclude that $\varepsilon_{p,\rm max} \approx \Gamma_{cj} \min[\varepsilon_{p,c}, \varepsilon_{p,\rm acc}]$, where $\varepsilon_{p,c}$ is determined by the equation $t_{p,c}^{-1} + t_{i,\rm dyn}^{-1} = t_{p,\rm acc}^{-1}$. For the FS and RS cases, considering that these shocks are initially relativistic and then rapidly decrease to being sub-relativistic as the jet expands, we expect that the corresponding neutrino emissions are not beamed and we replace $L_{k,\rm iso}$ with $L_{k,j}$ in Eq. (4.26). In the following text, we show the neutrino light curves and spectra for each site by fixing the luminosity distance to be $d_L = 6.7$ Gpc ($z = 1$); (see section 4.4.2 for the reason of this choice). Fig. 4.6 shows the light curves for specified neutrino energies $E_\nu = 100$ TeV (blue lines), 1 PeV (orange lines) and 10 PeV (green lines). As for the forward shock and the reverse shock, no neutrinos are expected before

the onset time t_*. One common feature for all the four light curves is that the neutrino fluxes decreases monotonically in the later time, due to a decreasing $f_{p\gamma}$ resulting from a less denser photon environment.

For the convenience of the detectability discussion below, it is useful to calculate the observed cumulative muon neutrino fluence at a given time $t_\nu^{\rm obs}$ after the jet is launched by integrating the flux over time

$$E_\nu^2 \phi_{\nu_\mu - i}(t_\nu^{\rm obs}) = \int_0^{t_\nu^{\rm obs}/(1+z)} dt_j E_\nu F_{E_\nu, i}. \tag{4.27}$$

Cumulative muon neutrino fluences for various observation times $t_\nu^{\rm obs} = 10^{-2}$ yr, 10^{-1} yr and 1 yr for CS, IS, FS and RS scenarios in the optimistic case are shown in Fig. 4.7. From Fig. 4.7, we find that the neutrino flux from IS is subdominant comparing to that from CS. The main reason is that the comoving photon density at IS is much lower than the CS site, noting that $n_{\gamma,\rm cs} \propto \Gamma_{\rm cj}^{-2}$ whereas $n_{\gamma,\rm is} \propto \Gamma_j^{-2}$. The thin dashed lines in Fig. 4.7 depict the corresponding neutrino fluences for a denser circumnuclear material with $\eta_w = 0.1$. Comparing with the solid lines, we conclude that the neutrino emission does not sensitively depend on η_w and the results obtained from previous assumptions are not sensitive to the uncertainties of the outflow model. The neutrino fluences of the FS and RS scenarios are clearly lower than for the CS and IS cases since the neutrinos from the FS and RS are not beamed.

To calculate the observed flavor ratio, we write down the ratio of neutrino fluences of different flavors at the source $\nu_\mu : \nu_e : \nu_\tau \sim 1 : 2 : 0$. According to tri-bimaximal mixing, the observed neutrino fluences after long-distance oscillation is (e.g., Ref. [334])

$$\begin{aligned} \phi_{\nu_e} &= \frac{10}{18}\phi^0_{\nu_e} + \frac{4}{18}\left(\phi^0_{\nu_\mu} + \phi^0_{\nu_\tau}\right) \\ \phi_{\nu_\mu} &= \frac{4}{18}\phi^0_{\nu_e} + \frac{7}{18}\left(\phi^0_{\nu_\mu} + \phi^0_{\nu_\tau}\right) \end{aligned} \tag{4.28}$$

implying that the observed favor ratio is $\nu_\mu : \nu_e : \nu_\tau \sim 1 : 1 : 1$. We need to keep in mind that the flavor ratio may deviate from $1 : 1 : 1$ if the muon decay suppression factor becomes less than unity, e.g., $f_{\mu,\rm sup} < 1$.

Table 4.1. Detectability of jet-induced muon neutrino emissions by IceCube (IC) and IceCube-Gen2 (IC-Gen2)

Neutrino event number $\mathcal{N}_i$ ($t_\nu^{\rm obs} = 1$ yr) for an on-axis source at d_L =6.7 Gpc ($z = 1$)

	Optimistic parameters $\dot{m} = 10,\ L_{k,j} \simeq 3.4 \times 10^{46}$ erg s^{-1}, $\epsilon_p = 0.5,\ h = 0.3$			Conservative parameters $\dot{m} = 0.1,\ L_{k,j} \simeq 3.4 \times 10^{44}$ erg s^{-1}, $\epsilon_p = 0.5$, $h = 0.01$		
Scenario	IC (up+hor)	IC (down)	IC-Gen2 (up+hor)	IC (up+hor)	IC (down)	IC-Gen2 (up+hor)
CS	0.031	0.027	0.21	1.2×10^{-4}	9.5×10^{-5}	$7.6{\times}10^{-4}$
IS	1.3×10^{-3}	1.1×10^{-3}	7.0×10^{-3}	2.6×10^{-6}	2.3×10^{-6}	1.5×10^{-5}
FS	2.6×10^{-4}	2.1×10^{-4}	1.4×10^{-3}	8.1×10^{-6}	6.2×10^{-6}	4.1×10^{-5}
RS	8.8×10^{-4}	7.2×10^{-4}	4.7×10^{-3}	3.6×10^{-5}	2.7×10^{-5}	1.8×10^{-4}

Neutrino event number $\mathcal{N}_i$ ($t_\nu^{\rm obs} = 10$ yr) for an on-axis source at d_L =6.7 Gpc ($z = 1$)

	Optimistic parameters $\dot{m} = 10,\ L_{k,j} \simeq 3.4 \times 10^{46}$ erg s^{-1}, $\epsilon_p = 0.5,\ h = 0.3$			Conservative parameters $\dot{m} = 0.1,\ L_{k,j} \simeq 3.4 \times 10^{44}$ erg s^{-1}, $\epsilon_p = 0.5$, $h = 0.01$		
Scenario	IC (up+hor)	IC (down)	IC-Gen2 (up+hor)	IC (up+hor)	IC (down)	IC-Gen2 (up+hor)
CS	0.17	0.14	1.04	6.1×10^{-4}	4.7×10^{-4}	$3.2{\times}10^{-3}$
IS	6.9×10^{-3}	4.9×10^{-3}	2.6×10^{-3}	1.01×10^{-5}	8.9×10^{-6}	$6.1{\times}10^{-5}$
FS	1.1×10^{-3}	8.4×10^{-4}	5.1×10^{-3}	3.1×10^{-5}	2.4×10^{-5}	2.4×10^{-4}
RS	3.3×10^{-3}	2.9×10^{-3}	1.9×10^{-2}	1.4×10^{-4}	9.8×10^{-5}	8.1×10^{-4}

Neutrino detection rate $\dot{N}_{\nu,i}$ for SMBH mergers within the LISA detection range $z \lesssim 6$ [yr^{-1}]

	Optimistic parameters $\dot{m} = 10,\ L_{k,j} \simeq 3.4 \times 10^{46}$ erg s^{-1}, $\epsilon_p = 0.5,\ h = 0.3$			Conservative parameters $\dot{m} = 0.1,\ L_{k,j} \simeq 3.4 \times 10^{44}$ erg s^{-1}, $\epsilon_p = 0.5$, $h = 0.01$		
Scenario	IC (up+hor)	IC (down)	IC-Gen2 (up+hor)	IC (up+hor)	IC (down)	IC-Gen2 (up+hor)
IS	0.019	0.014	0.16	8.2×10^{-5}	4.3×10^{-5}	$3.7{\times}10^{-4}$
FS	2.6×10^{-3}	1.8×10^{-3}	0.013	9.6×10^{-5}	7.2×10^{-5}	4.1×10^{-4}
RS	0.011	$8.4{\times}10^{-3}$	0.044	3.5×10^{-4}	1.9×10^{-4}	2.1×10^{-3}

4.4.2 Detectability

Using the muon neutrino fluence $\phi_{\nu_\mu - i}$ at $t_\nu^{\rm obs}$ and the detector effective area $A_{\rm eff}(\delta, E_\nu)$, we estimate the observed muon neutrino event number to be

$$\mathcal{N}_i(t_\nu^{\rm obs}) = \int \phi_{\nu_\mu - i} A_{\rm eff}(\delta, E_\nu) dE_\nu, \tag{4.29}$$

where $A_{\rm eff}$ typically depends on the declination δ. For IceCube (IC), the effective areas for 79- and 86-string configurations are similar and we use the $A_{\rm eff}$ shown in Ref. [335] to calculate the 1-year event numbers of downgoing and upgoing+horizontal neutrinos. In the future, foreseeing a substantial expansion of the detector size, IceCube-Gen2 is expected to have a larger effective area [336]. Here we assume that the effective area of IceCube-Gen2 (IC-Gen2) is a factor of $10^{2/3}$ larger that that of IceCube. The threshold neutrino energies for IceCube and IceCube-Gen2 are fixed to be 0.1 TeV and 1 TeV respectively. In our case, we focus on the detectability of track events considering that the effective area for shower events is much smaller that that of track events. Note that we only consider the contribution of upgoing+horizontal neutrinos. KM3NeT, a network of deep underwater neutrino detectors that will be constructed in the Mediterranean Sea [337], will cover the southern sky and will further enhance the discovery potential of the jets produced by SMBH mergers as neutrino sources in the near future.

We calculate the expected one-year, e.g., $t_\nu^{\rm obs} = 1$ yr, neutrino detection numbers of the CS, IS, FS and RS scenarios for an on-axis merger event located at $z = 1$ (~ 6.7 Gpc) with the parameters used before, $\dot{m} = 10,\ \epsilon_p = 0.5,\ \eta_w = 10^{-2},\ \eta_j = 3,\ \epsilon_e = 0.1$, $\epsilon_B = 0.01$, $\Gamma_j = 10$ and $\Gamma_{cj} = \theta_j^{-1} = 3$. The results are summarized in the upper part of Table 4.2. Correspondingly, the middle panel of Table 4.2 shows the expected event numbers for IceCube and IceCube-Gen2 in the 10-year operation (e.g., $t_\nu^{\rm obs} = 10$ yr). One caveat is that the accretion rate as well as the jet luminosity $L_{k,j}$ might be optimistic for SMBH mergers. Hence, we show also the results for a conservative case with a sub-Eddington accretion rate $\dot{m} = 0.1$ and the same baryon loading factor $\epsilon_p = 0.5$, for the purposes of comparison. In this case, the other parameters are unchanged except for modifying the disk scale height to $h = 0.01$, which is consistent with thin disk models of low mass accretion rates. The event numbers in the upper and middle parts of Table 4.2 demonstrate that IceCube-Gen2 could detect $\gtrsim 1$ events from an on-axis source located at $z = 1$ in a 10-year operation period, whereas the detection is difficult for IceCube.

It is also useful to discuss the neutrino detection rate for all SMBH mergers within a certain comoving volume $\mathcal{V}(z_{\rm lim})$ at redshift $z_{\rm lim}$. Given the SMBH merger rate $\mathcal{R}(z)$,

the number of mergers per unit comoving volume per unit time, and assuming that all SMBH mergers are identical, we obtain the average neutrino detection rate per year from the i-th component [129, 338]

$$\dot{N}_{\nu,i}(< z_{\rm lim}) = \frac{c}{H_0} f_i(\theta_j) \Delta\Omega_{\rm sur} \times \int_0^{z_{\rm lim}} dz \frac{P_{m\geq 1}(\mathcal{N}_i|_{t_\nu^{\rm obs}=1\ {\rm yr}}) \mathcal{R}(z) d_L^2}{(1+z)^3 \sqrt{\Omega_m (1+z)^3 + \Omega_\Lambda}}, \tag{4.30}$$

where $f_i(\theta_j)$ is the probability of on-axis mergers and the solid angle is $\Delta_{\rm sur} \approx 2\pi$ for the upgoing+horizontal detections, and $P_{m\geq 1}(\mathcal{N}_i|_{t_\nu^{\rm obs}=1\ {\rm yr}}) = 1 - \exp(-\mathcal{N}_i|_{t_\nu^{\rm obs}=1\ {\rm yr}})$ is the probability that a sigle source at z produces nonzero neutrino events. For $i =$ CS and IS, the neutrino emission is beamed and we conclude that $f_i(\theta_j) = \theta_j^2/2$, whereas $f_i = 1$ corresponds to the isotropic FS and RS. Note that the critical redshift that satisfies $\frac{1}{2}\theta_j^2 \mathcal{R}(z)\mathcal{V}(z) \times 1\ {\rm yr} \sim 1$ is $z \sim 1$, within which one may expect one on-axis merger in one year. Simulations based on the history of dark matter halo mergers [339, 340] and the history of seed black hole growth [341] have predicted the redshift evolution of SMBH merger rate, and we use the results of Ref. [341] for $\mathcal{R}(z)$.

It has been expected that LISA can detect SMBHs up to high redshifts (see, e.g., Ref. [342] and references therein). SMBH binary coalescences at high redshifts ($z \gtrsim 2-3$) dominate the total event rate, whereas approximately 10% of the event rate may come from the mergers at redshifts with $z \lesssim 1$ [339, 342–344]. The cumulative LISA event rate is expected to be $\sim 10\ {\rm yr}^{-1}$ [342]. But the number is subjected to large uncertainties coming from binary formation models. For example, Ref. [344] gives $\sim 1\ {\rm yr}^{-1}$ for $M_{\rm BH} \sim 10^6\ M_\odot$. We are interested in the neutrino detection rate from SMBH mergers detected by LISA, i.e., GW+neutrino detection rate. Combining Eqs. (4.29) and (4.30), we present the neutrino detection rates for SMBH mergers by setting $z_{\rm lim} = 6$ (given that LISA can detect such high-redshift SMBH mergers) in the lower part of Table 4.2. From the neutrino detection rates and event numbers presented in Table 4.2, we find that it may be challenging for IceCube-Gen2 to detect neutrinos from LISA-detected SMBH mergers with conservative parameters ($\dot{m} = 0.1$). On the other hand, if the LISA-detected binary SMBH systems are super-Eddington accreters (e.g., $\dot{m} = 10$) before and after the merger, the resulting neutrino emission from the jet-induced shocks may be detected by IceCube-Gen2 within a decade. Note that the atmospheric neutrino background would be negligibly small even for a time window of $t_\nu^{\rm obs} \sim 1$ yr because the neutrino energy is expected to be very high.

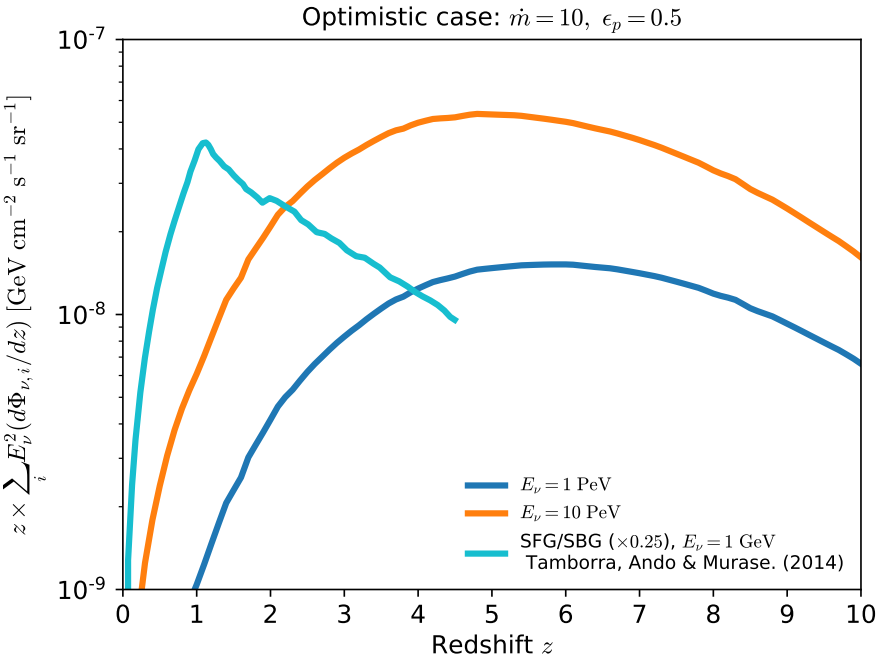

Figure 4.8. Differential contributions to the diffuse neutrino intensity $z \times \sum_i E_\nu^2 (d\Phi_{\nu,i}/dz)$ for the optimistic case at E_ν =1 PeV (blue line) and 10 PeV (orange line). The cyan line depicts the contributions ($\times 0.25$) from starforming/starburst galaxies (SFG/SBG) [140] at E_ν =1 GeV.

4.4.3 Cumulative Neutrino Background

It is useful to evaluate the contribution of SMBH mergers to the diffuse neutrino background and to check if this model can alleviate the tension between the diffuse neutrino and the gamma-ray backgrounds. In the scenario of jet induced neutrinos, the all-flavor diffuse neutrino flux from each site is calculated via [48]

$$\begin{aligned} E_\nu^2 \Phi_{\nu,i} =& \frac{c}{4\pi H_0} \int dz \int^{t_\nu} dt_j \frac{\mathcal{R}(z)}{(1+z)^2 \sqrt{\Omega_m (1+z)^3 + \Omega_\Lambda}} \\ & \times \left(\frac{3}{8} f_{p\gamma - i} + \frac{1}{2} f_{pp-i} \right) f_{\pi,\mathrm{sup}-i} \frac{\theta_j^2 \epsilon_p L_{k,\mathrm{iso}}}{2\mathcal{C}_p} \\ & \times H(t_j - t_*) e^{-\frac{\varepsilon_p}{\varepsilon_{p,\max}}}, \end{aligned} \tag{4.31}$$

where the summation takes all neutrino production sites into account. From the light curves in Fig. 4.6, we find that the neutrino emissions can last as long as one hundred years. To calculate the contribution to the diffuse neutrino background, we treat these jets as long-duration neutrino sources and take the rest-frame jet time to be 100 yr in

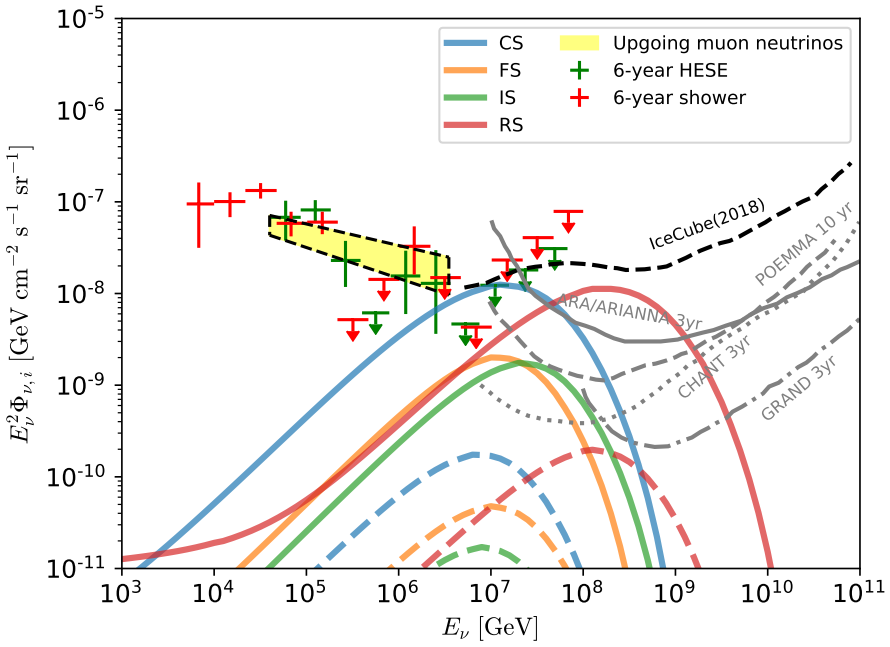

Figure 4.9. Redshift-integrated all-flavor diffuse neutrino flux expected from relativistic jets in SMBH mergers. The CS, IS, FS and RS components are illustrated as blue, orange, green and red lines. The solid and dashed lines respectively correspond to the optimistic ($\dot{m} = 10,\ \epsilon_p = 0.5$) and conservative ($\dot{m} = 0.1,\ \epsilon_p = 0.5$) cases. The fiducial value $\eta_w = 0.01$ is adopted for both cases. Parameters for these two cases are listed in table 4.2. For each case, we use $t_\nu = 100$ yr as the rest-frame duration of the neutrino emission in the jets. The 90% C.L. Sensitivities of current (black-dashed; IceCube [345]) and some future ultrahigh-energy neutrino detectors (gray lines; ARA/ARIANNA, POEMMA, CHANT, GRAND) are also shown.

the integral. The Fig. 4.8 illustrates the differential contributions to the diffuse neutrino intensity, $z \times \sum_i E_\nu^2 (d\Phi_{\nu,i}/dz)$, for the optimistic parameters at $E_\nu = 1$ PeV (blue line) and 10 PeV (orange lines). The fiducial parameter $\eta_w = 0.01$ is used to obtain these curves. For the purpose of comparison, we also show in cyan the contribution ($\times 0.25$) to $E_\nu = 1$GeV neutrino background from starforming/starburst galaxies (SBG/SFG) [140]. Using the redshift evolution of SMBH merger rate $\mathcal{R}(z)$ provided by Ref. [341], we show the diffuse neutrino fluxes from each shock site for optimistic and conservative cases in Fig. 4.9. In this figure, the yellow area, green and red data points corresponds to the diffuse neutrino fluxes deduced from upgoing muon neutrinos, six-year high-energy start events (HESE) analysis and six-year shower analysis Ref. [26, 188, 290, 346], respectively.

The results obtained from Eq. (4.31) is consistent with the analytical estimation [48]

$$
\begin{aligned}
E_\nu^2 \Phi_\nu &\sim \frac{c}{4\pi H_0} \frac{3}{8} f_{p\gamma} f_{\pi,\mathrm{sup}} \xi_z \mathcal{R}|_{z=0} t_\nu \mathcal{C}_p^{-1} \epsilon_p L_{k,j} \\
&\sim 10^{-8}\ \mathrm{GeV\ cm^{-2}\ s^{-1}\ sr^{-1}} \\
&\times (\epsilon_p \dot{m}/5) f_{p\gamma} \left(\frac{\xi_z}{12}\right) \left(\frac{t_{\nu,\mathrm{eff}} \mathcal{R}|_{z=0}}{0.11 \mathrm{Gpc^{-3}}}\right),
\end{aligned}
\tag{4.32}
$$

where $f_{p\gamma}$ is close to unity at $E_\nu \sim 10$PeV in the effective duration $t_{\nu,\mathrm{eff}} = 10$ yr, $\mathcal{C}_p \simeq 15 - 20$ depends on the jet time and ξ_z is the redshift evolution parameter (see e.g., Ref. [347]). Here, the analytical estimation is energy-dependent, since at different E_ν, the effective neutrino emission time $t_{\nu,\mathrm{eff}}$, during which $f_{p\gamma}$ remains close to unity, strongly depends on the neutrino energy according to the light curves in Fig. 4.6. From this figure we find that the CS and RS contribute to the diffuse neutrino flux roughly in the same level. The main reason is that these sites can continuously produce very high-energy neutrinos in a longer duration, e.g., ~ 10 yr (see the green curves in Fig. 4.6). Moreover, since the dynamic time of the reverse shock $t_{\mathrm{rs,dyn}} \approx R_h/(\beta_h c)$ is longer than that of the collimation shock, $t_{\mathrm{cs,dyn}} \approx R_{\mathrm{cs}}/(\Gamma_{\mathrm{cj}} c)$, the reverse shock scenario predicts higher-energy neutrinos (in the EeV range).

One simplification in Eq. (4.31) is that all sources have the same physical conditions and share the same set of parameters throughout the universe. However, in reality, the situation is more complicated. Nevertheless, one can infer that the jet-induced neutrino emissions from SMBH mergers could significantly contribute to the diffuse neutrino flux in the very high-energy range, i.e., $E_\nu \gtrsim 1$ PeV, if the optimistic parameters are applied.

Since SMBH mergers are promising emitters of ultrahigh-energy neutrinos, these sources will become important candidates for future neutrino detectors, such as the giant radio array for neutrino detection (GRAND [348]), Cherenkov from astrophysical neutrinos telescope (CHANT [349]), Probe Of Extreme Multi-Messenger Astrophysics (POEMMA [350]), Askaryan Radio Array (ARA [351]) and Antarctic Ross Ice Shelf Antenna Neutrino Array (ARIANNA [352]). An absence of detection can in return constrain the jet luminosity/accretion rate and the source distribution. Typically, the source density and jet luminosity are constrained by the nondetection of multiplet sources [129, 353, 354]. However, such multiplet constraint is very stringent in the energy range $E_\nu \sim 30 - 100$ TeV (see e.g., Ref. [129]) and becomes very weak for $E_\nu \gtrsim 10$ PeV. In this work, the neutrino emission concentrates in the ultrahigh-energy band, e.g., 10 PeV - 1 EeV, implying that the our model can avoid the multiplet constraint.

From the previous sections we find that the neutrino fluxes produced through the pp process are negligible compared to that from $p\gamma$ interactions, implying a low contribution to the gamma-ray background in the GeV-TeV range covered by the *Fermi* large Area Telescope (LAT). Most importantly, $p\gamma$ interactions in our model mainly produce very high-energy neutrinos of energies greater than 100 TeV. The accompanied very high-energy gamma rays can avoid the constraint from *Fermi* LAT, since the gamma-ray constraint is stringent for neutrinos in the range 10-100 TeV if the source is dominated by $p\gamma$ interactions [296]. On the other hand, according to the redshift evolution of the SMBH merger rate and the differential contributions to the diffuse neutrino intensity shown in Fig. 4.8, the sources located at high redshifts $z \sim 4-6$ contribute a significant fraction of the cumulative neutrino background, and the sources are fast evolving objects with a redshift evolution parameter $\xi_z \sim 12$. In this case the very high-energy gamma rays produced through π^0 decay can be sufficiently attenuated through $\gamma\gamma$ interactions with the extragalactic background light (EBL) and the cosmic microwave background (CMB; see, e.g., Ref. [355] for the optical depth). Hence, this model can significantly contribute to the very high-energy ($\gtrsim 1$ PeV) diffuse neutrino background without violating the gamma-ray background observed by *Fermi* LAT (cf. Figs. 5 and 6 of Ref. [202]).

4.5 Summary and Discussion

In this work, we studied jet-induced neutrino emission from SMBH mergers under the assumption that the jet is launched after the merger and it subsequently propagates inside the premerger circumnuclear region formed by the disk wind which precedes the merger. We showed that with optimistic but plausible parameters, the overall neutrino emission from four different shock sites, CS, IS, FS and RS, can be detected by IceCube-Gen2 within ten years of operation. If the accretion rate of the newborn SMBHs are sub-Eddington, e.g., $\dot{m} = 0.1$, it may be challenging to detect neutrinos even with IceCube-Gen2 because of the low SMBH merger rate in the local Universe. On the other hand, the expected rapid redshift evolution rate of SMBH mergers implies that they could be promising sources that contribute to the diffuse neutrino background. In the previous section, we found that even using the conservative parameters the SMBH merger scenario can significantly contribute to the diffuse neutrino background flux in the 1-100 PeV range. Importantly our model mainly produces very high-energy neutrinos of $E_\nu \gtrsim 1$ PeV via $p\gamma$ interactions, making it possible to simultaneously avoid the gamma-ray constraints.

As noted before, one crucial parameter of the model is the mass accretion rate

$\dot{M}_{\rm BH} = \dot{m}\dot{M}_{\rm Edd}$ since it determines the jet luminosity $L_{k,j}$. Many simulations have shown that the ratio of the mass loss rate by the wind and the accretion rate, $\eta_w = \dot{M}_w/\dot{M}_{\rm BH}$, strongly depends on the accretion rate, which implies that the density of the circumnuclear material is also sensitive to the accretion rate. In reality, the mass accretion rates before and after the merger may range from extreme sub-Eddington cases (e.g., $\dot{m} \sim 10^{-4}$) to extreme super-Eddington cases ($\dot{m} \sim 100$), depending on the model of accretion disks. We adopted the moderately super- and sub-Eddington accretion rates as fiducial values. With such assumptions, the ratio $\eta_w \sim 10^{-2}$ used in our calculation is justified by the global three-dimensional radiation MHD simulations [320–323]. Our results show that with the reasonably optimistic parameters, $\dot{m} = 10$ and $\epsilon_p = 0.5$, it is possible for IceCube-Gen2 to see neutrinos from SMBH mergers within the operation of approximately ten years if the jet opening angle $\theta_j \sim 0.3$ is comparable with that of AGN.

Noting that a SMBH coalescence will produce strong GWs that will be detected by LISA, we discussed the expected coincident detection rates of both neutrinos and GWs. From the bottom part of Table 4.2, we found that it would be possible for LISA and IceCube-Gen2 to make a coincident detection of SMBH mergers within the observation of five to ten years in the optimistic case. One advantage of this model is that we can use the GW detection as the alert of the post-merger neutrino emission. The time lag between the GW burst and the prompt neutrino emission is approximately $\sim 10^{-3} - 10^{-2}$ yr (hours to days, similar as $t_{\rm m}$ and/or $t_{\rm vis}$ in Sec. refchapter4phys-condition), depending on the properties of the circumbinary disk. Since currently there does not exist an accurate function to describe the redshift and mass dependence of SMBH merger rate, the single-mass approximation adopted here will unavoidably leads to uncertainties in equation 4.30. In the future, the GW detections of SMBH mergers will shed more light on our understanding toward such systems and then our model can provide more accurate predictions on the GW+neutrino coincident detection rate.

The relativistic jets of SMBH mergers can also produce detectable electromagnetic emission, analogous to that of GRB afterglows. High-energy electrons that are accelerated in the relativistic shocks caused by the jets will produce high-energy photon emission through synchrotron radiation and inverse-Compton scattering. The recent detection of the IceCube-170922A neutrino coincident with the flaring blazar TXS 0506+056 shows that EM+neutrino multi-messenger analyses are coming on stage and will play an increasingly important role in the future astronomy. It has been argued that the outburst signature of TXS 0506+056 could be caused by a “binary" of two host galaxies and/or their SMBHs [356, 357] (in which periodic neutrino emission can be expected by the jet

precession [358]), although the radio signatures may also be explained by structured jets [359]. In a continuation of this work, we will explore the electromagnetic signatures of the relativistic jets of SMBH mergers, which together with the results presented paper will provide more complete insights into the multi-messenger study of SMBH mergers.

Acknowledgments

We would like to thank Julia Becker Tjus, Ali Kheirandish and B. Theodore Zhang for fruitful discussions and comments. The work of K.M. is supported by the Alfred P. Sloan Foundation, NSF Grant No. AST-1908689, and KAKENHI No. 20H01901. The work of S.S.K is supported by JSPS Research Fellowship and KAKENHI No. 19J00198. C.C.Y. and P.M. acknowledge support from the Eberly Foundation.

Disclaimer

The findings and conclusions do not necessarily reflect the view of the funding agencies.

4.6 Appendix 1: Uncollimated Jets with Accurate ξ_w

In the previous treatment, we suggested that the jet could be collimated in $\sim 10^{-3}$ yr after the jet is launch if the parameters $\eta_w = 0.01, \eta_j = 3$, $\theta_j = 0.33$ and $\dot{m} = 10$ are used [268], where η_w is the fraction of the total mass accretion rate that goes into the winds, η_j represents the efficiency with which the accretion system converts accretion energy into jet energy, $\dot{m}$ is defined as the ratio of the accretion rate to the SMBH formed after the merger and the Eddington value and θ_j is the jet opening angle. We noticed that the definition of the average wind density over the cocoon volume, $\hat{\varrho}_w$, in Ref. [268] was not accurate, and the previous treatment to the jet collimation condition was not consistent with the modifications to the jet head radius R_h and the position of collimation shocks $R_{\rm cs}$ by numerical simulations (e.g., Ref. [360]). In this work, we will correct these two issues and discuss the impacts on results. We find that a denser wind density (for example $\eta_w \gtrsim 0.5$) is required to collimate the jet if these two errors mentioned above are fixed. Using the previous parameters, $\eta_w \sim 0.01$, $\eta_j \sim 1$, $\dot{m} = 10$ and $\theta_j = 0.33$, the jet is uncollimated and we do not expect the neurino emission from the collimation shock region. The conclusions in Ref. [268] does not change since the results the internal shock

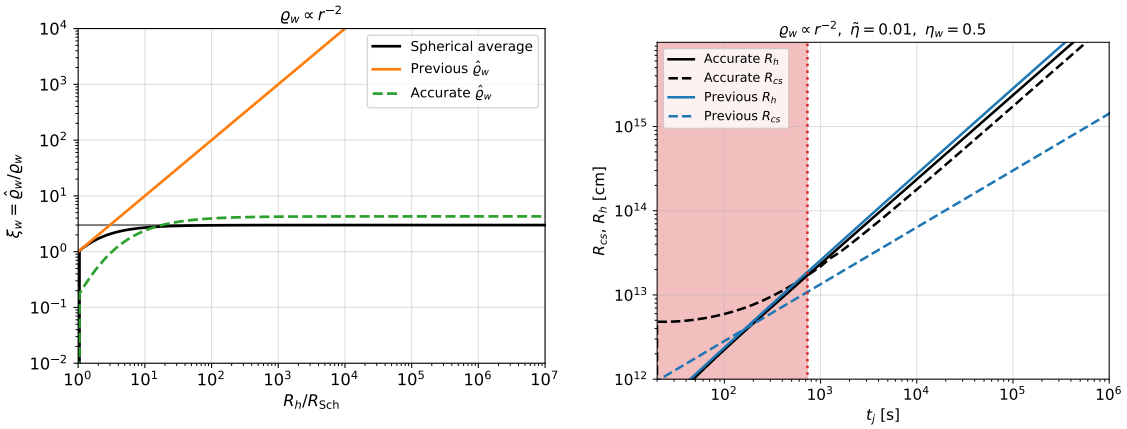

Figure 4.10. Left panel: ξ_w v.s. $R_h/R_{\rm Sch}$ calculated with the spherical approximation (type I, black solid line), the linear approximation (type II, yellow line) and the accurate approach (type III, dashed green line). **Right panel:** Comparison of the accurate $R_{\rm cs}$, R_h (black lines) with previous ones (blue lines).

would dominate the neutrino production in the corrected version. In this paper, we use the conventional notation $Q_x = Q/10^x$, unless otherwise specified.

4.6.1 Average Wind Density $\hat{\varrho}_w$

Assuming a jet propagating in the gaseous environment formed by the pre-merger disk winds, we expect the density distribution of the wind bubble to be

$$\varrho_w(R) = \frac{\eta_w(1+\chi)\dot{M}_{\rm BH}}{4\pi R^2 v_d} \equiv Dr^{-2},\ R > R_{\rm Sch} \tag{4.33}$$

where $R_{\rm Sch} = 2GM_{\rm BH}/c^2$ is the Schwarzschild radius, $\chi \sim 1$ takes into account the contribution of mini-disks and $v_d \simeq 0.1c$ is the velocity of disk winds. Explicitly, we have $D \simeq 3.8\times10^{14}$ g cm$^{-3}\eta'_w\dot{m}_1 M_{\rm BH,6}\beta_{d,-1}^{-1}$, where $\eta'_w \equiv (1+\chi)\eta_w \sim 1$ and $\beta_{d,-1} \equiv v_d/(0.1c)$.

One crucial parameter that determines jet geometry is

$$\xi_w = \frac{1}{\varrho_w V_c}\int \varrho_w dV_c, \tag{4.34}$$

where the integration is carried out over the cocoon volume V_c. Generally, the quantity ξ_w depends on the position of jet head R_h as well as the shape of the cocoon. Here we describe three types of the approximation to ξ_w.

I. Spherical approximation with $dV_c = 4\pi R^2 dR$, which leads to $\xi_w = 3R_h^2(R_h - R_{\rm Sch})/(R_h^3 - R_{\rm Sch}^3)$. Asymptotically at $R_h \gg R_{\rm Sch}$, we have $\xi_w = 3$ (e.g., Refs.

[360, 361]).

II. Linear approximation (used in Ref. [268]) with $dV_c \propto dR$, which yields $\xi_w = R_h/R_{\rm Sch}$.

III. Accurate approach with $\xi_w = \int \varrho_w dV_c = \int\int 2\pi r_c \varrho_w dr_c dR$, where πr_c^2 is the cross section of the cocoon at the radius R along the jet axis. In this case, the integrand in Eq. 4.34 can be rewritten as $\varrho_w = D/(R^2 + r_c^2)$.

The left panel in Fig. 4.10 illustrates how ξ_h depends on $R_h/R_{\rm Sch}$ in these three cases. The accurate ξ_w (dashed green line) is numerically estimated in the collimated jet regime with the cocoon boundary $r_c = \tilde{L}^{1/2}\theta_j R$. In this expression, $\tilde{L}$ is defined as the ratio of the energy density of the jet and the rest-mass energy density of ambient medium (see, e.g., Ref. [361]). We find that the spherical approximation is close to the accurate case, whereas the linear approximation used in our previous estimation overestimates ξ_w, making the jets considered in Ref. [268] easier to be collimated. In the following literature, we use the accurate ξ_w to calculate R_h and $R_{\rm cs}$.

4.6.2 Jet Collimation Condition

After the coalescence, a jet with kinetic luminosity

$$\begin{aligned} L_{k,j} &= \eta_j(1-\eta_w)\dot{M}_{\rm BH}c^2 \\ &\simeq 1.1\times10^{46}\ {\rm erg\ s^{-1}}\eta_j(1-\eta_w)\dot{m}_1 M_{\rm BH,6}, \end{aligned} \tag{4.35}$$

will be launched and subsequently propagate in the wind bubble formed before merger. In the collimated regime, the positions of jet head and collimation shock can be written respectively as,

$$R_h = \left(\frac{16}{3\pi}\frac{\tilde{\eta}\xi_w\xi_h^4}{\xi_c^2}\right)^{1/5} t_j^{3/5} L_{k,j}^{1/5}\varrho_w^{-1/5}\theta_j^{-4/5}, \tag{4.36}$$

and

$$R_{\rm cs} = \left(\frac{6}{\pi^{3/2}}\frac{\xi_h\xi_c^2}{\tilde{\eta}\xi_w}\right)^{1/5} t_j^{2/5} L_{k,j}^{3/10} c^{-1/2}\varrho_w^{-3/10}\theta_j^{-1/5}, \tag{4.37}$$

where $\xi_a = \xi_c = 1$ for the wind density distribution and $\tilde{\eta} = 0.01$ is introduced to ensure that the analytical formulae are consistent with numerical simulations. In Ref. [268], $\tilde{\eta} = 0.01$ was missed when discussing jet collimation. R_h and $R_{\rm cs}$ can be obtained by combining equations 4.34, 4.36 and 4.37. We find that a denser wind density with $\eta_w \sim 0.5$ and a less efficient jet parameter $\eta_j = 1.0$ are required to collimate the jet with

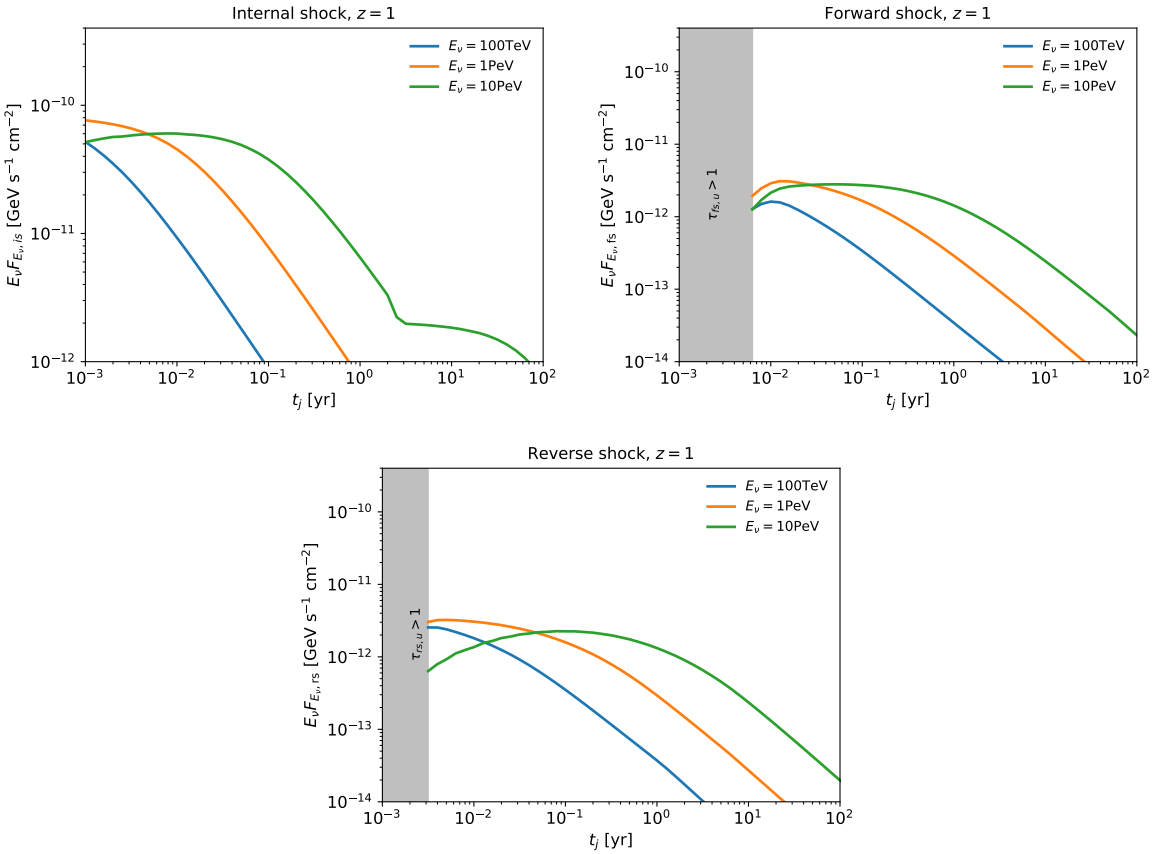

Figure 4.11. Time evolution of neutrino fluxes from the IS, FS and RS regions with the corrected $R_{\rm cs}$ and R_h. The jet is on-axis and located at $z = 1$. The parameters, $\eta_w = 0.5$, $\theta_j = 0.33$, $\dot{m} = 10$ and $\eta_j = 1.0$, are assumed.

$\tilde{\eta} = 0.01$ and the corrected ξ_w. The right panel of Fig. 4.10 shows the time dependence of R_h (blue lines) and $R_{\rm cs}$ for the accurate ξ_w and the previous one used in Ref. [268]. In both cases, $\tilde{\eta} = 0.01$ is applied. In the red region, e.g., $t_j \lesssim 800$ s, the jet is uncollimated. After that the calculation of R_h and $R_{\rm cs}$ becomes self-consistent since jet collimation is assumed as a precondition. The blue solid and blud dashed lines correspond to R_h and $R_{\rm cs}$ obtained in the original paper.

4.6.3 Results

Figure 2 shows the neutrino light curves for the internal shock (IS), reverse shock (IS) and forward shock (FS) regions assuming an on-axis jet located at $z = 1$. We find that the corrected neutrino flux from each shock site in the collimated jet propagating in a denser wind bubble ($\eta'_w \sim 2$) does not change significantly comparing to the previous

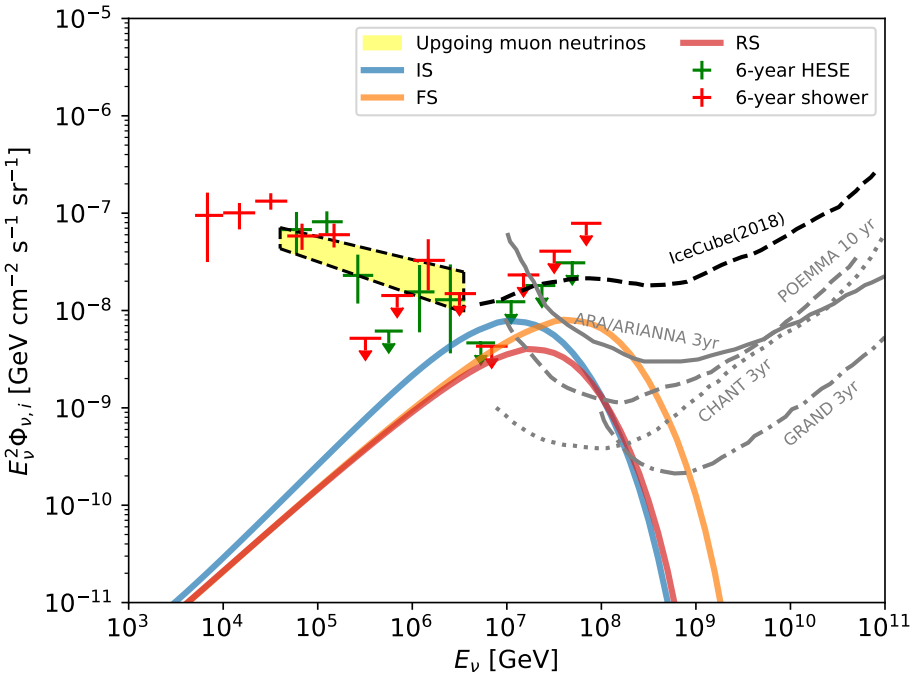

Figure 4.12. All-flavor diffuse neutrino flux obtained from the accurate ξ_w, $R_{\rm cs}$ and R_h. The CS, IS, FS and RS components are illustrated as blue, orange, green and red lines. The same parameters with Fig. 4.11 are used.

results. We still expect that in the optimistic case with a super-Eddington accretion rate $\dot{m} = 10$, IceCube-Gen2 could detect the LISA-detected mergers in a 10-year operation period. In addition, we estimated the contribution to the diffuse neutrino background from each shock site, which is shown in Fig. 3. The conclusion in Ref. [268] that SMBH mergers can explain a significant portion of the neutrino background in the energy range $1 - 10$ PeV is still valid if the binary SMBH systems are super-Eddington accreters before and after the merger.

One caveat is that after correcting the average wind density $\hat{\varrho}_w$ and introducing the parameter $\tilde{\eta} = 0.01$ to R_h and $R_{\rm cs}$, a denser wind bubble with $\eta_w' = (1+\chi)\eta_w = 1.0$ is required to guarantee the jet collimation. It is possible for super-Eddington accretors to produce powerful outflows in magnetically arrested disk (MAD) model [362]. However, these sources may not be universal in the whole population and it is likely only a small fraction of SMBH mergers can produce collimated jets. For the mergers that have a sub-Eddington accretion rate and a less efficient wind conversion rate $\eta_w \sim 10^{-3} - 10^{-1}$ [320–322], jet collimation would not be achievable and in this case the IS regions would dominate the neutrino production.

Table 4.2. Neutrino detection rate $\dot{N}_{\nu,i}$ for SMBH mergers within the LISA detection range $z \lesssim 6$ [yr^{-1}]

	Optimistic parameters $\dot{m} = 10,\ L_{k,j} \simeq 3.4 \times 10^{46}$ erg s^{-1}, $\epsilon_p = 0.5,\ h = 0.3$			Conservative parameters $\dot{m} = 0.1,\ L_{k,j} \simeq 3.4 \times 10^{44}$ erg s^{-1}, $\epsilon_p = 0.5$, $h = 0.01$		
Scenario	IC (up+hor)	IC (down)	IC-Gen2 (up+hor)	IC (up+hor)	IC (down)	IC-Gen2 (up+hor)
IS	0.019	0.014	0.13	8.2×10^{-4}	4.3×10^{-4}	$3.7{\times}10^{-3}$
FS	0.011	$8.4{\times}10^{-3}$	0.044	9.6×10^{-5}	7.2×10^{-5}	4.1×10^{-4}
RS	4.6×10^{-3}	2.8×10^{-3}	0.028	3.5×10^{-5}	2.9×10^{-5}	2.1×10^{-4}

Chapter 5
Post-Merger Jets from SMBH Coalescences as Electromagnetic Counterparts of GW Emission

Note: The material in this Chapter is based on my paper [363], with co-authors Kohta Murase, B. Theodore Zhang, Shigeo S. Kimura, and Peter Mészáros.

5.1 Introduction

Supermassive black hole (SMBH) mergers are ubiquitous in the history of the Universe [70, 71,364] and can produce powerful gravitational wave (GW) bursts when they coalesce [365, 366], making them promising candidates for GW detectors such as Laser Interferometer Space Antenna (LISA, [72,367]) and pulsar timing arrays (PAT, [368–370]) in single-source and/or stochastic GW background searches. The accretion activity between the binary system and the surrounding disk can produce multi-wavelength electromagnetic (EM) emission [74, 319, 371–374], and the time-variable EM signatures from the circumbinary disks could be detectable [375–377]. The spinning SMBH expected to form after the SMBHs have coalesced may also lead to relativistic jets, in which particle acceleration will take place. The resulting non-thermal emission from the accelerated electrons may provide a promising post-merger EM counterpart of the GW emission, and will not only provide complementary information on SMBH mergers but also shed light on the physical processes in these systems [378–380]. [381] recently suggested that the SMBH mergers can also be high-energy neutrino emitters, and demonstrated that they are also promising targets for high-energy multi-messenger astrophysics [273].

We study the EM emission produced in relativistic jets launched after the coalescence

of SMBHs. The physical picture is that the disk winds originating from the circumbinary disk and mini-disks around each SMBH form a pre-merger wind bubble, and jets powered by the Blandford-Znajek (BZ, [76]) mechanism are launched after the merger. The jets push ahead inside the pre-merger disk wind material, resulting in the formation of forward and reverse shocks. In the forward shock region, electrons are accelerated to high energies with a power-law distribution as observed in afterglows of gamma-ray bursts (GRBs) [77]. These particles then produce broadband non-thermal EM emission through synchrotron and synchrotron self-Compton (SSC) processes.

This letter is organized as follows. In Sec. 5.2, we introduce the physical conditions of the pre-merger wind bubble and model the propagation of jets. The radiation processes and the resulting photon spectra, light curves and detection horizons are presented in Sec. 5.3. In Sec. 5.4, we discuss implications of our results. Throughout the letter, we use the conventional notation $Q_x = Q/10^x$ and physical quantities are written in the centimeter-gram-second units, unless otherwise specified.

5.2 Jet Dynamics

We discuss here the physical conditions in a pre-merger circumbinary environment and derive relevant quantities that describe the jet propagation. We consider on-axis observers, which is sufficient for the purpose of this work. The emission region is typically expected to be only mildly relativistic on time scales of interest (the corresponding observation time after the jet launch is $T \sim 10^5 - 10^6$ s).

Numerical simulations have demonstrated that binary SMBH mergers can produce jet-like emissions driven by the Poynting outflow [372]. We assume that a jet is launched after the coalescence and subsequently propagates in the wind bubble formed by pre-merger disk winds. Fig. 5.1 schematically illustrates the configuration of the system. The disk wind expands in the gaseous environment of the host galaxy. We focus on emissions from the shock between the jet and the wind bubble. Initially, the circumbinary disk can react promptly to the evolution of the binary system. The ratio between the disk radius R_d and the semi-major axis of the binary system a remains unchanged ($R_d/a \sim 2$), until the inspiral time scale $t_{\rm GW}$ of the binary system [318] equals the viscosity time scale $t_{\rm vis}$ [316], which is known as the disk decoupling. After the disk becomes decoupled, the merger of SMBHs in binary system occurs within the time interval $t_m \sim 3 \times 10^{-2}$ yr $M_{\rm BH,6}\alpha_{-1}^{-8/5}h_{-1}^{-16/5}$, where $M_{\rm BH} = 10^6\ M_{\rm BH,6}M_\odot$ is the mass of the binary system, the dimensionless parameter h is defined as $h = H/R_d$, $\alpha \sim 0.1$ is the

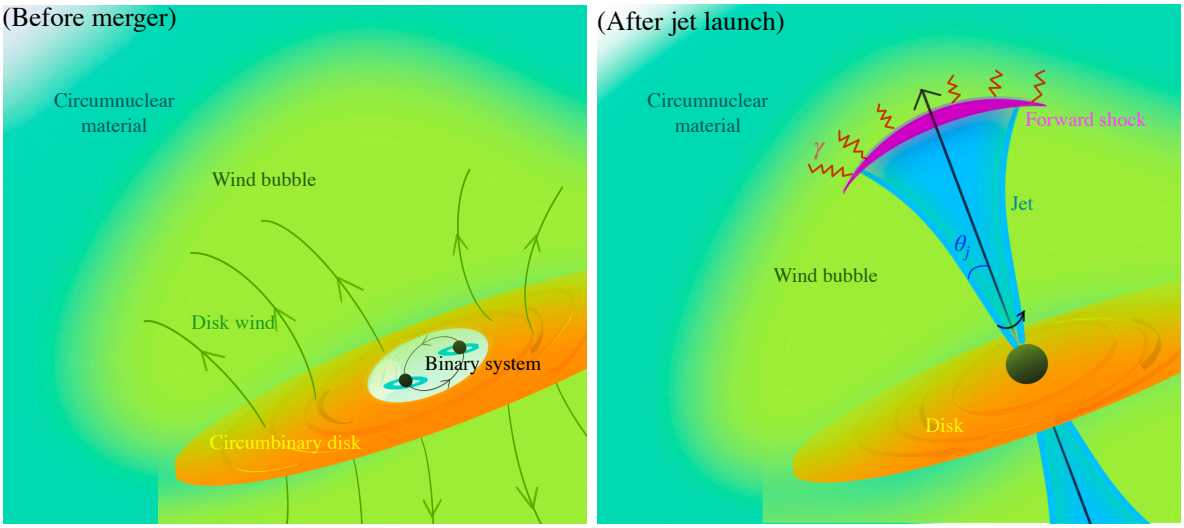

Figure 5.1. Schematic description of our model. **Left panel:** pre-merger disk winds launched from the circumbinary disk. The green arrows illustrate the disk-driven outflows that form a wind bubble. Mini-disks around each SMBH are also shown. **Right panel:** post-merger jets launched by a merged SMBH. The forward shock region is shown as the purple area. The cocoon is not depicted.

viscosity parameter, and H is the disk scale height. The disk gas starts to fill the cavity between the disk and the SMBHs in the viscosity timescale,

$$t_{\rm vis} \sim 0.1 \text{ yr } M_{\rm BH,6}\alpha_{-1}^{-8/5}h_{-1}^{-16/5} \tag{5.1}$$

after the coalescence [319]. This leads to a time delay ($t_{\rm delay} \sim t_{\rm vis}$) of days to months between the GW burst and the launch of post-merger jets, if $h \sim 0.1 - 0.3$ is assumed. However, for a thick and highly magnetized disk with $h \sim \alpha \sim 1$, $t_{\rm delay}$ could be much shorter.

On the other hand, within the duration of these two short-term processes, e.g., $t_{\rm m}$ and $t_{\rm vis}$, the disk wind radius may reach $v_d(t_{\rm vis} - t_m) \sim 10^{14} - 10^{16}$ cm above the disk, where v_d is the disk wind velocity that is of the order of the escape velocity, $v_{\rm esc}(R_{d,\rm dec}) \approx \sqrt{2GM_{\rm BH}/R_{d,\rm dec}}$ for the circumbinary disk, and $R_{d,\rm dec} \approx 1.2\times10^{13}$ cm $M_{\rm BH,6}\alpha_{-1}^{-2/5}h_{-1}^{-4/5}$ is the radius of the circumbinary disk at the decoupling. In reality, not only the circumbinary disk but also mini-disks around two SMBHs contribute, which would make the wind bubble more complicated. For simplicity, we assume the density profile of the winds at the decoupling to obtain the density distribution of the wind bubble at larger distances,

$$\varrho_w(r) = \frac{\eta_w(1+\chi)\dot{M}_{\rm BH}}{4\pi r^2 v_d} \equiv Dr^{-2}, \tag{5.2}$$

where $\dot{M}_{\rm BH}$ is the mass accretion rate onto the binary system, $\chi \sim 1$ is introduced to take into account the contribution of mini-disks, and η_w represents the fraction of accreted mass converted to the disk wind. According to the simulations, for SANE (Standard And Normal Evolution) models, the parameter η_w may vary from 10^{-4} to 10^{-1} [382–384] when the mass accretion rate changes from sub-Eddington to super-Eddington. In MAD (Magnetically Arrested Disk) models, η_w can reach 10^{-2} to 10^{-1} [385]. With $v_d \sim v_{\rm esc}(R_{d,\rm dec})$, we have $D \simeq 5.9 \times 10^{11}$ g cm^{-1} $\tilde{\eta}_{w,-1.5}(\dot{m}/0.5)M_{\rm BH,6}\beta_{d,-1}^{-1}$, where $\tilde{\eta}_w \equiv (1+\chi)\eta_w$, $\beta_{d,-1} \equiv v_d/(0.1c)$, the parameter $\dot{m}$ is defined as the ratio of $\dot{M}_{\rm BH}$, and the Eddington value $\dot{M}_{\rm Edd} \equiv 10L_{\rm Edd}/c^2$ (assuming a radiation efficiency of 0.1).

After the coalescence, a powerful jet driven by the spin energy of the newly formed SMBH can appear, subsequently propagating in the pre-merger wind bubble. Considering a sub-Eddington accretion rate with the MAD configuration, we estimate the jet kinetic luminosity to be

$$\begin{aligned} L_{k,j} &= \eta_j \dot{M}_{\rm BH} c^2 \\ &\simeq 6.3 \times 10^{44} \text{ erg s}^{-1} \eta_j (\dot{m}/0.5) M_{\rm BH,6}, \end{aligned} \tag{5.3}$$

where $\eta_j \sim 0.3 - 1$ is the ratio of the accretion energy converted to the jet energy [324].

Following the standard jet propagation theory [305, 306], we write down the dimensionless parameter that represents the ratio of the energy density of the jet and the rest-mass energy density of the surrounding medium

$$\tilde{L} \approx \frac{L_{k,\rm iso}}{4\pi r^2 \varrho_w c^3} \simeq 63\ \tilde{\eta}_{w,-1.5}^{-1} \eta_j \theta_{j,-0.5}^{-2} \beta_{d,-1}, \tag{5.4}$$

where θ_j is the jet opening angle, $L_{k,\rm iso} \approx 2L_{k,j}/\theta_j^2$ is the isotropic-equivalent luminosity. Since the quantity $\tilde{L}$ lies in the regime $\theta_j^{-4/3} \ll \tilde{L}$, we expect that the jet is "uncollimated" for our fiducial parameters[1]. This situation is similar to that in choked jet propagation in the circumstellar material [386, 387], and β_h is evaluated from $\tilde{L}$. In the relativistic limit, the jet head Lorentz factor is $\Gamma_h \approx \tilde{L}^{1/4}/\sqrt{2}$ [386], and we have $\Gamma_h \sim 2$ in our fiducial case with $\tilde{\eta}_w = 10^{-1.5}$. Note that the jet head radius is $R_h = c\beta_h \hat{T} \approx c\hat{T}$, and $\hat{T}$ is introduced to represent time measured in the central engine frame, which can be converted to the observation time T via $T = (1+z)(1-\beta_h)\hat{T}$ (that is $T \approx (1+z)\hat{T}/[2\Gamma_h^2]$ in the relativistic limit) for on-axis observers.

Furthermore, to ensure particle acceleration, we impose radiation constraints requiring

[1]However, jet collimation, which was assumed in Ref. [381], would be achievable for the super-Eddington accretion accompanied by disk winds with $\eta_w \sim 0.1 - 0.3$.

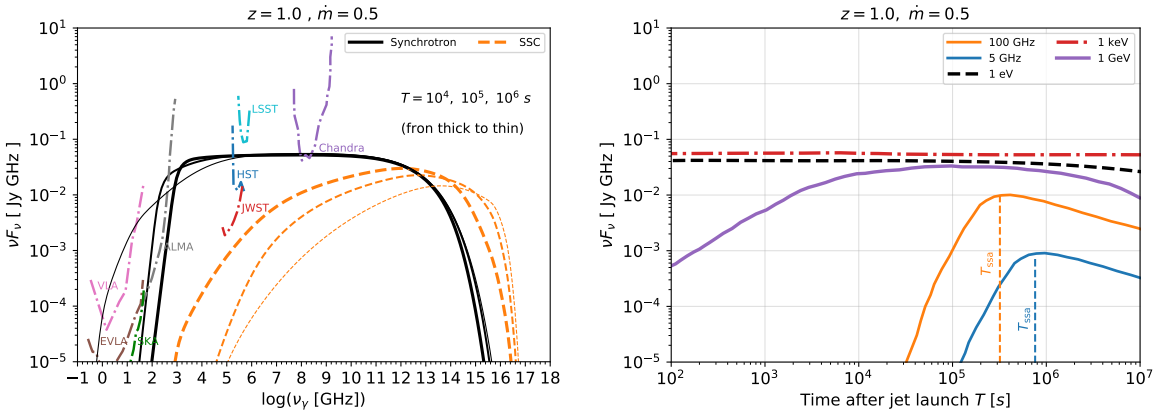

Figure 5.2. Left panel: Non-thermal energy spectra expected for uncollimated post-merger jets from a SMBH merger located at $z = 1$. The solid and dashed lines represent the synchrotron and SSC components. The dash-dotted lines show the sensitivity curves for current and future detectors. **Right panel:** Multi-wavelength light curves. The yellow and blue dashed vertical lines illustrate respectively the characteristic times, e.g., $T_{\rm ssa}$, of 100 GHz and 5 GHz emissions. The used parameters are $\dot{m} = 0.5$, $M_{\rm BH} = 10^6\ M_\odot$, $\tilde{\eta}_w = 10^{-1.5}$, $\eta_j = 1$, $\theta_j = 10^{-0.5}$, $s = 2.0$, $\zeta_e = 0.4$, $\epsilon_e = 0.1$ and $\epsilon_B = 0.01$.

that the shock is collisionless, without being mediated by radiation [386, 388]. Here, ignoring effects of pair production, we use the conservative condition, $\tau_T \approx \varrho_w \sigma_T R_h / m_p < 1$, where σ_T is the Thomson cross section. Numerically, this condition is satisfied at $\hat{T} \gtrsim 10$ s, which is much shorter than the duration of EM emission.

5.3 Electromagnetic Emission from Post-Merger jets

With the jet dynamics presented in the previous section, we calculate the EM spectra resulting from synchrotron and SSC emission. As in the standard theory of GRB afterglows [77], we assume that electrons are accelerated at the external forward shock with a power-law spectral index s. The energy fractions of the downstream energy density converted to non-thermal electron and magnetic field energy are defined as ϵ_e and ϵ_B, respectively. The upstream number density is given by $n_{h,u} \approx \varrho_w(R_h)/m_p \propto R_h^{-2}$, and $B \approx [\epsilon_B 32\pi\Gamma_h(\Gamma_h - 1)n_{h,u}m_p c^2]^{1/2}$ is the downstream magnetic field strength.

In the relativistic limit ($\Gamma_h \gg 1$), the characteristic injection frequency ν_m and the

cooling frequency ν_c in the observer frame are written respectively as,

$$\begin{aligned}\nu_m &\approx \frac{3\Gamma_h\gamma_m^2 eB}{4\pi(1+z)m_e c} \\ &\simeq 3.4\times10^3\ \mathrm{GHz}\ \epsilon_{e,-1}^2\zeta_{e,-0.4}^2\epsilon_{B,-2}^{1/2}\eta_j^{1/2}T_4^{-1} \\ &\quad\times(\dot{m}/0.5)^{1/2}M_{\rm BH,6}^{1/2}\theta_{j,-0.5}^{-1}\end{aligned} \tag{5.5}$$

and

$$\begin{aligned}\nu_c &\approx \frac{3\Gamma_h\gamma_c^2 eB}{4\pi(1+z)m_e c} \\ &\simeq 4.6\times10^2\ \mathrm{GHz}\ (1+z)^{-2}(1+Y)^{-2}\epsilon_{B,-2}^{-3/2} \\ &\quad\times\tilde{\eta}_{w,-1.5}^{-2}\theta_{j,-0.5}^{-1}(\dot{m}/0.5)^{-3/2}T_4\beta_{d,-1}^2 M_{\rm BH,6}^{-3/2},\end{aligned} \tag{5.6}$$

where $\gamma_m = \epsilon_e\zeta_e(\Gamma_h-1)m_p/m_e$ is the electron minimum Lorentz factor, and $\gamma_c = 6\pi m_e c/[(1+Y)T'\sigma_T B^2]$ is the cooling Lorentz factor. Here, $\zeta_e = g_s/f_e = 1/[f_e\ln(\gamma_M/\gamma_m)]\sim 0.3-0.4$ is constrained by the particle-in-cell simulations [212] (where f_e is the fraction of accelerated electrons and the maximum Lorentz factor of electrons is $\gamma_M = (6\pi e)^{1/2}/[\sigma_T B(1+Y)]^{1/2}$), Y is the Compton parameter, and $T' = \hat{T}/\Gamma_h \approx 2\Gamma_h T/(1+z)$ is the comoving time. For example, at $T = 10^4$ s, we have $Y\simeq 2.4$, corresponding to the fast cooling regime. It changes to the slow cooling regime on a time scale from days to weeks. We obtain the peak synchrotron flux [389]

$$\begin{aligned}F_{\nu,\rm syn}^{\rm max} &\approx \frac{(1+z)(0.6 f_e n_{h,u}R_h^3)\Gamma_h e^3 B}{\sqrt{3}m_e c^2 d_L^2} \\ &\simeq 0.24\ \mathrm{mJy}\ (1+z)g_{s,-1.2}\zeta_{e,-0.4}^{-1}(\dot{m}/0.5)^{3/2} \\ &\quad\times\eta_j^{1/2}\epsilon_{B,-2}^{1/2}\tilde{\eta}_{w,-1.5}\beta_{d,-1}^{-1}\theta_{j,-0.5}^{-1}M_{\rm BH,6}^{3/2}d_{L,28}^{-2}.\end{aligned} \tag{5.7}$$

The low-frequency synchrotron emission is subject to synchrotron self-absorption (SSA). The SSA optical depth is written as $\tau_{\rm ssa}(\nu) = \xi_s e n_{h,u}R_h(\nu/\nu_n)^{-p}/[B\gamma_n^5]$, where ν is the observed frequency, $\xi_s\sim 5-10$ depends on the electron spectral index, $\gamma_n = \min[\gamma_m,\ \gamma_c]$, $\nu_n = \gamma_n^2 eB/[(1+z)m_e c]$, $p = 5/3$ for $\nu<\nu_n$ and $p=(4+s)/2$ or $p=3$ for $\nu>\nu_n$ depending on the slow or fast cooling regime (e.g., Refs. [330, 390]). The critical time scales set by $\tau_{\rm ssa}=1$ for $\nu<\nu_n$ and for $\nu>\nu_n$ are $T_{\rm ssa}\simeq 5.4\times 10^5$ s $\xi_{s,1}^{3/10}(1+z)^{1/2}(1+Y)^{1/2}\epsilon_{B,-2}^{3/5}\left(\frac{\nu}{1\ \mathrm{GHz}}\right)^{-1/2}\tilde{\eta}_{w,-1.5}^{11/10}\beta_{d,-1}^{-11/10}(\dot{m}/0.5)^{9/10}M_{\rm BH,6}^{9/10}$ and $T_{\rm ssa}\simeq 3.5\times10^5$ s $\xi_{s,1}^{1/2}(1+z)^{-1/2}(1+Y)^{-1/2}M_{\rm BH,6}^{1/2}\left(\frac{\nu}{100\ \mathrm{GHz}}\right)^{-3/2}(\dot{m}/0.5)^{1/2}M_{\rm BH,6}^{1/2}\tilde{\eta}_{w,-1.5}^{1/2}\beta_{d,-1}^{-1/2}$, respectively. Thus, we expect that EM emission at 5 GHz and 100 GHz reaches a peak

about a few days after the jet launch ($T_{\rm ssa} \simeq 7.1\times10^5$ s and $T_{\rm ssa} \simeq 3.1\times10^5$ s, respectively, in our fiducial case with $\xi_s = 8.7$).

We numerically calculate the electron distribution and the resulting synchrotron and SSC spectra of the forward shock, following the method used in Refs. [233] and [391]. We solve the continuity equation that describes the evolution of the electron spectra and calculate the synchrotron/SSC components, in which the trans-relativistic regime can be consistently treated as in Refs. [391]. Combining the obtained radio, millimeter, optical and X-ray light curves with the sensitivities of corresponding detectors, we discuss the possibility of follow-up observations of the EM counterpart.

The left panel of Fig. 5.2 shows the snapshots of synchrotron and SSC spectra at $T = 10^4 - 10^6$ s for an on-axis source located at $z = 1$. We assume $s = 2.0$, $\epsilon_e = 0.1$, and $\epsilon_B = 0.01$. The solid and dashed lines correspond to the synchrotron and SSC components. Very high-energy gamma-ray emission at $\gtrsim 1$ TeV energies is suppressed due to the Klein-Nishina effect [233, 391], and the $\gamma\gamma$ annihilation with the extragalactic background light (EBL). For the EBL correction, $\gamma\gamma$ optical depth data from Model C in Ref. [184] is used. To show how the EM signal evolves with time, we illustrate the gamma-ray (1 GeV), X-ray (1 keV), UV (1 eV) and radio (5 GHz and 100 GHz) light curves in the right panel. In particular, before the characteristic time $T_{\rm ssa}$ (shown as the vertical yellow and blue lines). The radio emission is suppressed by the SSA process, which is implemented by multiplying $(1 - e^{-\tau_{\rm ssa}})/\tau_{\rm ssa}$.

It is useful to discuss the detection horizon $d_{\rm lim}$ for some detectors such as the Square Kilometre Array (SKA), Very Large Array (VLA), Expanded VLA (EVLA), Atacama Large Millimeter Array (ALMA), Hubble Space Telescope (HST), James Webb Space Telescope (JWST), Large Synoptic Survey Telescope (LSST) and the high-resolution camera on the Chandra X-ray Observatory (Chandra) [2] as functions of the observation time T. Given the observed flux $F_\nu(\nu_\gamma, T, z)$ at the observer time T from an on-axis source located at redshift z, the horizon can be calculated iteratively via

$$d_{\rm lim}(\nu_\gamma, T) = d_L \left(\frac{\frac{1}{\Delta T_{\rm exp}} \int_T^{T+\Delta T_{\rm exp}} F_\nu(\nu_\gamma, t, z) dt}{F_{\rm lim}(\nu_\gamma, \Delta T_{\rm exp})} \right)^{1/2}, \tag{5.8}$$

where $F_{\rm lim}(\nu_\gamma, \Delta T_{\rm exp})$ is the detector sensitivity normalized to the exposure time $\Delta T_{\rm exp}$.

[2] For information on these facilities see, e.g., : VLA (`http://www.vla.nrao.edu`), EVLA (`http://www.aoc.nrao.edu/evla/`), SKA (`https://www.skatelescope.org`), ALMA (`https://public.nrao.edu/telescopes/alma/`), HST (`https://www.nasa.gov/mission_pages/hubble/main/index.html`), JWST (`https://stsci.edu/jwst`), LSST (`https://www.lsst.org/scientists/scibook`) and Chandra (`https://cxc.cfa.harvard.edu/cdo/about_chandra/`)

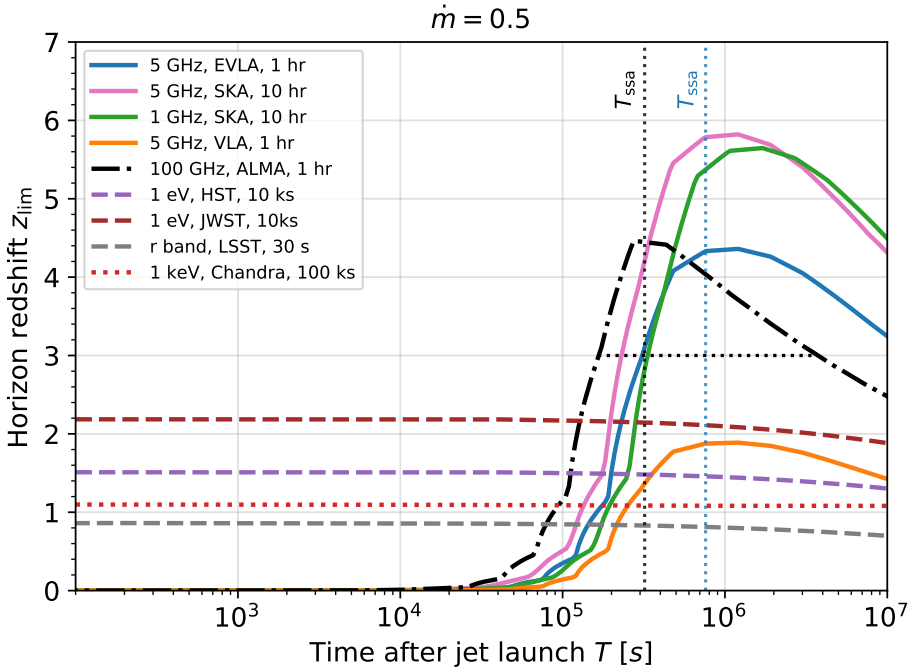

Figure 5.3. Detection horizons for multi-wavelength detectors, e.g., SKA, VLA, EVLA, ALMA, HST, JWST, LSST and Chandra. The horizontal dotted line shows the 100 GHz detection window for ALMA assuming a source located at $z = 3$. Similar to Fig. 5.2, the dotted vertical lines are the characteristic times of 5 GHz and 100 GHz signals.

For example, specifying the detection frequency $\nu = 100$ GHz, the sensitivity of ALMA is approximately 34 μJy for one-hour integration, e.g., $\Delta T_{\rm exp} = 1$ hour. Fig. 5.3 indicates the detection horizons for SKA (5 GHz, $\Delta T_{\rm exp} = 10$ hr), SKA (1 GHz[3], $\Delta T_{\rm exp} = 10$ hr), VLA (5 GHz, $\Delta T_{\rm exp} = 1$ hr), ALMA (100 GHz, $\Delta T_{\rm exp} = 1$ hr), JWST (1 eV, $\Delta T_{\rm exp} = 10$ ks), HST (1 eV, $\Delta T_{\rm exp} = 10$ ks), LSST (r-band, point source exposure time $\Delta T_{\rm exp} = 30$ s in the 3-day revisit time), and Chandra (1 keV, $\Delta T_{\rm exp} = 100$ ks). The vertical black and blue dotted lines respectively illustrate the times $T_{\rm ssa}$ at which photons at 100 GHz and 5 GHz bands start to survive from the synchrotron self-absorption.

From Fig. 5.3, we expect that ALMA, SKA and EVLA can detect SMBH mergers in the radio bands respectively out to redshifts of $z \sim 4 - 6$. Remarkably, the optical and X-ray signals from the mergers in the range $1 \lesssim z \lesssim 2$ can also be identified through targeted searches by Chandra, HST and JWST in a long duration after the merger. In addition, we can estimate the observation time for each detector if the luminosity distance of the merger is specified. For example, a source located at $z = 3$ would remain

[3]At 1 GHz, the SKA field-of-view can reach $\gtrsim$1 deg^2

detectable by ALMA for roughly 20-30 days (see the black dotted horizontal line). One caveat is that this calculation is carried out in the ideal case where the detectors can point to the position of the source and start the observation immediately after the EM signal reaches the Earth. We discuss the sky coverage and a detection strategy in the following Sec. 5.4.

5.4 Summary and Discussion

We investigated broadband non-thermal EM emission from electrons accelerated at the external forward shock expected in post-merger jets from the coalescence of SMBHs. In our model, the jets can be launched at $t_{\rm delay} \sim t_{\rm vis} \sim (0.003 - 0.1) M_{\rm BH,6}$ yr after the coalescence. The time lag is primarily determined by the scale height of the circumbinary disk and the viscosity parameter. We found that, for a moderate accretion rate ($\dot{m} \sim 0.5$), the multi-wavelength emission from such a system may persist at detectable levels for months after the jet launch, depending on the facilities and the luminosity distance. Moreover, according to our model, the sources with moderate $\dot{m} = 0.5$ can be detected up to $z \sim 5 - 6$, covering the range that LISA-like GW detectors have the best detection chance, e.g., $z \sim 1{-}2$, in which $(1{-}10) f_b$ mergers per year are expected [339,344,392–395]. Here $f_b \sim 1/(2\Gamma_h^2)$ is the beaming factor in our model. Because the jet head Lorentz factor is as low as $\Gamma_h \lesssim 2$, the EM emission from the forward shock region is not highly beamed and we expect $f_b \sim 0.1 - 1$. This makes the binary SMBH mergers interesting targets for future multi-messenger studies. If super-Eddington accretion (e.g., $\dot{m} \sim 10$) occurs, as was optimistically assumed in Ref. [381], even LSST and Chandra could detect EM signals from the sources in the redshift range $4 \lesssim z \lesssim 6$. We showed the case of $s = 2.0$ for the demonstration. If a larger spectral index, e.g., $s \sim 2.2 - 2.4$, is used, as expected from observations of GRB afterglows, the radio detection would be more promising whereas a higher accretion rate would be required for successful optical and X-ray observations.

The density of the premerger bubble, which was assumed to be a wind profile, is subject to large uncertainties. The extrapolation in the density distribution would be applicable up to an outer wind radius of $\sim 10^{14} - 10^{16}$ cm. The density predicted by equation 5.2 would drop below that of the central molecular zone (indicated as the circumnuclear environment in Fig.5.1), which may lead to the increase of radio emission. In addition, a cocoon formed along with the jet, depending on uncertain details of the medium, could produce thermal photons which may not only lead to detectable signals

but also serve as seed photons for inverse-Compton emission. We focused on the more secure EM emission from the forward shock region as the jet propagates in the wind. In this sense, our prediction for the fluxes are conservative.

EM emission from the external reverse shock and internal shocks can also be expected [396, 397]. Qualitatively, the ratio between the peak fluxes of the reverse and forward shock emission depends on the value of Γ_j, and the reverse shock contribution might be important for $\Gamma_j \gg \Gamma_h$.

Previous studies based on general relativistic three dimensional magnetohydrodynamics simulations have shown that the circumbinary disk and the corona can emit light in UV/EUV bands [374], while X-ray and infrared emission from the post-merger circumbinary disk are expected to last for years [74, 375]. In the pre-merger phase, the orbits of dual SMBH cores may be identified by radio facilities such as VLBI [398]. Blind searches could identify radio or UV/EUV sources from the binary SMBH systems, which would provide complementary constraints on the source location, the accretion rate and the ambient gaseous environment.

Our model can provide a guidance, including the onset times and the detection windows, in developing detection strategies for future EM follow-up observations, once GW signals are detected. Considering the large uncertainties in the localization with GW detectors, an initial follow-up using large field-of-view (FOV) telescopes, like SKA and LSST, would be necessary to more precisely localize the position of the source. After that, we can use the putative positional information from the initial follow-up imaging to guide the observation of narrower FOV telescopes. In particular, for high-redshift mergers in the range $z \sim 2-5$, EM follow-up observations rely more on radio detectors, and the detection is possible a few weeks after the merger. SKA needs the source localization before follow-up observations by VLA and ALMA. On the other hand, if the merger is close enough (e.g., $z \sim 1$), LISA observations staring from a few weeks before the merger can localize the merger with a median precision of $\sim$1 deg^2 [399]. In this case, LISA and LSST can jointly guide other X-ray and optical facilities in the very early stage. Amid these two regimes, e.g., $z \sim 1-2$, detections in the optical and X-ray bands using HST, JWST and Chandra would be promising if the source is localized by SKA.

Acknowledgements

C.C.Y. and P.M. acknowledge support from the Eberly Foundation. The work of K.M. is supported by NSF Grant No. AST-1908689, and KAKENHI No. 20H01901 and

No. 20H05852. B.T.Z. acknowledges the IGC fellowship. S.S.K. acknowledges the JSPS Research Fellowship, JSPS KAKENHI Grant No. 19J00198.

Disclaimer

The findings and conclusions do not necessarily reflect the view of the funding agencies.

Chapter 6
GeV Signatures of Short GRBs in Active Galactic Nuclei

Note: The material in this Chapter is based on my paper [400], with co-authors Kohta Murase, Dafne Guetta, Pe'er Asaf, Imre Bartos, and Peter Mészáros.

6.1 Introduction

As one of the most luminous and energetic phenomena in the universe, gamma-ray bursts (GRBs) have fueled a vibrant field of astrophysics research for several decades. Based on the duration of the bursts, the population can be divided into two subclasses, long GRBs and short GRBs, which are thought to arise from different progenitors. The general view is that short GRBs result from compact binary object (CBO) mergers [78–83], such as binary neutron star mergers and potentially NS-black hole mergers, whereas long GRBs are generated during the death of massive stars [84–89]. In 2017, the coincident detection of gravitational waves (GWs) and the corresponding electromagnetic counterpart from the binary neutron star merger GW170817, located in the host galaxy NGC 4933, marked a triumph of multi-messenger astronomy [90–92]. The spatial and temporal association between GW170817 and the gamma-ray burst GRB 170817A also consolidates the theory that CBO mergers are the origin of short GRBs. Extensive efforts have shown that the broadband emission is consistent with a relativistic jet viewed from an off-axis angle [92–102]. Moreover, Ref. [103] investigated the upscattered cocoon emission as the source of the γ-ray counterpart. The long-lasting high-energy signatures of the central engine left after the coalescence was studied in Ref. [104].

Alternatively, unlike in the case of GW170817, one can expect a sub-population of short GRBs which occur in the accretion disks of AGNs. Studies of the CBO formation and

evolution in AGN disks demonstrate that hierarchical mergers of embedded binary black hole systems are promising for reconstructing the parameters of LIGO/VIRGO detected mergers [105–108]. These mergers can harden the black hole mass distribution [109–112] as well. [113] pointed out that mergers involving neutron stars, such as GW190814 and GW190425, could also arise in AGN disks. Recent progress on the optical counterpart to GW190521 could support this [114], although the confirmation needs further observations [115]. Ref. [116] systematically studied the electromagnetic signatures of both long GRBs and short GRBs in AGN disks and discussed the conditions for shock breakout. Refs. [117] and [118] focused more on the neutrino production of embedded explosions. However, Ref. [119] showed that CBO environments are likely to be thin because of outflows that are common in super-Eddington accretion.

In this work, we study γ-ray emission from short GRBs that are embedded in AGN disks. Inside the accretion disk, the embedded objects can migrate towards a migration trap due to angular momentum exchange via the torques originated from the disk density perturbations. At the migration trap, the gas torque changes sign, and an equilibrium is achieved as the outwardly migrating objects meet inwardly migrating objects. Numerical calculations show that compact binaries are typically formed near the migration trap at distances around $R_d \sim 20 - 300 R_{\rm S}$ to the central supermassive black hole (SMBH, [121]), where $R_S = 2GM_\star/c^2$ is the Schwarzschild radius. Employing one-dimensional N-body simulations, Ref. [111] obtained a more distant location for typical mergers at $\sim 10^{-2}$–10^{-1} pc ($\sim 10^3 - 10^4 R_{\rm S}$ for a SMBH with mass $M_\star = 10^8 M_\odot$). We concentrate on the embedded GRBs with distances $R_d \sim 10 - 10^3 R_{\rm S}$. We will show that AGN disks would not influence the γ-ray emission if the CBO mergers happen further outside in the disk. We also note that $R_d = 10 R_{\rm S}$ is an extreme case where the population is stringently limited. The outflows from the binary systems with super-Eddington accretion rates are expected to form a low-density cavity-like structure before the merger occurs [119]. Within such a cavity a successful GRB jet is likely to develop, since the ambient gas density is not sufficiently high to stall the jet, in contrast to the choked-jet case discussed in Ref. [118].

In GRB theories, EIC processes can be important when seed photons in the external regions or late/early-time dissipation processes can be efficiently upscattered to the GeV-TeV bands by accelerated electrons [103, 401, 402]. The EIC scenario can be used to explain the observed very-high-energy (VHE) emission from GRBs [403, 404]. In the present case, the disk black body emission provides an appropriate supply of thermal photons to the short GRB jets.

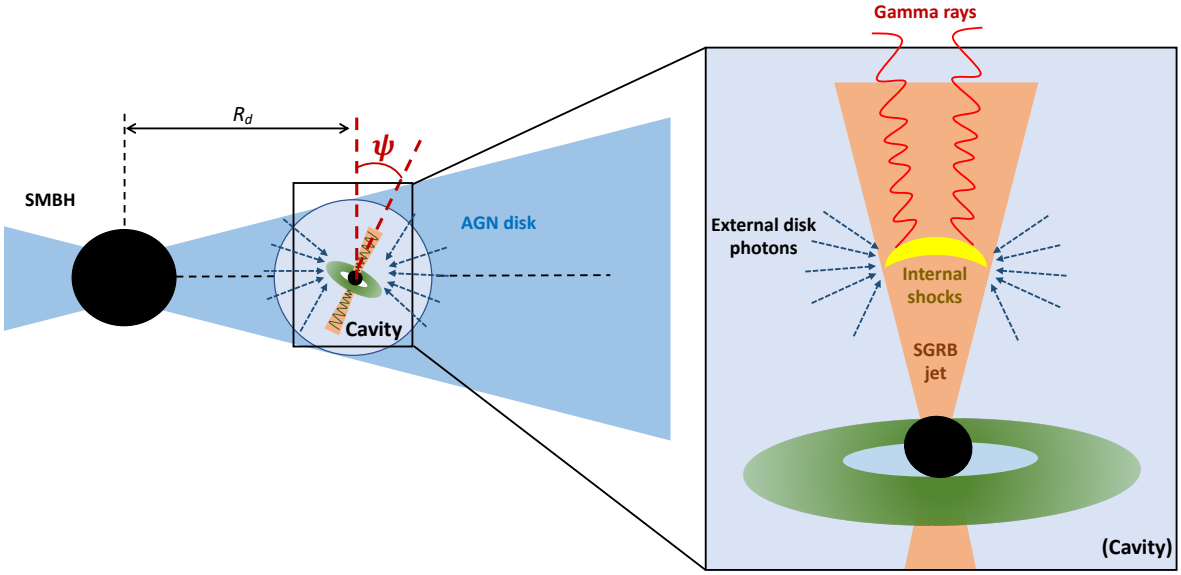

Figure 6.1. Schematic picture of the CBO mergers embedded in AGN disks. A cavity is formed due to the powerful outflows from the circumbinary disk. In this configuration, ψ represents the angle between the CBO orbital plane and the AGN disk, and R_d is the distance between the CBO and the central SMBH. Non-thermal electrons accelerated in the internal dissipation region are responsible for the production of γ-rays. These electrons can upscatter the disk photons, leading to the EIC emission.

Adopting a thin-disk model, we derive the conditions for cavity formation and calculate disk photon spectra in Sec. 6.2. In Sec. 6.3, we numerically solve the steady-state transport equation to obtain the electron distribution inside the jet. In Sec. 6.4, we calculate the synchrotron, synchrotron self-Compton (SSC) and EIC components. The effects of $\gamma\gamma$ absorption in the AGN disk and electromagnetic cascades are also taken into account. We also present the detection perspectives for the *Fermi* Large Area Telescope (*Fermi*-LAT) and the VHE γ-ray facilities, such as the Major Atmospheric Gamma Imaging Cherenkov (MAGIC), the High Energy Stereoscopic System (H.E.S.S.), the Very Energetic Radiation Imaging Telescope Array System (VERITAS), the Cherenkov Telescope Array (CTA), and the water Cherenkov detector array in the Large High Altitude Air Shower Observatory (LHAASO-WCDA), in Sec. 6.4.2. The prompt emissions are discussed in Sec. 6.4.3. We summarize and discuss the results in Sec. 6.5.

Throughout the paper, we use the notation $Q_x = Q/10^x$, and physical quantities are written in CGS units unless otherwise specified. Quantities with the prime symbol, e.g., Q', are written in the jet comoving frame. We use the symbol $F[a, b, c, ...]$ to represent the value of a function F evaluated at the point $(a, b, c, ...)$.

6.2 Cavity Formation and Disk Photon Spectra

In this section we derive the conditions for the formation of a low-density cavity around the CBO, following the treatment in Ref. [119], and model the AGN disk temperature distribution assuming a steady thin disk.

6.2.1 Cavity Formation

For a thin AGN disk with an aspect ratio $h_{\rm AGN} = H_{\rm AGN}/R_d \sim 0.01$ surrounding a SMBH with mass $M_\star = 10^8 M_{\star,8} M_\odot$, we write down the accretion rate onto the SMBH and the radial drift velocity v_R as, respectively, $\dot{M}_\star = \dot{m}_\star L_{\rm Edd,\star}/c^2 \simeq 1.4 \times 10^{25}\ \dot{m}_\star M_{\star,8}$ g s^{-1} and $v_R = \nu/R_d \approx \alpha h_{\rm AGN}^2 v_K \simeq 2.1 \times 10^4\ \alpha_{-1} h_{\rm AGN,-2}^2 \mathcal{R}_2^{-1/2}$ cm s^{-1} [405], where $H_{\rm AGN}$ is the scale height of the AGN disk, $\alpha \sim 0.1$ is the viscous parameter, ν is the kinematic viscosity, $v_K = \sqrt{GM_\star/R_d}$ is the Kepler velocity, R_d is the distance between the CBO and the central SMBH, the dimensionless parameter $\mathcal{R}$ is defined as $\mathcal{R} \equiv R_d/R_{\rm S}$, and $L_{\rm Edd,\star}$ stands for the Eddington luminosity. The surface density for a stable disk can then be written as $\Sigma_{\rm AGN} = \dot{M}_\star/(2\pi R_d v_R) \simeq 3.6 \times 10^4\ \dot{m}_\star M_{\star,8} \mathcal{R}_2^{-1/2} \alpha_{-1}^{-1} h_{\rm AGN,-2}^{-2}$ g cm^{-2}. When a CBO is present in the AGN disk, the surface density is perturbed, and a density gap will appear bracketing the binary's orbit around the SMBH [406]. For a typical short GRB progenitor, we expect the total mass of the binary system to be $M_{\rm CBO} \lesssim 10 M_\odot$. In this case $\Sigma_{\rm CBO} \approx \Sigma_{\rm AGN}$ is a good approximation to the surface density of the AGN disk at the binary's position [119]. We obtain the disk gas density in the vicinity of the CBO

$$\begin{aligned}\rho_{\rm CBO} = \frac{\Sigma_{\rm CBO}}{2H_{\rm AGN}} \simeq & 6.1 \times 10^{-10}\ \dot{m}_\star M_{\star,8} \\ & \times \mathcal{R}_2^{-3/2} \alpha_{-1}^{-1} h_{\rm AGN,-2}^{-3}\ {\rm g\ cm^{-3}},\end{aligned} \tag{6.1}$$

and the disk magnetic field

$$\begin{aligned}B_d &= \sqrt{8\pi\beta^{-1}(\rho_{\rm CBO}/m_p)k_B T_d} \\ &\simeq 2.1 \times 10^2\ \beta_{0.48}^{-1/2} \dot{m}_\star^{1/2} M_{\star,8}^{1/2} R_2^{-3/4} \alpha_{-1}^{-1/2} \\ &\times h_{\rm AGN,-2}^{-3/2} T_{d,5}^{1/2}\ {\rm G},\end{aligned} \tag{6.2}$$

where $\beta \sim 3 - 30$ is define as the ratio of the plasma pressure to the magnetic pressure and T_d is the disk temperature. Henceforth, the sub-index 'CBO' will be used to stand for quantities describing CBOs.

We estimate the accretion rate of the CBO to be $\dot{M}_{\rm CBO} \approx \eta_{\rm CBO} \dot{M}_\star \simeq 1.4 \times$

$10^{24}\ \dot{m}_\star M_{\star,8}\eta_{\rm CBO,-1}$ erg s^{-1}, where $\eta_{\rm CBO}$ is the ratio of the CBO accretion rate to the SMBH accretion rate. This approximation is justified in Ref. [119]. We find that the accretion is highly super-Eddington, e.g., $\dot{m}_{\rm CBO} = \dot{M}_{\rm CBO}c^2/L_{\rm Edd,CBO} \simeq 10^6 \dot{m}_\star M_{\star,8} M_{\rm CBO,1}^{-1}\eta_{\rm CBO,-1}$, and expect a wind bubble to be produced by the strong radiation-driven outflows [407–409]. The bubble's expansion in a uniform medium can be described by the formula $r_B \approx 0.88(L_w t^3/\rho_{\rm CBO})^{1/5}$ [410, 411], where r_B is the bubble radius, $L_w = \eta_w \dot{M}_{\rm CBO} v_w^2 \simeq 1.4\times10^{42}\ \dot{m}_\star M_{\star,8}\eta_{\rm CBO,-1}\eta_w v_{w,9}^2$ erg s^{-1} and $v_w \sim 10^9 v_{w,9}$ cm s^{-1} is the outflow velocity. Since the accretion is highly super-Eddington, the factor η_w can reach $\sim 90-100\%$ [412, 413]. However, we use a conservative value $\eta_w \sim 0.3\ \eta_{w,-0.5}$ [414]. Equating the bubble radius r_B to $H_{\rm AGN}/\cos\psi$, we obtain the timescale to create a cavity reaching the approximate boundary of the AGN disk along the direction of the GRB jet,

$$\begin{aligned} t_{\rm cav} &\approx 1.2\left(\frac{\rho_{\rm CBO}H_{\rm AGN}^5}{L_w\cos^5\psi}\right)^{1/3} \\ &\simeq 4.0\times10^5\ (\cos\psi)^{-5}\mathcal{R}_2^{7/6}\alpha_{-1}^{-1/3}h_{\rm AGN,-2}^{2/3} \\ &\quad\times\eta_{\rm CBO,-1}^{-1/3}\eta_{w,-0.5}^{-1/3}v_{w,9}^{-2/3}\ {\rm s}, \end{aligned} \tag{6.3}$$

where ψ is the angle between binary orbital plane and the AGN disk (see the schematic picture in Fig. 6.1). One caveat is that we assumed a spherical outflow to derive the cavity timescale, equation 6.3. Ref. [409] pointed out that the outflow is concentrated in a wide-angle funnel that surrounds the jet if the accretion rate is highly super-Eddington. In the following text, we will continue using the spherical cavity timescale for simplicity to obtain sufficient but unnecessary conditions for the cavity formation.

The formation of a cavity for a CBO located at R_d before the merger occurs requires

$$t_{\rm cav} \lesssim \min\left[t_{\rm gw},\ t_{\rm mig},\ t_{\rm vis}\right], \tag{6.4}$$

where $t_{\rm gw}$, $t_{\rm mig}$, $t_{\rm vis}$ are binary merger, migration and AGN disk viscosity timescales,

respectively. We write down the timescales for an equal-mass binary explicitly as

$$\begin{aligned} t_{\rm gw} &= \frac{5}{128}\frac{\dot{m}_{\rm CBO}^4}{A_{\rm in}^4}\frac{GM_{\rm CBO}}{c^3} \\ &\simeq 1.9\times10^{14}\ \dot{m}_{\rm CBO,6}^4 A_{\rm in,1}^{-4} M_{\rm CBO,1}\ {\rm s}, \\ t_{\rm mig} &= \frac{h_{\rm AGN}^2 M_\star^2}{M_{\rm CBO}R_d v_K \Sigma_{\rm AGN}} \\ &\simeq 1.47\times10^{14}\ \alpha_{-1} h_{\rm AGN,-2}^4 M_{\star,8}^{1/2} M_{\rm CBO,1}^{-1}\dot{m}_\star^{-1}\ {\rm s}, \\ t_{\rm vis} &= \frac{R_d}{\alpha h_{\rm AGN}^2 v_K} \\ &\simeq 1.39\times10^{11}\ \alpha_{-1}^{-1} h_{\rm AGN,-2}^{-2}\mathcal{R}_2^{3/2} M_{\star,8}^{-1/2}\ {\rm s}, \end{aligned} \tag{6.5}$$

where $A_{\rm in}\sim 10$ is the ratio of the inner edge of the circumbinary disk surrounding the CBO and the major axis of the binary's orbit [415]. We define a critical angle ψ_c above which the condition described by equation 6.4 is no longer satisfied, and obtain

$$\psi_c \simeq \frac{\pi}{2} - \max\left[h_{\rm AGN},\ 0.076\mathcal{R}_2^{-1/15} h_{\rm AGN,-2}^{8/15} M_{\star,8}^{1/10}\right]. \tag{6.6}$$

In the equation above, the dependence on the parameters $\alpha,\ \eta_w,\ \eta_{\rm CBO}$ and v_w are not shown, to simplify the notation. Varying $\mathcal{R}$ in the fiducial range $10-10^3$, we estimate the critical angle $\psi_c\simeq 85.6^\circ$ and find that ψ_c depends very weakly on $\mathcal{R}$ and $M_\star$. This result supports the argument that in most cases a cavity surrounding the CBO is unavoidable and the jet is not choked, except if the binary orbital plane is perpendicular to the AGN disk [119].

6.2.2 Disk Photon Spectra

The accretion disk can become optically thick to ultraviolet/infrared photons as the plasma gets ionized. We estimate the vertical optical depth, for a fully ionized disk with temperature $T_d \gtrsim 10^4$ K,

$$\begin{aligned} \tau_d &\approx \Sigma_{\rm AGN}\kappa_{\rm R} \\ &\simeq 7.2\times10^3\ (1+X)\dot{m}_\star M_{\star,8}\mathcal{R}_2^{-1/2}\alpha_{-1}^{-1}h_{\rm AGN,-2}^{-2}, \end{aligned} \tag{6.7}$$

where $\kappa_{\rm R}\approx 0.2(1+X)$ is the Rosseland mean opacity for Thomson scattering and X is the hydrogen mass fraction. Since the disk remains optically thick ($\tau_d>1$) in the range $\mathcal{R}\sim 10-10^3$, we use a black-body spectrum to approximate the local photon density

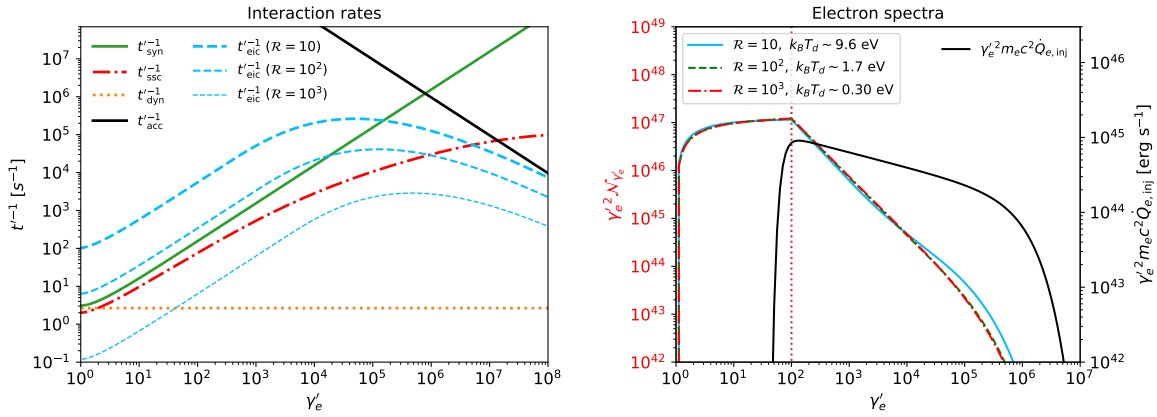

Figure 6.2. *Left panel:* Energy loss rates of accelerated electrons in the internal dissipation region. The green solid and red dash-dotted lines respectively show the synchrotron and SSC rates. From thick to thin, the blue dashed lines depict the EIC cooling rate for the CBOs at $\mathcal{R}=10, 10^2$ and 10^3, respectively. The reciprocals of the dynamic and acceleration times are illustrated as the yellow dotted and black solid lines. *Right panel:* The electron number spectra as functions of the electron Lorentz factor. The minimum injected Lorentz factor is $\gamma'_{e,m}=100$. The blue solid, green dashed and red dash-dotted lines correspond to $\mathcal{R}=10,\ 10^2$ and 10^3 cases. The black solid line is the electron injection function.

(in the units of $\mathrm{eV}^{-1}\ \mathrm{cm}^{-3}$), e.g.,

$$n^{(\mathrm{eic})}_{\varepsilon_\gamma}=\frac{8\pi}{(hc)^3}\frac{\varepsilon_\gamma^2}{\exp\left(\frac{\varepsilon_\gamma}{k_BT_d}\right)-1}, \tag{6.8}$$

where ε_γ is the energy of seed disk photons in the engine frame. The disk temperature T_d at the position of the CBO can be written as [405]

$$\begin{aligned} T_d&=\left\{\frac{2GM_\star\dot{M}_\star}{8\pi\sigma_S R_d^3}\left[1-\left(\frac{R_*}{R_d}\right)^{1/2}\right]\right\}^{1/4}\\ &\simeq 2.0\times10^4\ \dot{m}_\star^{1/4}M_{\star,8}^{-1/4}\mathcal{R}_2^{-3/4}\ \mathrm{K}, \end{aligned} \tag{6.9}$$

where σ_S is the Stefan-Boltzmann constants and R_* is the innermost edge of the disk. In this paper, we consider three distances $\mathcal{R}=10,\ 10^2$ and 10^3. The corresponding disk temperatures are $k_BT_d=9.1$ eV, 1.7 eV and 0.3 eV. For $R_d\gg R_*$, we have $T_d\propto\mathcal{R}^{-3/4}$, implying that the EIC component becomes increasing important when we move the CBO close to the central SMBH.

6.3 Non-Thermal Electrons

We consider a successful (i.e.non-choked) GRB jet whose extended emission has a luminosity $L_{j,\rm iso} = 10^{48.5}$ erg s^{-1}. We focus on the internal dissipation model in which the jet kinetic energy is dissipated at $R_{\rm dis} = 2\Gamma_j^2 c t_{\rm var} \simeq 1.5\times10^{12}\ \Gamma_{j,1.7}^2 t_{\rm var,-2}$ cm via internal shocks [416] or magnetic reconnections [417], where $\Gamma_j = 50\Gamma_{j,1.7}$ is the jet Lorentz factor, $t_{\rm var} = 10^{-2} t_{\rm var,-2}$ s is the variability time of velocity fluctuations. One necessary condition for electron acceleration is that the upstream region should be optically thin for the shock not to be radiation mediated, namely, $\tau_{\rm in} = n'\sigma_T R_{\rm dis}/\Gamma_j \lesssim 1$ [268, 418, 419], where $n' = L_{j,\rm iso}/(4\pi R_{\rm dis}^2 \Gamma_j^2 m_p c^3) \simeq 9.6\times10^{11}\ L_{j,\rm iso,48.5}\Gamma_{j,1.7}^{-6} t_{\rm var}^{-1}$ cm^{-3} is the comoving number density and σ_T is the Thomson cross section. Explicitly, we write down the optical depth as $\tau_{\rm in} \simeq 1.8\times10^{-2}\ L_{j,\rm iso,48.5}\Gamma_{j,1.7}^{-5} t_{\rm var,-2}^{-1}$, which indicates that efficient electron acceleration is plausible.

To get the electron distribution we numerically solve the steady-state transport equation

$$\frac{\mathcal{N}_{\gamma_e'}}{t'_{\rm dyn}} - \frac{\partial}{\partial\gamma_e'}\left(\frac{\gamma_e'}{t'_{e,c}}\mathcal{N}_{\gamma_e'}\right) = \dot{Q}'_{e,\rm inj}, \tag{6.10}$$

where γ_e' is the Lorentz factor, $\mathcal{N}_{\gamma_e'} = dN_e/d\gamma_e'$ is the differential spectrum, $t'_{\rm dyn} = R_{\rm dis}/(\Gamma_j c)$ is the dynamical time that may represent adiabatic losses or escape, $t'_{e,c}$ represents the electron cooling time scale, and the function $\dot{Q}_{e,\rm inj}$ is the electron injection rate from shock acceleration. Specifying a spectral index $s = 2.2$, e.g., $\dot{Q}'_{e,\rm inj} \propto {\gamma_e'}^{-s}$, we normalize the injection function via $\int d\gamma_e'(\gamma_e' m_e c^2 \dot{Q}'_{e,\rm inj}) = \epsilon_e L_{j,\rm iso}/\Gamma_j^2$. The factor ϵ_e, defined as the fraction of jet kinetic energy that is converted to electrons, is assumed to be $\epsilon_e = 0.1$. The minimum Lorentz factor $\gamma'_{e,m}$ for injected electrons is assumed to be $\gamma'_{e,m} = 100$.

In the dissipation region, the magnetic field is $B'_{\rm dis} = [8\pi\epsilon_B(\Gamma_{\rm rel}-1)n' m_p c^2]^{1/2} \simeq 3.8\times10^4\ \epsilon_{B,-2}^{1/2} L_{j,\rm iso,48.5}^{1/2}\Gamma_{j,1.7}^{-3} t_{\rm var}^{-1/2}$ G, where $\Gamma_{\rm rel} \simeq 5$ is the relative Lorentz factor between the fast and slow shells. The ratio of $B'_{\rm dis}$ to the disk magnetic field B_d is $B'_{\rm dis}/(\Gamma_j B_d) \simeq 3.8\,\mathcal{R}_2^{9/8}\beta_{0.48}^{1/2}$. Here, we focus on the $\mathcal{R}$-dependence of the magnetic fields, using the fiducial values for all other parameters. We use the modulated magnetic field $B' = \max[B'_{\rm dis}, \Gamma_j B_d]$ to calculate the electromagnetic emission in the dissipation region.

The accelerated electrons lose energy through synchrotron, SSC, and EIC processes within the corresponding timescales $t'_{e,\rm syn}$, $t'_{e,\rm ssc}$ and $t'_{e,\rm eic}$. The net cooling timescale is given by $t'_{e,c} = ({t'}_{e,\rm syn}^{-1} + {t'}_{e,\rm ssc}^{-1} + {t'}_{e,\rm eic}^{-1})^{-1}$. Electrons with higher γ_e' cool down faster while a longer acceleration time, e.g., $t'_{\rm acc} = \gamma_e' m_e c/(eB')$, is required to reach such a high energy.

We thus expect a cutoff Lorentz factor $\gamma'_{e,\rm cut}$ determined by the equation $t'_{\rm acc} = t'_{e,c}$, above which electrons cannot accumulate energy due to the rapid radiation. Using these arguments, the injection function for a spectral index $s > 2.0$ can be written as,

$$\dot{Q}'_{e,\rm inj} = \frac{(s-2)\epsilon_e L_{j,\rm iso}}{\Gamma_j^2 m_e c^2 \gamma'^2_{e,m}} \left(\frac{\gamma'_e}{\gamma'_{e,m}}\right)^{-s} \exp\left(-\frac{\gamma'_e}{\gamma'_{e,\rm cut}}\right). \tag{6.11}$$

The photons from the synchrotron process play the role of seed photons in EIC scattering. Therefore, we need a trial electron spectrum, e.g. $\mathcal{N}'^{(0)}_{\gamma'_e} \sim (t'^{-1}_{\rm dyn} + t'^{-1}_{e,\rm syn} + t'^{-1}_{e,\rm eic})^{-1} \dot{Q}'_{e,\rm inj}$, to evaluate $t'_{\rm ssc}$, and solve the differential equation 6.10 iteratively to obtain a convergent solution as in Ref. [403].

The left panel in Fig. 6.2 shows the energy loss rates. The blue dashed lines show the EIC cooling rate for $\mathcal{R} = 10,\ 10^2$ and 10^3. The synchrotron (green line) and SSC (red dash-dotted line) cooling rates are not sensitive to the CBO's position, whereas the EIC rate increases as the distance between the CBO and the SMBH reduces. This tendency is consistent with equation 6.9, which predicts a hotter and photon-denser environment close to the SMBH. Remarkably, the EIC process starts to dominate the electron cooling at a distance range $\mathcal{R} \lesssim 10^2$, leading to a softer electron spectrum, e.g., the blue line ($\mathcal{R} = 10$) in the right panel of Fig. 6.2, in contrast to the high-$\mathcal{R}$ cases. The black solid line in the right panel shows the electron injection function. In the low-energy band, there is no injection, e.g., $\dot{Q}_{e,\rm inj} = 0$ for $\gamma'_e \lesssim \gamma'_{e,m}$, we can analytically solve equation 6.10 and connect this segment to the $\gamma'_e > \gamma'_{e,m}$ part. Using the simplification $t'^{-1}_c \sim b\gamma'_e$, which is consistent with the EIC and synchrotron cooling rates in the left panel, we obtain

$$\mathcal{N}_{\gamma'_e} = \mathcal{N}_{\gamma'_{e,m}} \exp\left[-\frac{1}{b t'_{\rm dyn}}(\gamma'_{e,m} - \gamma'_e)\right],\ \gamma'_e \lesssim \gamma'_{e,m}, \tag{6.12}$$

where $\mathcal{N}_{\gamma'_{e,m}}$ represents the electron number distribution at $\gamma'_{e,m}$. Equation 6.12 explains the electron spectrum softening at lower values of $\mathcal{R}$ (equivalently at larger values of b).

6.4 Results

6.4.1 γ-Ray Spectra

Using the electron spectra obtained in Sec. 6.3 and following the formalism and procedures presented in Refs. [401], [403] and [363], we numerically compute the γ-ray spectra taking into account the synchrotron, SSC and EIC processes. We consider three merger-induced

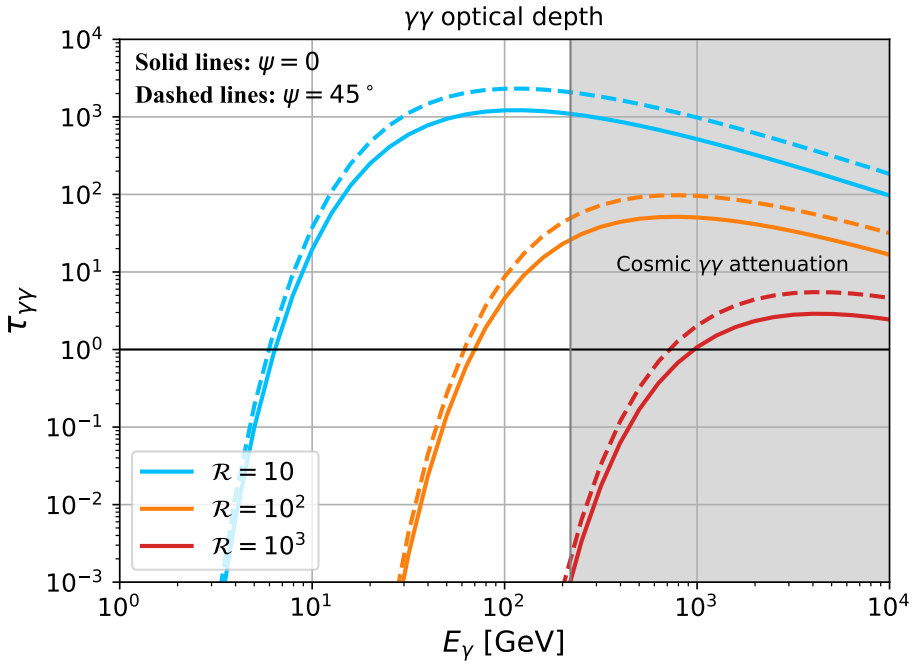

Figure 6.3. The blue ($\mathcal{R} = 10$), yellow ($\mathcal{R} = 10^2$) and red ($\mathcal{R} = 10^3$) lines are the optical depth $\tau_{\gamma\gamma}$ for $\gamma\gamma$ annihilation between γ-rays and disk photons. The solid and dashed lines correspond to the inclination $\psi = 0$ and $\psi = 45°$. The optical depth to cosmic $\gamma\gamma$ annihilation becomes greater than 1.0 in the energy range $E_\gamma \gtrsim 220$ GeV (the gray shaded area), assuming that the CBO merger is located at $z = 1.0$.

GRBs in an AGN located at redshift $z = 1$ (the equivalent luminosity distance is $d_L \simeq 6.7$ Gpc). We focus on the on-axis case and assume the CBOs' orbit planes are all aligned with the AGN disk plane, e.g., $\psi = 0$. A discussion on the influence of ψ will be given in Sec. 6.4.2.

While propagating in the jet and in the AGN disk, high-energy γ-rays will annihilate with ambient UV/IR disk photons, resulting in their attenuation and EM cascades. The optical depth for $\gamma\gamma$ annihilation depends on the photon energy in the short GRB's engine frame $\varepsilon_\gamma = \Gamma_j \varepsilon'_\gamma$, the position of the jet and the misalignment angle ψ, via

$$\tau_{\gamma\gamma}[\varepsilon_\gamma, \mathcal{R}, \psi] \approx \int_0^{H_{\rm AGN}} \frac{dy}{\cos\psi} \lambda_{\gamma\gamma}^{-1}[\varepsilon_\gamma, R_d + y\tan\psi], \tag{6.13}$$

where the reciprocal of the mean free path $\lambda_{\gamma\gamma}[R_d]$ for an isotropic disk photon field can be calculated as [420]

$$\lambda_{\gamma\gamma}^{-1}[\varepsilon_\gamma, R_d] = \frac{1}{2}\int_{-1}^{1} d\mu(1-\mu) \int d\tilde{\varepsilon}_\gamma n_{\epsilon_\gamma}^{(\rm eic)}[\tilde{\varepsilon}_\gamma]\sigma_{\gamma\gamma}[x]. \tag{6.14}$$

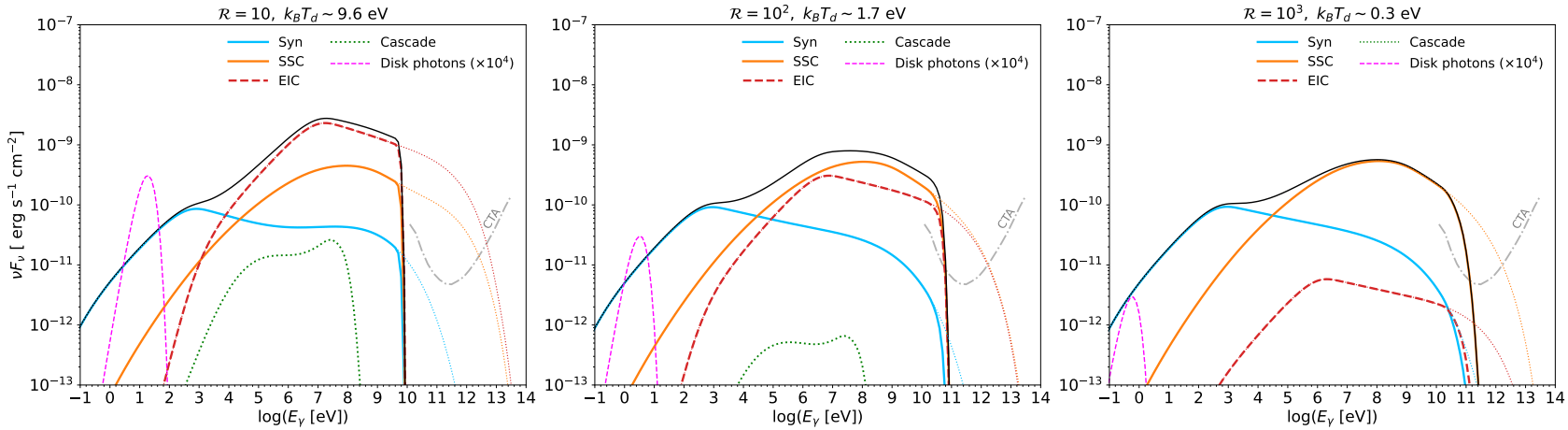

Figure 6.4. The observed γ-ray spectra from embedded short GRBs at $z = 1$ with distances $\mathcal{R} = 10$ (left panel), 10^2 (middle panel) and 10^3 (right panel) to the central SMBH. The GRB parameters used here are the fiducial parameters assumed in Sec. 6.3, e.g., $L_{j,\rm iso} = 10^{48.5}$ erg s^{-1}, $\Gamma_j = 50$, $\epsilon_B = 0.01$, and $\epsilon_e = 0.1$. The blue, yellow and red solid lines show the synchrotron, SSC and EIC emission after $\gamma\gamma$ attenuation. The dotted lines in the corresponding colors depict the unattenuated fluxes. The cascade emissions are depicted as the green lines. The magenta dashed lines show the disk target photon fluxes (multiplied by 10^4). In both cases, $\psi = 0$ is applied. The gray dash-dotted lines indicate the CTA flux sensitivity for the 10^3 s observation time.

In this expression, $x = \tilde{\varepsilon}_\gamma \varepsilon_\gamma (1-\mu)/2$ is the particle Lorentz factor in the center-of-momentum frame and $\sigma_{\gamma\gamma}$ is the $\gamma\gamma$ annihilation cross section.

Fig. 6.3 shows the optical depth in the observer's frame, where the observed energy is connected with ε_γ and ε'_γ via $E_\gamma = \varepsilon_\gamma/(1+z) = \Gamma_j \varepsilon'_\gamma/(1+z)$. The solid blue, yellow and red lines illustrates $\tau_{\gamma\gamma}$ at $\mathcal{R} = 10,\ 10^2$ and 10^3 with $\psi = 0$, whereas the dashed lines correspond to the case of an inclined jet, e.g., $\psi = 45^\circ$. The universe becomes opaque for γ-rays produced at $z = 1$ with energies $E_\gamma \gtrsim 220$ GeV (see the gray area in Fig. 6.3) due to $\gamma\gamma$ annihilation between γ-rays and cosmic backgrounds [421] e.g. extragalactic background light (EBL) and cosmic microwave background (CMB). From Fig. 6.3, we find that γ-rays with energy $E_\gamma \gtrsim 10$ GeV are strongly suppressed due to $\gamma\gamma$ annihilation for a GRB close to the SMBH, i.e. $\mathcal{R} \simeq 10$. For a GRB at positions with a larger $\mathcal{R} \sim 10^2 - 10^3$, γ-ray photons with energy $E_\gamma \sim 100$ GeV can escape from the AGN disk.

Applying the factor $\exp(-\tau_{\gamma\gamma})$ to the γ-ray spectra, we obtain the $\gamma\gamma$-attenuated spectra for embedded GRBs at redshift $z = 1$, as shown in Fig. 6.4. In this figure, $\psi = 0$ is used. The blue solid, yellow solid, and red dashed lines respectively illustrate the synchrotron, SSC, and EIC components. The dotted lines with corresponding colors show the fluxes before $\gamma\gamma$ attenuation. The gray dash-dotted lines indicate the Cherenkov Telescope Array (CTA) flux sensitivity for the 10^3 s observation time [422]. The magenta dashed lines show the disk photon fluxes multiplied by 10^4. From the red dashed lines in Fig. 6.4, we find that a closely embedded GRB can produce brighter γ-ray emission due to the EIC enhancement. The "Compton dominance" induced by EIC enhancement can be used as the prominent feature to distinguish these embedded short GRBs from others.

The e^+/e^- pairs produced in the $\gamma\gamma$ annihilation process will induce electromagnetic cascades while diffusing and cooling down in the AGN disk via synchrotron and inverse Compton processes. Following the treatment in Ref. [423], we write down the distribution for the secondary electrons and positrons,

$$\mathcal{N}^{\rm cas}_{\gamma_e} \approx 2\mathcal{N}^{\rm ph}_{\hat{\varepsilon}_\gamma} \left(\frac{d\hat{\varepsilon}_\gamma}{d\gamma_e}\right) \left(1 - e^{-\tau_{\gamma\gamma}[\hat{\varepsilon}_\gamma, \mathcal{R}, \psi]}\right) \tag{6.15}$$

where $N^{\rm ph}_{\hat{\varepsilon}_\gamma}$ is the pre-attenuation gamma-ray number spectra (in the units of eV^{-1}) in the engine frame and $\hat{\varepsilon}_\gamma = 2\gamma_e m_e c^2$ is the energy of primary electrons. Using the cavity

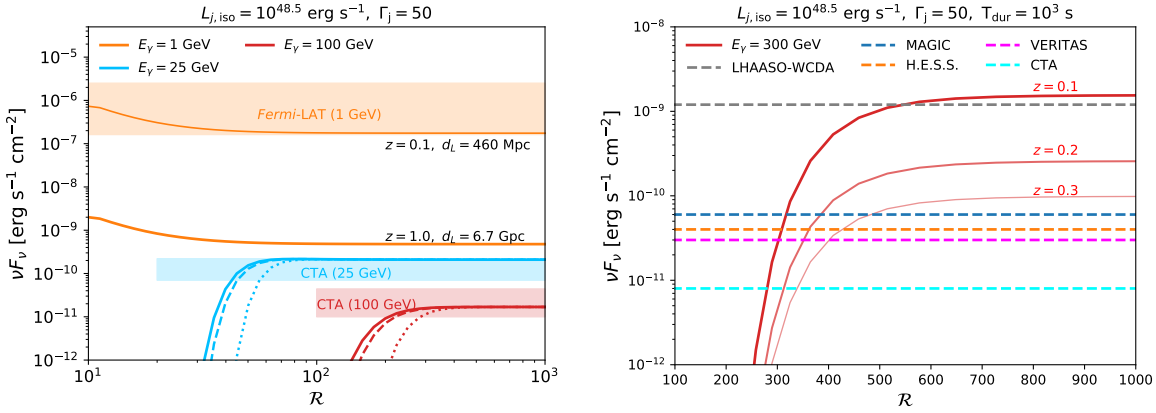

Figure 6.5. *Left panel:* γ-ray fluxes at 1 GeV (yellow lines), 25 GeV (blue lines) and 100 GeV (red lines) as functions of $\mathcal{R}$. The thick lines are obtained with $L_{j,\rm iso} = 10^{48.5}$ erg s^{-1} and $z = 1.0$, whereas a closer short GRB at $z = 0.1$ is considered for the thin yellow line. The point-source performance for *Fermi*-LAT and CTA at corresponding energies are shown as the yellow, blue and red areas, respectively. The upper and lower bounds show the sensitivities for the observation time $T_{\rm dur} = 10^2$ s and $T_{\rm dur} = 10^3$ s. *Right panel:* The red solid lines from thick to thin show the $\mathcal{R}$-dependence of 300 GeV γ-ray fluxes from the embedded short GRBs at $z = 0.1$, 0.2, and 0.3. The horizontal dashed lines from top to bottom correspond the the sensitivities of LHAASO-WCDA, MAGIC, H.E.S.S., VERITAS, and CTA.

magnetic field

$$B_{\rm cav} \approx (2\epsilon_B \eta_w \dot{M}_{\rm CBO} v_w / H_{\rm AGN}^2)^{1/2} \simeq 98\ \epsilon_{B,-2}^{1/2} \eta_{w,-0.5}^{1/2} h_{\rm AGN.-2}^{-1} \eta_{\rm CBO,-1}^{1/2} \mathcal{R}_2^{-1} \dot{m}_\star^{1/2} M_{\star,8}^{-1/2} v_{w,9}^{1/2}\ {\rm G}, \tag{6.16}$$

we numerically calculate the cascade emission. The green dotted lines in Fig. 6.4 show the cascade emission. Comparing to the beamed emission produced in the jet, the cascade emission is subdominant for $\mathcal{R} \gtrsim 100$ and typically peaks at a lower energy ~ 100 MeV. We find that the cascade flux drops dramatically as $\mathcal{R}$ increases, which is consistent with the $\mathcal{R}$-dependence of the $\gamma\gamma$ optical depth in Fig. 6.3. When the disk becomes transparent to the γ-ray photons, the e^-/e^+ pair production is suspended and the cascade emission is strongly suppressed. Typically, we need to solve the time-dependent equations to obtain the secondary electron/position distributions and the cascade spectrum. Our approach can provide a good estimation since these secondary particles cools down very fast, e.g., $t_{e,c}^{\rm cas} \lesssim 10$ s.

6.4.2 Detectability with Fermi-LAT and VHE γ-Ray Facilities

It is useful to compare the expected γ-ray fluxes in the extended emission phase against the sensitivities of current and future facilities, such as *Fermi*-LAT, MAGIC, H.E.S.S., VERITAS, CTA, and LHAASO-WCDA, and discuss how the parameters $\mathcal{R}$ and ψ influence the results.

Observationally, a significant fraction of short GRBs exhibit 'long-lasting' extended or plateau emission peaking in X-ray bands [424–427] with the duration $T_{\rm dur} \sim 10^2 - 10^5$ s, following the prompt phase where 90% of the kinetic energy is dissipated in ~ 2 seconds, e.g., $T_{90} \lesssim 2$ s. Such prolonged emission may originate from the continuous energy injection by the accreting black holes formed after the merger or the fast rotating magnetars [428–434]. Considering a prolonged γ-ray emission of luminosity $L_{j,\rm iso} = 10^{48.5}$ erg s^{-1} and the corresponding duration in the observer's frame $T_{\rm dur} \sim 10^2$ s $- 10^3$ s, we show the integral sensitivities within $T_{\rm dur}$ for *Fermi*-LAT[1] and CTA [422] at the $E_\gamma =$ 1 GeV (yellow area), 25 GeV (blue area) and 100 GeV (red area) in the left panel of Fig. 6.5. The upper and lower bounds of each shaded area demonstrate the performances for the detectors given the observation time $T_{\rm dur} = 10^2$ s and $T_{\rm dur} = 10^3$ s, respectively. We plot also the 1 GeV (yellow lines), 25 GeV (blue lines) and 100 GeV (red lines) fluxes as functions of $\mathcal{R}$ in the left panel of Fig. 6.5. The solid lines correspond to the $\psi = 0$ case, whereas the dashed and dash-dotted lines depict the $\psi = 45^\circ$ and $\psi = 75^\circ$ cases. The thick lines are for the GRBs at $z = 1$, while the thin yellow line shows the 1 GeV fluxes for a closer GRB at $z = 0.1$ ($d_L \simeq 460$ Mpc).

The influence of disk photons is encoded in the shapes of the yellow, blue and red curves. The 1 GeV flux decreases to a flat level as $\mathcal{R}$ increases because the EIC component gradually becomes less important as the CBO is moved to a cooler outer region. In the ranges $\mathcal{R} \lesssim 50$ and $\mathcal{R} \lesssim 300$, the $\gamma\gamma$ attenuation caused by dense disk photons suppresses the 25 GeV and 100 GeV emission, respectively. Since the $\gamma\gamma$ annihilation is negligible for 1 GeV photons even if the CBO is very close to the SMBH (see the blue lines in Fig. 6.3), we expect that the flux does not depend on ψ. On the other hand, the 25 GeV and 100 GeV fluxes decrease as ψ approaches $\psi_c \simeq 85.6^\circ$.

From the left panel of Fig. 6.5, we find that CTA will be capable of detecting 25 GeV and 100 GeV γ-rays up to $z = 1$ if an embedded short GRB is appropriately distant from the SMBH, e.g., $\mathcal{R} \gtrsim 40$ for 25 GeV γ-rays and $\mathcal{R} \gtrsim 200$ for 100 GeV γ-rays. By contrast, it is challenging for *Fermi*-LAT to detect the 1 GeV photons from sources located at

[1]The *Fermi*-LAT sensitivity can be found in `https://www.slac.stanford.edu/exp/glast/groups/canda/lat_Performance.htm`

$z = 1$ via point source search within the duration $T_{\rm dur} \sim 10^3$ s. For the short GRBs embedded in AGN disks, we would require a nearby CBO merger ($d_L \lesssim 460$ Mpc) at the position with the distance greater than $40R_{\rm S}$ ($\mathcal{R} \gtrsim 40$) to the central SMBH in order to be detected simultaneously by CTA and *Fermi*-LAT.

MAGIC, H.E.S.S., and VERITAS are current ground Imaging Atmospheric Cherenkov Telescopes with very good performance in the energy range 150 GeV to 30 TeV. LHAASO is a new generation multi-component instrument and LHAASO-WCDA is operated in the energy range ∼300 GeV to 10 TeV. We present the $\mathcal{R}$-dependence of 300 GeV γ-ray fluxes at $z = 0.1$, 0.2, and 0.3 (the red solid lines, from thick to thin) in the right panel of Fig. 6.5. The horizontal dashed lines from top to bottom corresponds to the flux sensitivities of LHAASO-WCDA [435], MAGIC [436], H.E.S.S. [437], VERITAS[2], and CTA for $T_{\rm dur} = 10^3$ s and $\psi = 0$. At 300 GeV, the sensitivity of LHAASO-WCDA is $\sim 10^{-9}$ erg s^{-1} cm^{-2} in 10^3 s observation. The nearby embedded GRBs with redshift $z < 0.1$ can be observed. MAGIC, H.E.S.S., VERITAS and CTA can detect 300 GeV photons from embedded GRBs upto redshift $z = 0.3$ if $\mathcal{R} \gtrsim 500$ is satisfied. For the sources with farther distance, the Universe could be opaque to VHE γ-rays.

6.4.3 Prompt Emission

As for the prompt emission, besides the cutoff with energy $\gtrsim 100$ GeV caused by the $\gamma\gamma$ absorption in the AGN disk, we found that there may be no significant difference between short GRBs embedded in AGN disks and other short GRBs. The reason is that, given a higher isotropic luminosity $L_{j,\rm iso}^{\rm prompt} = 10^{51}$ erg s^{-1} and a higher Lorentz factor $\Gamma_j^{\rm prompt} = 200$ ($\Gamma_j^{\rm prompt} = 100$) in the prompt emission phase of $T_{90} = 1$ s, the EIC emission is subdominant (comparable) compared to the synchrotron/SSC components. Using the parameters in the prompt emission phase, we estimate photon flux in the energy range 50 - 300 keV,

$$F_{\nu,50-300\ \rm keV}^{\rm prompt} \simeq 1.9\ (1+z) d_{L,28}^{-2}\ \rm ph\ s^{-1}\ cm^{-2}. \tag{6.17}$$

Noting that the onboard trigger threshold of the *Fermi* Gamma-Ray Burst Monitor (*Fermi*-GBM) is $\sim$ 0.7 ph s^{-1} cm^{-2} [438], it can detect the prompt emission and localize the short GRB. At 10 GeV, the flux of the prompt emission is $\nu F_{\nu,10\ \rm GeV}^{\rm prompt} \sim 2\times10^{-6}\ (1+z) d_{L,28}^{-2}$ erg s^{-1} cm^{-2}, implying the possible detection of the embedded GRBs

[2]The differential sensitivity of VERITAS can be found in `https://veritas.sao.arizona.edu/about-veritas/veritas-specifications`

at $z \sim 0.5 - 1$ with the High Altitude Water Cherenkov (HAWC) observatory [439]. If the short GRB is GRB 090510-like, e.g., $L_{j,\rm iso}^{\rm prompt} \gtrsim 10^{53}$ erg s^{-1}, *Fermi*-LAT would also be able to see γ-ray photons upto ~ 30 GeV in the prompt emission phase [440]. Above all, the prompt emission diagnosis can provide valuable information for the follow-up observations of extended emissions.

6.5 Summary and Discussion

We studied γ-ray emission from short GRBs embedded in AGN disks and showed that successful jets are expected from these, since the CBOs in the disks are highly super-Eddington accretors and can produce low-density cavities around the CBO via powerful outflows. Our work demonstrates that the AGN disks influence the γ-ray emission mainly in two ways, namely, via the EIC enhancement and $\gamma\gamma$ attenuation, depending on the distance to the SMBH and the inclination ψ. If a CBO merger occurs very close to the SMBH, e.g., $\mathcal{R} \sim 10 - 40$, the dense disk photon field will lead to a luminous EIC component in the GeV band and a firm cutoff at $E_\gamma \simeq 10$ GeV. On the other hand, the SSC process dominates the GeV emission for CBO mergers at $\mathcal{R} \gtrsim 100$, and the disk gradually becomes transparent for 10-100 GeV photons unless the GRB jet is entirely buried inside the AGN disk, e.g., $\psi \gtrsim \psi_c \simeq 85.6°$. Considering the ratio of the peak flux of the inverse Compton component to the synchrotron peak flux and the cutoff energy, we may be able to distinguish the short GRBs embedded in AGN disks from other types of isolated short GRBs [103, 104]. To identify the embedded short GRBs, we can utilize these two signatures, "Compton dominance" and $\gamma\gamma$ annihilation cutoff. Such spectral information can also be used to determine the parameters of the short GRB - AGN disk system such as T_d, $\mathcal{R}$ and ψ. According to the simulations of compact binary formations in AGN disks, it is reasonable to expect the embedded short GRBs to occur in the region $\mathcal{R} \gtrsim 40 - 100$ [111, 121]. The detection of these short GRBs can, in return, be used to test current AGN-assisted CBO formation theories and constrain the CBO distributions in AGN disks.

Since approximately $f_{\rm EE} \sim 1/4 - 1/2$ [431] of *Swift* short GRBs are accompanied by extend emission, we investigated the detectability of GRBs in the AGN disk for CTA and *Fermi*-LAT considering a jet of luminosity $L_{j,\rm iso} = 10^{48.5}$ erg s^{-1} lasting for $T_{\rm dur} \sim 10^2 - 10^3$ s. From now on, we discuss the detection perspectives of the extended emissions with $T_{\rm dur} = 10^2 - 10^3$ s, $L_{\rm j,iso} = 10^{48.5}$ erg s^{-1} cm^{-2}, and $\Gamma_j = 50$. For the embedded short GRBs within $z = 1.0$, CTA will be able to detect the γ-rays in the

energy range $E_\gamma \sim 25 - 100$ GeV if the requirements $\mathcal{R} \gtrsim \mathcal{R}_c$ and $\psi \lesssim \psi_c$ are satisfied, where $\mathcal{R}_c \sim 40 - 100$ is the critical distance defined by $\tau_{\gamma\gamma}[(1+z)E_\gamma, \mathcal{R}_c, \psi] = 1$. To estimate the CTA detection rate, we use $f_\mathcal{R}$ and $f_\psi \sim 1$ to represent the fractions of embedded short GRBs that meet the conditions $\mathcal{R} \gtrsim \mathcal{R}_c$ and $\psi \lesssim \psi_c$, respectively. Taking into account both NS-NS and NS-BH mergers, Ref. [441] estimated the occurance rate of short GRB in AGN disks at $z < 1$, $\dot{R}_{\rm SGRB,AGN} \sim (300 - 2 \times 10^4) f_{\rm AGN,-1}$ yr^{-1}, where $f_{\rm AGN} \sim 0.1$ is the fraction of BH-BH mergers. We estimate the CTA detection rate of the on-axis prolonged γ-ray emission from short GRBs embedded in AGN disks via $\dot{R}_{\rm CTA} \sim f_{\rm CTA} f_b f_{\rm EE} f_\mathcal{R} f_\psi \dot{R}_{\rm GRB,AGN} \sim (0.2 - 22)\ f_\mathcal{R} \theta_{j,-1}^2 f_{\rm AGN,-1}$ yr^{-1}, where $f_{\rm CTA} \sim 0.3 - 0.5$ is the CTA detection efficiency defined as the ratio of detectable events to events that can be followed up by CTA [442], $f_b = (\theta_j + 1/\Gamma_j)^2/2 \sim \theta_j^2/2$ is the beaming factor and $\theta_j \sim 0.1$ is the jet opening angle. Despite the large uncertainty in the CTA detection rate, we estimate that it is feasible for CTA to detect the prolonged γ-ray emission from short GRBs embedded in AGN disks in the time scale of one year.

We now discuss the implications to multi-messenger analyses with GWs and γ-rays. Ref. [443] estimated that the merger rate of binary black holes (BBHs) embedded in AGN disks within the advanced Laser Interferometer Gravitational-wave Observatory's (aLIGO's) horizon, e.g., $D_h \simeq 450$ Mpc, could be $\dot{R}_{\rm L,BBH} \sim 20$ yr^{-1}. Implementing the ratio of the cumulative NS-BH and NS-NS merger rates to the BBH merger rate in the AGN channel, $f_{\rm L,CBO/BBH} = (\dot{R}_{\rm L,NS-NS} + \dot{R}_{\rm L,NS-BH})/\dot{R}_{\rm L,BBH} \sim 0.1 - 7.0$ [441], we estimate the occurrence rate of on-axis short GRBs with extended emission originating from LIGO-detectable CBO mergers in the AGN channel,

$$\begin{aligned} \dot{R}^{(L)}_{\rm SGRB-AGN} &= f_{\rm EE} f_b f_{\rm L,CBO/BBH} \dot{R}_{\rm L,BBH} \\ &\sim (2.5 \times 10^{-3} - 0.35)\ \theta_{j,-1}^2\ {\rm yr}^{-1}. \end{aligned} \tag{6.18}$$

The physical meaning of this equation is that among all detectable mergers within LIGO's horizon, MAGIC, H.E.S.S., VERITAS, CTA, and LHAASO-WCDA can observe $2.5 \times 10^{-3} - 0.35$ short GRBs with extended γ-ray emission each year. In the optimistic case, it is possible to detect the on-axis extended emission simultaneously with GWs originated from CBO mergers embedded in AGN disks in one decade.

We note also that, while this is not the subject of the present work, the model predicts that short GRBs from CBO mergers are efficient neutrino emitters. Our model does not require choked jets, unlike Ref. [118, 444]. The CRs accelerated in the successful jet can efficiently interact with disk photons and produce high-energy neutrinos via the photomeson production process. Using equations 8 and 9 of Ref. [445] and Fig. 6.3 of

this work, the photomeson optical depth is $f_{p\gamma} \sim 1$ for $\mathcal{R} \sim 10$ and $f_{p\gamma} \sim 0.1$ for $\mathcal{R} \sim 100$. High-energy neutrinos are expected in the PeV range, and they will make additional contribution to those predicted by Ref. [446]. The enhancement is more prominent for prompt neutrino emission, because the efficiency is low for usual short GRBs.

In conclusion, future multi-messenger analyses of AGN short GRBs can provide unprecedented insights for understanding the formation and evolution of CBOs inside the AGN disks as well as on the origin of their high-energy emission.

Acknowledgements

We thank B. Theodore Zhang, Mukul Bhattacharya, Zsuzsa Márka and Szabolcs Márka for fruitful discussions. C.C.Y. and P.M. acknowledge support from the Eberly Foundation. The work of K.M. is supported by the NSF Grant No. AST-1908689, No. AST-2108466 and No. AST-2108467, and KAKENHI No. 20H01901 and No. 20H05852. A.P. is supported by the European Research Council via ERC consolidating grant 773062 (acronym O.M.J.). I.B. acknowledges the support of NSF under awards PHY-1911796 and PHY-2110060 and the Alfred P. Sloan Foundation.

Disclaimer

The findings and conclusions do not necessarily reflect the view of the funding agencies.

Chapter 7
Complementarity of Stacking and Multiplet Constraints on the Blazar Contribution to the Cumulative Diffuse Neutrino Flux

Note: The material in this Chapter is based on my paper [447], with co-authors Kohta Murase, and Peter Mészáros.

7.1 Introduction

Since the initial detection of high-energy astrophysical neutrinos by the IceCube Neutrino Observatory [263, 264], a cumulative flux of astrophysical neutrinos in the energy range from $\sim$ 10 TeV to several PeV has been unveiled and measured to a higher precision [26, 188, 265]. The isotropic distribution of the cumulative flux as well as the background-only results from recent searches for point-like sources and multi-messenger analyses support an extragalactic origin of these neutrinos [131, 448, 449]. Up to now, however, the main origin of the cumulative neutrinos still remains unknown.

The flavor ratio measured at Earth, $(\nu_e : \nu_\mu : \nu_\tau) \approx (1 : 1 : 1)$, is consistent with the prediction from the long-distance oscillations of neutrinos produced through pion decays [450], which provides one common framework for the astrophysical models dedicated to explain the cumulative neutrino flux. Many candidates have been proposed and studied [451, 452]. Among these candidates, blazars, which are known as a subclass of AGNs with a relativistic jet pointing nearly towards the Earth [453, 454], have

been frequently considered as promising ultra-high-energy cosmic-ray (CR) accelerators and high-energy neutrino emitters [52, 455–457]. Recently, the IceCube collaboration announced the spatial and temporal coincidence between a muon track neutrino event IceCube170922A and a blazar TXS 0506+056 [122] at the significance $\sim 3\sigma$. Intuitively, if this association is physical, the intimate link between this IceCube neutrino event and the blazar may favor blazars as the main sources of the cumulative neutrino flux, but this is not the case [123].

The maximum likelihood stacking searches for cumulative neutrino flux from the second *Fermi*-LAT AGN catalog (2LAC) as well as the point-source searches using the IceCube muon track events and blazars in *Fermi*-LAT 3LAC have independently shown that *Fermi*-LAT-resolved blazars only contribute a small portion of the IceCube cumulative neutrino flux [124–126] and the hadronic models of blazar activity are strongly constrained [127], if the specific correlation $L_\nu \propto L_{\rm ph}$ is assumed as a prior. Ref. [128] evaluated the contribution of unresolved sources, and showed that the blazar contribution to the cumulative neutrino flux is constrained unless one makes an ad hoc assumption that lower-luminosity blazars entrain a larger amount of CRs.

Here we argue that, in addition to the stacking analysis, the absence of clustering in high-energy neutrino events, i.e., neutrino multiplets and auto-correleation, can also provide relevant constraints on various classes of proposed sources as the dominant origin of the cumulative neutrino flux [129–134]. The constraints are sensitive to the redshift evolution of the sources, which are especially powerful for weakly or non-evolving sources such as BL Lac objects [123, 129]. But the limits are weaker for rapidly evolving sources such as FSRQs, which could significantly alleviate the constraints, as remarked by Ref. [123]. Ref. [135] studied the constraints on evolving blazar populations and confirmed that fast evolving sources (e.g., $\xi_z = 5.0$) may indeed relax the neutrino multiplet limits.

In this work, we consider the "joint" implications of these independent analyses for the global blazar population and extend the constraints to a common case where a generic relationship between neutrino and gamma-ray luminosities, e.g., $L_\nu \propto (L_{\rm ph})^{\gamma_{\rm lw}}$, is presumed, which is more general than what has been previously considered in such analyses. Physically, the correlation between L_ν and $L_{\rm ph}$ is determined by the interactions between particles and radiation fields inside the sources. Most of physically reasonable models developed on the basis of photohadronic (e.g., $p\gamma$) interactions predict $L_\nu \propto (L_{\rm ph})^{\gamma_{\rm lw}}$ with indices of $1.0 \lesssim \gamma_{\rm lw} \lesssim 2.0$ [48, 51, 52, 123, 129, 458–461]. The index $\gamma_{\rm lw}$ characterizes the source models and may deviate from this fiducial range for models with increasing complexity. Motivated by this, we treat $\gamma_{\rm lw}$ as a free parameter and attempt to

reveal the $\gamma_{\rm lw}$-dependence of the upper limits on all-blazar contributions. In addition, a new feature of our analysis is that we also consider the effect of *Fermi*-unresolved blazars. One caveat is that, in this study, we assume all sources are equal and emit steadily with a single power-law spectrum. Prior to the the IceCube-170922A alert, IceCube collaboration has found a neutrino excess from the direction of TXS 0506+056 during a 158-day time window in 2014-2015 [266], which reveals the the transient nature of the neutrino emission. We need to keep in mind that the multiplet limits are stronger for flaring sources [123]. The stacking limits are also applicable to time-averaged emission of the flaring sources, as long as the scaling between neutrino and gamma-ray luminosities hold [123].

In the first part (Sec. 7.2), we calculate the ratio of neutrino fluxes from *Fermi*-LAT-resolved blazars and all blazars (including both resolved and unresolved contributions). Combining this ratio with the existing constraints on *Fermi*-LAT-resolved blazars, we estimate the upper limits for all-blazar contributions. The multiplet constraints are given in the second part (Sec. 7.3) where we also derive the effective number densities $n_0^{\rm eff}(\gamma_{\rm lw})$ and the redshift evolution factor $\xi_z(\gamma_{\rm lw})$ for blazars and the subclasses, FSRQs and BL Lacs. In either case, we use the blazar gamma-ray luminosity functions provided by Refs. [462–464] to reconstruct the neutrino luminosity density. In Sec. 7.4 we conclude with a discussion.

7.2 Implications of Stacking Limits

Given the differential density of blazars as a function of rest-frame 100 MeV-100 GeV luminosity $L_{\rm ph}$, redshift z and photon index Γ defined by the gamma-ray flux $F \propto \varepsilon_{\rm ph}^{-\Gamma}$,

$$\frac{d^3N_{\rm bl}}{dL_{\rm ph}dzd\Gamma} = \phi_{\rm bl}(L_{\rm ph}, z)\frac{dP_{\rm bl}}{d\Gamma}\frac{dV}{dz}, \tag{7.1}$$

where the subscript "bl" represents blazars considered in the calculation, $\phi_{\rm bl}(L_{\rm ph}, \Gamma) = d^2N_{\rm bl}/dL_{\rm ph}dV$ is the luminosity function and $dP_{\rm bl}/d\Gamma$ is the probability distribution of spectral index Γ, we can directly write down the (differential) luminosity density of neutrinos from *Fermi*-LAT-resolved blazars at redshift z,

$$\begin{aligned}\varepsilon_\nu Q_{\varepsilon_\nu}^{\rm (bl,R)}(z, \gamma_{\rm lw}) = \int_{L_{\rm ph,th}}^{L_{\rm ph,max}} \int_{\Gamma_{\rm min}}^{\Gamma_{\rm max}} \mathcal{C}^{-1}\phi_{\rm bl}(L_{\rm ph}, z)L_\nu(L_{\rm ph}) \\ \times \frac{dP_{\rm bl}}{d\Gamma}d\Gamma dL_{\rm ph}\end{aligned} \tag{7.2}$$

where $L_\nu \propto (L_{\rm ph})^{\gamma_{\rm lw}}$ is the neutrino luminosity, $L_{\rm ph,max}$ is a fixed upper limit of blazar luminosity and the lower limit $L_{\rm ph,th}(L_{\rm ph}, z, \Gamma)$ is determined by the *Fermi* LAT threshold flux $F_{100,\rm th}$ in the energy range of 100 MeV – 100 GeV. In this equation, $\mathcal{C}$ is the normalization coefficient determined by $\varepsilon_{\rm CR,max}$ and $\varepsilon_{\rm CR,min}$, the maximum and minimum energy that CRs in blazars can achieve. Since we aim to estimate the neutrino flux from a general luminosity relationship, $L_\nu \propto (L_{\rm ph})^{\gamma_{\rm lw}}$, and the physics may be unknown for a general $\gamma_{\rm lw}$, we do not try to provide the details of the gamma-ray and neutrino radiation processes. In this work, we assume that the maximum CR energy is the same for all blazars, as is the normalization factor once the spectral index s of the IceCube neutrino flux is specified.

Here, we present one method to rewrite the integrals in equation 7.2 by incorporating the *Fermi*-LAT detection efficiency. For a blazar at redshift z with the luminosity $L_{\rm ph} \propto \int_{\varepsilon_{\rm min}}^{\varepsilon_{\rm max}} F(\varepsilon)\varepsilon d\varepsilon$, where $\varepsilon_{\rm max} = 100(1+z)$ GeV and $\varepsilon_{\rm min} = 100(1+z)$ MeV, and the photon index Γ, the integrated photon flux at earth can be written as

$$\begin{aligned} F_{100}(L_{\rm ph}, z, \Gamma) &= \int_{\varepsilon_{\rm min}}^{\varepsilon_{\rm max}} F(\varepsilon) d\varepsilon \\ &= \frac{L_{\rm ph}}{4\pi d_L^2(z)} \times \begin{cases} \ln\left(\frac{\varepsilon_{\rm max}}{\varepsilon_{\rm min}}\right) \frac{1}{\varepsilon_{\rm max}-\varepsilon_{\rm min}} & \Gamma = 1 \\ \frac{\varepsilon_{\rm max}-\varepsilon_{\rm min}}{\varepsilon_{\rm max}\varepsilon_{\rm min}\ln\left(\frac{\varepsilon_{\rm max}}{\varepsilon_{\rm min}}\right)} & \Gamma = 2 \\ \frac{2-\Gamma}{1-\Gamma}\frac{\varepsilon_{\rm max}^{1-\Gamma}-\varepsilon_{\rm min}^{1-\Gamma}}{\varepsilon_{\rm max}^{2-\Gamma}-\varepsilon_{\rm min}^{2-\Gamma}} & \Gamma \neq 1, 2, \end{cases} \end{aligned} \tag{7.3}$$

where d_L is the luminosity distance between the blazar and the detector. Then the lower limit of the integral in equation 7.2 can be obtained by requiring $F_{100}(L_{\rm ph,th}, z, \Gamma) = F_{100,\rm th}$. Alternatively, thanks to the *Fermi*-LAT detection efficiency $\epsilon(F_{100})$ provided by Ref. [465], we can simplify equation 7.2 by using the equivalent detection efficiency $\epsilon(L_{\rm ph}, z, \Gamma) = \epsilon(F_{100})$,

$$\begin{aligned} \varepsilon_\nu Q_{\varepsilon_\nu}^{\rm (bl,R)}(z, \gamma_{\rm lw}) = \int_{L_{\rm ph,min}}^{L_{\rm ph,max}} \int_{\Gamma_{\rm min}}^{\Gamma_{\rm max}} \mathcal{C}^{-1} \phi_{\rm bl}(L_{\rm ph}, z) L_\nu(L_{\rm ph}) \\ \times \epsilon(L_{\rm ph}, z, \Gamma) \frac{dP_{\rm bl}}{d\Gamma} d\Gamma dL_{\rm ph}, \end{aligned} \tag{7.4}$$

where the lower limit $L_{\rm ph,min}$ reduces to a constant and represents the minimal luminosity of blazars that are considered in this work. To eliminate the instrumental selection effect produced by the low detection efficiency for dimmer blazars and to take all blazars into account, we replace the $L_{\rm ph,th}$ in equation 7.2 by $L_{\rm ph,min}$, which yields the neutrino

luminosity density from all blazars $\varepsilon_\nu Q_{\varepsilon_\nu}^{(\rm bl,all)}(z,\gamma_{\rm lw})$, which can be written explicitly as

$$\begin{aligned}\varepsilon_\nu Q_{\varepsilon_\nu}^{(\rm bl,all)}(z,\gamma_{\rm lw}) = &\int_{L_{\rm ph,min}}^{L_{\rm ph,max}}\int_{\Gamma_{\rm min}}^{\Gamma_{\rm max}} \mathcal{C}^{-1}\phi_{\rm bl}(L_{\rm ph},z)L_\nu(L_{\rm ph}) \\ &\times \frac{dP_{\rm bl}}{d\Gamma}d\Gamma dL_{\rm ph}.\end{aligned} \tag{7.5}$$

Meanwhile, using the LFs for luminosity-dependent density evolution (LDDE) models and parameters provided by Refs. [463, 464], we successfully reproduced the redshift evolution of FSRQ and BL Lac luminosity densities illustrated in the Figure 6 of Ref. [464]. At this stage, during the integration of $L_{\rm ph}$, we set the maximum and minimum luminosities to be 10^{50} erg s^{-1} and 10^{40} erg s^{-1}, respectively. We also found that the results are consistent with the uncertainties in Ref. [464] when the limits of the integration were varied by one or two orders of magnitude. Another thing that we need to keep in mind is that we assume the *Fermi*-LAT-unresolved blazars share the identical LFs with the resolved ones. Ref. [466] pointed that the index distributions for different blazar classes both for the detected ones and undetected ones are slightly different: the photon spectra of newly-detected FSRQs are slightly softer than the 2LAC ones ($\Delta\Gamma < 0.1$) while in contrast there is no significant spectral difference between the two sets of BL Lacs. For the completeness, we also consider a deviation, e.g., 0.2, of the photon spectral index from the best-fit values provided by Refs. [462–464]. Such a test reveals that the resulting $\mathcal{F}(\gamma_{\rm lw})$ remains almost unchanged under a slight derivation of Γ.

Assuming the neutrino spectra from all blazars have the similar power-law form, e.g., $\varepsilon_\nu^2\Phi_{\varepsilon_\nu} \propto \varepsilon_\nu Q_{\varepsilon_\nu}^{(\rm bl,R/all)} \propto \varepsilon_\nu^{2-s}$, and using the comoving neutrino luminosities $\varepsilon_\nu Q_{\varepsilon_\nu}^{(\rm bl,all)}(z,\gamma_{\rm lw})$ and $\varepsilon_\nu Q_{\varepsilon_\nu}^{(\rm bl,R)}(z,\gamma_{\rm lw})$, the all-flavor neutrino fluxes from *Fermi*-LAT-resolved and all blazars at earth are expected to be

$$E_\nu^2\Phi_{E_\nu}^{(\rm bl,R/all)}(\gamma_{\rm lw}) = \frac{c}{4\pi}\int dz\ \frac{\varepsilon_\nu Q_{\varepsilon_\nu}^{(\rm bl,R/all)}(z,\gamma_{\rm lw})}{(1+z)}\left|\frac{dt}{dz}\right|, \tag{7.6}$$

where $\varepsilon_\nu = (1+z)E_\nu$. Hence, we can write down the fraction of *Fermi*-LAT-resolved blazars to the cumulative neutrino flux in a simple way that depends only on $\gamma_{\rm lw}$,

$$\mathcal{F}(\gamma_{\rm lw}) = \frac{E_\nu^2\Phi_{E_\nu}^{(\rm bl,R)}(\gamma_{\rm lw})}{E_\nu^2\Phi_{E_\nu}^{(\rm bl,all)}(\gamma_{\rm lw})}. \tag{7.7}$$

Ref. [462] presented the best-fit parameters in the blazar luminosity functions $\phi_{\rm bl}$, which enables us to compute $\mathcal{F}(\gamma_{\rm lw})$. Since the redshift correction to the energies leads to one

extra term $(1+z)^{2-s}$ to the integrand in equation 7.6 and another factor $(1+z)^{-1}$ to the integrated flux in equation 7.3, we conclude that, as a consequence, low-redshift blazars become more important when $s = 2.5$, in comparison with the $s = 2$ case. Therefore, considering nearby blazars are easier to be detected, a steeper neutrino spectrum predicts a larger $\mathcal{F}(\gamma_{\rm lw})$, which is confirmed by the thin lines in Fig. 7.1. Moreover, noting that the selection of the minimum and maximum luminosities, e.g., $L_{\rm ph,min}$ and $L_{\rm ph,max}$ of a blazar is arbitrary, we tested the reliability of $\mathcal{F}(\gamma_{\rm lw})$ by varying the integral limits and found that the results are not sensitive to $L_{\rm ph,max}$ and $\mathcal{F}(\gamma_{\rm lw})$ does not change dramatically in the range $\gamma_{\rm lw} \lesssim 1.0$ as $L_{\rm ph,min}$ increases from 10^{41} erg s^{-1} to 10^{43} erg s^{-1}, as shown in Fig. 7.1. Intuitively, a lower $L_{\rm ph,min}$ implies that more low-luminosity blazars in the sample are less likely to be detected. Also, for a weaker luminosity dependance ($\gamma_{\rm lw} \lesssim 1.0$), the low-luminosity blazars dominate the luminosity density due to the large population. The combined effect is that $\mathcal{F}(\gamma_{\rm lw})$ decreases in the range $\gamma_{\rm lw} \lesssim 1.0$. Remarkably, from Fig. 7.1, we can conclude that the contribution from *Fermi*-LAT-resolved blazars is nearly the same as the neutrino flux from all blazars when $\gamma_{\rm lw}$ is larger than 1.0. The reason is that, assuming a stronger luminosity dependance (on other words, a higher $\gamma_{\rm lw}$), the brighter blazars become increasingly important. These high-luminosity blazars have a higher chance to be detected and in this case the neutrinos luminosity densities from *Fermi*-LAT-resolved blazars and all blazars are comparable.

To compute the upper limit of cumulative neutrino flux from all blazars, we use the existing constraints, $E_\nu^2\Phi_{E_\nu}^{\rm (2LAC,stacking)}$ and $E_\nu^2\Phi_{E_\nu}^{\rm (3LAC,stacking)}$, from blazar stacking analyses and point-source searches [124, 126], which are based on *Fermi*-LAT 2LAC and 3LAC blazars. Combining these existing limits with the fraction of the neutrino flux from *Fermi*-LAT-resolved blazars, we estimate the upper limits of all-blazar contributions from *Fermi*-LAT 2LAC and 3LAC analysis,

$$E_\nu^2\Phi_{E_\nu}^{\rm (2LAC/3LAC)} = \frac{E_\nu^2\Phi_{E_\nu}^{\rm (2LAC/3LAC,stacking)}}{\mathcal{F}(\gamma_{\rm lw})}. \tag{7.8}$$

The stacking results themselves have some model dependence. Here, to obtain conservative limits, we adopt the results based on the equal flux weighting for $E_\nu^2\Phi_{E_\nu}^{\rm (2LAC/3LAC,stacking)}$. In general this gives conservative limits, and the luminosity weighting improves the constraints. We will see that, even in this most conservative case, the combined constraints of stacking and multiplet analysis are stringent.

Fig. 7.2 illustrates the upper limits for the all-blazar neutrino flux from *Fermi*-LAT 2LAC and *Fermi*-LAT 3LAC analysis. We show all-flavor neutrino fluxes for

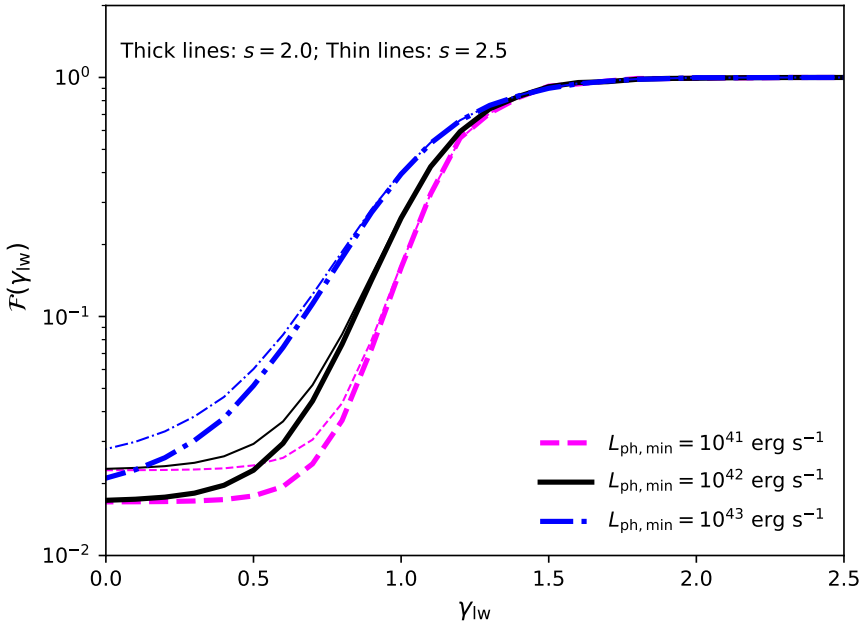

Figure 7.1. The fraction of *Fermi*-LAT-resolved blazars in the cumulative neutrino flux, $\mathcal{F}(\gamma_{\rm lw})$. The thick and thin lines are calculated for the neutrino spectral indices $s = 2.0$ and $s = 2.5$. The blue dashed, black solid and red dash-dotted lines correspond to the minimum luminosities $L_{\rm ph,min} = 10^{41}$ erg s^{-1}, 10^{42} erg s^{-1} and 10^{43} erg s^{-1}, respectively. The upper limit is fixed to be $L_{\rm ph,max} = 10^{50}$ erg s^{-1}.

all curves and data points in this figure. In the left panel, we assume $s = 2$ for the neutrino spectrum. In this case, the stacking analysis of *Fermi*-LAT-2LAC blazars gives $1.2\times10^{-8} \lesssim E_\nu^2\Phi_{E_\nu}^{\rm (2LAC,stacking)} \lesssim 1.6\times10^{-8}$ (in the unit of GeV cm^{-2} s^{-1} sr^{-1}, hereafter). The corresponding upper limits for all blazars calculated using equation 7.8 are illustrated as the magenta area. The green area in the left panel shows the constraints derived from *Fermi*−LAT 3LAC analysis which predicts $8.0\times10^{-9} \lesssim E_\nu^2\Phi_{E_\nu}^{\rm (3LAC,stacking)} \lesssim 1.4\times10^{-8}$. For the illustration purpose, we include the IceCube all-flavor neutrino flux $4.8\times10^{-8} \lesssim E_\nu^2\Phi_{E_\nu}^{\rm (IC)} \lesssim 8.4\times10^{-8}$ in Fig. 7.2 (the cyan area). To avoid underestimating the upper limits due to the uncertainties of the existing results, we introduced a 50% uncertainty to the constraints derived from stacking analysis, which broadens the areas in the left panel of Fig. 7.2. The right panel shows the energy-dependent upper limits for an $\varepsilon_\nu^{-2.5}$ neutrino spectrum. The solid lines are obtained by assuming $\gamma_{\rm lw} = 1.0$ whereas the dashed lines correspond to the case $\gamma_{\rm lw} = 2.0$. The upper limits from *Fermi*-LAT 2LAC and 3LAC analysis are illustrated as magenta lines and green lines, respectively. In this figure, we showed also the all-flavor neutrinos flux (red points, [26, 188]), the 6-year

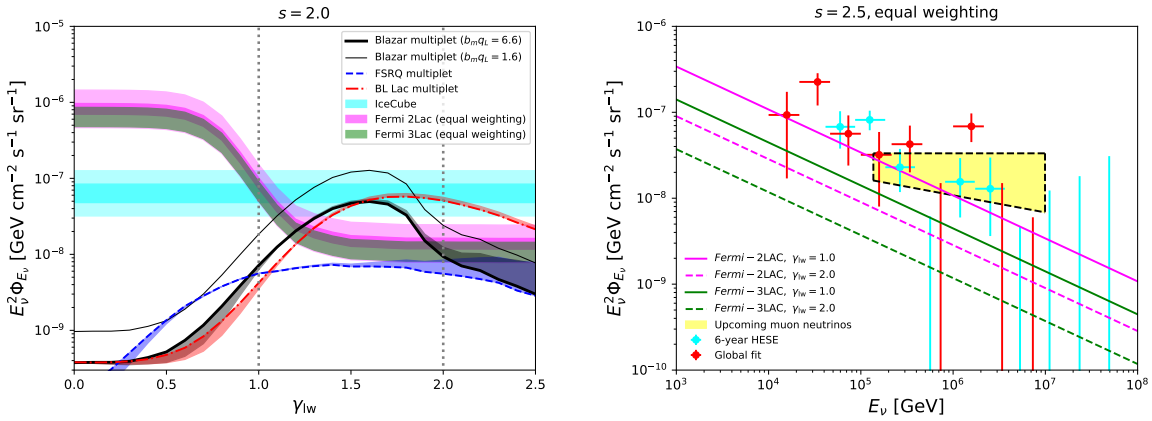

Figure 7.2. All curves and data points in this figure illustrate all-flavor neutrino fluxes. Left panel: Stacking constraints on the contributions of all blazars to the cumulative neutrino flux ($L_{\rm ph,min} = 10^{42}$ erg s^{-1} is used) and high-energy neutrino multiplet constraints on the blazar contributions in the neutrino sky for an ε_ν^{-2} neutrino spectrum. The magenta and green areas correspond to the all-blazar upper limit from *Fermi*-LAT-2LAC and *Fermi*−3LAC equal weighting analysis, respectively. The cyan horizontal area shows the cumulative neutrino flux detected by IceCube. The blue dashed, red dash-dotted and thick black lines illustrate the $m \geq 2$ multiplet constraints for FSRQs, BL Lacs and all blazars whereas the corresponding areas show the uncertainties. The thin black line is the $m \geq 3$ multiplet constraint for all blazars. Right panel: the energy-dependent upper limits from the stacking analysis for the all-blazar contributions, assuming a neutrino spectral index $s = 2.5$.

high-energy starting events (cyan points, [189]) and the the best fit to the upcoming muon neutrinos scaled to three-flavor case (yellow area). The previous discussion reveals that $\mathcal{F}(\gamma_{\rm lw})$ may depend on $L_{\rm ph,min}$ moderately, when $\gamma_{\rm lw}$ is smaller than 1.0. We will further demonstrate in Sec. 7.3 that, in the range of $\gamma_{\rm lw} \lesssim 1.0$, the neutrino multiplet constraints are more stringent than the upper limits derived from the stacking analyses, which manifests its complementarity in constraining the cumulative neutrino flux from all blazars over a wide range of $\gamma_{\rm lw}$.

7.3 Implications of High-Energy Neutrino Multiplet Limits

Here, we present another type of constraints on the origins of IceCube diffuse neutrinos, using the negative results from the clustering test of neutrino-induced muon track events. These high-energy track events are generally detected by IceCube with the angular resolution ~ 0.5 deg, which enables us to determine the incoming directions and perform

clustering analysis on their time and spatial distributions. So far, all the clustering tests based on high-energy muon neutrinos have found no statistically significant evidence of clustering in the arrival distribution of neutrinos [265, 467–469].

In this section, we investigate the implications of the non-detection of neutrino multiplet sources, and consider the limits on blazar contributions to the cumulative neutrino background. To achieve this goal, we follow Ref. [129] and write down the limits on the effective source densities. The formalism presented by Ref. [129] is applicable to blazars with a general luminosity weighting $L_\nu \propto (L_{\rm ph})^{\gamma_{\rm lw}}$ since the functions $L_\nu(dN_{\rm bl}/dL_{\rm ph}) \propto (L_{\rm ph})^{\gamma_{\rm lw}+1}\phi_{\rm bl}$ are sharply peaked around some effective luminosities $L_{\rm ph}^{\rm eff}$, which demonstrates that the effective source densities and the neutrino luminosity densities are well defined and constrained. Below, we define these crucial quantities and derive the neutrino multiplet constraints for our blazar case.

Assuming the number of sources that produce more than $k-1$ multiplet events is $N_{m\geq k}$, the constraint from the non-detection of $m \geq k$ multiplet events can be obtained by requiring $N_{m\geq k} \leq 1$. Ref. [129] studied the implications to the neutrino sources using the absence of "high-energy" multiplet neutrino sources, and calculated the upper limit on the local source number density for an ε_ν^{-2} neutrino spectrum,

$$
\begin{aligned}
n_0^{\rm eff} \lesssim 1.9\times10^{-10}\ {\rm Mpc}^{-3} &\left(\frac{\varepsilon_\nu L_{\varepsilon_\nu}^{\rm ave}}{10^{44}\ {\rm erg\ s^{-1}}}\right)^{-3/2}\left(\frac{b_m q_L}{6.6}\right)^{-1} \\
&\times\left(\frac{F_{\rm lim}}{10^{-9.2}\ {\rm GeV\ cm^{-2}\ s^{-1}}}\right)^{3/2}\left(\frac{2\pi}{\Delta\Omega}\right),
\end{aligned}
\tag{7.9}
$$

where $\varepsilon_\nu L_{\varepsilon_\nu}^{\rm ave}$ is the time-averaged neutrino luminosity of the source, $F_{\rm lim} \sim (5-6)\times 10^{-10}$ GeV cm^{-2} s^{-1} is the 8-year IceCube point-source sensitivity at the 90% confidence level [470], $q_L \sim 1-3$ denotes a luminosity-dependent correction factor, $\Delta\Omega$ represents the sky coverage of the detector and the details of $m \geq k$ neutrino multiplet constraints are encoded in the factor b_m. Ref. [129] find $b_m \simeq 6.6$ for $m \geq 2$ multiplets and $b_m \simeq 1.6$ for triplets or higher multiplets (e.g., $m \geq 3$). Note that the point-source sensitivity enters the above expression but the numerical results are obtained by calculating the number of tracks using the muon effective area [129].

The purpose of this work is to explore the implications for blazar models using existing equations from previous work without making new analyses on multiplet sources. We simply use the results of the previous analysis by Ref. [129], which gives the upper limit on the effective number density, $n_0^{\rm eff}(\varepsilon_\nu L_{\varepsilon_\nu}^{\rm ave})$. Moreover, another reason that we choose this approach is that these results are also consistent with the latest limits on transient

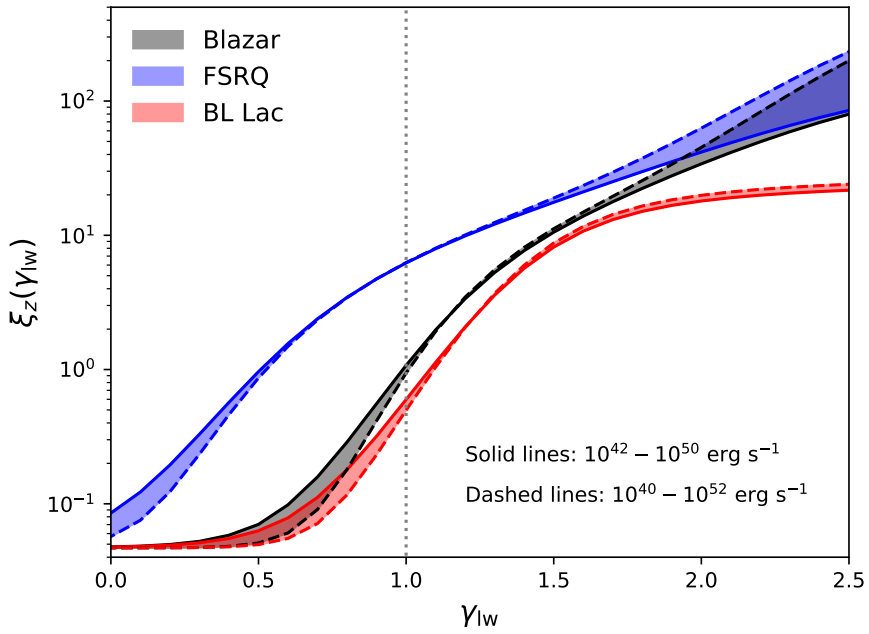

Figure 7.3. The redshift evolution factor ξ_z for FSRQs (blue area), BL Lacs (red area) and all blazars (black area). The solid and dashed boundaries correspond to different schemes of $L_{\rm ph,min}$ and $L_{\rm ph,max}$.

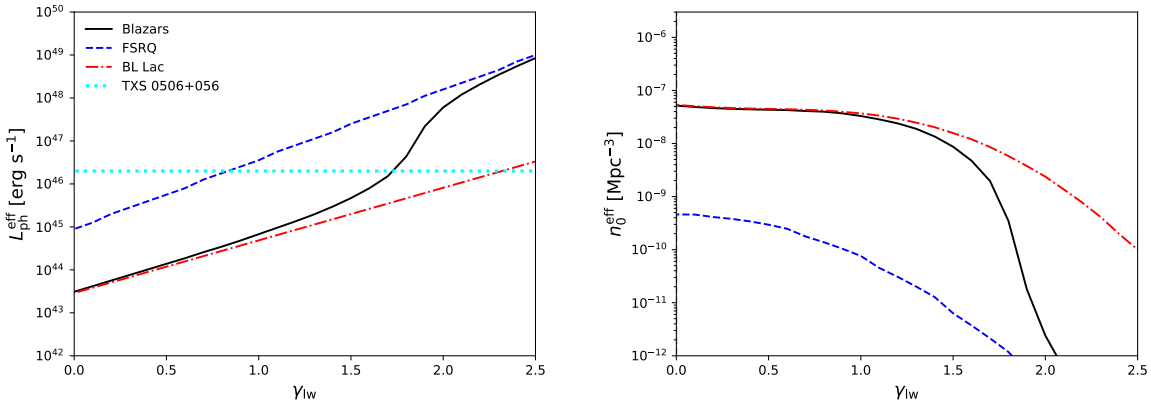

Figure 7.4. Left panel: The effective gamma-ray luminosity for FSRQs (blue dashed line), BL Lacs (red dash-dotted line) and all blazars (black line). The dotted horizontal line indicates the luminosity of TXS 0506+056, one blazar that features an intermediate luminosity, $L_{\rm TXS} \simeq 10^{46.3}$ erg s^{-1} [123]. Right panel: The effective local number densities for different source classes. The line styles in this panel have the same meaning as the left panel.

sources (after the number density is converted into the rate density, [471]) [1]

One can write the limit on the cumulative neutrino flux from the sources as a function of $n_0^{\rm eff}$ and the redshift evolution factor ξ_z [123]:

$$\begin{aligned} E_\nu^2 \Phi_{E_\nu}^{\rm (m)} &\approx \frac{3\xi_z c t_H}{4\pi} n_0^{\rm eff} (\varepsilon_\nu L_{\varepsilon_\nu}^{\rm ave}) \\ &\lesssim 6.9\times10^{-9}\ {\rm GeV cm^{-2} s^{-1} sr^{-1}} \left(\frac{\Delta\Omega}{2\pi}\right)^{2/3} \left(\frac{\xi_z}{0.7}\right) \\ &\times \left(\frac{b_m q_L}{6.6}\right)^{-2/3} \left(\frac{n_0^{\rm eff}}{10^{-7}\ {\rm Mpc^{-3}}}\right)^{1/3} \\ &\times \left(\frac{F_{\rm lim}}{10^{-9.2}\ {\rm GeV\ cm^{-2}\ s^{-1}}}\right), \end{aligned} \tag{7.10}$$

where t_H is the Hubble time. In this expression, ξ_z represents the redshift weighting of the neutrino luminosity of the sources and can be evaluated through [347]

$$\xi_z(\gamma_{\rm lw}) = \frac{\int dz (1+z)^{-1} \left|\frac{dt}{dz}\right| f(z,\gamma_{\rm lw})}{\int dz \left|\frac{dt}{dz}\right|}, \tag{7.11}$$

where $f(z,\gamma_{\rm lw})$ is the redshift evolution function of the neutrino luminosity density normalized to unity at $z=0$ for the luminosity correlation $L_\nu \propto (L_{\rm ph})^{\gamma_{\rm lw}}$, e.g., for blazars we have $f^{\rm (bl)}(z,\gamma_{\rm lw}) = [\varepsilon_\nu Q_{\varepsilon_\nu}^{\rm (bl,all)}(z,\gamma_{\rm lw})]/[\varepsilon_\nu Q_{\varepsilon_\nu}^{\rm (bl,all)}(0,\gamma_{\rm lw})]$. Similarly, we can also calculate the ξ_z for the blazar subclasses, FSRQs and BL Lacs using the luminosity functions from Refs. [463, 464]. The black, blue and red areas in Fig. 7.3 illustrate the redshift evolution factor $\xi_z(\gamma_{\rm lw})$ for all blazars, FSRQs and BL Lacs, respectively. When $\gamma_{\rm lw}=1$, we find $\xi_z \sim 7-8$ for the gamma-ray luminosity density evolution of FSRQs and $\xi_z \sim 0.6-0.7$ for that of BL Lacs, which are consistent with the values found by Refs. [48] and [129]. The solid and dashed boundaries in Fig. 7.3 correspond to the sample schemes, ($L_{\rm ph,min}=10^{42}$ erg s^{-1}, $L_{\rm ph,max}=10^{50}$ erg s^{-1}) and ($L_{\rm ph,min}=10^{40}$ erg s^{-1}, $L_{\rm ph,max}=10^{52}$ erg s^{-1}), respectively. If $\gamma_{\rm lw}$ is lower than 1.0, low-luminosity sources at lower redshift contribute a significant component to the total neutrino luminosity density, therefore, a smaller $L_{\rm ph,min}$ results in a smaller ξ_z. On the

[1] The limit on the rate density of neutrino transients accounting for the diffuse flux is $\rho_0^{\rm eff} \gtrsim 1.7\times10^4\,{\rm Gpc^{-3}\,yr^{-1}}\,(b_m q_L/6.6)^2(\Delta\Omega/2\pi)^2(T_{\rm obs}/8\ {\rm yr})^2(\xi_z/0.7)^{-3}\phi_{\rm lim,-1}^{-3}$ $\max[N_{\rm fl},1]$, where $N_{\rm fl}\approx f_{\rm fl}T_{\rm obs}/t_{\rm dur}\approx T_{\rm obs}/\Delta T_{\rm fl}$ is the number of flaring periods and $\Delta T_{\rm fl}$ is the typical flare interval [123]. For $\Delta T_{\rm fl}\lesssim T_{\rm obs}$, the density and diffuse limits become similar to those for steady sources. Substituting the time-averaged sensitivity gives conservative results because of $F_{\rm lim}>\phi_{\rm lim}/T_{\rm obs}$. For $\Delta T_{\rm fl}\gtrsim T_{\rm obs}$, we expect $\rho_0^{\rm eff}T_{\rm obs}\approx n_0^{\rm eff}(T_{\rm obs}/\Delta T_{\rm fl})$. Because of $n_0^{\rm eff}(T_{\rm obs}/\Delta T_{\rm fl})\lesssim n_0^{\rm eff}$, the limits for steady sources can be regarded as conservative.

contrary, a strong luminosity correlation with $\gamma_{\rm lw} \gtrsim 1.5$ boosts the contribution from high-redshift bright blazars, which leads to a larger $f(z, \gamma_{\rm lw})$ at higher redshift and as a result makes ξ_z larger, as $L_{\rm ph,max}$ increases.

Besides the factor ξ_z, it is also necessary to calculate the effective local number density $n_0^{\rm eff}$, which characterizes the the number density of sources that dominate the neutrino luminosity density for each specified source population. In this work, we use the luminosity functions in combination with the luminosity weighting relation $L_\nu \propto (L_{\rm ph})^{\gamma_{\rm lw}}$ to estimate the effective number densities $n_0^{\rm eff}$ for blazars, FSRQs and BL Lacs. Here, we follow the procedure presented by Ref. [129]. For each class of neutrino sources, we define an effective neutrino luminosity $L_\nu^{\rm eff} \propto (L_{\rm ph}^{\rm eff})^{\gamma_{\rm lw}}$ using the corresponding effective gamma-ray luminosity $L_{\rm ph}^{\rm eff}$ obtained by maximizing $(L_{\rm ph})^{\gamma_{\rm lw}}(dN/d\ln L_{\rm ph}) = (L_{\rm ph})^{\gamma_{\rm lw}+1}\phi(L_{\rm ph}, z=0)$, where $\phi(L_{\rm ph}, z=0)$ is the local luminosity function of the sources that we are interested in. Since the function $(L_{\rm ph})^{\gamma_{\rm lw}+1}\phi(L_{\rm ph}, z=0)$ has a maximum around its extreme point for each source population, we may regard blazars, FSRQs and BL Lacs as "quasi-standard candle" sources, among which the neutrino productions are dominated by the sources distributed closely around one certain effective luminosity $L_{\rm ph}^{\rm eff}$. In this case, we have justified the applicability of the equation appeared in this section to constrain the neutrino fluxes from blazars and the subclasses. The left panel of Fig. 7.4 shows the effective gamma-ray luminosity densities for all blazars (black solid line), FSRQs (blue dashed line) and BL Lacs (red dash-dotted line). Intuitively, $L_{\rm ph}^{\rm eff}$ of FSRQ should be larger than that of BL Lacs since FSRQs are more luminous than BL Lacs. Moreover, the function $(L_{\rm ph})^{\gamma_{\rm lw}+1}\phi(L_{\rm ph}, z=0)$ achieves its maximum at higher luminosity as $\gamma_{\rm lw}$ increases, which naturally explains the monotonic increase of $L_{\rm ph}^{\rm eff}(\gamma_{\rm lw})$. Considering that low-luminosity BL Lacs dominate the neutrino luminosity density if the luminosity correlation is weak (e.g., $\gamma_{\rm lw} \lesssim 1$) whereas bright FSRQs become increasingly important as $\gamma_{\rm lw}$ increases, the blazar effective luminosity $L_{\rm ph}^{\rm eff}$ converges to the BL Lac case when $\gamma_{\rm lw}$ is less than 1.0 and then gradually approaches to the FSRQ curve, as is confirmed in Fig. 7.4. With the effective neutrino/gamma-ray luminosity, we can write down the effective local number density of the sources

$$n_0^{\rm eff} = \frac{1}{L_\nu^{\rm eff}} \int dL_{\rm ph} L_\nu(L_{\rm ph}) \phi(L_{\rm ph}, 0). \tag{7.12}$$

The right panel of Fig. 7.4 shows the effective number densities of all blazars (black solid line), FSRQs (blue dashed line) and BL Lacs (red dash-dotted line). As expected, BL Lacs dominate the number density and the blazar effective number density converges

to BL Lac and FSRQ curves respectively when $\gamma_{\rm lw} \lesssim 1.0$ and $\gamma_{\rm lw} \gtrsim 2.0$. Different from $\mathcal{F}(\gamma_{\rm lw})$ and ξ_z, $L_{\rm ph}^{\rm eff}$ and $n_0^{\rm eff}$ does not depend sensitively on the value of $L_{\rm ph,min}$ and $L_{\rm ph,max}$ in the range $0 \lesssim \gamma_{\rm lw} \lesssim 2.5$. To interpret this, we need to keep in mind that the former two quantities are determined by the integrations over $L_{\rm ph}$, while $L_{\rm ph}^{\rm eff}$ depends only on the shape/slope of the function $(L_{\rm ph})^{\gamma_{\rm lw}+1}\phi(L_{\rm ph}, z=0)$. From the left panel of Fig. 7.4, we find that $L_{\rm ph}^{\rm eff}$ lies roughly in the range $10^{43} - 10^{49}$ erg s^{-1} which is covered by the interval $10^{42} - 10^{50}$ erg s^{-1}, the fiducial range used in our calculation. Meanwhile, the integrand in equation 7.12 peaks around $L_{\rm ph}^{\rm eff}$, therefore once the peak is included, the effective number density $n_0^{\rm eff}$ will not vary too much as the lower and upper bounds of the integral changes.

The above calculations provide the preliminary work and the ingredients needed for calculating the neutrino multiplet limits. Selecting $b_m q_L \simeq 6.6$ for $m \geq 2$ multiplets and $F_{\rm lim} \simeq 10^{9.2}$ GeV cm^{-2} s^{-1} for an ε_ν^{-2} neutrino spectrum, the blue dashed, red dashed-dotted and thick black lines in the left panel of Fig. 7.2 illustrate the neutrino multiplet limits for FSRQs, BL Lacs and all blazars, respectively. The blue, red and black areas shows the corresponding uncertainties due to $L_{\rm ph,min}$ and $L_{\rm ph,max}$, as discussed before. From this figure we find that the all-blazar multiplet constraint converges to the FSRQ case at higher $\gamma_{\rm lw}$ and to the BL Lac case if $\gamma_{\rm lw}$ is less than 1.0, just as expected. We also considered the upper limits for triplet or higher multiplets ($m \geq 3$) by changing the value of $b_m q_L$ to 1.6. In this case, the constraints relax to the thin black line. This consequence can be interpreted as the concession of allowing blazars to produce $m = 2$ multiplet events. So far, all calculations on the multiplet constraints were based on the ε_ν^{-2} neutrino spectrum, and to extend the results to a general spectrum, e.g., $s = 2.5$, detailed calculations on $F_{\rm lim}$ and $n_0^{\rm eff}$ (equation 7.12) are needed, and our results are conservative in this point. Therefore, in the right panel of Fig. 7.2, only upper limits inferred from stacking analysis are shown.

7.4 Discussion

In this paper, we considered how two types of analyses, namely stacking and multiplets, constrain on the contribution of blazars to the cumulative neutrino flux, assuming a generalized luminosity weighting $L_\nu \propto (L_{\rm ph})^{\gamma_{\rm lw}}$. Using the gamma-ray luminosity functions for blazars, FSRQs and BL Lacs, we estimated the ratio of the neutrino fluxes from *Fermi*-LAT-resolved blazars and from all blazars (including unresolved ones), $\mathcal{F}(\gamma_{\rm lw})$, and the effective number densities, $n_0^{\rm eff}(\gamma_{\rm lw})$, and the redshift evolution

factor, ξ_z, for different source classes. The joint use of a stacking and multiplet analysis, as well as the use of a generalized luminosity function and inclusion of the effect of unresolved blazars, are new aspects which distinguish this analysis from previous ones. The main results are summarized in Figure 7.2. From this figure we found that the multiplet constraints are the most important at lower values of $\gamma_{\rm lw}$, e.g. $\gamma_{\rm lw} \lesssim 1.0$, whereas all-blazar constraints derived from the existing stacking upper limits are more stringent for a stronger luminosity correlation, e.g., $\gamma_{\rm lw} \gtrsim 1.5$. The joint consideration of these two kinds of limits supports the extended argument that all blazars, including *Fermi*−unresolved ones, are unlikely to dominate the cumulative neutrino background for a generic correlation between the neutrino and gamma-ray luminosities, $L_\nu \propto (L_{\rm ph})^{\gamma_{\rm lw}}$, with the index $0 \lesssim \gamma_{\rm lw} \lesssim 2.5$. Canonical blazar models, which are physically motivated and based on the leptonic scenario, predict $\gamma_{\rm lw} \sim 1.5 - 2.0$ [48]. Our results suggest that the stacking constraints are the most stringent for such physically motivated cases. The multiplet and stacking limits are "complementary", in the sense that these methods have their own advantages in different regimes, and in combination they provide a stronger and tighter constraint than previously, over a wide range of $\gamma_{\rm lw}$, as pointed out by Ref. [123]. We also found that while the multiplet constraints are weaker at larger values of $\gamma_{\rm lw}$ they become more stringent again for $\gamma_{\rm lw} \gtrsim 1.5$ due to the rapid decrease of the effective source density.

In this work, we focus on power-law spectra. The limits are stringent for the neutrino flux in the 0.1 PeV range and become weaker at higher energies. For example, neutrino multiplet limits are weaker if one is interested in the origin of ~ 1 PeV neutrinos [123, 128, 129]. It is possible for blazars to explain the dominant fraction of PeV neutrinos by introducing a lower-energy cutoff of the proton maximum energy [458], although neutrinos at 0.1 PeV and lower energies should come from another population of the sources [472].

One of the uncertainties in this work comes primarily from the selection of the lower and upper limits of the luminosity integral, $L_{\rm ph,min}$ and $L_{\rm ph,max}$. As discussed above, we showed that these uncertainties are well controlled, and the final results are reliable if $L_{\rm ph,min}$ and $L_{\rm ph,max}$ are selected in the fiducial ranges $10^{40} - 10^{42}$ erg s^{-1} and $10^{50} - 10^{52}$ erg s^{-1}, respectively. From the joint constraints illustrated in Fig. 7.2, we conclude that blazars are disfavored as a dominant source of the cumulative neutrino flux measured by IceCube for a luminosity weighting $L_\nu \propto (L_{\rm ph})^{\gamma_{\rm lw}}$ with $0.0 \lesssim \gamma_{\rm lw} \lesssim 2.5$. Since different blazar models considered for explaining the cumulative neutrino flux can be commonly characterized by the correlation index $\gamma_{\rm lw}$ within this range, our calculations on

the upper limits and effective number densities would provide rather general constraints for future studies of blazar neutrinos.

Acknowledgements

We thank Marco Ajello for useful discussion on the usage of the luminosity function and Nick Rodd for the useful communication. The work of K.M. is supported by the Alfred P. Sloan Foundation and NSF grants No. PHY-1620777 and No. AST-1908689, while that of C.C.Y and P.M. is supported by the Eberly Foundation.

Disclaimer

The findings and conclusions do not necessarily reflect the view of the funding agencies.

Chapter 8
Summary and Outlook

8.1 Summary

We are currently in the stage where we are able to unveil the nature of the extreme astrophysical phenomena with the synergies between electromagnetic photons, neutrinos, gravitational waves, and cosmic rays. In this thesis, we studied the neutrino and electromagnetic signals from various promising sources, such as galaxy mergers, SMBH mergers, short GRBs in AGN disks, and blazars. We attempted to answer these two essential questions in theoretical aspects: what physical mechanisms and processes produce the high-energy astrophysical electromagnetic and neutrino signals, and how we can reconstruct the physical conditions of the source and the environment from the observations using different messengers. All works included in this dissertation are summarized below.

In chapter 2, we calculated the cumulative diffuse neutrino and γ-ray fluxes contributed by galaxy/cluster mergers. We found that high-redshift mergers contribute a significant amount of the cosmic-ray luminosity density, and the resulting neutrino spectra could explain a large part of the observed diffuse neutrino flux above 0.1 PeV up to $\sim$ PeV. We also showed that our model can somewhat alleviate tensions with the extragalactic γ-ray background. First, since a larger fraction of the CR luminosity density comes from high redshifts, the accompanying γ-rays are more strongly suppressed through $\gamma\gamma$ annihilations with CMB and EBL. Second, mildly radiative-cooled shocks may lead to a harder CR spectrum with spectral indices of $1.5 \lesssim s \lesssim 2.0$. Our study suggests that halo mergers, a fraction of which may also induce starbursts in the merged galaxies, can be promising neutrino emitters without violating the existing *Fermi* γ-ray constraints on the non-blazar component of the extragalactic γ-ray background.

In chapter 3, we demonstrated that the synchrotron and inverse Compton emissions

produced by secondary electrons/positrons can explain the radio and X-ray fluxes of merging galaxies such as NGC 660 and NGC 3256. Using our model in combination with the observations, we can constrain the gas mass, shock velocity, magnetic field and the CR spectral index s of these systems. For NGC 660 a single-zone model with a spectral index $2.1 \lesssim s \lesssim 2.2$ is able to reproduce simultaneously the radio and X-ray observations, while a simple one-zone scenario with $s \sim 2$ can describe the radio and a large fraction of X-ray observations of NGC 3256. Our work provided a useful approach for studying the dynamics and physical parameters of galaxy mergers, which can play an important part in future multi-messenger studies of similar and related extragalactic sources.

In chapter 4, we considered neutrino counterpart emission originating from the jets launched after the SMBH merger. We modeled the jet structures and relevant interactions therein, and then evaluated neutrino emission from jet-induced shocks. We found that month-to-year high-energy neutrino emission from the post-merger jet after the gravitational wave event is detectable by IceCube-Gen2 within approximately five to ten years of operation in optimistic cases where the cosmic-ray loading is sufficiently high and a mildly super-Eddington accretion is achieved. We also estimated the contribution of SMBH mergers to the diffuse neutrino intensity, and found that a significant fraction of the observed very high-energy ($E_\nu \gtrsim 1$ PeV) IceCube neutrinos could originate from them in the optimistic cases. In the future, such neutrino counterparts together with gravitational wave observations can be used in a multi-messenger approach to elucidate in greater detail the evolution and the physical mechanism of SMBH mergers. In chapter 5, we showed that the non-thermal EM signals from SMBH mergers would be detectable up to the detection horizon of future GW facilities such as the LISA. Calculations based on our model predict slowly fading transients with time delays from days to months after the coalescence, leading to implications for EM follow-up observations after the GW detection.

In chapter 6, we focused on a special scenario where short gamma-ray bursts produced by CBO mergers are embedded in disks of AGN, and we investigate the γ-ray emission produced in the internal dissipation region via synchrotron, synchrotron self-Compton and EIC processes. In this scenario, isotropic thermal photons from the AGN disks contribute to the EIC component. We showed that a low-density cavity can be formed in the migration traps, leading to the embedded mergers producing successful GRB jets. We found that the EIC component would dominate the GeV emission for typical CBO mergers with an isotropic-equivalent luminosity of $L_{j,\rm iso} = 10^{48.5}$ erg s^{-1} which are located close to the central supermassive black hole. Considering a long-lasting jet

of duration $T_{\rm dur} \sim 10^2 - 10^3$ s, we find that the future CTA will be able to detect its $25 - 100$ GeV emission out to a redshift $z = 1.0$. In the optimistic case, it is possible to detect the on-axis extended emission simultaneously with GWs within one decade using MAGIC, H.E.S.S., VERITAS, CTA, and LHAASO-WCDA. Early diagnosis of prompt emissions with *Fermi*-GBM and HAWC can provide valuable directional information for the follow-up observations.

We investigated also the blazar contribution to the cumulative neutrino intensity in chapter 7, assuming a generic relationship between neutrino and gamma-ray luminosities, $L_\nu \propto (L_{\rm ph})^{\gamma_{\rm lw}}$. Using the gamma-ray luminosity functions for blazars including flat spectrum radio quasars (FSRQs) and BL Lac objects, as well as the *Fermi*-LAT detection efficiency, we estimated contributions from blazars resolved by *Fermi*-LAT as well as the unresolved counterpart. Combining the existing upper limits from stacking analyses, the cumulative neutrino flux from all blazars (including *Fermi*-LAT resolved and unresolved ones) are constrained in the range $0 \lesssim \gamma_{\rm lw} \lesssim 2.5$. We also evaluated the effects of the redshift evolution and the effective local number densities for each class of FSRQs, BL Lacs, and all blazars, by which we place another type of constraint on the blazar contribution using the non-detection of high-energy neutrino multiplets. We demonstrated that these two upper limits are complementary, and that the joint consideration of the stacking and multiplet analyses not only supports the argument that blazars are disfavored as the dominant sources of the 100-TeV neutrino background, but it extends this argument by including also *Fermi*-LAT-unresolved blazars as well, for a more generic luminosity correlation $L_\nu \propto (L_{\rm ph})^{\gamma_{\rm lw}}$.

8.2 Outlook

More joint multi-messenger detections are expected in the next few decades with upgraded instruments and newly built next-generation facilities. For high-energy neutrinos in the energy range $E_\nu \gtrsim 10^{17}$ eV (100 PeV), POEMMA, ARA/ARIANNA, CHANT, and GRAND would shed more light on the cosmogenic neutrinos produced by UHECRs and test our SMBH merger models. Here I list some possible projects for the future research program on multi-messenger astrophysics.

- *HE neutrinos from short GRBs in AGN disks*
  In addition to the γ-ray emitters, CB mergers are also promising origins of high-energy neutrinos. The cosmic rays accelerated in the jet will interact with the dense non-thermal photons and produce neutrinos via the photohadronic process, which is

also crucial for neutrinos originating in AGNs. The CRs accelerated in the successful jet can efficiently interact with disk photons and produce high-energy neutrinos via the photomeson production process. High-energy neutrinos are expected in the PeV range, and they will make an additional contribution to those predicted by isolated short GRBs, e.g., Ref. [446]. Future multi-messenger analyses of the embedded short GRBs can provide unprecedented insights into understanding the formation and evolution of CBs inside the AGN disks and the origin of high-energy emissions. Next, I propose to study the high-energy neutrino emission associated with GRBs in AGN disks and discuss the implications for future astrophysical surveys and how the AGN-assisted short GRBs contribute to the diffuse neutrino background.

- *Asrophysical neutrinos from AGNs*
  Despite the fact that the current constraints disfavor the blazars as the primary source of diffuse neutrino background, it would be intriguing to study the contribution from γ-ray faint blazars, low-luminosity AGNs, AGN cores, disks, jets, and cluster regions. The motivation is that the IceCube collaboration searched the archival data and found that the neutrino flux from the blazar TXS 0506+056 is dominated by a previous neutrino flare in 2014 [473]. One prominent task is to unveil the physical mechanism of neutrino flares in the γ-ray quiet epoch. The multizone scenarios that systematically model the particle interactions in the AGN disk, jet, and core regions to interpret the neutrino flares should be implemented to explain the efficient neutrino production and strong γ-ray suppression.

- *Proton synchrotron model for the VHE γ-ray emissions from GRBs*
  The recent detection of TeV photons from GRB 190114C [3,4] and GRB 180720B [5] has opened a new window for multi-messenger and multi-wavelength astrophysics of high-energy transients. The detection of VHE γ-rays from GRBs can exert stringent constraints on the physics of relativistic shocks involving particle acceleration, as well as the radiation mechanisms of GRBs. [391, 404] suggest that the VHE γ-rays reported by MAGIC Collaboration at a $\sim 3\sigma$ statistical significance could be attributed to the EIC emission associated with the extended and plateau emission. Such EIC VHE γ-rays are promising targets for future Imaging Atmospheric Cherenkov Telescopes. In the following work, we propose to calculate the VHE γ-ray emission from protons and nuclei synchrotron process in the ultra-relativistic jets with the presence of very strong magnetic fields. We plan to implement the hadronic model to explain the origins of the TeV γ-ray photons detected by MAGIC

and HESS and discuss the implications for CTA and LHAASO.

In addition to the breakthroughs with more specialized theoretical models and advanced next-generation detectors, the multi-messenger collaboration programs will also play an integral role in exploiting the synergies between the four messengers. Among the existing programs, the Astrophysical Multimessenger Observatory Network (AMON) will enhance the coincident discovery abilities of astrophysical transients by combining the sub-threshold signals received by collaborating observatories [474, 475]. Another purpose of AMON is to send following-up alerts to guide the other observatories rapidly. The Scalable Cyberinfrastructure to support Multi-Messenger Astrophysics (SCiMMA) program enables the multi-messenger astrophysics organizations, including AMON, IceCube, and LIGO, to rapidly handle, combine, and analyze the very large-scale distributed data from all types of astronomical measurements [476], which makes the multi-messenger analyses faster and more reliable in the data transfer, storage, and processing levels. Our understanding of the most energetic and extreme processes in the universe will keep refreshing by combining detailed analytical and semi-analytical models, numerical simulations, powerful detectors, and well-designed data analysis networks. We may also observe the unknowns in the uncharted universe.

Bibliography

[1] M. Ackermann et al. The spectrum of isotropic diffuse gamma-ray emission between 100 mev and 820 gev. *The Astrophysical Journal*, 799(1):86, 2015.

[2] T. Montaruli. Gamma-rays and their future. *Nuclear and Particle Physics Proceedings*, 306-308:1–11, September 2019.

[3] P. Veres et al. Observation of inverse compton emission from a long γ-ray burst. *Nature*, 575(7783):459–463, 2019.

[4] MAGIC Collaboration et al. Teraelectronvolt emission from the γ-ray burst GRB 190114C. *Nature*, 575(7783):455–458, November 2019.

[5] H. Abdalla et al. A very-high-energy component deep in the γ-ray burst afterglow. *Nature*, 575(7783):464–467, November 2019.

[6] Cherenkov Telescope Array Consortium et al. *Science with the Cherenkov Telescope Array*. 2019.

[7] G. di Sciascio and Lhaaso Collaboration. The LHAASO experiment: From Gamma-Ray Astronomy to Cosmic Rays. *Nuclear and Particle Physics Proceedings*, 279-281:166–173, October 2016.

[8] LSST Science Collaboration et al. Science-Driven Optimization of the LSST Observing Strategy. *arXiv e-prints*, pp. arXiv:1708.04058, August 2017.

[9] N. Dagoneau et al. Detection capability of ultra-long gamma-ray bursts with the ECLAIRs telescope aboard the SVOM mission under development. In *42nd COSPAR Scientific Assembly*, volume 42, pp. E1.17–46–18, July 2018.

[10] M. T. Patterson et al. The Zwicky Transient Facility Alert Distribution System. *Publications of the Astronomical Society of the Pacific*, 131(995):018001, January 2019.

[11] J. Beringer et al. Review of Particle Physics. *Physical Review D*, 86(1):010001, July 2012.

[12] L. O. C. Drury. Origin of cosmic rays. *Astroparticle Physics*, 39:52–60, December 2012.

[13] D. Caprioli. Cosmic-ray acceleration and propagation. In *34th International Cosmic Ray Conference (ICRC2015)*, volume 34 of *International Cosmic Ray Conference*, pp. 8, July 2015.

[14] M. Aglietta et al. The cosmic ray primary composition in the "knee" region through the EAS electromagnetic and muon measurements at EAS-TOP. *Astroparticle Physics*, 21(6):583–596, September 2004.

[15] J. R. Hoerandel. On the knee in the energy spectrum of cosmic rays. *Astroparticle Physics*, 19(2):193–220, 2003.

[16] Pierre Auger Collaboration. The Pierre Auger Cosmic Ray Observatory. *Nuclear Instruments and Methods in Physics Research A*, 798:172–213, October 2015.

[17] K. Greisen. End to the Cosmic-Ray Spectrum? *Physical Review Letters*, 16(17):748–750, April 1966.

[18] G. T. Zatsepin and V. A. Kuz'min. Upper Limit of the Spectrum of Cosmic Rays. *Soviet Journal of Experimental and Theoretical Physics Letters*, 4:78, August 1966.

[19] A. M. Hillas. The Origin of Ultra-High-Energy Cosmic Rays. *Annual Review of Astronomy and Astrophysics*, 22:425–444, January 1984.

[20] Katrin Collaboration et al. Direct neutrino-mass measurement with sub-electronvolt sensitivity. *Nature Physics*, 18(2):160–166, February 2022.

[21] T. Gaisser and F. Halzen. Icecube. *Annual Review of Nuclear and Particle Science*, 64(1):101–123, 2014.

[22] F. Halzen. High-energy neutrino astrophysics. *Nature Phys.*, 13(3):232–238, 2016.

[23] M. Aartsen et al. First observation of PeV-energy neutrinos with IceCube. *Phys.Rev.Lett.*, 111:021103, 2013.

[24] M. Aartsen et al. Evidence for High-Energy Extraterrestrial Neutrinos at the IceCube Detector. *Science*, 342:1242856, 2013.

[25] M. Aartsen et al. Observation of High-Energy Astrophysical Neutrinos in Three Years of IceCube Data. *Phys.Rev.Lett.*, 113:101101, 2014.

[26] M. Aartsen et al. A combined maximum-likelihood analysis of the high-energy astrophysical neutrino flux measured with icecube. *The Astrophysical Journal*, 809(1):98, 2015.

[27] M. Ahlers and K. Murase. Probing the Galactic Origin of the IceCube Excess with Gamma-Rays. *Phys. Rev.*, D90(2):023010, 2014.

[28] W. D. Apel et al. KASCADE-Grande Limits on the Isotropic Diffuse Gamma-Ray Flux between 100 TeV and 1 EeV. *Astrophys. J.*, 848(1):1, 2017.

[29] A. U. Abeysekara et al. Search for Very High-energy Gamma Rays from the Northern Fermi Bubble Region with HAWC. *Astrophys. J.*, 842(2):85, 2017.

[30] A. U. Abeysekara et al. A Search for Dark Matter in the Galactic Halo with HAWC. *arXiv: 1710.10288*, 2017.

[31] E. Waxman and J. Bahcall. High energy neutrinos from cosmological gamma-ray burst fireballs. *Physical Review Letters*, 78(12):2292, 1997.

[32] P. Meszaros and E. Waxman. Tev neutrinos from successful and choked gamma-ray bursts. *Physical Review Letters*, 87(17):171102, 2001.

[33] K. Murase. Prompt high-energy neutrinos from gamma-ray bursts in photospheric and synchrotron self-compton scenarios. *Physical Review D*, 78(10):101302, 2008.

[34] X.-Y. Wang and Z.-G. Dai. Prompt tev neutrinos from the dissipative photospheres of gamma-ray bursts. *The Astrophysical Journal Letters*, 691(2):L67, 2009.

[35] P. Baerwald et al. Uhecr escape mechanisms for protons and neutrons from gamma-ray bursts, and the cosmic-ray-neutrino connection. *The Astrophysical Journal*, 768(2):186, 2013.

[36] M. Bustamante et al. Neutrino and cosmic-ray emission from multiple internal shocks in gamma-ray bursts. 2014. [Nature Commun.6,6783(2015)].

[37] I. Tamborra and S. Ando. Inspecting the supernova–gamma-ray-burst connection with high-energy neutrinos. *Physical Review D*, 93(5):053010, 2016.

[38] K. Murase et al. High-energy neutrinos and cosmic rays from low-luminosity gamma-ray bursts? *The Astrophysical Journal Letters*, 651(1):L5, 2006.

[39] N. Gupta and B. Zhang. Neutrino spectra from low and high luminosity populations of gamma ray bursts. *Astroparticle Physics*, 27(5):386–391, 2007.

[40] K. Murase and K. Ioka. Tev–pev neutrinos from low-power gamma-ray burst jets inside stars. *Physical Review Letters*, 111(12):121102, 2013.

[41] D. Xiao and Z. Dai. Neutrino emission in the jet propagation process. *The Astrophysical Journal*, 790(1):59, 2014.

[42] D. Xiao and Z. Dai. Tev–pev neutrino oscillation of low-luminosity gamma-ray bursts. *The Astrophysical Journal*, 805(2):137, 2015.

[43] N. Senno et al. Choked jets and low-luminosity gamma-ray bursts as hidden neutrino sources. *Physical Review D*, 93(8):083003, 2016.

[44] P. B. Denton and I. Tamborra. Exploring the Properties of Choked Gamma-Ray Bursts with IceCube's High Energy Neutrinos. *arXiv: 1711.00470*, 2017.

[45] K. Mannheim. High-energy neutrinos from extragalactic jets. *Astropart. Phys.*, 3:295–302, 1995.

[46] F. Halzen and E. Zas. Neutrino fluxes from active galaxies: A Model independent estimate. *Astrophys. J.*, 488:669–674, 1997.

[47] L. A. Anchordoqui et al. High energy neutrinos from astrophysical accelerators of cosmic ray nuclei. *Astroparticle Physics*, 29(1):1–13, 2008.

[48] K. Murase et al. Diffuse neutrino intensity from the inner jets of active galactic nuclei: impacts of external photon fields and the blazar sequence. *Physical Review D*, 90(2):023007, 2014.

[49] C. D. Dermer et al. Photopion production in black-hole jets and flat-spectrum radio quasars as pev neutrino sources. *Journal of High Energy Astrophysics*, 3:29–40, 2014.

[50] J. Becker Tjus et al. High-energy neutrinos from radio galaxies. *Phys. Rev.*, D89(12):123005, 2014.

[51] M. Petropoulou et al. Photohadronic origin of-ray bl lac emission: implications for icecube neutrinos. *Monthly Notices of the Royal Astronomical Society*, 448(3):2412–2429, 2015.

[52] P. Padovani et al. A simplified view of blazars: the neutrino background. *Mon. Not. Roy. Astron. Soc.*, 452(2):1877–1887, 2015.

[53] C. Blanco and D. Hooper. High-Energy Gamma Rays and Neutrinos from Nearby Radio Galaxies. *JCAP*, 1712(12):017, 2017.

[54] F. W. Stecker et al. High-energy neutrinos from active galactic nuclei. *Physical Review Letters*, 66(21):2697, 1991.

[55] J. Alvarez-Muñiz and P. Mészáros. High energy neutrinos from radio-quiet active galactic nuclei. *Physical Review D*, 70(12):123001, 2004.

[56] F. W. Stecker. Pev neutrinos observed by icecube from cores of active galactic nuclei. *Physical Review D*, 88(4):047301, 2013.

[57] S. S. Kimura et al. Neutrino and Cosmic-Ray Emission and Cumulative Background from Radiatively Inefficient Accretion Flows in Low-Luminosity Active Galactic Nuclei. *Astrophys. J.*, 806:159, 2015.

[58] K. Murase et al. Testing the hadronuclear origin of pev neutrinos observed with icecube. *Physical Review D*, 88(12):121301, 2013.

[59] K. Murase et al. Hidden Cosmic-Ray Accelerators as an Origin of TeV-PeV Cosmic Neutrinos. *Phys. Rev. Lett.*, 116(7):071101, 2016.

[60] K. Bechtol et al. Evidence against star-forming galaxies as the dominant source of icecube neutrinos. *The Astrophysical Journal*, 836(1):47, 2017.

[61] B. P. Abbott et al. Observation of Gravitational Waves from a Binary Black Hole Merger. *Physical Review Letters*, 116(6):061102, February 2016.

[62] M. Bailes et al. Gravitational-wave physics and astronomy in the 2020s and 2030s. *Nature Reviews Physics*, 3(5):344–366, 2021.

[63] B. P. Abbott et al. Exploring the sensitivity of next generation gravitational wave detectors. *Classical and Quantum Gravity*, 34(4):044001, February 2017.

[64] A. Klein et al. Science with the space-based interferometer eLISA: Supermassive black hole binaries. *Physical Review D*, 93(2):024003, January 2016.

[65] K. Schutz and C.-P. Ma. Constraints on individual supermassive black hole binaries from pulsar timing array limits on continuous gravitational waves. *Monthly Notices of the Royal Astronomical Society*, 459(2):1737–1744, June 2016.

[66] D. Clowe et al. Weak-lensing mass reconstruction of the interacting cluster 1e 0657–558: Direct evidence for the existence of dark matter. *The Astrophysical Journal*, 604(2):596, 2004.

[67] M. Markevitch et al. Direct constraints on the dark matter self-interaction cross section from the merging galaxy cluster 1e 0657–56. *The Astrophysical Journal*, 606(2):819, 2004.

[68] K. Kashiyama and P. Mészáros. Galaxy mergers as a source of cosmic rays, neutrinos, and gamma rays. *The Astrophysical Journal Letters*, 790(1):L14, 2014.

[69] D. Richstone et al. Supermassive black holes and the evolution of galaxies. *nature*, 395(6701):A14–A19, 1998.

[70] M. C. Begelman et al. Massive black hole binaries in active galactic nuclei. *Nature*, 287(5780):307–309, September 1980.

[71] J. Kormendy and L. C. Ho. Coevolution (or not) of supermassive black holes and host galaxies. *Annual Review of Astronomy and Astrophysics*, 51(1):511–653, August 2013.

[72] P. Amaro-Seoane et al. Laser interferometer space antenna. pp. arXiv:1702.00786, February 2017.

[73] J. E. Barnes and L. Hernquist. Transformations of galaxies. ii. gasdynamics in merging disk galaxies. *The Astrophysical Journal*, 471(1):115, 1996.

[74] M. Milosavljević and E. S. Phinney. The afterglow of massive black hole coalescence. *The Astrophysical Journal Letters*, 622(2):L93–L96, April 2005.

[75] D. B. Bowen et al. Quasi-periodicity of Supermassive Binary Black Hole Accretion Approaching Merger. *The Astrophysical Journal*, 879(2):76, July 2019.

[76] R. D. Blandford and R. L. Znajek. Electromagnetic extraction of energy from kerr black holes. *Monthly Notices of the Royal Astronomical Society*, 179:433–456, May 1977.

[77] P. Mészáros. Gamma-Ray Bursts. *Rept. Prog. Phys.*, 69:2259–2322, 2006.

[78] B. Paczynski. Gamma-ray bursters at cosmological distances. *The Astrophysical Journal Letters*, 308:L43–L46, September 1986.

[79] D. Eichler et al. Nucleosynthesis, neutrino bursts and γ-rays from coalescing neutron stars. *Nature*, 340(6229):126–128, July 1989.

[80] P. Meszaros and M. J. Rees. Tidal Heating and Mass Loss in Neutron Star Binaries: Implications for Gamma-Ray Burst Models. *The Astrophysical Journal*, 397:570, October 1992.

[81] R. Narayan et al. Gamma-Ray Bursts as the Death Throes of Massive Binary Stars. *The Astrophysical Journal Letters*, 395:L83, August 1992.

[82] W. H. Lee and E. Ramirez-Ruiz. The progenitors of short gamma-ray bursts. *New Journal of Physics*, 9(1):17, January 2007.

[83] E. Berger. Short-Duration Gamma-Ray Bursts. *Annual Review of Astronomy and Astrophysics*, 52:43–105, August 2014.

[84] S. E. Woosley. Gamma-Ray Bursts from Stellar Mass Accretion Disks around Black Holes. *The Astrophysical Journal*, 405:273, March 1993.

[85] B. Paczyński. Are Gamma-Ray Bursts in Star-Forming Regions? *The Astrophysical Journal Letters*, 494(1):L45–L48, February 1998.

[86] R. Popham et al. Hyperaccreting Black Holes and Gamma-Ray Bursts. *The Astrophysical Journal*, 518(1):356–374, June 1999.

[87] A. I. MacFadyen and S. E. Woosley. Collapsars: Gamma-Ray Bursts and Explosions in "Failed Supernovae". *The Astrophysical Journal*, 524(1):262–289, October 1999.

[88] P. Mészáros. Gamma-ray bursts. *Reports on Progress in Physics*, 69(8):2259–2321, August 2006.

[89] J. Hjorth and J. S. Bloom. *The GRB–supernova connection*, pp. 169–190. Cambridge Astrophysics. Cambridge University Press, 2012.

[90] B. P. Abbott et al. GW170817: Observation of Gravitational Waves from a Binary Neutron Star Inspiral. *Physical Review Letters*, 119(16):161101, October 2017.

[91] B. P. Abbott et al. A gravitational-wave standard siren measurement of the Hubble constant. *Nature*, 551(7678):85–88, November 2017.

[92] B. P. Abbott et al. *The Astrophysical Journal Letters*, 848(2):L13, October 2017.

[93] A. Goldstein et al. An Ordinary Short Gamma-Ray Burst with Extraordinary Implications: Fermi-GBM Detection of GRB 170817A. *The Astrophysical Journal Letters*, 848(2):L14, October 2017.

[94] G. Hallinan et al. A radio counterpart to a neutron star merger. *Science*, 358(6370):1579–1583, December 2017.

[95] V. Savchenko et al. INTEGRAL Detection of the First Prompt Gamma-Ray Signal Coincident with the Gravitational-wave Event GW170817. *The Astrophysical Journal Letters*, 848(2):L15, October 2017.

[96] E. Troja et al. The X-ray counterpart to the gravitational-wave event GW170817. *Nature*, 551(7678):71–74, November 2017.

[97] J. D. Lyman et al. The optical afterglow of the short gamma-ray burst associated with GW170817. *Nature Astronomy*, 2:751–754, July 2018.

[98] D. Lazzati et al. Late Time Afterglow Observations Reveal a Collimated Relativistic Jet in the Ejecta of the Binary Neutron Star Merger GW170817. *Physical Review Letters*, 120(24):241103, June 2018.

[99] K. P. Mooley et al. Superluminal motion of a relativistic jet in the neutron-star merger GW170817. *Nature*, 561(7723):355–359, September 2018.

[100] K. P. Mooley et al. A mildly relativistic wide-angle outflow in the neutron-star merger event GW170817. *Nature*, 554(7691):207–210, February 2018.

[101] O. Gottlieb et al. High efficiency photospheric emission entailed by formation of a collimation shock in gamma-ray bursts. *Monthly Notices of the Royal Astronomical Society*, 488(1):1416–1426, September 2019.

[102] K. Ioka and T. Nakamura. Spectral puzzle of the off-axis gamma-ray burst in GW170817. *Monthly Notices of the Royal Astronomical Society*, 487(4):4884–4889, August 2019.

[103] S. S. Kimura et al. Upscattered Cocoon Emission in Short Gamma-Ray Bursts as High-energy Gamma-Ray Counterparts to Gravitational Waves. *The Astrophysical Journal Letters*, 887(1):L16, December 2019.

[104] K. Murase et al. Double Neutron Star Mergers and Short Gamma-ray Bursts: Long-lasting High-energy Signatures and Remnant Dichotomy. *The Astrophysical Journal*, 854(1):60, February 2018.

[105] V. Gayathri et al. GW170817A as a Hierarchical Black Hole Merger. *The Astrophysical Journal Letters*, 890(2):L20, February 2020.

[106] J. Samsing et al. Active Galactic Nuclei as Factories for Eccentric Black Hole Mergers. *arXiv e-prints*, pp. arXiv:2010.09765, October 2020.

[107] I. Bartos. GW190521 as a Highly Eccentric Black Hole Merger. In *American Astronomical Society Meeting Abstracts*, volume 53 of *American Astronomical Society Meeting Abstracts*, pp. 234.02, January 2021.

[108] A. Tanikawa et al. Population III binary black holes: effects of convective overshooting on formation of GW190521. *Monthly Notices of the Royal Astronomical Society*, 505(2):2170–2176, August 2021.

[109] Y. Yang et al. AGN Disks Harden the Mass Distribution of Stellar-mass Binary Black Hole Mergers. *The Astrophysical Journal*, 876(2):122, May 2019.

[110] Y. Yang et al. Hierarchical Black Hole Mergers in Active Galactic Nuclei. *Physical Review Letters*, 123(18):181101, November 2019.

[111] H. Tagawa et al. Formation and Evolution of Compact-object Binaries in AGN Disks. *The Astrophysical Journal*, 898(1):25, July 2020.

[112] H. Tagawa et al. Mass-gap Mergers in Active Galactic Nuclei. *The Astrophysical Journal*, 908(2):194, February 2021.

[113] Y. Yang et al. Black Hole Formation in the Lower Mass Gap through Mergers and Accretion in AGN Disks. *The Astrophysical Journal Letters*, 901(2):L34, October 2020.

[114] M. J. Graham et al. Candidate Electromagnetic Counterpart to the Binary Black Hole Merger Gravitational-Wave Event S190521g*. *Physical Review Letters*, 124(25):251102, June 2020.

[115] G. Ashton et al. Current observations are insufficient to confidently associate the binary black hole merger GW190521 with AGN J124942.3 + 344929. *Classical and Quantum Gravity*, 38(23):235004, December 2021.

[116] R. Perna et al. Electromagnetic Signatures of Relativistic Explosions in the Disks of Active Galactic Nuclei. *The Astrophysical Journal Letters*, 906(2):L7, January 2021.

[117] J.-P. Zhu et al. High-energy Neutrinos from Stellar Explosions in Active Galactic Nuclei Accretion Disks. *arXiv e-prints*, pp. arXiv:2107.06070, July 2021.

[118] J.-P. Zhu et al. High-energy Neutrinos from Choked Gamma-Ray Bursts in Active Galactic Nucleus Accretion Disks. *The Astrophysical Journal Letters*, 911(2):L19, April 2021.

[119] S. S. Kimura et al. Outflow Bubbles from Compact Binary Mergers Embedded in Active Galactic Nuclei: Cavity Formation and the Impact on Electromagnetic Counterparts. *The Astrophysical Journal*, 916(2):111, August 2021.

[120] I. Bartos and M. Kowalski. *Multimessenger Astronomy*. 2017.

[121] J. M. Bellovary et al. Migration Traps in Disks around Supermassive Black Holes. *The Astrophysical Journal Letters*, 819(2):L17, March 2016.

[122] IceCube Collaboration et al. Multimessenger observations of a flaring blazar coincident with high-energy neutrino icecube-170922a. *Science*, 361(6398):eaat1378, 2018.

[123] K. Murase et al. Blazar flares as an origin of high-energy cosmic neutrinos? *The Astrophysical Journal*, 865(2):124, 2018.

[124] M. Aartsen et al. the contribution of fermi-2lac blazars to diffuse tev–pev neutrino flux. *The Astrophysical Journal*, 835(1):45, 2017.

[125] E. Pinat et al. Search for extended sources of neutrino emission with 7 years of IceCube data. In *35th International Cosmic Ray Conference (ICRC2017)*, volume 301 of *International Cosmic Ray Conference*, pp. 963, January 2017.

[126] D. Hooper et al. Active galactic nuclei and the origin of icecube's diffuse neutrino flux. *arXiv preprint arXiv:1810.02823*, 2018.

[127] A. Neronov et al. Strong constraints on hadronic models of blazar activity from fermi and icecube stacking analysis. *Astronomy & Astrophysics*, 603:A135, 2017.

[128] A. Palladino et al. Interpretation of the diffuse astrophysical neutrino flux in terms of the blazar sequence. *The Astrophysical Journal*, 871(1):41, 2019.

[129] K. Murase and E. Waxman. Constraining high-energy cosmic neutrino sources: Implications and prospects. *Physical Review D*, 94(10):103006, 2016.

[130] M. Ahlers and F. Halzen. Pinpointing extragalactic neutrino sources in light of recent icecube observations. *Physical Review D*, 90(4):043005, 2014.

[131] M. Aartsen et al. Searches for extended and point-like neutrino sources with four years of icecube data. *The Astrophysical Journal*, 796(2):109, 2014.

[132] M. R. Feyereisen et al. One-point fluctuation analysis of the high-energy neutrino sky. *Journal of Cosmology and Astroparticle Physics*, 2017(3):057, March 2017.

[133] T. Glauch et al. Search for weak neutrino point sources using angular auto-correlation analyses in IceCube. In *35th International Cosmic Ray Conference (ICRC2017)*, volume 301 of *International Cosmic Ray Conference*, pp. 1014, January 2017.

[134] A. Dekker and S. Ando. Angular power spectrum analysis on current and future high-energy neutrino data. *Journal of Cosmology and Astroparticle Physics*, 2019(2):002, February 2019.

[135] A. Neronov and D. Semikoz. Self-consistent model of extragalactic neutrino flux from evolving blazar population. *arXiv preprint arXiv:1811.06356*, 2018.

[136] C. Yuan et al. Cumulative Neutrino and Gamma-Ray Backgrounds from Halo and Galaxy Mergers. *The Astrophysical Journal*, 857(1):50, April 2018.

[137] K. Murase et al. Cosmic rays above the second knee from clusters of galaxies and associated high-energy neutrino emission. *The Astrophysical Journal Letters*, 689(2):L105, 2008.

[138] K. Fang and K. Murase. Linking high-energy cosmic particles by black-hole jets embedded in large-scale structures. *Nature Physics*, pp. 1, 2018.

[139] A. Loeb and E. Waxman. The cumulative background of high energy neutrinos from starburst galaxies. *Journal of Cosmology and Astroparticle Physics*, 2006(05):003, 2006.

[140] I. Tamborra et al. Star-forming galaxies as the origin of diffuse high-energy backgrounds: gamma-ray and neutrino connections, and implications for starburst history. *Journal of Cosmology and Astroparticle Physics*, 2014(09):043, 2014.

[141] L. A. Anchordoqui et al. What icecube data tell us about neutrino emission from star-forming galaxies (so far). *Physical Review D*, 89(12):127304, 2014.

[142] X.-C. Chang and X.-Y. Wang. The diffuse gamma-ray flux associated with sub-pev/pev neutrinos from starburst galaxies. *The Astrophysical Journal*, 793(2):131, 2014.

[143] X.-C. Chang et al. Star-forming galaxies as the origin of the icecube pev neutrinos. *The Astrophysical Journal*, 805(2):95, 2015.

[144] N. Senno et al. Extragalactic star-forming galaxies with hypernovae and supernovae as high-energy neutrino and gamma-ray sources: the case of the 10 tev neutrino data. *The Astrophysical Journal*, 806(1):24, 2015.

[145] S. Chakraborty and I. Izaguirre. Diffuse neutrinos from extragalactic supernova remnants: Dominating the 100 TeV IceCube flux. *Phys. Lett.*, B745:35–39, 2015.

[146] A. Lamastra et al. Extragalactic gamma-ray background from AGN winds and star-forming galaxies in cosmological galaxy formation models. *Astron. Astrophys.*, 607:A18, 2017.

[147] M. Ackermann et al. Resolving the Extragalactic γ -Ray Background above 50 GeV with the Fermi Large Area Telescope. *Physical Review Letters*, 116(15):151105, April 2016.

[148] M. Lisanti et al. Deciphering Contributions to the Extragalactic Gamma-Ray Background from 2 GeV to 2 TeV. *Astrophys. J.*, 832(2):117, 2016.

[149] D. Xiao et al. Revisiting the Contributions of Supernova and Hypernova Remnants to the Diffuse High-Energy Backgrounds: Constraints on Very High Redshift Injection. *The Astrophysical Journal*, 826:133, August 2016.

[150] V. Bonvin et al. H0licow–v. new cosmograil time delays of he 0435- 1223: H0 to 3.8 per cent precision from strong lensing in a flat λcdm model. *Monthly Notices of the Royal Astronomical Society*, 465(4):4914–4930, 2017.

[151] R. K. Sheth and G. Tormen. Large-scale bias and the peak background split. *Monthly Notices of the Royal Astronomical Society*, 308(1):119–126, 1999.

[152] W. H. Press and P. Schechter. Formation of galaxies and clusters of galaxies by self-similar gravitational condensation. *The Astrophysical Journal*, 187:425–438, 1974.

[153] A. Lewis et al. Efficient computation of CMB anisotropies in closed FRW models. *Astrophys. J.*, 538:473–476, 2000.

[154] A. Jenkins et al. The mass function of dark matter haloes. *Monthly Notices of the Royal Astronomical Society*, 321(2):372–384, 2001.

[155] D. S. Reed et al. The halo mass function from the dark ages through the present day. *Monthly Notices of the Royal Astronomical Society*, 374(1):2–15, 2006.

[156] S. Murray et al. How well do we know the halo mass function? *Monthly Notices of the Royal Astronomical Society: Letters*, 434(1):L61–L65, 2013.

[157] A. Fialkov and A. Loeb. Jetted tidal disruptions of stars as a flag of intermediate mass black holes at high redshifts. *arXiv preprint arXiv:1611.01386*, 2016.

[158] O. Fakhouri et al. The merger rates and mass assembly histories of dark matter haloes in the two millennium simulations. *Monthly Notices of the Royal Astronomical Society*, 406(4):2267–2278, 2010.

[159] P. S. Behroozi et al. The average star formation histories of galaxies in dark matter halos from z= 0-8. *The Astrophysical Journal*, 770(1):57, 2013.

[160] M. T. Sargent et al. Regularity underlying complexity: a redshift-independent description of the continuous variation of galaxy-scale molecular gas properties in the mass-star formation rate plane. *The Astrophysical Journal*, 793(1):19, 2014.

[161] M. Davis and P. Peebles. A survey of galaxy redshifts. v-the two-point position and velocity correlations. *The Astrophysical Journal*, 267:465–482, 1983.

[162] E. J. Groth and P. Peebles. Statistical analysis of catalogs of extragalactic objects. vii-two-and three-point correlation functions for the high-resolution shane-wirtanen catalog of galaxies. *The Astrophysical Journal*, 217:385–405, 1977.

[163] P. J. Peebles. The gravitational-instability picture and the nature of the distribution of galaxies. *The Astrophysical Journal*, 189:L51, 1974.

[164] M. Davis and P. Peebles. On the integration of the bbgky equations for the development of strongly nonlinear clustering in an expanding universe. *The Astrophysical Journal Supplement Series*, 34:425–450, 1977.

[165] A. Hamilton et al. Reconstructing the primordial spectrum of fluctuations of the universe from the observed nonlinear clustering of galaxies. *The Astrophysical Journal*, 374:L1–L4, 1991.

[166] J. Peacock and S. Dodds. Non-linear evolution of cosmological power spectra. *Monthly Notices of the Royal Astronomical Society*, 280(3):L19–L26, 1996.

[167] R. E. Smith et al. Stable clustering, the halo model and non-linear cosmological power spectra. *Monthly Notices of the Royal Astronomical Society*, 341:1311–1332, June 2003.

[168] Y. Jing et al. Spatial correlation function and pairwise velocity dispersion of galaxies: Cold dark matter models versus the las campanas survey. *The Astrophysical Journal*, 494(1):1, 1998.

[169] E. Hawkins et al. The 2df galaxy redshift survey: correlation functions, peculiar velocities and the matter density of the universe. *Monthly Notices of the Royal Astronomical Society*, 346(1):78–96, 2003.

[170] I. Zehavi et al. Galaxy clustering in early sloan digital sky survey redshift data. *The Astrophysical Journal*, 571(1):172, 2002.

[171] P. J. E. Peebles. *The large-scale structure of the universe*. Princeton university press, 1980.

[172] V. R. Eke et al. The evolution of x-ray clusters in a low-density universe. *The Astrophysical Journal*, 503(2):569, 1998.

[173] L. O. Drury. An introduction to the theory of diffusive shock acceleration of energetic particles in tenuous plasmas. *Reports on Progress in Physics*, 46(8):973, 1983.

[174] E. Kafexhiu et al. Parametrization of gamma-ray production cross sections for p p interactions in a broad proton energy range from the kinematic threshold to pev energies. *Physical Review D*, 90(12):123014, 2014.

[175] B. A. Keeney et al. Does the milky way produce a nuclear galactic wind? *The Astrophysical Journal*, 646(2):951, 2006.

[176] R. M. Crocker. Non-thermal insights on mass and energy flows through the galactic centre and into the fermi bubbles. *Monthly Notices of the Royal Astronomical Society*, 423(4):3512–3539, 2012.

[177] T. Shibuya et al. Morphologies of 190,000 galaxies at z= 0–10 revealed with hst legacy data. i. size evolution. *The Astrophysical Journal Supplement Series*, 219(2):15, 2015.

[178] J. N. Bahcall and R. M. Soneira. The universe at faint magnitudes. i-models for the galaxy and the predicted star counts. *The Astrophysical Journal Supplement Series*, 44:73–110, 1980.

[179] P. Van Der Kruit and L. Searle. Surface photometry of edge-on spiral galaxies. ii-the distribution of light and colour in the disk and spheroid of ngc891. *Astronomy & Astrophysics*, 95:116, 1981.

[180] N. D. Kylafis and J. N. Bahcall. Dust distribution in spiral galaxies. *The Astrophysical Journal*, 317:637–645, 1987.

[181] D. Barnaby and H. A. Thronson Jr. The distribution of light in galaxies-the edge-on spiral ngc 5907. *The Astronomical Journal*, 103:41–53, 1992.

[182] J. Croston et al. Galaxy-cluster gas-density distributions of the representative xmm-newton cluster structure survey (rexcess). *Astronomy & Astrophysics*, 487(2):431–443, 2008.

[183] X.-C. Chang et al. How Far Away Are the Sources of IceCube Neutrinos? Constraints from the Diffuse Teraelectronvolt Gamma-ray Background. *The Astrophysical Journal*, 825:148, July 2016.

[184] J. D. Finke et al. Modeling the extragalactic background light from stars and dust. *The Astrophysical Journal*, 712(1):238, 2010.

[185] Y. Inoue et al. Extragalactic background light from hierarchical galaxy formation: gamma-ray attenuation up to the epoch of cosmic reionization and the first stars. *The Astrophysical Journal*, 768(2):197, 2013.

[186] V. Berezinsky and A. Y. Smirnov. Cosmic neutrinos of ultra-high energies and detection possibility. *Astrophysics and Space Science*, 32(2):461–482, 1975.

[187] K. Murase and J. F. Beacom. Constraining very heavy dark matter using diffuse backgrounds of neutrinos and cascaded gamma rays. *Journal of Cosmology and Astroparticle Physics*, 2012(10):043, 2012.

[188] M. Aartsen et al. Observation and characterization of a cosmic muon neutrino flux from the northern hemisphere using six years of icecube data. *The Astrophysical Journal*, 833(1):3, 2016.

[189] M. G. Aartsen et al. The IceCube Neutrino Observatory - Contributions to ICRC 2017 Part II: Properties of the Atmospheric and Astrophysical Neutrino Flux. *arXiv: 1710.01191*, 2017.

[190] V. Rodriguez-Gomez et al. The merger rate of galaxies in the illustris simulation: a comparison with observations and semi-empirical models. *Monthly Notices of the Royal Astronomical Society*, 449(1):49–64, 2015.

[191] R. C. Berrington and C. D. Dermer. Nonthermal particles and radiation produced by cluster merger shocks. *Astrophys. J.*, 594:709–731, 2003.

[192] Y. Fujita and C. L. Sarazin. Nonthermal emission from accreting and merging clusters of galaxies. *The Astrophysical Journal*, 563(2):660, 2001.

[193] C. Charbonnel et al. Star formation in galaxy interactions and mergers. *European Astronomical Society Publications Series*, 51:107–131, 2011.

[194] R.-Y. Liu et al. Can winds driven by active galactic nuclei account for the extragalactic gamma-ray and neutrino backgrounds? *Astrophys. J.*, 858(1):9, 2018.

[195] R. Blandford and D. Eichler. Particle acceleration at astrophysical shocks: A theory of cosmic ray origin. *Physics Reports*, 154(1):1–75, 1987.

[196] R. Yamazaki et al. Tev γ-rays from old supernova remnants. *Monthly Notices of the Royal Astronomical Society*, 371(4):1975–1982, 2006.

[197] K. Murase and E. Waxman. Constraining High-Energy Cosmic Neutrino Sources: Implications and Prospects. *Phys. Rev.*, D94(10):103006, 2016.

[198] C. Yuan et al. Secondary Radio and X-Ray Emissions from Galaxy Mergers. *The Astrophysical Journal*, 878(2):76, June 2019.

[199] A. Loeb and E. Waxman. The Cumulative background of high energy neutrinos from starburst galaxies. *JCAP*, 0605:003, 2006.

[200] T. A. Thompson et al. The starburst contribution to the extragalactic γ-ray background. *The Astrophysical Journal*, 654(1):219, 2007.

[201] K. Murase et al. Testing the Hadronuclear Origin of PeV Neutrinos Observed with IceCube. *Phys. Rev.*, D88(12):121301, 2013.

[202] D. Xiao et al. Revisiting the Contributions of Supernova and Hypernova Remnants to the Diffuse High-energy Backgrounds: Constraints on Very High Redshift Injection. *Astrophys. J.*, 826(2):133, 2016.

[203] I. Tamborra et al. Star-forming galaxies as the origin of diffuse high-energy backgrounds: Gamma-ray and neutrino connections, and implications for starburst history. *JCAP*, 1409:043, 2014.

[204] X. Wang and A. Loeb. Contribution of quasar-driven outflows to the extragalactic gamma-ray background. *Nature Physics*, 12:1116–1118, December 2016.

[205] A. Lamastra et al. Extragalactic gamma-ray background from AGN winds and star-forming galaxies in cosmological galaxy-formation models. *Astronomy & Astrophysics*, 607:A18, October 2017.

[206] C. Yuan et al. Cumulative neutrino and gamma-ray backgrounds from halo and galaxy mergers. *The Astrophysical Journal*, 857(1):50, 2018.

[207] U. Lisenfeld and H. J. Voelk. Shock acceleration of relativistic particles in galaxy-galaxy collisions. *Astronomy & Astrophysics*, 524:A27, 2010.

[208] T. W. Jones. Particle acceleration at shocks: Insights from supernova remnant shocks. *Journal of Astrophysics and Astronomy*, 32(4):427–435, Dec 2011.

[209] G. Morlino and D. Caprioli. Strong evidence for hadron acceleration in tycho's supernova remnant. *Astronomy & Astrophysics*, 538:A81, 2012.

[210] B. Katz and E. Waxman. In which shell-type snrs should we look for gamma-rays and neutrinos from p–p collisions? *Journal of Cosmology and Astroparticle Physics*, 2008(01):018, 2008.

[211] D. Caprioli and A. Spitkovsky. Simulations of ion acceleration at non-relativistic shocks. i. acceleration efficiency. *The Astrophysical Journal*, 783(2):91, 2014.

[212] J. Park et al. Simultaneous acceleration of protons and electrons at nonrelativistic quasiparallel collisionless shocks. *Physical review letters*, 114(8):085003, 2015.

[213] K. Murase et al. High-energy emission from interacting supernovae: New constraints on cosmic-ray acceleration in dense circumstellar environments. *arXiv preprint arXiv:1807.01460*, 2018.

[214] W. van Driel et al. Polar ring spiral galaxy ngc 660. *The Astronomical Journal*, 109:942–959, 1995.

[215] J. N. Douglas et al. The texas survey of radio sources covering-35.5 degrees< declination< 71.5 degrees at 365 mhz. *The Astronomical Journal*, 111:1945, 1996.

[216] M. Large et al. The molonglo reference catalogue of radio sources. *Monthly Notices of the Royal Astronomical Society*, 194(3):693–704, 1981.

[217] J. Condon et al. Radio sources and star formation in the local universe. *The Astronomical Journal*, 124(2):675, 2002.

[218] J. J. Condon et al. The nrao vla sky survey. *The Astronomical Journal*, 115(5):1693, 1998.

[219] L. Dressel and J. Condon. The arecibo 2380 mhz survey of bright galaxies. *The Astrophysical Journal Supplement Series*, 36:53–75, 1978.

[220] C. Bennett et al. The mit-green bank (mg) 5 ghz survey. *The Astrophysical Journal Supplement Series*, 61:1–104, 1986.

[221] R. H. Becker et al. A new catalog of 53,522 4.85 ghz sources. *The Astrophysical Journal Supplement Series*, 75:1–229, 1991.

[222] P. Gregory and J. Condon. The 87gb catalog of radio sources covering delta between o and+ 75 deg at 4.85 ghz. *The Astrophysical Journal Supplement Series*, 75:1011–1291, 1991.

[223] R. Sramek. 5-ghz survey of bright galaxies. *The Astronomical Journal*, 80:771–777, 1975.

[224] F. Fraternali et al. Further clues to the nature of composite liner/h ii galaxies. *Astronomy & Astrophysics*, 418(2):429–443, 2004.

[225] J. Liu. Chandra acis survey of x-ray point sources in 383 nearby galaxies. i. the source catalog. *The Astrophysical Journal Supplement Series*, 192(1):10, 2010.

[226] M. Brightman and K. Nandra. An xmm–newton spectral survey of 12 μm selected galaxies–i. x-ray data. *Monthly Notices of the Royal Astronomical Society*, 413(2):1206–1235, 2011.

[227] N. White et al. The wgacat version of rosat sources. *VizieR On-line Data Catalog: IX/31. Originally published in: Laboratory for High Energy Astrophysics (LHEA/NASA), Greenbelt*, 2000.

[228] R. T. Drzazga et al. Magnetic field evolution in interacting galaxies. *Astronomy & Astrophysics*, 533:A22, 2011.

[229] F. Casse et al. Transport of cosmic rays in chaotic magnetic fields. *Physical Review D*, 65(2):023002, 2001.

[230] R. M. Crocker. Non-thermal insights on mass and energy flows through the galactic centre and into the fermi bubbles. *Monthly Notices of the Royal Astronomical Society*, 423(4):3512–3539, 2012.

[231] B. A. Keeney et al. Does the milky way produce a nuclear galactic wind? *The Astrophysical Journal*, 646(2):951, 2006.

[232] D. K. Strickland and T. M. Heckman. Supernova feedback efficiency and mass loading in the starburst and galactic superwind exemplar m82. *The Astrophysical Journal*, 697(2):2030, 2009.

[233] K. Murase et al. On the implications of late internal dissipation for shallow-decay afterglow emission and associated high-energy gamma-ray signals. *The Astrophysical Journal*, 732(2):77, 2011.

[234] G. R. Blumenthal and R. J. Gould. Bremsstrahlung, synchrotron radiation, and compton scattering of high-energy electrons traversing dilute gases. *Reviews of Modern Physics*, 42(2):237, 1970.

[235] J. Condon et al. Strong radio sources in bright spiral galaxies. ii-rapid star formation and galaxy-galaxy interactions. *The Astrophysical Journal*, 252:102–124, 1982.

[236] M. E. Filho et al. Further clues to the nature of composite liner/h ii galaxies. *Astronomy & Astrophysics*, 418(2):429–443, 2004.

[237] M. K. Argo et al. A new period of activity in the core of ngc 660. *Monthly Notices of the Royal Astronomical Society*, 452(1):1081–1088, 2015.

[238] J. G. Mangum et al. Ammonia thermometry of star-forming galaxies. *The Astrophysical Journal*, 779(1):33, 2013.

[239] M. J. Meyer et al. The hipass catalogue–i. data presentation. *Monthly Notices of the Royal Astronomical Society*, 350(4):1195–1209, 2004.

[240] M. Skrutskie et al. The two micron all sky survey (2mass). *The Astronomical Journal*, 131(2):1163, 2006.

[241] S. Laine et al. A hubble space telescope wfpc2 investigation of the nuclear morphology in the toomre sequence of merging galaxies. *The Astronomical Journal*, 126(6):2717, 2003.

[242] Y. Ueda et al. The asca medium sensitivity survey (the gis catalog project): Source catalog. *The Astrophysical Journal Supplement Series*, 133(1):1, 2001.

[243] M. Pereira-Santaella et al. The x-ray emission of local luminous infrared galaxies. *Astronomy & Astrophysics*, 535:A93, 2011.

[244] L. Jenkins et al. Xmm–newton observations of the starburst merger galaxies ngc 3256 and ngc 3310. *Monthly Notices of the Royal Astronomical Society*, 352(4):1335–1346, 2004.

[245] W. Brinkmann et al. The x-ray agn content of the molonglo 408 mhz survey: Bulk properties of previously optically identified sources. *Astronomy & Astrophysics*, 281:355–374, 1994.

[246] O. Slee. Radio sources observed with the culgoora circular array. *Australian Journal of Physics*, 48(1):143–186, 1995.

[247] J. Condon et al. A 1.425 ghz atlas of the iras bright galaxy sample, part ii. *The Astrophysical Journal Supplement Series*, 103:81–108, 1996.

[248] A. E. Wright et al. The parkes-mit-nrao (pmn) surveys. 2: Source catalog for the southern survey (delta greater than-87.5 deg and less than-37 deg). *The Astrophysical Journal Supplement Series*, 91:111–308, 1994.

[249] J. Whiteoak. Observations of normal galaxies at 5 ghz. *Astrophysical Letters*, 5:29, 1970.

[250] M. Holler et al. Observations of the crab nebula with hess phase ii. *arXiv preprint arXiv:1509.02902*, 2015.

[251] J. Aleksić et al. The major upgrade of the magic telescopes, part ii: A performance study using observations of the crab nebula. *Astroparticle Physics*, 72:76–94, 2016.

[252] A. Abeysekara et al. Observation of the crab nebula with the hawc gamma-ray observatory. *The Astrophysical Journal*, 843(1):39, 2017.

[253] N. Park et al. Performance of the veritas experiment. *arXiv preprint arXiv:1508.07070*, 2015.

[254] K. Bernlöhr et al. Monte carlo design studies for the cherenkov telescope array. *Astroparticle Physics*, 43:171–188, 2013.

[255] T. M. Yoast-Hull et al. Winds, clumps, and interacting cosmic rays in m82. *The Astrophysical Journal*, 768(1):53, 2013.

[256] T. M. Yoast-Hull et al. Gamma-ray puzzle in cygnus x: Implications for high-energy neutrinos. *Physical Review D*, 96(4):043011, 2017.

[257] T. M. Yoast-Hull et al. γ-ray emission from arp 220: indications of an active galactic nucleus. *Monthly Notices of the Royal Astronomical Society: Letters*, 469(1):L89–L93, 2017.

[258] K. Sakamoto et al. Submillimeter array imaging of the co (3-2) line and 860 μm continuum of arp 220: Tracing the spatial distribution of luminosity. *The Astrophysical Journal*, 684(2):957, 2008.

[259] D. Downes and A. Eckart. Black hole in the west nucleus of arp 220. *Astronomy & Astrophysics*, 468(3):L57–L61, 2007.

[260] T. M. Yoast-Hull et al. Cosmic rays, γ-rays, and neutrinos in the starburst nuclei of arp 220. *Monthly Notices of the Royal Astronomical Society*, 453(1):222–228, 2015.

[261] B. C. Lacki et al. The star-forming galaxy contribution to the cosmic mev and gev gamma-ray background. *The Astrophysical Journal*, 786(1):40, 2014.

[262] F. Halzen. High-energy neutrino astrophysics. *Nature Physics*, 13(3):232, 2017.

[263] M. Aartsen et al. First observation of pev-energy neutrinos with icecube. *Physical review letters*, 111(2):021103, 2013.

[264] M. Aartsen et al. Evidence for high-energy extraterrestrial neutrinos at the icecube detector. *Science*, 342(6161):1242856, 2013.

[265] M. Aartsen et al. Observation of high-energy astrophysical neutrinos in three years of icecube data. *Physical review letters*, 113(10):101101, 2014.

[266] M. Aartsen et al. Neutrino emission from the direction of the blazar txs 0506+ 056 prior to the icecube-170922a alert. *Science*, 361(6398):147–151, 2018.

[267] A. Keivani et al. A Multimessenger Picture of the Flaring Blazar TXS 0506+056: implications for High-Energy Neutrino Emission and Cosmic Ray Acceleration. *Astrophys. J.*, 864(1):84, 2018.

[268] C. Yuan et al. High-energy neutrino emission subsequent to gravitational wave radiation from supermassive black hole mergers. *Physical Review D*, 102(8):083013, October 2020.

[269] B. P. Abbott et al. Gw170817: observation of gravitational waves from a binary neutron star inspiral. *Physical Review Letters*, 119(16):161101, 2017.

[270] B. P. Abbott et al. Multi-messenger observations of a binary neutron star merger. *The Astrophysical Journal Letters*, 848(2):L12, October 2017.

[271] B. P. Abbott et al. Observation of gravitational waves from a binary black hole merger. *Physical review letters*, 116(6):061102, 2016.

[272] B. P. Abbott et al. Gw170814: a three-detector observation of gravitational waves from a binary black hole coalescence. *Physical review letters*, 119(14):141101, 2017.

[273] K. Murase and I. Bartos. High-Energy Multimessenger Transient Astrophysics. *Ann. Rev. Nucl. Part. Sci.*, 69:477–506, 2019.

[274] A. Albert et al. Search for high-energy neutrinos from binary neutron star merger gw170817 with antares, icecube, and the pierre auger observatory. *arXiv preprint arXiv:1710.05839*, 2017.

[275] A. Albert et al. *Astrophysical Journal*, 870(2):134, January 2019.

[276] S. S. Kimura et al. High-energy neutrino emission from short gamma-ray bursts: prospects for coincident detection with gravitational waves. *The Astrophysical Journal Letters*, 848(1):L4, 2017.

[277] S. S. Kimura et al. Transejecta high-energy neutrino emission from binary neutron star mergers. *Physical Review D*, 98(4):043020, 2018.

[278] K. Fang and B. D. Metzger. High-energy neutrinos from millisecond magnetars formed from the merger of binary neutron stars. *The Astrophysical Journal*, 849(2):153, 2017.

[279] V. Decoene et al. High-energy neutrinos from fallback accretion of binary neutron star merger remnants. *Journal of Cosmology and Astroparticle Physics*, 2020(04):045, 2020.

[280] M. G. Aartsen et al. Multimessenger observations of a flaring blazar coincident with high-energy neutrino icecube-170922a. *Science*, 361(6398):eaat1378, 2018.

[281] A. Keivani et al. A multimessenger picture of the flaring blazar txs 0506+ 056: Implications for high-energy neutrino emission and cosmic-ray acceleration. *The Astrophysical Journal*, 864(1):84, 2018.

[282] K. Murase et al. Blazar Flares as an Origin of High-Energy Cosmic Neutrinos? *Astrophys. J.*, 865(2):124, 2018.

[283] S. Ansoldi et al. The blazar txs 0506+ 056 associated with a high-energy neutrino: Insights into extragalactic jets and cosmic-ray acceleration. *The Astrophysical Journal Letters*, 863(1):L10, 2018.

[284] P. Padovani et al. Dissecting the region around icecube-170922a: the blazar txs 0506+ 056 as the first cosmic neutrino source. *Monthly Notices of the Royal Astronomical Society*, 480(1):192–203, 2018.

[285] M. Cerruti et al. Leptohadronic single-zone models for the electromagnetic and neutrino emission of txs 0506+ 056. *Monthly Notices of the Royal Astronomical Society: Letters*, 483(1):L12–L16, 2019.

[286] S. Gao et al. Modelling the coincident observation of a high-energy neutrino and a bright blazar flare. *Nature Astronomy*, 3(1):88–92, 2019.

[287] A. Reimer et al. Cascading constraints from neutrino-emitting blazars: the case of txs 0506+ 056. *The Astrophysical Journal*, 881(1):46, 2019.

[288] X. Rodrigues et al. Leptohadronic blazar models applied to the 2014–2015 flare of txs 0506+ 056. *The Astrophysical Journal Letters*, 874(2):L29, 2019.

[289] M. Petropoulou et al. Multi-Epoch Modeling of TXS 0506+056 and Implications for Long-Term High-Energy Neutrino Emission. *Astrophys. J.*, 891:115, 2020.

[290] M. Aartsen et al. Characteristics of the diffuse astrophysical electron and tau neutrino flux with six years of icecube high energy cascade data. *arXiv preprint arXiv:2001.09520*, 2020.

[291] M. Ahlers and F. Halzen. Opening a new window onto the universe with icecube. *Progress in Particle and Nuclear Physics*, 102:73–88, 2018.

[292] P. Mészáros et al. Multi-Messenger Astrophysics. *Nature Rev. Phys.*, 1:585–599, 2019.

[293] P. Padovani et al. A simplified view of blazars: the neutrino background. *Monthly Notices of the Royal Astronomical Society*, 452(2):1877–1887, 2015.

[294] C. Yuan et al. Complementarity of stacking and multiplet constraints on the blazar contribution to the cumulative high-energy neutrino intensity. *The Astrophysical Journal*, 890(1):25, 2020.

[295] S. S. Kimura et al. Neutrino and cosmic-ray emission and cumulative background from radiatively inefficient accretion flows in low-luminosity active galactic nuclei. *The Astrophysical Journal*, 806(2):159, 2015.

[296] K. Murase et al. Hidden cosmic-ray accelerators as an origin of tev-pev cosmic neutrinos. *Physical review letters*, 116(7):071101, 2016.

[297] K. Murase et al. Hidden Cores of Active Galactic Nuclei as the Origin of Medium-Energy Neutrinos: Critical Tests with the MeV Gamma-Ray Connection. *Phys. Rev. Lett.*, 125(1):011101, 2020.

[298] M. Ackermann et al. Resolving the extragalactic γ-ray background above 50 gev with the fermi large area telescope. *Physical Review Letters*, 116(15):151105, 2016.

[299] R. Narayan et al. Grmhd simulations of magnetized advection-dominated accretion on a non-spinning black hole: role of outflows. *Monthly Notices of the Royal Astronomical Society*, 426(4):3241–3259, 2012.

[300] F. Yuan et al. Numerical simulation of hot accretion flows. ii. nature, origin, and properties of outflows and their possible observational applications. *The Astrophysical Journal*, 761(2):130, 2012.

[301] A. Sadowski et al. Energy, momentum and mass outflows and feedback from thick accretion discs around rotating black holes. *Monthly Notices of the Royal Astronomical Society*, 436(4):3856–3874, 2013.

[302] E. Ramirez-Ruiz et al. Events in the life of a cocoon surrounding a light, collapsar jet. *Monthly Notices of the Royal Astronomical Society*, 337(4):1349–1356, December 2002.

[303] W. Zhang et al. Relativistic jets in collapsars. *The Astrophysical Journal*, 586(1):356, 2003.

[304] C. D. Matzner. Supernova hosts for gamma-ray burst jets: dynamical constraints. *Monthly Notices of the Royal Astronomical Society*, 345(2):575–589, October 2003.

[305] O. Bromberg et al. The propagation of relativistic jets in external media. *The Astrophysical Journal*, 740(2):100, October 2011.

[306] A. Mizuta and K. Ioka. Opening angles of collapsar jets. *The Astrophysical Journal*, 777(2):162, November 2013.

[307] E. Nakar and T. Piran. The observable signatures of grb cocoons. *The Astrophysical Journal*, 834(1):28, 2016.

[308] D. Lazzati et al. Off-axis emission of short γ-ray bursts and the detectability of electromagnetic counterparts of gravitational-wave-detected binary mergers. *Monthly Notices of the Royal Astronomical Society*, 471(2):1652–1661, 2017.

[309] T. Matsumoto and S. S. Kimura. Delayed jet breakouts from binary neutron star mergers. *The Astrophysical Journal Letters*, 866(2):L16, 2018.

[310] M. Lyutikov. Conditions for jet breakout in neutron stars' mergers. *Monthly Notices of the Royal Astronomical Society*, 491(1):483–487, 11 2019.

[311] H. Hamidani et al. Jet propagation in neutron star mergers and gw170817. *Monthly Notices of the Royal Astronomical Society*, 491(3):3192–3216, 2020.

[312] M. J. Rees and P. Mészáros. Unsteady outflow models for cosmological gamma-ray bursts. *arXiv preprint astro-ph/9404038*, 1994.

[313] P. J. Armitage and P. Natarajan. Accretion during the merger of supermassive black holes. *The Astrophysical Journal Letters*, 567(1):L9, 2002.

[314] A. Escala et al. The role of gas in the merging of massive black holes in galactic nuclei. ii. black hole merging in a nuclear gas disk. *The Astrophysical Journal*, 630(1):152, 2005.

[315] M. Dotti et al. Supermassive black hole binaries in gaseous and stellar circumnuclear discs: orbital dynamics and gas accretion. *Monthly Notices of the Royal Astronomical Society*, 379(3):956–962, 2007.

[316] J. Pringle. Accretion discs in astrophysics. *Annual Review of Astronomy and Astrophysics*, 19:137–162, January 1981.

[317] S. D'Ascoli et al. Electromagnetic Emission from Supermassive Binary Black Holes Approaching Merger. *The Astrophysical Journal*, 865(2):140, 2018.

[318] S. L. Shapiro and S. A. Teukolsky. *Black holes, white dwarfs, and neutron stars: The physics of compact objects*. 1983.

[319] B. D. Farris et al. Binary black hole accretion during inspiral and merger. *Monthly Notices of the Royal Astronomical Society*, 447:L80–L84, February 2015.

[320] Y.-F. Jiang et al. Super-Eddington Accretion Disks around Supermassive Black Holes. *The Astrophysical Journal*, 880(2):67, 2019.

[321] Y.-F. Jiang et al. Global Radiation Magnetohydrodynamic Simulations of sub-Eddington Accretion Disks around Supermassive Black Holes. *The Astrophysical Journal*, 885(2):144, 2019.

[322] K. Ohsuga et al. Global radiation-magnetohydrodynamic simulations of black-hole accretion flow and outflow: Unified model of three states. *Publications of the Astronomical Society of Japan*, 61(3):7–11, 2009.

[323] K. Akiyama et al. First M87 Event Horizon Telescope Results. V. Physical Origin of the Asymmetric Ring. *The Astrophysical Journal*, 875(1):L5, 2019.

[324] A. Tchekhovskoy et al. Efficient generation of jets from magnetically arrested accretion on a rapidly spinning black hole. *Monthly Notices of the Royal Astronomical Society*, 418(1):L79–L83, November 2011.

[325] R. Harrison et al. Numerically calibrated model for propagation of a relativistic unmagnetized jet in dense media. *Monthly Notices of the Royal Astronomical Society*, 477(2):2128–2140, 2018.

[326] O. Gottlieb et al. High efficiency photospheric emission entailed by formation of a collimation shock in gamma-ray bursts. *Monthly Notices of the Royal Astronomical Society*, 488(1):1416–1426, 2019.

[327] R. Budnik et al. Relativistic radiation mediated shocks. *The Astrophysical Journal*, 725(1):63, 2010.

[328] E. Nakar et al. Relativistic shock breakouts—a variety of gamma-ray flares: from low-luminosity gamma-ray bursts to type ia supernovae. *The Astrophysical Journal*, 747(2):88, March 2012.

[329] R. Sari and A. A. Esin. On the synchrotron self-compton emission from relativistic shocks and its implications for gamma-ray burst afterglows. *The Astrophysical Journal*, 548(2):787, 2001.

[330] A. Panaitescu and P. Kumar. Analytic Light Curves of Gamma-Ray Burst Afterglows: Homogeneous versus Wind External Media. *The Astrophysical Journal*, 543(1):66–76, November 2000.

[331] B. Zhang and P. Meszaros. High-energy spectral components in gamma-ray burst afterglows. *The Astrophysical Journal*, 559(1):110, 2001.

[332] S. Stepney and P. W. Guilbert. Numerical fits to important rates in high temperature astrophysical plasmas. *Monthly Notices of the Royal Astronomical Society*, 204(4):1269–1277, 1983.

[333] M. J. Chodorowski et al. Reaction rate and energy-loss rate for photopair production by relativistic nuclei. *The Astrophysical Journal*, 400:181–185, 1992.

[334] P. F. Harrison et al. Tri-bimaximal mixing and the neutrino oscillation data. *Physics Letters B*, 530(1-4):167–173, 2002.

[335] M. G. Aartsen et al. Extending the Search for Muon Neutrinos Coincident with Gamma-Ray Bursts in IceCube Data. *The Astrophysical Journal*, 843(2):112, 2017.

[336] M. Aartsen et al. Icecube-gen2: a vision for the future of neutrino astronomy in antarctica. *arXiv preprint arXiv:1412.5106*, 2014.

[337] S. Adrian-Martinez et al. Letter of intent for km3net 2.0. *Journal of Physics G: Nuclear and Particle Physics*, 43(8):084001, 2016.

[338] K. Murase et al. Effects of Cosmic Infrared Background on High Energy Delayed Gamma-Rays from Gamma-Ray Bursts. *Astrophys. J.*, 671:1886–1895, 2007.

[339] K. Menou et al. The merger history of supermassive black holes in galaxies. *The Astrophysical Journal*, 558(2):535–542, September 2001.

[340] A. L. Erickcek et al. Supermassive black hole merger rates: uncertainties from halo merger theory. *Monthly Notices of the Royal Astronomical Society*, 371(4):1992–2000, 2006.

[341] M. Micic et al. Supermassive black hole growth and merger rates from cosmological n-body simulations. *Monthly Notices of the Royal Astronomical Society*, 380(4):1533–1540, 2007.

[342] E. Berti. Lisa observations of massive black hole mergers: event rates and issues in waveform modelling. *Classical and Quantum Gravity*, 23(19):S785, 2006.

[343] M. G. Haehnelt. Low frequency gravitational waves from supermassive black holes. *Mon. Not. Roy. Astron. Soc.*, 269:199, 1994.

[344] M. Enoki et al. Gravitational waves from supermassive black hole coalescence in a hierarchical galaxy formation model. *The Astrophysical Journal*, 615(1):19–28, November 2004.

[345] M. Aartsen et al. Differential limit on the extremely-high-energy cosmic neutrino flux in the presence of astrophysical background from nine years of icecube data. *Physical Review D*, 98(6):062003, 2018.

[346] J. Stettner. Measurement of the diffuse astrophysical muon-neutrino spectrum with ten years of icecube data. *arXiv preprint arXiv:1908.09551*, 2019.

[347] E. Waxman and J. Bahcall. High energy neutrinos from astrophysical sources: An upper bound. *Physical Review D*, 59(2):023002, 1998.

[348] O. Martineau-Huynh et al. The giant radio array for neutrino detection. In *EPJ Web of Conferences*, volume 135, pp. 02001. EDP Sciences, 2017.

[349] A. Neronov et al. Sensitivity of a proposed space-based cherenkov astrophysical-neutrino telescope. *Physical Review D*, 95(2):023004, 2017.

[350] T. M. Venters et al. Poemma's target of opportunity sensitivity to cosmic neutrino transient sources. *arXiv preprint arXiv:1906.07209*, 2019.

[351] P. Allison et al. Design and initial performance of the askaryan radio array prototype eev neutrino detector at the south pole. *Astroparticle Physics*, 35(7):457–477, 2012.

[352] S. Barwick et al. A first search for cosmogenic neutrinos with the arianna hexagonal radio array. *Astroparticle Physics*, 70:12–26, 2015.

[353] N. Senno et al. High-energy neutrino flares from x-ray bright and dark tidal disruption events. *The Astrophysical Journal*, 838(1):3, 2017.

[354] M. Ackermann et al. Astrophysics uniquely enabled by observations of high-energy cosmic neutrinos. *arXiv preprint arXiv:1903.04334*, 2019.

[355] A. Franceschini and G. Rodighiero. The extragalactic background light revisited and the cosmic photon-photon opacity. *Astronomy & Astrophysics*, 603:A34, 2017.

[356] E. Kun et al. Very long baseline interferometry radio structure and radio brightening of the high-energy neutrino emitting blazar txs 0506+ 056. *Monthly Notices of the Royal Astronomical Society: Letters*, 483(1):L42–L46, 2019.

[357] S. Britzen et al. A cosmic collider: Was the icecube neutrino generated in a precessing jet-jet interaction in txs 0506+ 056? *Astronomy & Astrophysics*, 630:A103, 2019.

[358] O. de Bruijn et al. Recurrent neutrino emission from supermassive black hole mergers. *arXiv preprint arXiv:2006.11288*, 2020.

[359] E. Ros et al. Apparent superluminal core expansion and limb brightening in the candidate neutrino blazar TXS 0506+056. *Astron. Astrophys.*, 633:L1, 2020.

[360] A. Mizuta and K. Ioka. Opening Angles of Collapsar Jets. *The Astrophysical Journal*, 777(2):162, November 2013.

[361] O. Bromberg et al. The Propagation of Relativistic Jets in External Media. *The Astrophysical Journal*, 740(2):100, October 2011.

[362] K. Akiyama et al. First M87 Event Horizon Telescope Results. V. Physical Origin of the Asymmetric Ring. *ApJL*, 875(1):L5, April 2019.

[363] C. Yuan et al. Post-merger Jets from Supermassive Black Hole Coalescences as Electromagnetic Counterparts of Gravitational Wave Emission. *The Astrophysical Journal Letters*, 911(1):L15, April 2021.

[364] P. Kroupa et al. Very high redshift quasars and the rapid emergence of supermassive black holes. *Monthly Notices of the Royal Astronomical Society*, 498(4):5652–5683, August 2020.

[365] K. S. Thorne and V. Braginskii. Gravitational-wave bursts from the nuclei of distant galaxies and quasars-proposal for detection using doppler tracking of interplanetary spacecraft. *The Astrophysical Journal Letters*, 204:L1–L6, February 1976.

[366] A. Sesana et al. Low-Frequency Gravitational Radiation from Coalescing Massive Black Hole Binaries in Hierarchical Cosmologies. *The Astrophysical Journal*, 611(2):623–632, August 2004.

[367] J. Baker et al. Space based gravitational wave astronomy beyond lisa. 51:243, September 2019.

[368] C. M. F. Mingarelli et al. The local nanohertz gravitational-wave landscape from supermassive black hole binaries. *Nature Astronomy*, 1:886–892, November 2017.

[369] S. R. Taylor et al. Supermassive black-hole demographics & environments with pulsar timing arrays. *Bulletin of the American Astronomical Society*, 51(3):336, May 2019.

[370] Z. Arzoumanian et al. The NANOGrav 12.5 yr Data Set: Search for an Isotropic Stochastic Gravitational-wave Background. *The Astrophysical Journal Letters*, 905(2):L34, December 2020.

[371] P. Moesta et al. On the Detectability of Dual Jets from Binary Black Holes. *The Astrophysical Journal Letters*, 749(2):L32, April 2012.

[372] B. J. Kelly et al. Prompt electromagnetic transients from binary black hole mergers. *Physical Review D*, 96(12):123003, December 2017.

[373] Z. Haiman. Electromagnetic chirp of a compact binary black hole: A phase template for the gravitational wave inspiral. *Physical Review D*, 96(2):023004, July 2017.

[374] S. d'Ascoli et al. Electromagnetic emission from supermassive binary black holes approaching merger. *The Astrophysical Journal*, 865(2):140, October 2018.

[375] J. D. Schnittman and J. H. Krolik. The infrared afterglow of supermassive black hole mergers. *The Astrophysical Journal*, 684(2):835–844, September 2008.

[376] Z. Haiman et al. Identifying decaying supermassive black hole binaries from their variable electromagnetic emission. *Classical and Quantum Gravity*, 26(9):094032, May 2009.

[377] T. Tanaka and K. Menou. Time-dependent models for the afterglows of massive black hole mergers. *The Astrophysical Journal*, 714(1):404–422, May 2010.

[378] J. D. Schnittman. Electromagnetic counterparts to black hole mergers. *Classical and Quantum Gravity*, 28(9):094021, May 2011.

[379] V. Ravi. Flares from Coalescing Black Holes in the Centimeter-Wavelength Transient Sky. In E. Murphy, editor, *Science with a Next Generation Very Large Array*, volume 517 of *Astronomical Society of the Pacific Conference Series*, pp. 781, December 2018.

[380] P. Mészáros et al. Multi-messenger astrophysics. *Nature Reviews Physics*, 1(10):585–599, October 2019.

[381] C. Yuan et al. High-energy neutrino emission subsequent to gravitational wave radiation from supermassive black hole mergers. *Phys. Rev. D*, 102(8):083013, 2020.

[382] Y.-F. Jiang et al. Super-eddington accretion disks around supermassive black holes. *The Astrophysical Journal*, 880(2):67, August 2019.

[383] Y.-F. Jiang et al. Global radiation magnetohydrodynamic simulations of sub-eddington accretion disks around supermassive black holes. *The Astrophysical Journal*, 885(2):144, November 2019.

[384] K. Ohsuga et al. Global radiation-magnetohydrodynamic simulations of black-hole accretion flow and outflow: unified model of three states. *Publications of the Astronomical Society of Japan*, 61(3):L7–L11, June 2009.

[385] K. Akiyama et al. First m87 event horizon telescope results. v. physical origin of the asymmetric ring. *The Astrophysical Journal Letters*, 875(1):L5, April 2019.

[386] N. Senno et al. Choked Jets and Low-Luminosity Gamma-Ray Bursts as Hidden Neutrino Sources. *Phys. Rev. D*, 93(8):083003, 2016.

[387] E. Nakar. A unified picture for low-luminosity and long gamma-ray bursts based on the extended progenitor of llgrb 060218/SN 2006aj. *Astrophys. J.*, 807(2):172, 2015.

[388] K. Murase and K. Ioka. TeV–PeV Neutrinos from Low-Power Gamma-Ray Burst Jets inside Stars. *Phys. Rev. Lett.*, 111(12):121102, 2013.

[389] R. Wijers and T. Galama. Physical parameters of grb 970508 and grb 971214 from their afterglow synchrotron emission. *The Astrophysical Journal*, 523(1):177–186, September 1999.

[390] K. Murase et al. Probing cosmic ray ion acceleration with radio-submm and gamma-ray emission from interaction-powered supernovae. *Monthly Notices of the Royal Astronomical Society*, 440(3):2528–2543, May 2014.

[391] B. T. Zhang et al. External Inverse-Compton Emission from Low-Luminosity Gamma-Ray Bursts: Application to GRB 190829A. *arXiv: 2012.07796*, 2020.

[392] K. Arun et al. Massive black-hole binary inspirals: results from the lisa parameter estimation taskforce. *Classical and Quantum Gravity*, 26(9):094027, May 2009.

[393] P. Amaro-Seoane et al. Low-frequency gravitational-wave science with elisa/ngo. *Classical and Quantum Gravity*, 29(12):124016, June 2012.

[394] T. Dal Canton et al. Detectability of Modulated X-Rays from LISA's Supermassive Black Hole Mergers. *The Astrophysical Journal*, 886(2):146, December 2019.

[395] E. Kara et al. X-ray follow-up of extragalactic transients. *Bulletin of the American Astronomical Society*, 51(3):112, May 2019.

[396] P. Mészáros and M. J. Rees. Grb 990123: reverse and internal shock flashes and late afterglow behaviour. *Monthly Notices of the Royal Astronomical Society*, 306(3):L39–L43, July 1999.

[397] S. Kobayashi and B. Zhang. Grb 021004: reverse shock emission. *The Astrophysical Journal Letters*, 582(2):L75–L78, January 2003.

[398] C. Rodriguez et al. A Compact Supermassive Binary Black Hole System. *The Astrophysical Journal*, 646(1):49–60, July 2006.

[399] A. Mangiagli et al. Observing the inspiral of coalescing massive black hole binaries with LISA in the era of multimessenger astrophysics. *Physical Review D*, 102(8):084056, October 2020.

[400] C. Yuan et al. GeV Signature of Short Gamma-Ray Bursts in Active Galactic Nuclei. *arXiv e-prints*, pp. arXiv:2112.07653, December 2021.

[401] K. Murase et al. On the Implications of Late Internal Dissipation for Shallow-decay Afterglow Emission and Associated High-energy Gamma-ray Signals. *The Astrophysical Journal*, 732(2):77, May 2011.

[402] P. Veres and P. Mészáros. Single- and Two-component Gamma-Ray Burst Spectra in the Fermi GBM-LAT Energy Range. *The Astrophysical Journal*, 755(1):12, August 2012.

[403] B. T. Zhang et al. External Inverse-Compton Emission from Low-luminosity Gamma-Ray Bursts: Application to GRB 190829A. *The Astrophysical Journal*, 920(1):55, October 2021.

[404] B. T. Zhang et al. External Inverse-Compton Emission Associated with Extended and Plateau Emission of Short Gamma-Ray Bursts: Application to GRB 160821B. *The Astrophysical Journal Letters*, 908(2):L36, February 2021.

[405] J. Frank et al. *Accretion Power in Astrophysics: Third Edition*. 2002.

[406] K. D. Kanagawa et al. Formation of a disc gap induced by a planet: effect of the deviation from Keplerian disc rotation. *Monthly Notices of the Royal Astronomical Society*, 448(1):994–1006, March 2015.

[407] K. Ohsuga et al. Global Radiation-Magnetohydrodynamic Simulations of Black-Hole Accretion Flow and Outflow: Unified Model of Three States. *Publications of the Astronomical Society of Japan*, 61(3):L7–L11, June 2009.

[408] Y.-F. Jiang et al. A global three-dimensional radiation magneto-hydrodynamic simulation of super-eddington accretion disks. *The Astrophysical Journal*, 796(2):106, 2014.

[409] A. Sadowski et al. Numerical simulations of super-critical black hole accretion flows in general relativity. *Monthly Notices of the Royal Astronomical Society*, 439(1):503–520, March 2014.

[410] R. Weaver et al. Interstellar bubbles. II. Structure and evolution. *The Astrophysical Journal*, 218:377–395, December 1977.

[411] B.-C. Koo and C. F. McKee. Dynamics of Wind Bubbles and Superbubbles. I. Slow Winds and Fast Winds. *The Astrophysical Journal*, 388:93, March 1992.

[412] C.-L. Jiao et al. Comparison between Radiation-Hydrodynamic Simulation of Supercritical Accretion Flows and a Steady Model with Outflows. *The Astrophysical Journal*, 806(1):93, June 2015.

[413] T. Kitaki et al. Systematic two-dimensional radiation-hydrodynamic simulations of super-Eddington accretion flow and outflow: Comparison with the slim disk model. *Publications of the Astronomical Society of Japan*, 70(6):108, December 2018.

[414] Y.-F. Jiang et al. A Global Three-dimensional Radiation Magneto-hydrodynamic Simulation of Super-Eddington Accretion Disks. *The Astrophysical Journal*, 796(2):106, December 2014.

[415] C. Nixon et al. Tearing up the disc: misaligned accretion on to a binary. *Monthly Notices of the Royal Astronomical Society*, 434(3):1946–1954, September 2013.

[416] M. J. Rees and P. Meszaros. Unsteady Outflow Models for Cosmological Gamma-Ray Bursts. *The Astrophysical Journal Letters*, 430:L93, August 1994.

[417] J. C. McKinney and D. A. Uzdensky. A reconnection switch to trigger gamma-ray burst jet dissipation. *Monthly Notices of the Royal Astronomical Society*, 419(1):573–607, January 2012.

[418] K. Murase and K. Ioka. TeV-PeV Neutrinos from Low-Power Gamma-Ray Burst Jets inside Stars. *Physical Review Letters*, 111(12):121102, September 2013.

[419] S. S. Kimura et al. Transejecta high-energy neutrino emission from binary neutron star mergers. *Physical Review D*, 98(4):043020, August 2018.

[420] C. D. Dermer and G. Menon. *High Energy Radiation from Black Holes: Gamma Rays, Cosmic Rays, and Neutrinos*. 2009.

[421] J. D. Finke et al. Modeling the Extragalactic Background Light from Stars and Dust. *The Astrophysical Journal*, 712(1):238–249, March 2010.

[422] I. Al Samarai et al. Science with the cherenkov telescope array. 2019.

[423] K. Murase et al. Effects of the Cosmic Infrared Background on Delayed High-Energy Emission from Gamma-Ray Bursts. *The Astrophysical Journal*, 671(2):1886–1895, December 2007.

[424] J. P. Norris and J. T. Bonnell. Short Gamma-Ray Bursts with Extended Emission. *The Astrophysical Journal*, 643(1):266–275, May 2006.

[425] T. Sakamoto et al. The Second Swift Burst Alert Telescope Gamma-Ray Burst Catalog. *The Astrophysical Journals*, 195(1):2, July 2011.

[426] Y. Kaneko et al. Short gamma-ray bursts with extended emission observed with Swift/BAT and Fermi/GBM. *Monthly Notices of the Royal Astronomical Society*, 452(1):824–837, September 2015.

[427] S. Kisaka et al. Bimodal Long-lasting Components in Short Gamma-Ray Bursts: Promising Electromagnetic Counterparts to Neutron Star Binary Mergers. *The Astrophysical Journal*, 846(2):142, September 2017.

[428] Z. G. Dai et al. X-ray Flares from Postmerger Millisecond Pulsars. *Science*, 311(5764):1127–1129, February 2006.

[429] B. D. Metzger et al. Short-duration gamma-ray bursts with extended emission from protomagnetar spin-down. *Monthly Notices of the Royal Astronomical Society*, 385(3):1455–1460, April 2008.

[430] M. V. Barkov and A. S. Pozanenko. Model of the extended emission of short gamma-ray bursts. *Monthly Notices of the Royal Astronomical Society*, 417(3):2161–2165, November 2011.

[431] N. Bucciantini et al. Short gamma-ray bursts with extended emission from magnetar birth: jet formation and collimation. *Monthly Notices of the Royal Astronomical Society*, 419(2):1537–1545, January 2012.

[432] A. Rowlinson et al. Signatures of magnetar central engines in short GRB light curves. *Monthly Notices of the Royal Astronomical Society*, 430(2):1061–1087, April 2013.

[433] B. P. Gompertz et al. Magnetar powered GRBs: explaining the extended emission and X-ray plateau of short GRB light curves. *Monthly Notices of the Royal Astronomical Society*, 438(1):240–250, February 2014.

[434] S. Kisaka and K. Ioka. Long-lasting Black Hole Jets in Short Gamma-Ray Bursts. *The Astrophysical Journal Letters*, 804(1):L16, May 2015.

[435] X. Bai et al. The Large High Altitude Air Shower Observatory (LHAASO) Science White Paper. *arXiv e-prints*, pp. arXiv:1905.02773, May 2019.

[436] J. Aleksić et al. The major upgrade of the MAGIC telescopes, Part II: A performance study using observations of the Crab Nebula. *Astroparticle Physics*, 72:76–94, January 2016.

[437] M. Holler et al. Observations of the Crab Nebula with H.E.S.S. Phase II. *arXiv e-prints*, pp. arXiv:1509.02902, September 2015.

[438] C. Meegan et al. The Fermi Gamma-ray Burst Monitor. *The Astrophysical Journal*, 702(1):791–804, September 2009.

[439] A. U. Abeysekara et al. On the sensitivity of the HAWC observatory to gamma-ray bursts. *Astroparticle Physics*, 35(10):641–650, May 2012.

[440] M. Ackermann et al. Fermi Observations of GRB 090510: A Short-Hard Gamma-ray Burst with an Additional, Hard Power-law Component from 10 keV TO GeV Energies. *The Astrophysical Journal*, 716(2):1178–1190, June 2010.

[441] B. McKernan et al. Black hole, neutron star, and white dwarf merger rates in AGN discs. *Monthly Notices of the Royal Astronomical Society*, 498(3):4088–4094, November 2020.

[442] S. Inoue et al. Gamma-ray burst science in the era of the Cherenkov Telescope Array. *Astroparticle Physics*, 43:252–275, March 2013.

[443] I. Bartos et al. Rapid and Bright Stellar-mass Binary Black Hole Mergers in Active Galactic Nuclei. *The Astrophysical Journal*, 835(2):165, February 2017.

[444] J.-P. Zhu et al. Neutron Star Mergers in Active Galactic Nucleus Accretion Disks: Cocoon and Ejecta Shock Breakouts. *The Astrophysical Journal Letters*, 906(2):L11, January 2021.

[445] K. Murase et al. Hidden Cosmic-Ray Accelerators as an Origin of TeV-PeV Cosmic Neutrinos. *Physical Review Letters*, 116(7):071101, February 2016.

[446] S. S. Kimura et al. High-energy Neutrino Emission from Short Gamma-Ray Bursts: Prospects for Coincident Detection with Gravitational Waves. *The Astrophysical Journal Letters*, 848(1):L4, October 2017.

[447] C. Yuan et al. Complementarity of Stacking and Multiplet Constraints on the Blazar Contribution to the Cumulative High-energy Neutrino Intensity. *The Astrophysical Journal*, 890(1):25, February 2020.

[448] M. Ahlers and K. Murase. Probing the galactic origin of the icecube excess with gamma rays. *Physical Review D*, 90(2):023010, 2014.

[449] M. Aartsen et al. Searches for time-dependent neutrino sources with icecube data from 2008 to 2012. *The Astrophysical Journal*, 807(1):46, 2015.

[450] M. Aartsen et al. Flavor ratio of astrophysical neutrinos above 35 tev in icecube. *Physical review letters*, 114(17):171102, 2015.

[451] M. Ahlers and F. Halzen. High-energy cosmic neutrino puzzle: a review. *Reports on Progress in Physics*, 78(12):126901, December 2015.

[452] P. Mészáros. Astrophysical Sources of High-Energy Neutrinos in the IceCube Era. *Annual Review of Nuclear and Particle Science*, 67:45–67, October 2017.

[453] R. D. Blandford and M. J. Rees. Extended and compact extragalactic radio sources: Interpretation and theory. *Physica Scripta*, 17(3):265–274, mar 1978.

[454] C. M. Urry and P. Padovani. Unified schemes for radio-loud active galactic nuclei. *Publications of the Astronomical Society of the Pacific*, 107(715):803, 1995.

[455] A. Mücke and R. Protheroe. Neutrino emission from hbls and lbls. *arXiv preprint astro-ph/0105543*, 2001.

[456] K. Murase. Active Galactic Nuclei as High-Energy Neutrino Sources. In T. Gaisser and A. Karle, editors, *Neutrino Astronomy: Current Status, Future Prospects*, pp. 15–31. 2017.

[457] E. Resconi et al. Connecting blazars with ultrahigh-energy cosmic rays and astrophysical neutrinos. *Monthly Notices of the Royal Astronomical Society*, 468(1):597–606, Jun 2017.

[458] C. D. Dermer et al. Photopion production in black-hole jets and flat-spectrum radio quasars as PeV neutrino sources. *Journal of High Energy Astrophysics*, 3:29–40, September 2014.

[459] F. Tavecchio and G. Ghisellini. High-energy cosmic neutrinos from spine-sheath bl lac jets. *Monthly Notices of the Royal Astronomical Society*, 451(2):1502–1510, 2015.

[460] C. Righi et al. High-energy emitting BL Lacs and high-energy neutrinos. Prospects for the direct association with IceCube and KM3NeT. *Astronomy & Astrophysics*, 2017.

[461] X. Rodrigues et al. Neutrinos and Ultra-high-energy Cosmic-ray Nuclei from Blazars. *The Astrophysical Journal*, 854(1):54, February 2018.

[462] M. Ajello et al. The origin of the extragalactic gamma-ray background and implications for dark matter annihilation. *The Astrophysical Journal Letters*, 800(2):L27, 2015.

[463] M. Ajello et al. The luminosity function of fermi-detected flat-spectrum radio quasars. *The Astrophysical Journal*, 751(2):108, 2012.

[464] M. Ajello et al. The cosmic evolution of fermi bl lacertae objects. *The Astrophysical Journal*, 780(1):73, 2013.

[465] A. Abdo et al. The fermi-lat high-latitude survey: source count distributions and the origin of the extragalactic diffuse background. *The Astrophysical Journal*, 720(1):435, 2010.

[466] M. Ackermann et al. The Third Catalog of Active Galactic Nuclei Detected by the Fermi Large Area Telescope. *The Astrophysical Journal*, 810(1):14, September 2015.

[467] M. G. Aartsen et al. Evidence for Astrophysical Muon Neutrinos from the Northern Sky with IceCube. *Physical Review Letters*, 115(8):081102, August 2015.

[468] M. G. Aartsen et al. All-sky Search for Time-integrated Neutrino Emission from Astrophysical Sources with 7 yr of IceCube Data. *The Astrophysical Journal*, 835(2):151, February 2017.

[469] M. G. Aartsen et al. Search for steady point-like sources in the astrophysical muon neutrino flux with 8 years of IceCube data. *European Physical Journal C*, 79(3):234, March 2019.

[470] M. Aartsen et al. The icecube neutrino observatory-contributions to icrc 2017 part i: Searches for the sources of astrophysical neutrinos. *arXiv preprint arXiv:1710.01179*, 2017.

[471] M. G. Aartsen et al. Constraints on Minute-Scale Transient Astrophysical Neutrino Sources. *Physical Review Letters*, 122(5):051102, February 2019.

[472] K. Murase et al. Hidden Cores of Active Galactic Nuclei as the Origin of Medium-Energy Neutrinos: Critical Tests with the MeV Gamma-Ray Connection. 2019.

[473] F. Halzen et al. On the Neutrino Flares from the Direction of TXS 0506+056. *The Astrophysical Journal Letters*, 874(1):L9, March 2019.

[474] M. W. E. Smith et al. The Astrophysical Multimessenger Observatory Network (AMON). *Astroparticle Physics*, 45:56–70, May 2013.

[475] H. A. Ayala Solares et al. The Astrophysical Multimessenger Observatory Network (AMON): Performance and science program. *Astroparticle Physics*, 114:68–76, January 2020.

[476] P. Chang et al. Cyberinfrastructure Requirements to Enhance Multi-messenger Astrophysics. *Bulletin of American Astronomy Society*, 51(3):436, May 2019.

Vita

Chengchao Yuan

Education

- *Ph.D. in Physics*, Department of Physics, 2022
  The Pennsylvania State University
- *B. Sc. in Astronomy*, School of Astronomy and Space Science, 2016
  Nanjing University

Selected Awards

- W. Donald Miller Graduate Fellowship, PSU, 2022 & 2021
- David C. Duncan Graduate Fellowship, PSU, 2019-2022
- Homer F. Braddock Scholarship, PSU, 2017

Publications

- **Yuan, C.**, Murase, K., Guetta, D., Pe'er, A., Bartos, I., & Mészáros, P., (2021) "GeV Signature of Short Gamma-Ray Bursts in Active Galactic Nuclei", arXiv: 2112.07653
- **Yuan, C.**, Murase, K., Zhang, B. T., Kimura, S. S. & Mészáros, P. (2021) "Post-Merger Jets from Supermassive Black Hole Coalescences as Electromagnetic Counterparts of Gravitational Wave Emission", *ApJL*, 911 L15
- Zhang, T. B., Murase, K., **Yuan, C**., Kimura, S. S. & Mészáros, P. (2020) "External Inverse-Compton Emission Associated with Extended and Plateau Emission of Short Gamma-Ray Bursts: Application to GRB 160821B", *ApJL* 908 L36
- **Yuan, C.**, Murase, K., Kimura, S. & Mészáros, P. (2020) "High-energy neutrino emission subsequent to gravitational wave radiation from supermassive black hole mergers", *Phys. Rev. D* 102, 083013
- **Yuan, C.**, Murase, K. & Mészáros, P. (2020) "Complementarity of Stacking and Multiplet Constraints on the Blazar Contribution to the Cumulative High-Energy Neutrino Intensity", *ApJ*, 890:1
- **Yuan, C.**, Murase, K. & Mészáros, P. (2019) "Secondary Radio and X-ray Emissions from Galaxy Mergers", *ApJ*, 878:76
- **Yuan, C.**, Mészáros, P., Murase K. & Jeong, D. (2018) "Cumulative Neutrino and Gamma-Ray Backgrounds from Halo and Galaxy Mergers", *ApJ*, 857:50
- **Yuan, C.** & Wang, F. (2015) "Cosmological Test Using Strong Gravitational Lensing Systems", *MNRAS*, 452:3.